Muon Antineutrino Disappearance Measurement by the T2K Experiment

Takahiro Hiraki

February 22, 2016

Department of Physics, Graduate School of Science
Kyoto University

Dissertation Committee:

Tsuyoshi Nakaya
Atsuko K. Ichikawa
Akihiro Minamino
Toru Tanimori
Takaaki Tanaka

Abstract

We report the measurement of the muon antineutrino disappearance in the T2K experiment.

The T2K (Tokai to Kamioka) experiment is an accelerator-based long-baseline neutrino oscillation experiment to measure the neutrino mixing parameters. The neutrino beam is produced by using the 30 GeV proton beam at the J-PARC accelerator and is detected by the near detector complex and by the far detector, Super-Kamiokande, which is 295 km away from J-PARC. The muon monitor and the on-axis near detector monitor the beam profile. The neutrino beam direction has been well-controlled during the whole period. The far detector and one of the near detectors are placed in the off-axis direction to the neutrino beam center, where the neutrino beam has a narrow energy peak of 0.6 GeV and the muon neutrino (ν_μ) survival probability is expected to be minimal.

In 2014, T2K took the first antineutrino beam data. We conducted beam commissioning studies in the antineutrino beam mode by using the muon monitor in order to understand the muon beam profile and its dependence on the changes of the beamline condition. Since the muon beam intensity at the muon monitor is very high, signal decrease of the MUMON sensors should be carefully monitored. We studied the long-term stability of the detectors in the muon monitor and the diamond detectors, which we installed on trial.

The neutrino fluxes and their uncertainties at the near and far detector in the antineutrino mode as well as in the neutrino mode are predicted by the Monte Carlo simulation with data from external hadron production experiments. We improve the neutrino flux prediction by including the recent data from the NA61/SHINE experiment at CERN. The uncertainties of the neutrino flux parameters and some types of the neutrino-nucleus interactions at the far detector are reduced by the measurement at the off-axis near detector. By using the improved neutrino event prediction, we performed the first muon antineutrino ($\overline{\nu}_\mu$) disappearance analysis in the T2K experiment. Using a dataset corresponding to 4.01×10^{20} protons on target which were accumulated between 2014 and 2015, we observed 34 fully contained μ-like events, while the expected number of events in case of the maximal disappearance is 34.6. By this measurement, we clearly observe the $\overline{\nu}_\mu$ disappearance. The best-fit antineutrino oscillation parameters are: $\sin^2\overline{\theta}_{23} = 0.45$ and $|\Delta\overline{m}^2_{32}| = 2.51\times10^{-3}$ eV^2, where $\overline{\theta}$ and $\Delta\overline{m}^2$ refer to the mixing angle and the mass-squared splitting of the antineutrino, respectively. The 68.3% confidence interval of $\sin^2\overline{\theta}_{23}$ is $0.38-0.64$ and that of $|\Delta\overline{m}^2_{32}|$ is $2.26-2.80$ ($\times10^{-3}$ eV^2). These results are in agreement with $\sin^2\theta_{23}$ and $|\Delta m^2_{32}|$ measured by T2K. The precision of these results is similar to the existing antineutrino parameter measurements. Sensitivities of the $\overline{\nu}_\mu$ disappearance analysis in cases of larger amount of data which will be taken in future are also studied.

Acknowledgments

I would like to thank a lot of people who have supported me in various scenes here.

First of all, I would like to express the deepest appreciation to Prof. Tsuyoshi Nakaya, who is my supervisor and the current spokesperson for the T2K experiment. He gave me great oppotunities to study neutrino physics. His advice and encouragements throughout my reserch have always motivated me. I am deeply indebted to Prof. Atsuko K. Ichikawa, who is also my supervisor. She has taught me enormous things and gave me valuable expertise since I was a master's student. She has introduced interesting works with muon monitor, flux simulation, and oscillation analyses which are the main topic of this thesis. I am grateful to Dr. Akihiro Minamino who shared the office in Kyoto University and gave me a lot of advice.

I owe my deep debt to KEK neutrino group. Prof. T. Kobayashi, who is former spokesperson for the T2K experiment, advances this experiment with his strong leadership. Prof. T. Nakadaira leads beam group and gave me fruitful oppotunities to execute muon monitor studies. Dr. K. Sakashita and Dr. M. Friend gave me heipful advice on muon monitor studies and flux simulation. I also would like to thank KEK neutrino group: Prof. T. Hasegawa, Prof. Y. Fujii, Prof. Y. Yamada, Prof. T. Ishii, Prof. T. Tsukamoto, Prof. M. Tada, Lect. Y. Oyama, Dr. T. Sekiguchi, Dr. T. Ishida, Dr. R. Oota, and L. Zambelli.

I would like to express my gratitude to past and present MUMONers. Prof. M. Yokoyama, Prof. T. Maruyama, Dr. K. Matsuoka, Mr. H. Kubo, Dr. A. Murakami, Dr. K. Suzuki, Mr. K. Nakamura, Dr. N. Patel, and Mr. K. Kondo. Without their excellent works and helps on operation and analyses, I could not accomplish my studies.

I would like to express my heartfelt appreciation to Dr. M. Hartz, who leads flux simulation group and neutrino oscillation analysis group for supporting my reserch on these groups. I would like to express my sincere appreciation to Dr. C. Bronner, Dr. H. Tanaka, Dr. J. Imber and Prof. M. Shiozawa who gave me plenty of advice on neutrino oscillation analyses.

I would like to thank all the collaborators of the T2K experiment. In particular, I would like to appreciate Dr. M. Ikeda, Dr. K. Ieki, Dr. K. Nakamura, Dr. T. Kikawa, Dr. K. Huang, Mr. S. Takahashi, Dr. S. Cao, Dr. B. Quilain, Mr. T. Yamauchi, Ms. S. Hirota, Mr. T. Hayashino, Mr. K. Yoshida, Mr. S. Ban, Mr. M. Jiang, Mr. K. Yoshida, Ms. M. Yamamoto who worked together as Kyoto University T2K group. I salute J-PARC accelerator people for their tremendous efforts to provide intense and stable proton beams.

I am thankful to the other members of High Energy Physics Laboratory in Kyoto University: Prof. M. Ishino, Prof. T. Nomura, Dr. H. Nanjo, Dr. T. Sumida, Dr. H. Morii, Dr. K. Shiomi, Dr. T. Masuda, Mr. N. Kawasaki, Dr. Y. Maeda, Mr. D. Naito, Mr. G. Takahashi, Mr. K. Goda, Mr. S. Seki, Mr. T. Tashiro, Mr. T. Nagasaki, Mr. S. Akiyama, Mr. N. Kamo, Mr. K. Tateishi, Mr. T. Hineno, Mr. Y. Ishiyama, Mr. I. Kamiji, Mr. T. Kunigo, Mr. K. Nakagiri, Mr. S. Shinohara, Mr. K. Haneda, Mr. R. Monden, Ms. S. Yanagita, Mr. S. Akatsuka, Mr. Y. Asida, Mr. S. Tanaka, Ms. Y. Nakanishi, Mr. Y. Noguchi, and Ms. A. Hiramoto. I appreciate the secretaries of Kyoto University, J-PARC Center Users Office and dormitory staff, and administrative staff in Kamioka Observatory. I acknowledge the financial support from Grant-in-Aid for JSPS Fellows (KAKENHI Grant Number 13J00383).

Last of all, I would like to express special thanks to my family.

Takahiro Hiraki
Kyoto University
March, 2016

Contents

Chapter 1

Introduction

High energy physics is an area of physics where fundamental laws governing our universe are investigated by researching various properties of elementary particles. Although the Standard Model (SM) of particle physics has been greatly successful in describing almost all of phenomena, some phenomena still remain unexplained by the SM.

Neutrino oscillation is a quantum mechanical phenomenon where a neutrino generated with a specific flavor converts into another type during flight. This is a physics beyond the SM because it occurs only when neutrinos have non-zero mass.

1.1 Brief history of neutrino

In 1930, W. Pauli [1] postulated a neutral particle with a spin of 1/2, which he called neutron and is now named neutrino, in order to explain the missing energy in β decay [2]. Detection of neutrinos was considered to be impossible because neutrinos very weakly interact with other particles, but in 1956 F. Reines and C.L. Cowan [3] succeeded in observing neutrinos from a nuclear reactor. Then in 1962, L.M. Lederman, M. Schwartz and J. Steinberger *et al.* [4] showed that neutrinos produced by the decay of pions generate muons rather than electrons using the 15 GeV proton accelerator (AGS) in Brookhaven. This means ν_μ is different particle from ν_e. Later in 2000, the DONUT collaboration [5] directly observed ν_τ produced by the 800 GeV proton accelerator (Tevatron) in Fermilab by identifying the tracks of tau leptons in the emulsion detectors. Detailed history of neutrino is found elsewhere [6].

1.2 Neutrino Sources

Neutrinos are emitted from varieties of sources. Accelerator neutrinos are artificially generated from decays of charged πs and Ks which are produced by hitting protons to a target. The measurement of neutrinos from an accelerator, the T2K experiment, is the main topic of this thesis. Nuclear reactor plants are also sources of artificial neutrinos: $\overline{\nu}_e$s are emitted from β decays of radioactive isotopes.

There are a couple of natural neutrino sources. In the sun, ν_es are always produced by nuclear fusion reactions. Cosmic ray hitting nuclei in the atmosphere of the Earth generates hadron showers which produce atmospheric neutrinos by their decays. When supernovae occur, in which a massive star collapses and explodes, a very strong neutrino flux is produced. A burst of neutrinos from the SN (SuperNova) 1987A was observed at Kamiokande [7], IMB [8], and Baksan [9]. High energy cosmogenic neutrinos were observed by the IceCube experiment [10]. Inside the Earth, the decays of Thorium, Uranium, and Potassium produce geoneutrinos. Measurements of neutrinos from each source have been giving unique information about its source and particle physics.

1.3 Neutrino oscillation theory

1.3.1 Neutrino mixing

Let $|\nu_\alpha\rangle = |\nu_{\alpha L}\rangle$ ($|\overline{\nu}_\alpha\rangle = |\overline{\nu}_{\alpha R}\rangle$) ($\alpha = e,\ \mu,\ \tau$) flavor eigenstates of left-handed neutrinos (right-handed antineutrinos) [1]. These states are orthogonal: $\langle\nu_\beta|\nu_\alpha\rangle = \delta_{\alpha\beta}$, $\langle\overline{\nu}_\beta|\overline{\nu}_\alpha\rangle = \delta_{\alpha\beta}$, $\langle\overline{\nu}_\beta|\nu_\alpha\rangle = 0$. $|\nu_\alpha\rangle$ are expressed as linear combinations of the mass eigenstates:

$$|\nu_\alpha\rangle = \sum_i U_{\alpha i}|\nu_i\rangle, \tag{1.3.1}$$

where U is a unitary mixing matrix and $|\nu_i\rangle$ are the mass eigenstates. This matrix is called PMNS matrix which is an acronym taken from its proposers, B. Pontecorvo [11] [12] [13], Z. Maki, M. Nakagawa, and S. Sakata [14] [15][2].

The number of total degrees of freedom and rotation angles (mixing angles) of n-dimensional unitary matrix is n^2 and $n(n-1)/2$, respectively. If neutrinos are Dirac particle, $2n-1$ parameters are unphysical and when we remove them $(n-1)(n-2)/2$ physical parameters remain [17]. These phase parameters (one parameter when $n = 3$) give rises to CP violations [18]. If neutrinos are Majorana particle, the number of CP-violating parameters is $n(n-1)/2$.

A free particle in a mass eigenstate propagates during flight as:

$$|\nu_i(t)\rangle = \exp(-i(E_i t - p_i L))|\nu_i(0)\rangle, \tag{1.3.2}$$

where t (L) is flight time (length) and E_i (p_i) is neutrino energy (momentum). By taking the untrarelativistic limit

$$E_i = \sqrt{p_i^2 + m_i^2} \simeq p_i + \frac{m_i^2}{2p_i} \simeq p_i + \frac{m_i^2}{2E},\ \ t \simeq L, \tag{1.3.3}$$

the propagation is written as

$$|\nu_i(t)\rangle \simeq \exp\left(-i\frac{m_i^2 L}{2E}\right)|\nu_i(0)\rangle. \tag{1.3.4}$$

1.3.2 Neutrino oscillation in vacuum

The time evolution of a flavor eigenstate $|\nu_\alpha\rangle$ is given by superposition of those of the mass eigenstates:

$$\begin{aligned} |\nu_\alpha(t)\rangle &= \sum_i U_{\alpha i}\exp\left(-i\frac{m_i^2 L}{2E}\right)|\nu_i(0)\rangle \\ &= \sum_{i,\beta} U_{\alpha i}U^*_{\beta i}\exp\left(-i\frac{m_i^2 L}{2E}\right)|\nu_\beta\rangle. \end{aligned} \tag{1.3.5}$$

Then the neutrino oscillation probability $P(\nu_\alpha \to \nu_\beta)$ is calculated as

$$\begin{aligned} P(\nu_\alpha \to \nu_\beta) &= |\langle\nu_\beta|\nu_\alpha(t)\rangle|^2 \\ &= \delta_{\alpha\beta} - 4\sum_{i>j}\mathrm{Re}(U_{\alpha i}U^*_{\beta i}U^*_{\alpha j}U_{\beta j})\sin^2\left(\frac{\Delta m_{ij}^2 L}{4E}\right) + 2\sum_{i>j}\mathrm{Im}(U_{\alpha i}U^*_{\beta i}U^*_{\alpha j}U_{\beta j})\sin\left(\frac{\Delta m_{ij}^2 L}{2E}\right). \end{aligned} \tag{1.3.6}$$

[1] Mixing of right-handed neutrinos can be considered in a similar manner.

[2] S. Tanaka, Y. Katayama, K. Matsumoto and E. Yamada [16] also proposed the neutrino oscillation around the same time.

From eq. 1.3.6, it follows that the oscillation probability is a function of $\Delta m^2_{ij} = m^2_i - m^2_j$. Oscillation probabilities of antineutrino are obtained by replacing U_{ab} with U^*_{ab}:

$$\begin{aligned} & P(\overline{\nu}_\alpha \to \overline{\nu}_\beta) \\ &= \delta_{\alpha\beta} - 4\sum_{i>j} \mathrm{Re}(U_{\alpha i}U^*_{\beta i}U^*_{\alpha j}U_{\beta j}) \sin^2\Big(\frac{\Delta m^2_{ij}L}{4E}\Big) - 2\sum_{i>j} \mathrm{Im}(U_{\alpha i}U^*_{\beta i}U^*_{\alpha j}U_{\beta j}) \sin\Big(\frac{\Delta m^2_{ij}L}{2E}\Big). \end{aligned} \quad (1.3.7)$$

Under the charge-conjugation transformation, $|\nu_{\alpha L}\rangle \to |\nu_{\beta L}\rangle$ corresponds to $|\overline{\nu}_{\alpha L}\rangle \to |\overline{\nu}_{\beta L}\rangle$ and under the parity transformation, $|\overline{\nu}_{\alpha L}\rangle \to |\overline{\nu}_{\beta L}\rangle$ corresponds to $|\overline{\nu}_{\alpha R}\rangle \to |\overline{\nu}_{\beta R}\rangle$. Hence, under the CP transformation, $|\nu_\alpha\rangle \to |\nu_\beta\rangle$ corresponds to $|\overline{\nu}_\alpha\rangle \to |\overline{\nu}_\beta\rangle$. The difference of the oscillation probabilities between neutrino and antineutrino corresponds to the CP-violating part and is written as:

$$\begin{aligned} A^{\alpha\beta}_{\mathrm{CP}} &= P(\nu_\alpha \to \nu_\beta) - P(\overline{\nu}_\alpha \to \overline{\nu}_\beta) \\ &= 4\sum_{i>j} \mathrm{Im}(U_{\alpha i}U^*_{\beta i}U^*_{\alpha j}U_{\beta j}) \sin\Big(\frac{\Delta m^2_{ij}L}{2E}\Big) \\ &= 0 \ \ (\text{if } \alpha = \beta). \end{aligned} \quad (1.3.8)$$

Under the CP transformation, $|\nu_\alpha\rangle \to |\nu_\beta\rangle$ corresponds to $|\overline{\nu}_\beta\rangle \to |\overline{\nu}_\alpha\rangle$. In this discussion, CPT invariance [22] [23] [24] is implicitly assumed and $P(\nu_\alpha \to \nu_\beta)$ always equals $P(\overline{\nu}_\beta \to \overline{\nu}_\alpha)$.

Standard parameterization

The PMNS matrix is often represented by mixing angles $\theta_{12}, \theta_{13}, \theta_{23}$ and CP-violating phase δ, λ_1, λ_2 as

$$\begin{aligned} U &= \begin{pmatrix} 1 & 0 & 0 \\ 0 & c_{23} & s_{23} \\ 0 & -s_{23} & c_{23} \end{pmatrix} \begin{pmatrix} 1 & 0 & 0 \\ 0 & 1 & 0 \\ 0 & 0 & e^{i\delta} \end{pmatrix} \begin{pmatrix} c_{13} & 0 & s_{13} \\ 0 & 1 & 0 \\ -s_{13} & 0 & c_{13} \end{pmatrix} \begin{pmatrix} 1 & 0 & 0 \\ 0 & 1 & 0 \\ 0 & 0 & e^{-i\delta} \end{pmatrix} \begin{pmatrix} c_{12} & s_{12} & 0 \\ -s_{12} & c_{12} & 0 \\ 0 & 0 & 1 \end{pmatrix} \cdot S \\ &= \begin{pmatrix} c_{12}c_{13} & s_{12}c_{13} & s_{13}e^{-i\delta} \\ -s_{12}c_{23} - c_{12}s_{13}s_{23}e^{i\delta} & c_{12}c_{23} - s_{12}s_{23}s_{13}e^{i\delta} & c_{13}s_{23} \\ s_{12}s_{23} - c_{12}s_{13}c_{23}e^{i\delta} & -c_{12}s_{23} - s_{12}s_{23}s_{13}e^{i\delta} & c_{13}c_{23} \end{pmatrix} \cdot S, \end{aligned} \quad (1.3.9)$$

where s_{ij} and c_{ij} $(i, j : 1, 2, 3)$ represent $\sin\theta_{ij}$ and $\cos\theta_{ij}$ respectively and S represents an identity matrix if neutrinos are Dirac particles and S represents $\mathrm{diag}(1, e^{i\lambda_1}, e^{i\lambda_2})$ if neutrinos are Majorana particles. Majorana CP phases do not affect neutrino oscillation probabilities due to their cancellation.

1.3.3 Matter effects in neutrino oscillations

Neutrinos interact with matters during flight. The inelastic scattering, quasi-elastic scattering and neutrino capture have negligible effect on neutrino oscillation in most cases[3]. However, the coherent elastic scattering affects the neutrino propagation. This effect was pointed out by L. Wolfenstein, S. Mikheyev and A. Smirnov and called the MSW effect or the matter effect [20] [21].

In the matter effect, the contribution from the neutral current interaction (ordinarily with e^-, p and n) is negligible because the contribution to each flavor cancels out when we consider neutrino oscillations,

[3]For cosmological or astrophysical neutrinos, these contribution are not always negligible [30] [31].

but that from the ν_e ($\overline{\nu}_e$) + e^- charged current interaction is important. The matter effect results in generating additional potential V_{MSW} to the Hamiltonian for vacuum in the Schrödinger equation :[4]

$$\begin{aligned} V_{\mathrm{MSW}} &= +\sqrt{2}G_F n_e \ \ (\text{for } \nu_e) \\ &= -\sqrt{2}G_F n_e \ \ (\text{for } \overline{\nu}_e), \end{aligned} \tag{1.3.10}$$

where G_F is the Fermi coupling constant and n_e is the number density of electrons. Due to the difference of V_{MSW} between ν_e and $\overline{\nu}_e$, neutrino oscillations in matter are not CPT invariant [32].

1.3.4 New physics which varies neutrino and antineutrino oscillation probabilities

Oscillation probabilities could be different between neutrino and antineutrino not only by the matter effect but also by some new physics processes.

CPT is a fundamental symmetry of the quantum field theory and called the CPT theorem. The CPT theorem [22] [23] [24] is based on weak local commutativity, Lorentz invariance and Hermiticity of the Hamiltonian. The CPT theorem holds in the framework for the SM, but it may not hold in the Planck-scale physics. The CPT invariance ensures that neutrino and antineutrino have the same mass and a test of the CPT invariance in neutrino oscillation experiments can be carried out by comparing Δm^2 with neutrino and antineutrino.

Standard Model Extension

Among CPT-violating new physics, models where the CPT violation is associated with the Lorentz violation are often considered [25]. In order to describe physics which violates Lorentz symmetry, the Standard Model Extension (SME) [26] [27] was developed. The SME is an effective field theory and its Lagrangian $\mathcal{L}_{\mathrm{SME}}$ has following form:

$$\mathcal{L}_{\mathrm{SME}} = \mathcal{L}_{\mathrm{SM}} + \mathcal{L}_{\mathrm{GR}} + \mathcal{L}_{\mathrm{NP}}, \tag{1.3.11}$$

where $\mathcal{L}_{\mathrm{SM}}$, $\mathcal{L}_{\mathrm{GR}}$ and $\mathcal{L}_{\mathrm{NP}}$ represent the Lagrangians of the standard model, general relativity and new physics which includes all the possible CPT-violating and Lorentz-violating effects. In the SME framework, sensitivities and limits of various new physics models are given by coefficients of Lorentz-violating operators. For the CPT-violating and Lorentz-violating effect which come from neutrino oscillation, the effective Hamiltonian H_{eff} is written by following form:

$$\mathcal{H}_{\mathrm{eff}} = \mathcal{H}_0 + \delta\mathcal{H}. \tag{1.3.12}$$

where $\mathcal{H}_{\mathrm{eff}}$, $\mathcal{H}_0$ and $\delta\mathcal{H}$ are 6×6 ($\nu + \overline{\nu}$ flavors) matrices, respectively and $\mathcal{H}_0$ represents the nominal Hamiltonian in the PMNS framework:

$$\mathcal{H}_0 = \begin{pmatrix} h_\nu & O \\ O & h_{\overline{\nu}}, \end{pmatrix} \tag{1.3.13}$$

h_ν and $h_{\overline{\nu}}$ indicate the Hamiltonian for the neutrino part and the antineutrino part, respectively. The Lorentz-violating term $\delta\mathcal{H}$ is written by following form:

$$\delta\mathcal{H} = \begin{pmatrix} \delta h_{ab}(\boldsymbol{p}) & \delta h_{a\bar{b}}(\boldsymbol{p}) \\ \delta h_{\bar{a}b}(\boldsymbol{p}) & \delta h_{\bar{a}\bar{b}}(\boldsymbol{p}) \end{pmatrix} = \begin{pmatrix} \delta h_{ab}(\boldsymbol{p}) & \delta h_{a\bar{b}}(\boldsymbol{p}) \\ \delta h^*_{\bar{a}\bar{b}}(-\boldsymbol{p}) & \delta h^*_{ab}(-\boldsymbol{p}), \end{pmatrix} \tag{1.3.14}$$

[4] Derivation of V_{MSW} can be found elsewhere [20]

where indices a, b ($\overline{a}, \overline{b}$) indicate neutrino (antineutrino) flavors and $\boldsymbol{p}$ represents the 3-momentum vector. In this matrix, the off-diagonal blocks have non-zero values, which causes the neutrino-antineutrino mixing [28]. The leading-order term of the top-left block Hamiltonian δh_{ab}, which corresponds to the neutrino-neutrino mixing part, is given as following:

$$\delta h_{ab} = \frac{1}{E}((a_L)^{\alpha} p_{\alpha} - (c_L)^{\alpha\beta} p_{\alpha} p_{\beta})_{ab}, \tag{1.3.15}$$

where p_{α}, p_{β} indicate the 4-momentum vectors, and $(a_L)^{\alpha}$ and $(c_L)^{\alpha\beta}$ are coefficients. Neutrino oscillation experiments can constrain some of these coefficients in the neutrino sector [29].

Non-standard neutrino interactions

Some BSM physics may also appear in couplings of (anti)neutrinos with matter [33]. Their physics models are generically called non-standard neutrino interactions (NSI). There are various kinds of NSI models [33] and NSI generally gives additional potential V_{NSI} to the SM Hamiltonian:

$$\mathcal{H} = \mathcal{H}_{\mathrm{vacuum}} + V_{\mathrm{MSW}} + V_{\mathrm{NSI}}, \tag{1.3.16}$$

$$V_{\mathrm{NSI}} = \begin{pmatrix} \varepsilon_{ee} & \varepsilon_{e\mu} & \varepsilon_{e\tau} \\ \varepsilon^*_{e\mu} & \varepsilon_{\mu\mu} & \varepsilon_{\mu\tau} \\ \varepsilon^*_{e\tau} & \varepsilon^*_{\mu\tau} & \varepsilon_{\tau\tau} \end{pmatrix} \tag{1.3.17}$$

That results in modification of neutrino oscillation probabilities in matter. Like matter effects, if the additional potential from NSI differs between neutrino and antineutrino, oscillation probabilities between them could be different. NSI effect may be seen in long-baseline neutrino oscillation experiments where neutrinos interact with matter during flight. The diagonal parameters work similar to the MSW potential while the off-diagonal parameters work as the mixing angle, i.e., even if there is no mixing in vacuum, neutrino flavor transition may occur due to the off-diagonal NSI parameters. Since the matter in the earth comprises u-quarks, d-quarks and electrons, NSI of u-quarks and d-quarks is especially important. (Effect of electrons are already considered in the MSW effect.)

In the simplified case where we consider only ν_μ-ν_τ transition, NSI with only d-quarks, and real ε parameters, Hamiltonian is written as:

$$\mathcal{H}' = \frac{1}{2E} U \begin{pmatrix} 0 & 0 \\ 0 & \Delta m^2 \end{pmatrix} U^{\dagger} \pm A \begin{pmatrix} \varepsilon_{\mu\mu} & \varepsilon_{\mu\tau} \\ \varepsilon_{\mu\tau} & \varepsilon_{\tau\tau} \end{pmatrix}, \tag{1.3.18}$$

here the sign of the NSI term is different between neutrino and antineutrino. The $\nu_\mu(\overline{\nu}_\mu)$ survival probability is approximately written as:

$$P = 1 - \sin^2(2\tilde{\theta}) \sin^2\left(\frac{\Delta \tilde{m}^2 L}{2E}\right), \tag{1.3.19}$$

where $\tilde{\theta}$ and $\Delta\tilde{m}^2$ are the effective mixing angle and the effective squared-mass difference and given by:

$$\tan 2\tilde{\theta} = \frac{\sin(2\theta)\Delta m^2/2E \pm 2A\varepsilon_{\mu\tau}}{\cos(2\theta)\Delta m^2/2E - A(\varepsilon_{\mu\mu} \mp \varepsilon_{\tau\tau})}, \tag{1.3.20}$$

$$(\Delta\tilde{m}^2)^2 = (\cos(2\theta)\Delta m^2 \pm 2AE(\varepsilon_{\mu\mu} - \varepsilon_{\tau\tau}))^2 + (\sin(2\theta)\Delta m^2 \pm 4AE\varepsilon_{\mu\tau})^2. \tag{1.3.21}$$

1.4 Measurements of neutrino oscillation parameters

1.4.1 Brief history

Indications of neutrino oscillation were reported from many experiments. Some of them had come from the measurements of solar neutrino, which had been called the solar neutrino problem. Neutrino flux from the sun is well-predicted by the standard solar model [34]. However, the observed fluxes from various kinds of experiments were all smaller than the expected fluxes [35] [36] [37] [38]. Indications had also come from the measurements of atmospheric neutrinos. Its flux ratio of $(\nu_\mu + \overline{\nu}_\mu)/(\nu_e + \overline{\nu}_e)$ is calculated with accuracy better than 5% [39]. The measured flux ratio from experiments was, however, smaller than the expected flux ratio [40] [41] [42]. In spite of these reports, they lacked the decisive factor.

In 1998, the Super-Kamiokande (SK) experiment [43] reported a conclusive evidence of neutrino oscillation. They measured zenith angle distribution of atmospheric neutrinos and observed up-down asymmetry of ν_μ which is consistent with neutrino oscillation. Later in 2001-2002, strong evidence of solar neutrino oscillation was reported by the Sudbury Neutrino Observatory (SNO) experiment [47] [48] by observing both charged current interactions (measure ν_e) and neutral current interactions (measure all flavor neutrinos) and comparing them to the neutrino-electron elastic scattering data measured by SK [49]. The neutrino-electron elastic scattering is sensitive to all the neutrino flavors but more sensitive to ν_e than ν_μ and ν_τ. In 2015, T. Kajita (Super-Kamiokande collaboration) and A.B. McDonald (SNO collaboration) were awarded the Nobel Prize for the discovery of neutrino oscillations.

1.4.2 Current knowledge about neutrino mass and mixing parameters

Though various types of experiments have been trying to measure the absolute values of the neutrino masses and mass type (Dirac or Majorana), they are still unknown [44] [45] [46]. Only the squared mass differences have been measured from neutrino oscillation experiments.

A summary of the measurements of the oscillation parameters are shown in table 1.1. As described in section 1.3, the neutrino oscillation probability depends on E/L. The values of $|\Delta m^2_{32}|$ and $|\Delta m^2_{31}|$ are roughly 30 times larger than that of Δm^2_{21}. For these reasons, the sensitivity to each oscillation parameter is different depending on experiments. The θ_{12} and Δm^2_{21} have been obtained from electron neutrino disappearance measured by solar neutrino experiments [47] [48] and by the KamLAND long-baseline reactor neutrino experiment [50]. The θ_{23} and $|\Delta m^2_{32}|$ have been obtained from atmospheric muon neutrino disappearance measured by SK [51] and from accelerator-produced muon neutrino disappearance measured by long-baseline accelerator neutrino oscillation experiments [52] [53]. The θ_{13} and $|\Delta m^2_{31}|$ have been obtained from electron neutrino disappearance measured by short-baseline reactor neutrino experiments [54] [55] [56] and from electron neutrino appearance measured by long-baseline accelerator neutrino experiments [53]. Recently measurements of the CP-violating phase δ was started by combining the results from short-baseline reactor neutrino experiments and long-baseline accelerator neutrino experiments but significance is not yet large [53]. The mass hierarchy, i.e., the sign of Δm^2_{32} or Δm^2_{31} is still unknown.

Comparison of neutrino oscillation parameters between neutrinos and antineutrinos

CPT violation can be searched for by comparing measured oscillation parameters between neutrino and antineutrino. For Δm^2_{21} and θ_{12}, their parameters have been measured by SK with neutrino [59] and those have been measured by KamLAND with antineutrino [50] and small but interesting tension is seen for Δm^2_{21}.

Table 1.1: Neutrino oscillation parameters taken from Particle Data Group 2014 [19].

$\sin^2 2\theta_{12}$	0.846 ± 0.021
Δm^2_{21}	$(7.53 \pm 0.18) \times 10^{-5}$ eV^2
$\sin^2 2\theta_{23}$	$0.999^{+0.001}_{-0.018}$ (normal hierarchy) $1.000^{+0.000}_{-0.017}$ (inverted hierarchy)
$\lvert\Delta m^2_{32}\rvert$	$(2.44 \pm 0.06) \times 10^{-3}$ eV^2 (normal hierarchy) $(2.52 \pm 0.07) \times 10^{-3}$ eV^2 (inverted hierarchy)
$\sin^2 2\theta_{13}$	0.093 ± 0.008

For Δm^2_{31} and θ_{13}, T2K has measured with neutrino and reactor neutrino experiments have measured with antineutrino. Measured θ_{13} from neutrinos have larger uncertainty than those for antineutrinos and they are consistent. For Δm^2_{32} and θ_{23}, their parameters for both neutrinos and antineutrinos have been measured by MINOS [60] and SK [61]. The Δm^2_{32} and θ_{23} measured with antineutrino have larger uncertainties than those with neutrino and they are consistent in these experiments. In this thesis, the first measurement of the $\overline{\nu}_\mu$ disappearance in the T2K experiment will be reported and the comparison of Δm^2_{32} and θ_{23} between neutrino and antinuetrino will be described.

1.5 Introduction to the T2K experiment

1.5.1 Experimental setup

The T2K (Tokai to Kamioka) experiment is a long-baseline neutrino oscillation experiment [62]. An overview of the T2K experiment is shown in fig. 1.1. An intense proton beam with kinetic energy of 30 GeV is produced at Japan Proton Accelerator Research Complex (J-PARC) in Tokai and is impinged on a graphite target. Secondary particles such as charged πs and Ks which are produced in the target are focused by three magnetic horns. The sign of focused particles can be changed by flipping the polarity of the magnetic horns. When π^+s (π^-s) are focused, we call that configuration the neutrino (antineutrino) mode. The ν_μ or $\bar{\nu}_\mu$ beam is produced by the decay ($\pi^+ \to \nu_\mu + \mu^+$, $\pi^- \to \bar{\nu}_\mu + \mu^-$) of the focused particles.

The neutrino beam axis is directed 2.5 degrees away from the far detector. This results in the narrower energy spectrum and higher flux at around 0.6 GeV where the oscillation probability at the far detector becomes maximal. This configuration is called the off-axis method [70] and enhances signal events and suppresses background events from high energy neutrinos. The beam direction is always measured by the muon monitor (MUMON) which measures muons and by the on-axis near detectors (INGRID) which measures neutrinos. The neutrino beam is measured with the off-axis near detector at 280 m from the target at J-PARC and by the far detector, Super-Kamiokande, which is 295 km away from J-PARC.

1.5.2 Measurement of neutrino oscillations

In the T2K experiment, we can measure $\nu_\mu \to \nu_e$ appearance and $\nu_\mu \to \nu_\mu$ disappearance [5]. The measurement of neutrino oscillations is carried out by comparing the observed data to the prediction assuming neutrino oscillation for a given set of values of the neutrino oscillation parameters.

[5] Though most of ν_μs oscillate ν_τ, we do not measure $\nu_\mu \to \nu_\tau$ appearance because the threshold energy of the τ production (about 3.5 GeV) is much larger than the peak energy of neutrino flux.

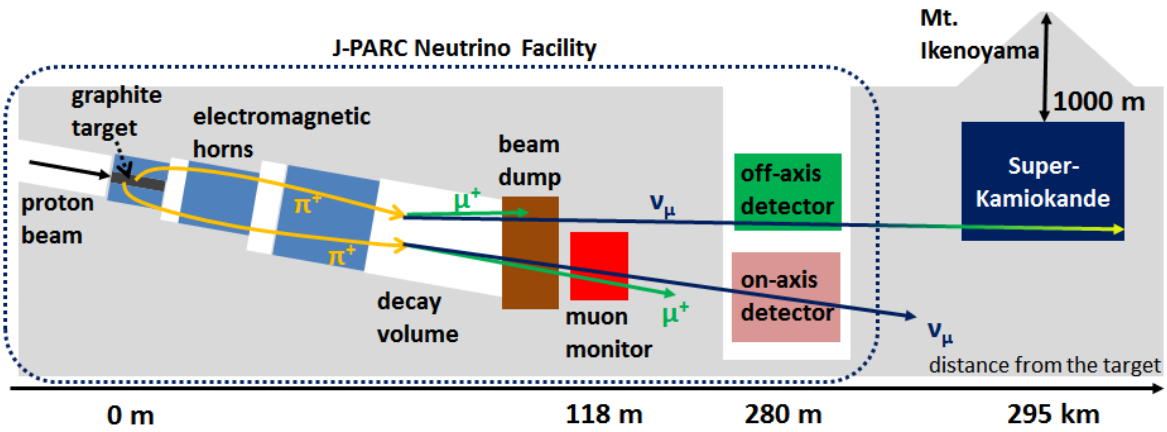

Figure 1.1: Overview of the T2K experiment.

1.5.3 Oscillation probabilities for the T2K experiment

The $\nu_\mu \to \nu_e$ appearance probability and the $\nu_\mu \to \nu_\mu$ survival probability with the first order of the matter effect are given by [57] [58]:

$$\begin{aligned}
P(\nu_\mu \to \nu_e) &= 4c_{13}^2 s_{13}^2 s_{23}^2 \left(1 + \frac{2a}{\Delta m_{31}^2}(1 - 2s_{13}^2)\right) \sin^2 \Phi_{31} \\
&+ 8c_{13}^2 s_{12} s_{13} s_{23} (c_{12} c_{23} \cos\delta - s_{12} s_{13} s_{23}) \cos\Phi_{32} \sin\Phi_{31} \sin\Phi_{21} \\
&- 8c_{13}^2 c_{12} c_{23} s_{12} s_{13} s_{23} \sin\delta \sin\Phi_{32} \sin\Phi_{31} \sin\Phi_{21} \\
&+ 4s_{12}^2 c_{13}^2 (c_{12}^2 c_{23}^2 + s_{12}^2 s_{23}^2 s_{13}^2 - 2c_{12} c_{23} s_{12} s_{13} \cos\delta) \sin^2 \Phi_{21} \\
&- 2c_{13}^2 s_{13}^2 s_{23}^2 \frac{aL}{E}(1 - 2s_{13}^2) \cos\Phi_{32} \sin\Phi_{31} \\
&\simeq \sin^2 2\theta_{13} \sin^2\theta_{23} \sin^2 \Phi_{31}, \qquad (1.5.1) \\
P(\nu_\mu \to \nu_\mu) &= 1 - 4c_{13}^2 s_{23}^2 (c_{12}^2 c_{23}^2 + s_{12}^2 s_{13}^2 s_{23}^2) \sin^2 \Phi_{32} - 4c_{13}^2 s_{23}^2 (s_{12}^2 c_{23}^2 + c_{12}^2 s_{13}^2 s_{23}^2) \sin^2 \Phi_{31} \\
&+ c_{13}^2 s_{13}^2 s_{23}^2 (1 - 2c_{13}^2 s_{23}^2) \frac{8a}{\Delta m_{31}^2} \sin\Phi_{31} (\sin\Phi_{31} - \Phi_{31} \cos(\Phi_{31})) \\
&- 8c_{12} c_{13}^2 c_{23} s_{12} s_{13} s_{23}^3 \cos\delta (\sin^2 \Phi_{31} - \sin^2 \Phi_{32}) \\
&- 4\Big((c_{12}^2 c_{23}^2 + s_{12}^2 s_{13}^2 s_{23}^2)(s_{12}^2 c_{23}^2 + c_{12}^2 s_{13}^2 s_{23}^2) \\
&+ 2c_{12} c_{23} s_{12} s_{13} s_{23} (c_{23}^2 - s_{13}^2 s_{23}^2)(c_{12}^2 - s_{12}^2) \cos\delta - 4c_{12}^2 c_{23}^2 s_{12}^2 s_{13}^2 s_{23}^2 \cos^2\delta\Big) \sin^2 \Phi_{21} \\
&\simeq 1 - (\cos^4\theta_{13} \sin^2 2\theta_{23} + \sin^2 2\theta_{13} \sin^2\theta_{23}) \sin^2 \Phi_{32}, \qquad (1.5.2)
\end{aligned}$$

where

$$\Phi_{ij} \equiv \frac{\Delta m_{ij}^2 L}{4E} \simeq 1.267 \cdot \frac{\Delta m_{ij}^2 (\mathrm{eV}^2) \cdot L(\mathrm{km})}{E(\mathrm{GeV})}, \qquad (1.5.3)$$

$$a \equiv 2\sqrt{2} G_F n_e E \simeq 7.6 \times 10^{-5} \cdot E(\mathrm{GeV}) \cdot \rho(\mathrm{g/cm}^3)[\mathrm{eV}^2]. \qquad (1.5.4)$$

Here $|\Delta m_{32}^2| \simeq |\Delta m_{31}^2| \gg \Delta m_{21}^2$, $|\Delta m_{31}^2| \gg a$ and $1 \gg \sin\Phi_{21}$ is used in the approximation parts of eqs. 1.5.1 and 1.5.2. $P(\bar{\nu}_\mu \to \bar{\nu}_e)$ and $P(\bar{\nu}_\mu \to \bar{\nu}_\mu)$ are obtained by replacing δ and a with $-\delta$ and $-a$. The

ν_e appearance mode is sensitive to θ_{13} while the ν_μ disappearance mode is sensitive to θ_{23}. Furthermore, precise measurements of ν_e appearance and ν_μ disappearance allow us to determine the CP phase δ_{CP}.

As described in section 1.3, in the PMNS framework where the CPT symmetry is conserved, the survival probability with neutrino and antineutrino is identical in vacuum and is slightly different in matter. In T2K, the size of the matter effect to the survival probability is as small as $O(0.1)\%$ and this cannot be measured. Therefore, if the difference of the survival probabilities with neutrino and antineutrino was observed, it could be said that we discovered new physics.

1.5.4 Oscillation analysis results of the T2K experiment obtained by the ν-mode data

Using the data collected until 2013, T2K has published measurements of the ν_μ disappearance and the ν_e appearance with a world-leading precision [63] [64] [65] [66] [67] [68] [69]. Figure 1.2 shows the reconstructed neutrino energy distributions of the ν_μ and ν_e samples using the T2K ν-mode dataset corresponding to 6.6×10^{20} protons on target (POT). Obvious ν_μ disappearance and ν_e appearance patterns are observed. Figures 1.3 and 1.4 show the 1σ and 90% confidence regions with the θ_{13} value from reactor experiments. The best-fit oscillation parameters by the ν_μ disappearance analysis, which will be used for this $\bar{\nu}_\mu$ disappearance analysis, are $\sin^2\theta_{23} = 0.527$ and $\Delta m^2_{32} = 2.51 \times 10^{-3}\mathrm{eV}^2$ in case of the normal mass hierarchy. The 1σ confidence level interval for these parameters are [0.465, 0.581] for $\sin^2\theta_{23}$ and [2.39, 2.62] $\times 10^{-3}$ eV^2 for Δm^2_{32}. The obtained θ_{23} is consistent with the maximal mixing. For the δ_{CP} measurement, δ_{CP}=[0.15π, 0.83π] for the normal mass hierarchy and δ_{CP}=[−0.08π, 1.09π] for the inverted mass hierarchy are excluded at the 90% confidence level.

The T2K and reactor data weakly favor the normal mass hierarchy, i.e., $\Delta m^2_{32} > 0$. Since the dominant uncertainty source is statistical uncertainty, it is crucial for the T2K experiment to keep taking data stably and increase the beam power which is described in Section 2.7.

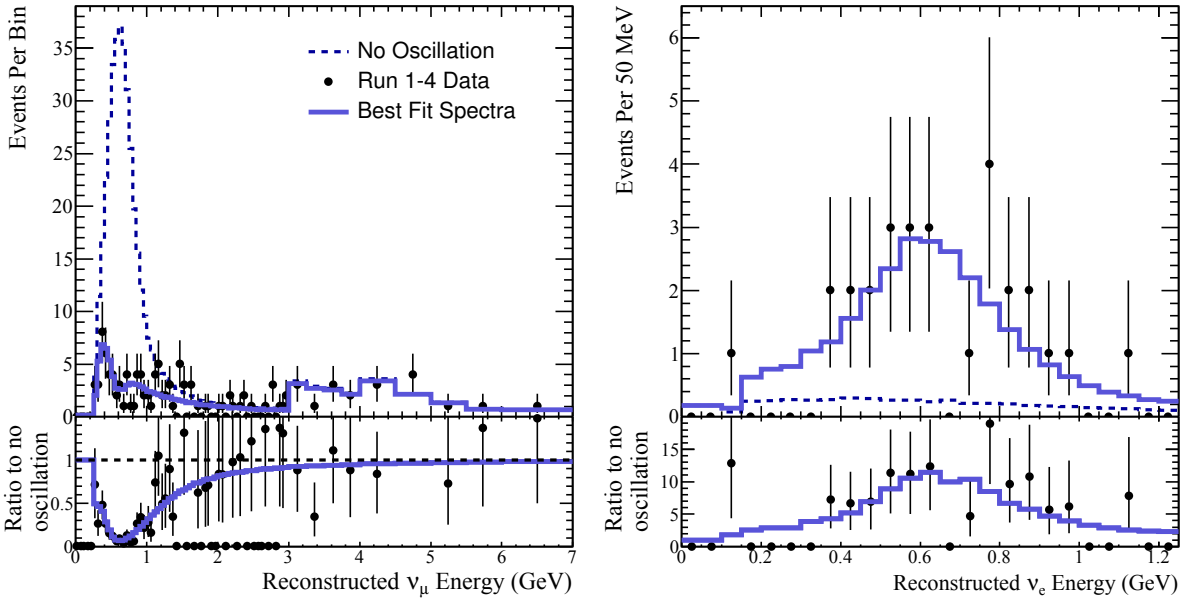

Figure 1.2: Reconstructed neutrino energy spectra for ν_μ (left top) candidate events and ν_e (right top) candidate events at the far detector using the ν-mode dataset corresponding to 6.6×10^{20} POT. Predicted spectra with the best-fit and no oscillation cases are also shown. Bottom plots are the predictions of observed data and the best-fit spectra as a ratio to the unoscillated prediction.

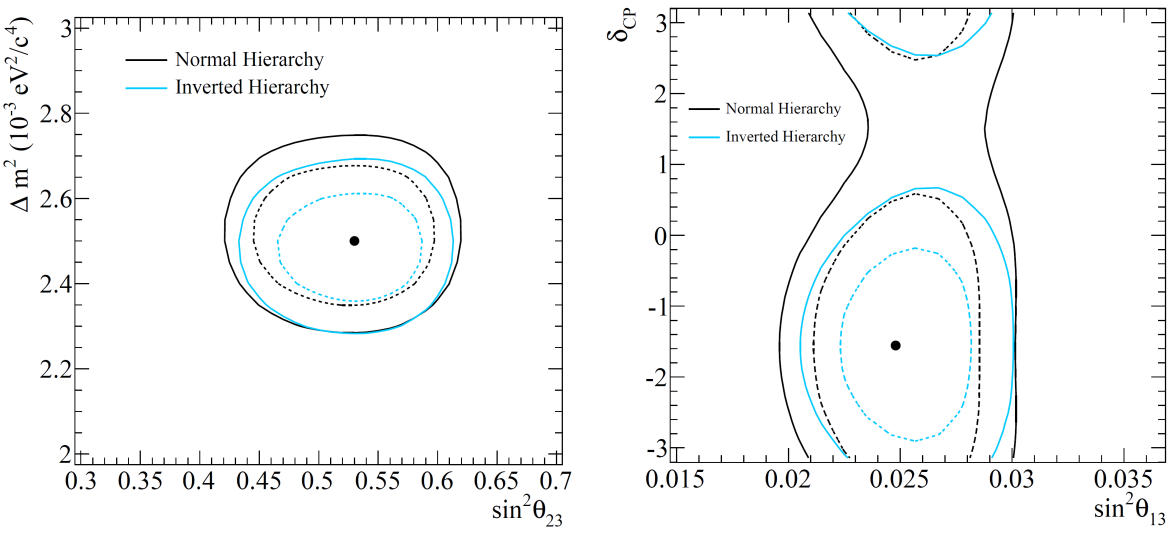

Figure 1.3: The 1σ (dashed lines) and 90% (solid lines) confidence regions with the θ_{13} value from reactor experiments with different mass hierarchy assumptions. Figure is taken from [69].

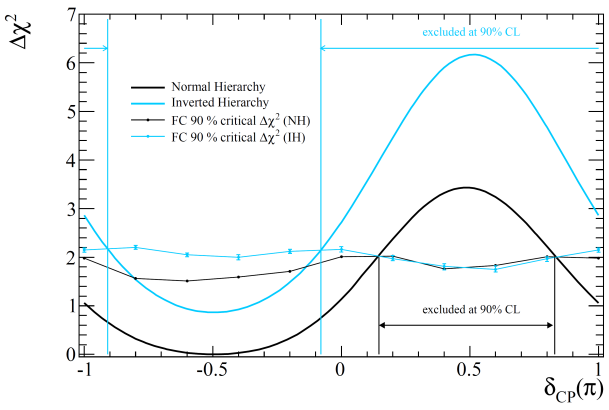

Figure 1.4: The 90% confidence regions for δ_{CP} for the normal and inverted hierarchies. This analysis uses the θ_{13} value from reactor experiments. Figure is taken from [69].

1.5.5 Motivation of the measurement of the antineutrino oscillation

As described in the next Chapter, T2K can measure both the neutrino oscillation and antineutrino oscillation. Here we note motivation of the measurement of the antineutrino oscillation.

Searching for the CP violation via ν_e ($\overline{\nu}_e$) appearance

The ν_e appearance probability (eq. 1.5.1) contains the term which is proportional to $\sin\delta$. Hence, by taking the difference of $P(\nu_\mu \to \nu_e)$ and $P(\overline{\nu}_\mu \to \overline{\nu}_e)$, the δ_{CP} can be measured by only the data of T2K. Moreover, the sensitivity for the δ_{CP} gets higher in the case of taking both the ν-mode data and the $\overline{\nu}$-mode data equally rather than that of taking only the ν-mode data. The sensitivity studies for discovering the non-zero δ_{CP} are discussed in [72].

Searching for new physics via ν_μ ($\overline{\nu}_\mu$) disappearance

By testing whether the measured oscillation parameters in the PMNS framework are identical between neutrino and antineutrino, the CPT violation and the NSI, which are described in Section 1.3.4, could be searched for. The simple test of the CPT violation is measuring the mass difference between neutrino and antineutrino. A strong limit is already obtained in the neutral kaon system, i.e., $|m(K^0) - m(\overline{K}^0)| < 4.0\times10^{-19}$ GeV [19]. However if this is converted to the mass-squared difference, which might be natural rather than the mass difference itself [73], the limit is $|m^2(K^0) - m^2(\overline{K}^0)| < 0.02$ eV^2. Compared to this limit, the mass-squared difference of neutrino and antineutrino is much better and that from the MINOS experiment [52] is $|\Delta\overline{m}^2| - |\Delta m^2| = (0.12^{+0.24}_{-0.26})\times10^{-3}$ eV^2, where $|\Delta\overline{m}^2|$ is an admixture of the three-flavor parameters Δm^2_{32} and Δm^2_{31}. Currently, MINOS has the best precision of both Δm^2_{32} and $\Delta\overline{m}^2_{32}$. T2K has similar precision of Δm^2_{32} with the data which correspond to roughly 17% of the total planned ν-mode data T2K will take and T2K will take similar amount of $\overline{\nu}$-mode data. Hence, T2K has a potential to measure the mass-squared difference of neutrino and antineutrino with a world-leading precision.

For the NSI case, T2K has a potential to measure $\varepsilon_{\mu\tau}$ and $|\varepsilon_{\mu\mu} - \varepsilon_{\tau\tau}|$, though these parameters are already strongly limited by the Super-Kamiokande atmospheric neutrino experiment [74] thanks to the long travel length in the earth. Since the precision of $\sin^2\theta_{23}$ and $|\Delta m^2_{32}|$ by T2K is better than that by the Super-Kamiokande atmospheric neutrino experiment, it is possible to give stronger limits to $\varepsilon_{\mu\tau}$ and $|\varepsilon_{\mu\mu} - \varepsilon_{\tau\tau}|$.

1.6 Thesis overview

This thesis describes the first $\overline{\nu}_\mu$ disappearance measurement with a dataset in antineutrino mode corresponding to 4.011×10^{20} protons on target (POT). Chapter 2 describes the T2K experimental apparatus and the dataset. Chapter 3 describes miscellaneous studies about the muon monitor which have been carried out by the author. In particular, the first beam commissioning studies in antineutrino mode are reported. Chapter 4 explains the neutrino flux prediction and describes its improvement which is carried out by the author. From Chapter 5 to 7 the $\overline{\nu}_\mu$ disappearance analysis [71] is described. Chapter 5 explains neutrino-nucleus interaction models. Chapter 6 explains measurements at the off-axis near detector and the far detector. Chapter 7 describes the analysis method and the results of the $\bar{\nu}_\mu$ disappearance analysis which is carried out by the author. In particular, the comparison of Δm^2_{32} and θ_{23} with antineutrino from this $\bar{\nu}_\mu$ disappearance analysis and those with neutrino from T2K is reported. Chapter 8 gives the conclusions and outlooks.

Chapter 2

Experimental components and data taking history

In this chapter, experimental components in the T2K experiment [62] are explained. Then, history of the beam data taken so far is described.

2.1 J-PARC accelerator

J-PARC [75] is a high-intensity proton beam accelerator complex located in Tokai, Japan. A wide range of sciences is aimed covering particle physics, nuclear physics, material science, and life science. J-PARC accelerator comprises 3 sequential components: LINear ACceelerators (LINAC), Rapid Cycling Syncrotron (RCS), and Main Ring (MR). First, a 50 mA negatively ionized hydrogen (H^-) beam is accelerated to 400 MeV by four types of accelerators in LINAC[1]. At the most downstream part of LINAC, electrons in H^- are removed by the carbon stripper foils and only protons are delivered to RCS. Proton beams are accelerated to 3 GeV in RCS with a 25 Hz cycle and most of protons are delivered to the Material and Life science Facility (MLF). The rest of the protons are delivered to MR. This proton beam is accelerated to 30 GeV in MR and is delivered to the Neutrino Facility (T2K beamline) or the Hadron Experimental Facility.

2.1.1 Machine parameters of the J-PARC Main Ring

Figure 2.1 shows the schematic structure of the proton beam and table 2.1 summarizes machine parameters of MR. In a cycle of the proton beam, there is a chain (called spill) of 8 bunches of the protons. From MR, the proton beam is transported to the neutrino beamline with conserving the spill structure This is called fast-extraction. Beam power has been and will have been increased by the accelerator group. At the time of 2015, beam power achieved is roughly 350 kW as shown in fig. 2.19. The beam power will be upgraded to 750 kW by increasing the number of protons per spill and shortening spill interval. Beam power is calculated as (number of protons per spill)×(proton beam energy)/(spill interval).

[1] Before 2013, 30 mA beam was accelerated to 181 MeV.

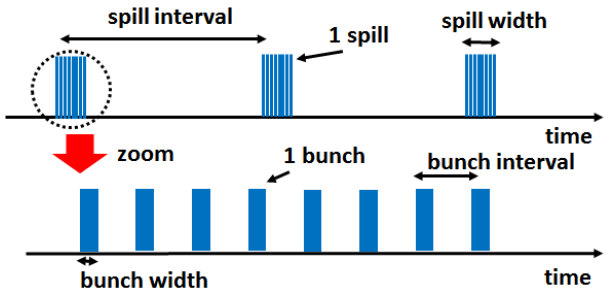

Figure 2.1: Beam structure for the T2K experiment. Protons are contained in each bunch.

Table 2.1: Machine parameters of the Main Ring of the J-PARC accelerator facility.

parameter	value (at the time of 2015)
circumference	1567.5 m
beam kinetic energy	30 GeV
number of bunches	8 bunches /spill
beam power	350 kW
number of protons	1.8×10^{14} /spill
spill interval	2.48 sec
bunch interval	581 nsec
bunch width	58 nsec
spill width	4.1 μsec

2.2 Neutrino beamline

Figure 2.2 shows an overview of the neutrino beamline. The T2K neutrino beamline comprises two sequential sections: the primary beamline and the secondary beamline which starts from the target station and the downstream side of the target. In the primary beamline, the beam is bent toward the direction of the far detector by normal conducting magnets and superconducting combined function magnets [76] [77] [78].

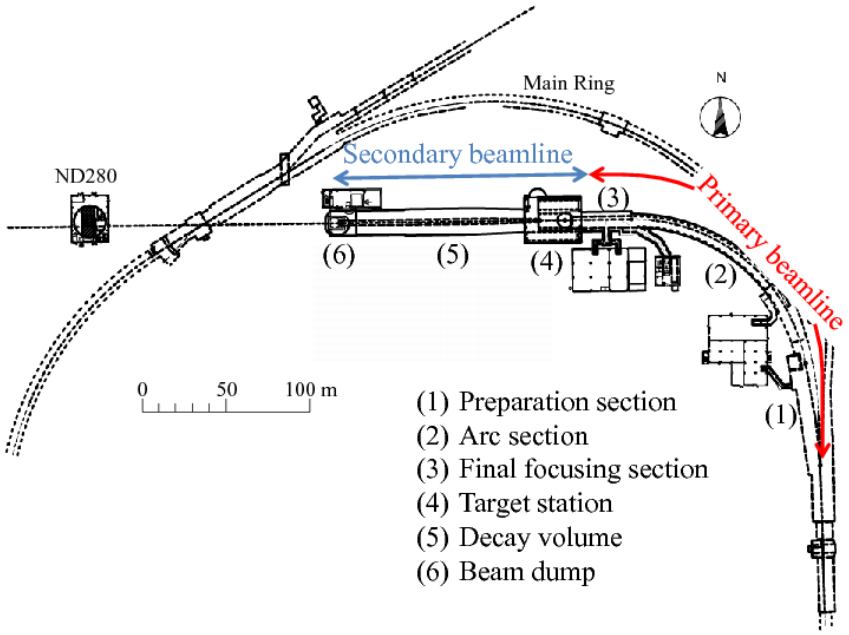

Figure 2.2: Overview of the neutrino beamline. Figure is taken from [62].

2.3 Beam monitors in the primary neutrino beamline

Monitoring the beam intensity, beam profiles and beam losses is crucial for the operation and the safety especially in the high-power beam operation. In the primary neutrino beamline, 5 current transformers (CT), 21 electrostatic monitors (ESM), 19 segmented secondary emission monitors (SSEM) [79] and 50 beam loss monitors (BLM) are installed for these purposes.

The CT is a 50-turn toroidal coil around a ferromagnetic core ring as shown in fig. 2.3. The signal is induced by the electromagnetic coupling with the beam. The signal size is proportional to the beam intensity. To achieve high-frequency response up to 50 MHz for the short-pulsed bunches and to avoid saturation caused by a large peak current of 200 A, CTs use the FINEMET® (nanocrystalline Fe-based soft magnetic material) core, which has a high permeability and a high saturation flux density over a broad range of frequencies. The proton beam intensity measured by CTs has a precision of 2.6%. The beam timing is also measured by CTs on a bunch-by-bunch basis.

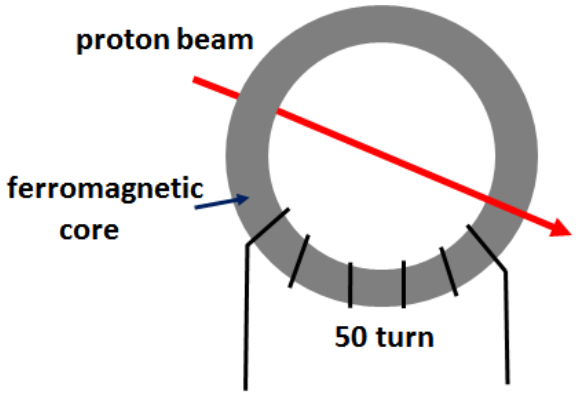

Figure 2.3: Illustration of the CT.

The ESM (fig. 2.4: left) has four segmented cylindrical electrodes surrounding the proton beam orbit. By measuring top-bottom and left-right asymmetries of the beam-induced current on the electrodes, it monitors the horizontal and vertical center positions of the proton beam nondestructively (without putting matters in the beam). The measurement precision on the beam position is better than 450 μm. The SSEM (fig. 2.4: right) is a beam profile monitor and has 5 μm thick titanium cathode foils stripped horizontally and vertically and an anode HV foil between them. The strip width of each SSEM ranges from 2 to 5 mm, which is optimized according to the expected beam size at the installed position. The strips emit secondary electrons by interactions with the proton beam in proportion to the number of protons that go through the strip. The beam profile is reconstructed from the size of signals from the strips. Since SSEMs cause beam losses, they are inserted only during the beam commissioning and extracted from the beam orbit in the physics data-taking periods except for the one which is placed at the most downstream of the beamline. The measurement precision on the beam width is 200 μm. The BLM is a wire proportional chamber filled with a mixture of Ar and CO_2. BLMs are installed evenly in the primary beamline and are used for the machine protection system and the estimation of the residual dose. BLMs have a sensitivity down to a 20 mW beam loss.

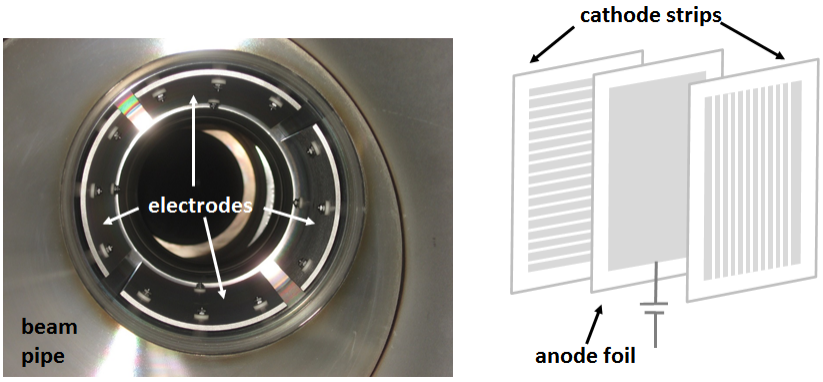

Figure 2.4: Photograph of ESM (left) and an illustration of SSEM (right).

Figure 2.5 summarizes the schematic view of the neutrino beamline around the target. In practice, the proton beam is bent 3.637° vertically by the most downstream vertical bending magnet to satisfy the off-axis beam configuration. Beam monitors listed in this figure are used for the measurement of proton beam properties at the target in the beam commissioning studies.

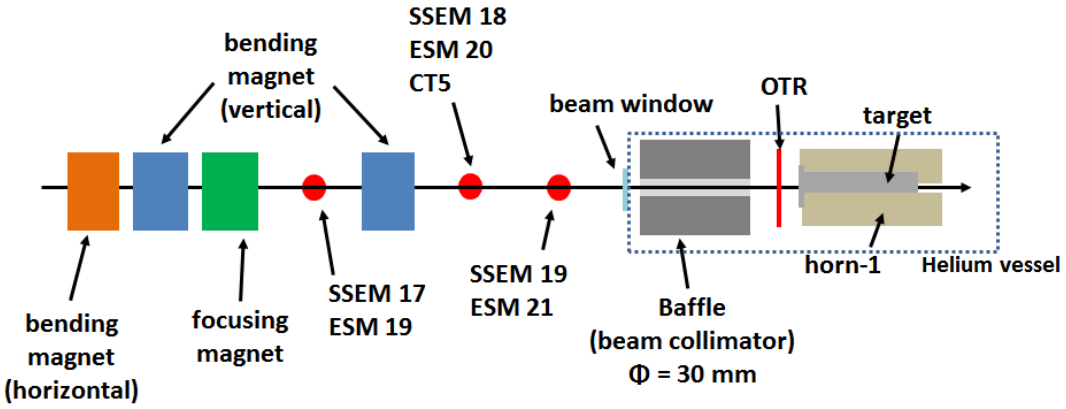

Figure 2.5: Schematic view of the neutrino beamline around the target. In practice, the proton beam is bent 3.637° vertically by the most downstream vertical bending magnet in order to satisfy the off-axis beam configuration.

2.4 Secondary neutrino beamline

The secondary beamline are composed of the following sequential sections as shown in fig. 2.6: the target station (TS), the decay volume, the beam dump and the muon monitor (MUMON). The TS and the decay volume are filled with the helium gas at atmospheric pressure in order to reduce interactions of the primary and secondary beam and to prevent production of tritium and nitrogen-oxide and oxidization of the material.

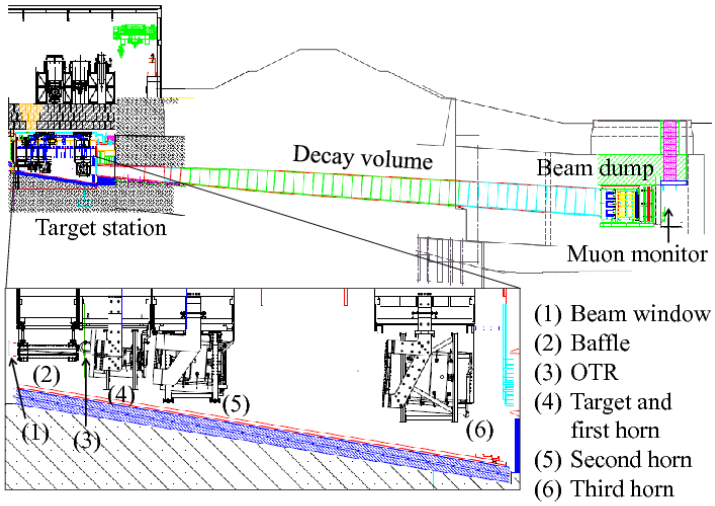

Figure 2.6: Cross-sectional view of the secondary beamline. Figure is taken from [62].

2.4.1 Apparatus in the target station

The proton beam enters the TS through the 0.3 mm thick beam window which separates the primary beamline from the TS. The baffle, which is a 1.7 m long graphite collimator block with a hole of 30 mm in diameter, is located upstream the target in order to absorb the misdirected beam.

An optical transition radiation monitor (OTR) [80] is installed just 29 cm upstream the target for the monitoring of the beam profile near the target. A titanium alloy thin foil is placed in front of the upstream surface of the target. It generates transition radiation lights when the beam penetrates. The lights are transported by mirrors and are detected by a camera. This is to avoid placing signal cables in the very high radiation environment. A radiation-resistant camera is used to image the two-dimensional profile of the proton beam.

The target [81] consists of the core and the surrounding materials as shown in fig. 2.7. The core is a graphite rod and is 91.4 cm in length, 2.6 cm in diameter and 1.8 g/cm^3.[2] It corresponds to 1.9 interaction length. The core is surrounded by a 2 mm thick graphite tube. Both the core and the tube are contained in the 0.3 mm thick titanium case and are cooled by the flowing helium gas as shown in fig. 2.7 (enlarged view).

The magnetic horns focus charged hadrons in the forward region so that the high intensity neutrino beam is obtained. The T2K magnetic horn system [82] [83] [84] comprises 3 horns: horn-1, horn-2, and horn-3, in order from upstream. Each horn is made of co-axial aluminum conductor tubes and current-feeding striplines. The target is inserted inside the inner conductor of horn-1 as shown in fig. 2.8 to collect pions effectively. Figure 2.9 depicts the schematics of horn focusing. A toroidal magnetic field is generated by a pulsed current of ±250 kA[3] which runs through the conductors.Horns are always cooled by water sprayed on the inner conductor and helium flowing through the stripline.

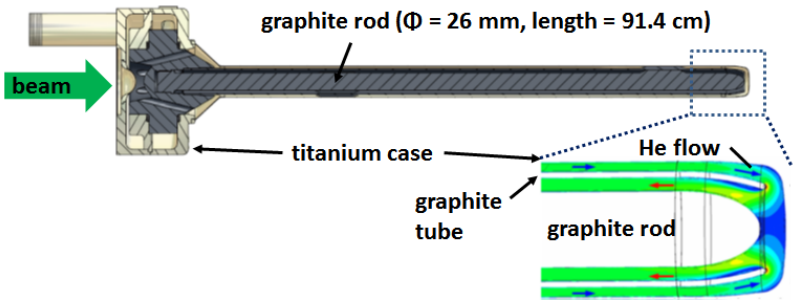

Figure 2.7: Cross-sectional view of the graphite target. Red and blue arrows in the enlarged view represent the direction of flowing helium gas.

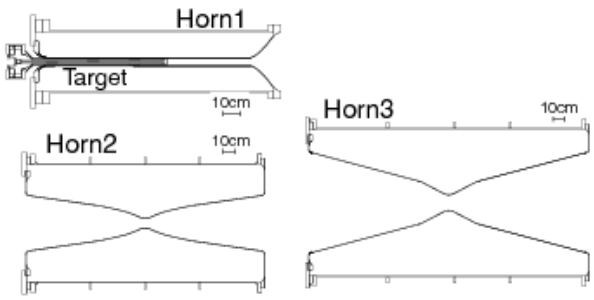

Figure 2.8: Cross-sectional view of the magnetic horn conductors. Figure is taken from [107].

[2] If a material significantly denser than graphite were used for the target core, it would be melted by the beam.
[3] Designed peak current of the horns is 320 kA.

2.4.2 Operation mode

T2K can measure both neutrino and antineutrino oscillations by changing the direction of the pulsed current in the conductors of the magnetic horns. When positively (negatively) charged hadrons from the target are focused, we call that configuration the neutrino mode or the ν mode (the antineutrino mode or the $\bar{\nu}$ mode). Even in neutrino (antineutrino) mode, some portions of antineutrinos (neutrinos), especially those from pions emitted very forward, contaminate neutrino (antineutrino) beam.

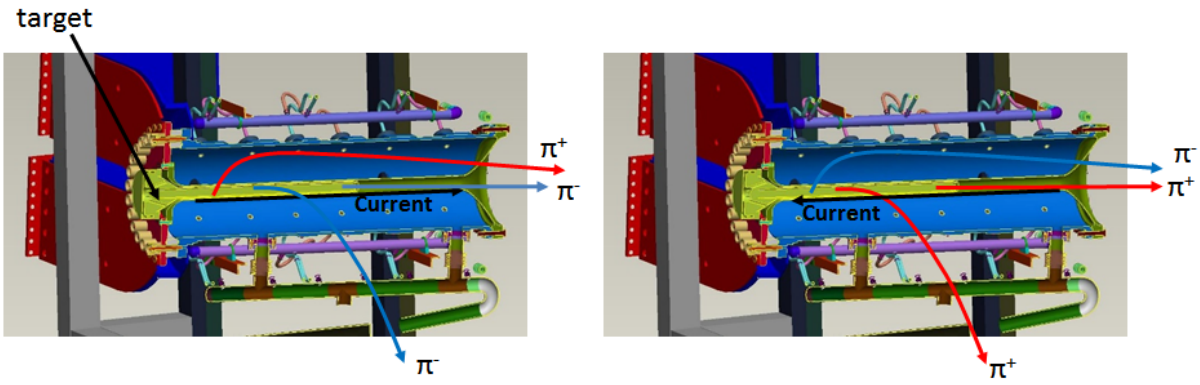

Figure 2.9: Illustration of pion focusing by magnetic horns in the neutrino mode (left) and the antineutrino mode (right).

2.4.3 Off-axis beam configuration

T2K adopts the off-axis beam configuration where the neutrino beam axis is displaced from the far detector direction by design. The angle between them is called the off-axis angle (OA). The purpose of the off-axis beam configuration is to produce a narrow neutrino energy spectrum. The bottom plot of fig. 2.10 shows the neutrino flux for different off-axis angles as a function of neutrino energy. With a non-zero off-axis angle, high energy neutrinos reduce and the neutrino flux is centered around a peak in the low energy region. This tendency can be understood by considering the two-body pion decay. The neutrino energy E_ν is calculated as:

$$E_\nu = \frac{(m_\pi^2 - m_\mu^2)\beta_\pi}{2p_\pi(1 - \beta_\pi \cos\theta_\nu)}, \tag{2.4.1}$$

where m_π and m_μ are the masses of the pion and the muon, β_π is the speed of the pion respectively, p_π is the momentum of the pion and θ_ν is the angle between the pion and the neutrino direction. E_ν gets smaller as $\cos\theta_\nu$ decreases. θ_ν is close to the off-axis angle because pions are focused to the beam axis direction by the magnetic horns. The top and middle plot of fig. 2.10 show the neutrino oscillation probabilities at the far detector. Muon neutrino disappearance probability and electron neutrino appearance probability at the far detector get maximum around 0.6 GeV. The off-axis angle to the far detector was determined to 2.5° so that the neutrino flux has a peak energy of this 0.6 GeV which corresponds to the energy of the maximal disappearance. The off-axis angle to the off-axis near detector from the target position is 2.04°. This angle was chosen to make the neutrino spectrum at the off-axis near detector as similar as possible to the spectrum at the far detector.

Another advantage of the off-axis angle method is the reduction of background events. Figure 2.11 shows neutrino-nucleus interaction cross sections for different interaction types. T2K uses the charged-

current quasi-elastic (CCQE) interaction as the signal events. The other types of interactions are backgrounds and their cross sections are large in high energy region where the flux is small in the off-axis beam.

The neutrino flux spectrum is largely affected by the off-axis angle, which may cause large uncertainty of the neutrino flux. Therefore, the beam direction should be monitored and controlled. In T2K, the beam direction of muons are monitored by the muon monitor and the beam direction of neutrinos are monitored by the on-axis near detector INGRID as explained later.

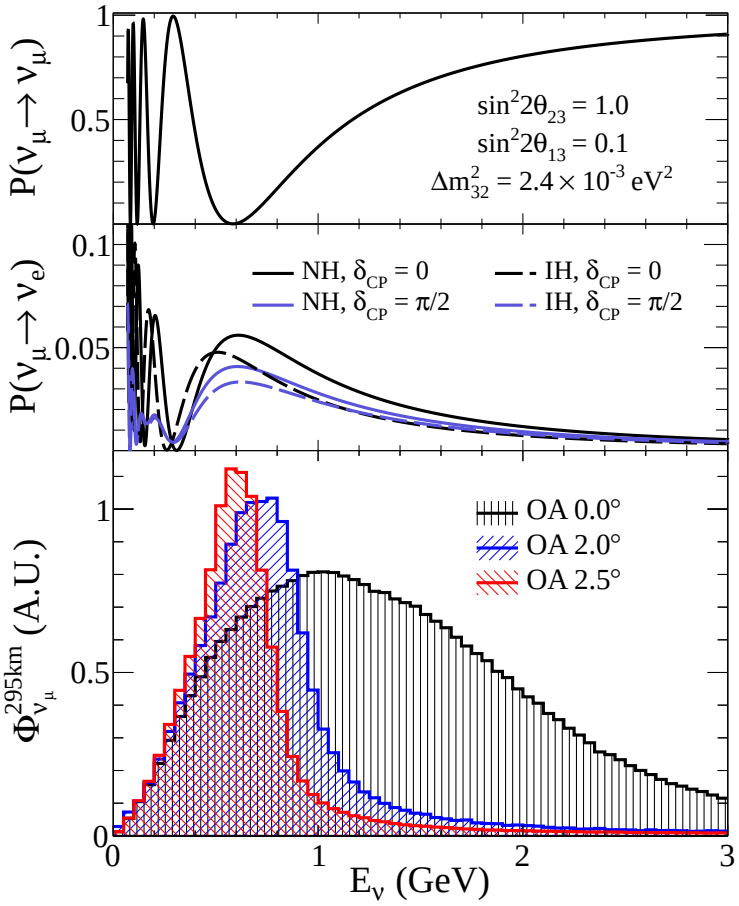

Figure 2.10: Muon neutrino disappearance probability (top), electron neutrino appearance probability (middle) at the far detector and the muon neutrino flux for different off-axis angles in the neutrino mode (bottom) as a function of neutrino energy. Figure is taken from [107].

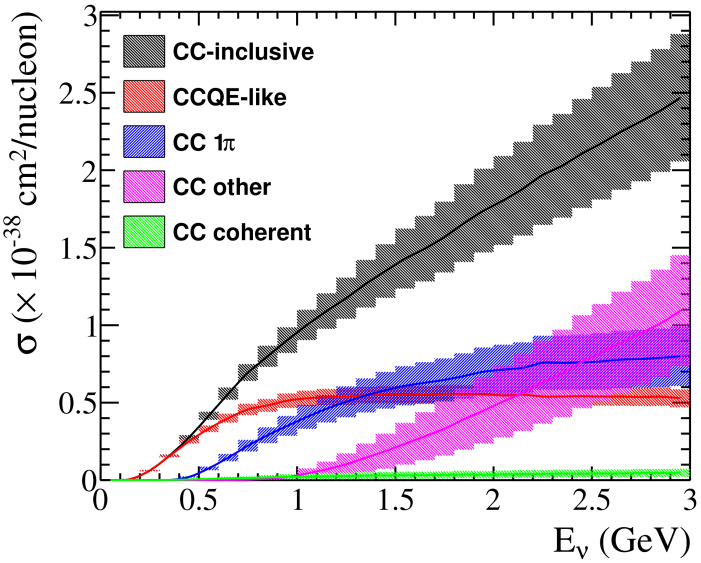

Figure 2.11: Neutrino-nucleus interaction cross sections for different interaction types as a function of neutrino energy. The band in this figure represent the uncertainty of each interaction type. Details of the neutrino-nucleus interaction cross sections are explained in Chapter 5.

2.4.4 Decay volume and beam dump

The decay volume is a 96 m long steel tunnel. The cross section is 1.4 m wide and 1.7 m high at the entrance, and 3.0 m wide and 5.0 m high at the end. The produced pions and kaons decay into muons and muon neutrinos during flight in the decay volume. The beam dump is located at the most downstream section of the decay volume. Figure 2.12 shows a photograph of the beam dump and the muon monitor. The core of the beam dump is the 3.174 m thick graphite block which is contained in the helium vessel. Downstream the graphite core, two iron plates are placed inside the helium vessel and fifteen iron plates are placed outside the helium vessel. Total thickness of the iron plates are 2.4 m. Downstream the iron plates, there is a 1 m long concrete wall. All the particles except for muons above roughly 5 GeV/c are stopped in the beam dump and only high energy muons penetrate the beam dump and reach the muon monitor. The thickness of the beam dump is chosen to minimize the hadron flux while retaining the sensitivity in the measurement of the muon beam direction.

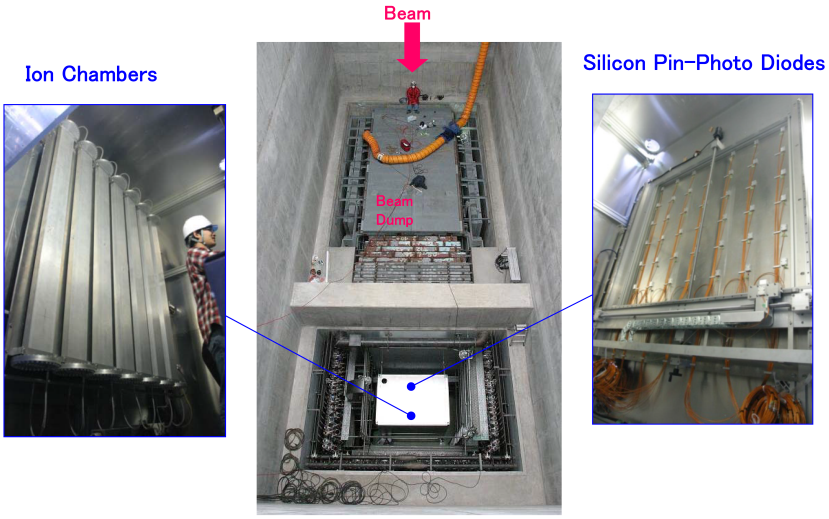

Figure 2.12: Photograph of the beam dump and the muon monitor. This photograph was took during the construction phase of the T2K experiment.

2.4.5 Muon monitor

The muon monitor (MUMON) [87] [88] [89] is located behind the beam dump at a distance of 118 m from the target. The purpose of MUMON is to monitor the beam intensity and beam direction on a bunch-by-bunch basis by measuring the muon beam which originates from the decays of pions. MUMON is the only monitor which can promptly find issues at the target and magnetic horns such as corruption of the target. The near detectors cannot find promptly these issues because it takes time to collect sufficient data to reconstruct neutrino beam profiles. The detailed configuration of the proton beam orbit is adjusted by monitoring the muon beam profiles. Further descriptions of the muon monitor are given in Chapter 3.

2.5 Near detectors

The neutrino beam properties and neutrino-nucleus interactions are studied at the near detectors located at 280 m from the proton-beam target. They comprises the on-axis neutrino profile detector and the off-axis tracking detector immersed in a magnetic field as shown in fig. 2.13.

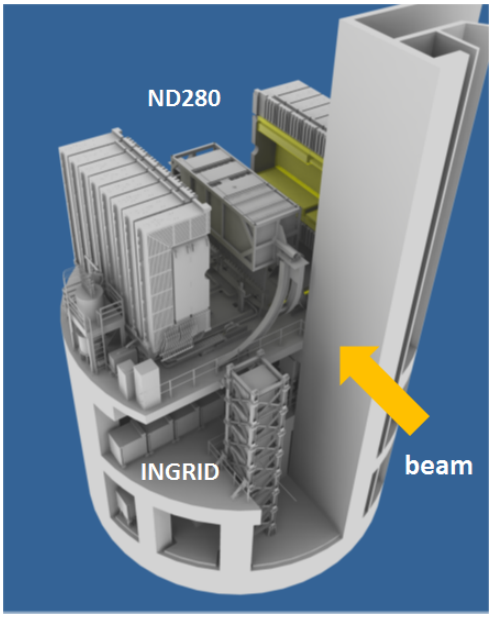

Figure 2.13: Near detector hall. The pit is 37 m deep and 17.5 m in diameter. The ND280 off-axis detector is located in the upper level. The INGRID detector is located in the lower level. Figure is taken from [62].

2.5.1 On-axis near detector INGRID

The on-axis detector, Interactive Neutrino GRID (INGRID) [90], is located around the neutrino beam axis and monitors the neutrino beam profile. It consists of Sixteen identical modules and an extra module called the Proton Module [91]. Fourteen modules are arranged in the horizontal and vertical arrays around the neutrino beam center as shown in fig. 2.14 (left). In addition, two modules are placed off the horizontal and vertical arrays[4]. Each module consists of a sandwich structure of nine iron target plates and eleven tracking scintillator two-layer planes oriented in the x and y directions and they are surrounded by veto scintillator planes as shown in fig. 2.14 (right). Each of the tracking planes consists of 24 scintillator bars. Scintillation lights produced by charged particles passing through each scintillator bar are read out by a Multi-Pixel Photon Counter (MPPC) detector and tracks are reconstructed from signals from each scintillator bar.

For the measurements of neutrino beam profile, seven horizontal and seven vertical modules have been used. Figure 2.15 shows the number of observed neutrino events in each module. The neutrino beam profile is obtained by fitting the number-of-event distribution by a Gaussian function.

The Proton Module is located at the beam center between the horizontal and vertical arrays. The Proton Module consists of only scintillator strips so that it can detect short-track protons and pions. The INGRID detector with the Proton Module is used for studies of various kinds of neutrino-nucleus interactions.

[4]One module was moved to the lowest floor of the ND hall in 2014

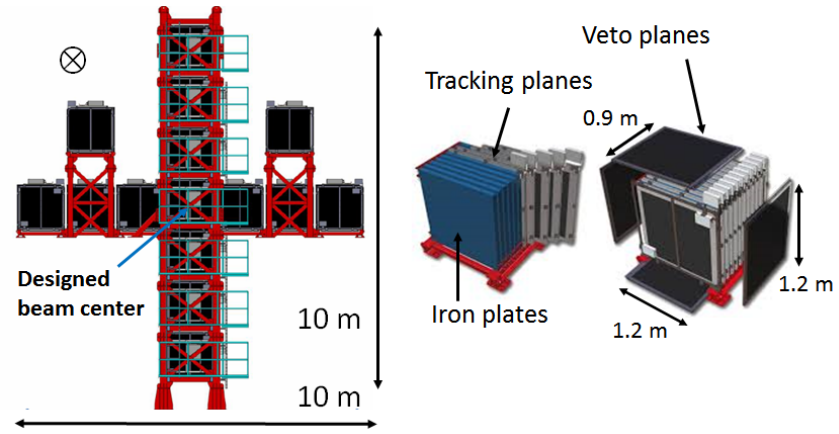

Figure 2.14: INGRID detector. left: schematic view of the 16 modules. The horizontal center module is hidden behind the vertical center module. right: Enlarged view of an INGRID module. Figure is taken from [62].

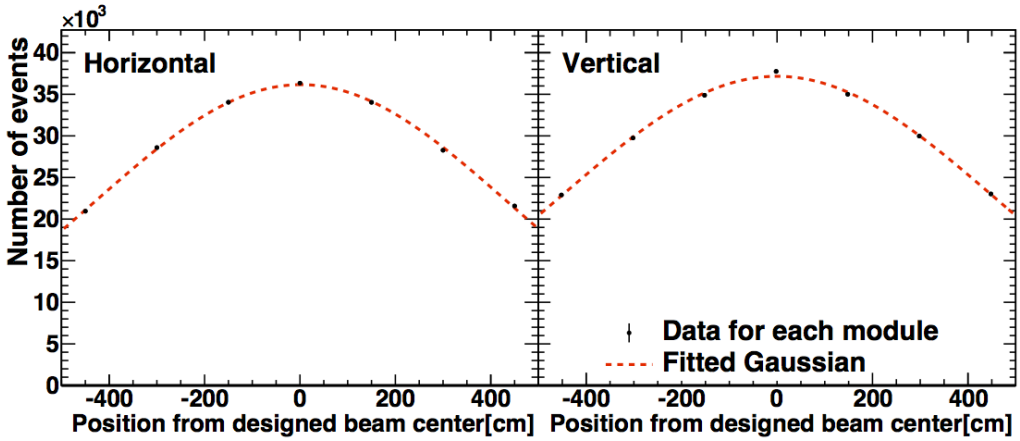

Figure 2.15: Neutrino profile measured by the INGRID detector for the horizontal (left) and vertical (right) direction in the neutrino mode.

2.5.2 Off-axis near detector ND280

The neutrino energy spectrum, flavor content, and neutrino-nucleus interactions of the unoscillated beam should be measured for the reliable measurement of neutrino oscillation. For this purpose, the off-axis detector complex ND280 is composed of following subdetectors as shown in fig. 2.16. Main detectors are contained inside the magnet recycled from the UA1 [92] and NOMAD [93] experiments at CERN. The magnetic field of 0.2 T perpendicular to the neutrino beam direction is applied by the coil and returned by the outer iron yoke. This magnetic field allows to identify the sign of the charge and momentum of tracks. Since the far detector cannot distinguish the charge of particles coming from either an antineutrino or a neutrino interaction, a precise understanding of the wrong-sign background in ND is important especially in the antineutrino mode where the fraction of the wrong-sign background is larger.

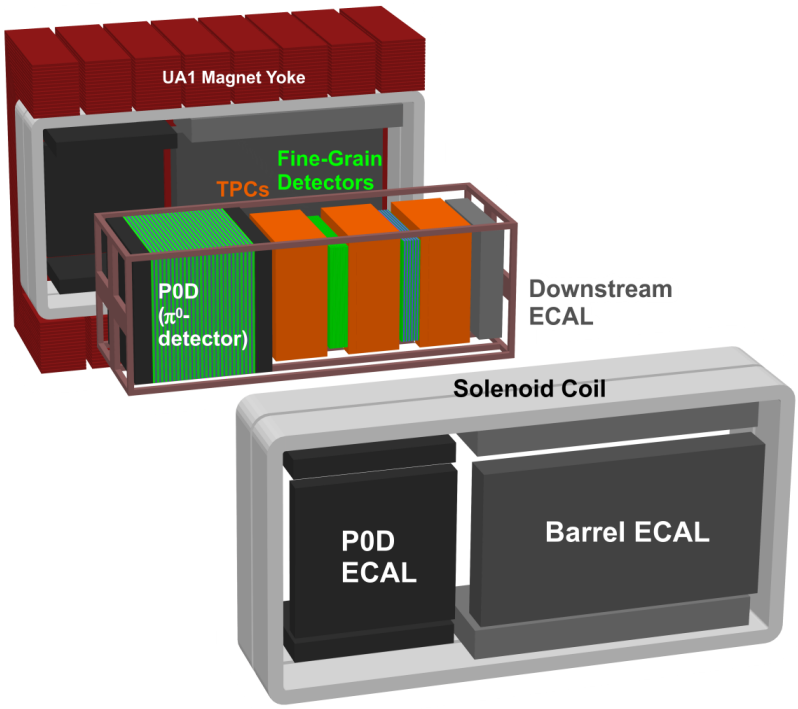

Figure 2.16: Exploded view of the off-axis near detector complex. The neutrino beam comes from the left side. The PØD, the TPCs, and the FGDs are surrounded by the ECals. The SMRD is inter-spaced in the return yoke. The neutrino beam comes from the left side. Figure is taken from [62].

The π^0 detector (PØD) [94] is located at the upstream end inside the magnet. The main purpose of the PØD is to measure the neutral current π^0 interactions on the water target. The PØD is composed of layers of plastic scintillator alternating with water bags and brass sheets or lead sheets.

Downstream the PØD the tracker detectors consisting of three Time Projection Chambers (TPC) [95] and two Fine Grained Detectors (FGD) [96] are placed. The FGD1 (upstream side) is composed solely of scintillator trackers oriented alternately in the x and y directions while the FGD2 is composed of scintillator bars and water targets.Detecting the short tracks of protons and charged pions by the finely segmented scintillators is important for identifying the neutrino interaction modes. Each FGD has outer dimensions of 230 cm (width) $\times$ 240 cm (height) $\times$ 36.5 cm (depth in beam direction), and contains 1.1 tonnes of target material.

Each TPC comprises a 230 cm (width) $\times$ 240 cm (height) $\times$ 100 cm (depth in beam direction) field cage filled with Ar:CF_4:isobutane (95:3:2) and 24 MicroMEGAS [97] readout plates. TPCs are used for the measurement of the momenta of the charged particles by curvatures of their tracks and particle identification by the amount of energy deposit. The near detector measurements used for the oscillation analysis in this paper are mainly based on the measurement by FGDs and TPCs. The Electromagnetic Calorimeters (ECal) [98] surrounds the PØD, the TPCs, and the FGDs to detect photons which penetrate from the inner detectors. Each ECal consists of alternating planes of scintillator bars and lead for generating electromagnetic showers.

The Side Muon Range Detectors (SMRD) [99] consist of the scintillator pads which are inserted in the gaps of the iron yokes. The SMRD acts as a veto for beam neutrino interaction events that originate outside the tracker.

2.6 Super-Kamiokande detector

The gigantic water Cherenkov detector, Super-Kamiokande (SK) [100], used as the far detector in the T2K experiment, is located 295 km away from the production target in J-PARC and roughly 1 km deep inside the Mt. Ikenoyama. Figure 2.17 shows a sketch of the SK detector. The SK detector consists of a cylindrical tank filled with 50 kt of ultra-pure water and a stainless steel structure with photomultiplier tubes (PMTs) which optically separates the volume. The inner detector (ID) is 36.2 m tall and 33.8 m in diameter. On the ID wall it holds 11129 20-inch inward-facing PMTs which correspond to a spatial coverage of 40%. The outer detector (OD) contains 1885 8-inch outward-facing PMTs on the OD wall with a refrective material. The OD PMTs are used to veto background events like cosmic muons and to discriminate charged particles which exit the ID. The fiducial volume (FV) is defined as the volume 2 m inside the ID wall and has 22.5 kt.

Neutrino interactions are detected via imaging of Cherencov radiation produced by ultrarelativistic charged particles. The kinematic information of neutrino (vertex position, event timing, zenith and azimuthal angles to the neutrino beam axis, and momentum), the number of ring and particle type is determined from timing and charge distributions of the PMTs. While a muon passes straightly through water and produces a sharp ring (called μ-like ring), an electron or a positron generates an electromagnetic shower in water and produces a fuzzy ring (called e-like ring) as shown in fig. 2.18. This ring information is essential for the particle identification (PID) in the analysis.

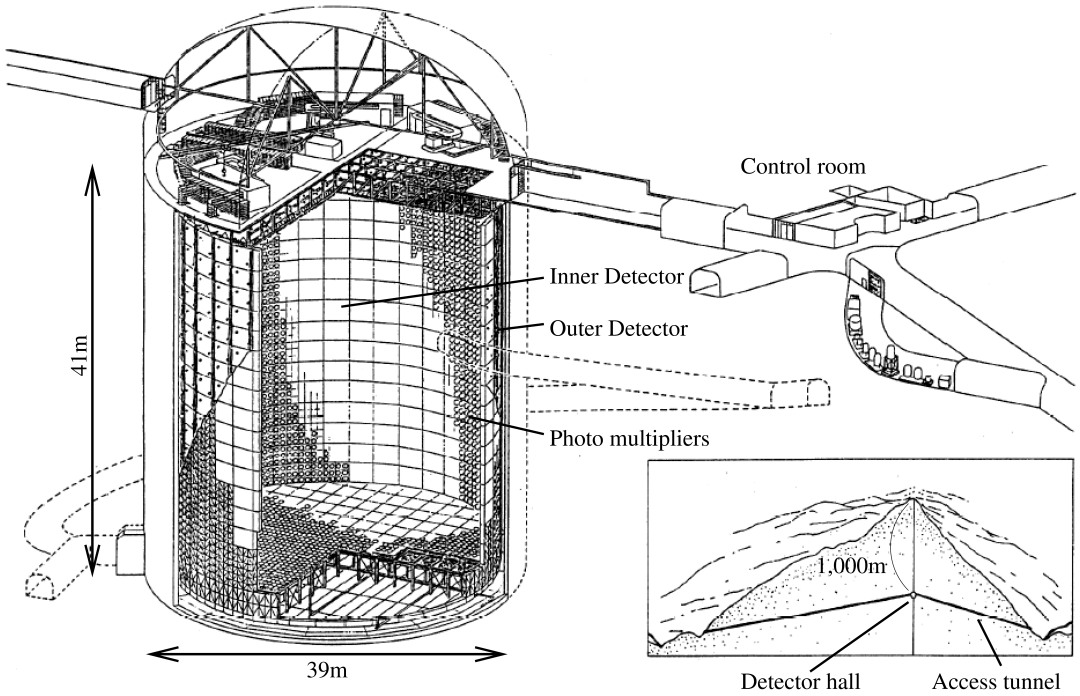

Figure 2.17: Sketch of the Super-Kamiokande detector. Figure is taken from [62].

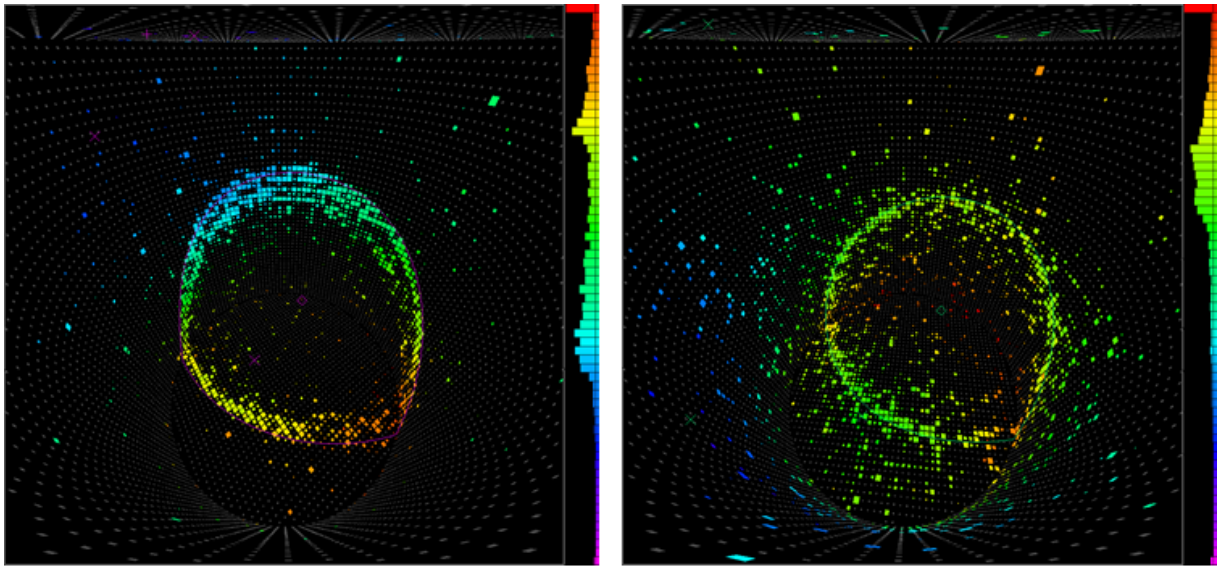

Figure 2.18: Example of event displays of typical neutrino events in the Super-Kamiokande detector. Left: μ-like event, right: e-like event. Figures are taken from http://www.ps.uci.edu/~tomba/sk/tscan/compare_mu_e .

2.6.1 Energy reconstruction

The main interaction type in the T2K neutrino energy region ($O(1)$ GeV) and used as signal is the charged-current quasi-elastic (CCQE) interaction:

$$\nu_l + n \rightarrow l + p \tag{2.6.1}$$

where l represents an electron or a muon and n represents a neutron inside nuclei[5]. In water, Cherenkov threshold energy for an electron and a positron is 0.8 MeV, a muon is 160 MeV and a proton is 1.4 GeV. Thus, SK can observe only one lepton because Cherenkov threshold energy for a proton is higher than ejected proton energy.

Since neutrino oscillation probabilities depend on neutrino energy, the energy of neutrinos observed in SK should be known. For CCQE interaction the neutrino energy can be reconstructed from kinematic information on the lepton alone because CCQE interaction is a two-body scattering. The reconstructed neutrino energy is given as:

$$E_{\mathrm{rec}} = \frac{m_p^2 - (m_n - E_b)^2 - m_l^2 + 2(m_n - E_b)E_l}{2(m_n - E_b - E_l + p_l \cos\theta_l)}, \tag{2.6.2}$$

where m_n, m_p and m_l represent masses of neutron, proton and lepton respectively, E_b represents the binding energy of nucleus, and E_l, p_l and θ_l represent the energy, the momentum and the emission angle relative to the beam direction of the lepton, respectively. The Fermi momentum of the target neutron is neglected in this equation and results in worsening of the energy resolution.

2.7 Data taking

T2K began to operate with the neutrino mode in 2010. After the observation of ν_e appearance [67], T2K began to take $\overline{\nu}$-mode data in 2014. The number of protons impinged on the target (POT) is generally used

[5] τ is not detected because its energy production threshold is high (3.5 GeV).

for representing the amount of data taken. The most downstream CT is mostly used for the measurement of POT. Figure 2.19 shows accumulated POT so far and table 2.2 summarizes each T2K data-taking period, the Main Ring run number (MR Run Number), horn current and POT[6]. During the data taking, the proton beam profile, horn currents, and the muon beam profile of every spill are monitored. We select good data quality spills for analyses in ND and SK by using the following criteria:

- No problem occurs in each hardware component, DAQ, and GPS for the timing synchronization between each beam spill at J-PARC and event trigger timestamps at SK.
- The deviation of all horns current from the mean is within ±5 kA.
- The deviation of the muon beam center from nominal position is within 1 mrad.
- The deviation of the total muon yield measured by MUMON from the mean is within ±5 %.

After the good quality cut, the fraction of beam data remained is approximately 99.8%. The total accumulated POT in the neutrino mode and the antineutrino mode is 7.09×10^{20} and 4.04×10^{20}, respectively. The proton beam power was increased and was roughly 350 kW at the latest period. In the T2K RUN5 and RUN6, mainly $\bar{\nu}$-mode data were taken but sometimes short-term ν-mode data have been taken in order to check whether beam configurations would change.

Table 2.2: Accumulated POT and horn current settings in each T2K data-taking period.

Run period	Dates	Main Ring run number	Horn current	POT
Run 1	Jan. 2010 – Jun. 2010	29-34	250 kA	0.32×10^{20}
Run 2	Nov. 2010 – Mar. 2011	36-38	250 kA	1.11×10^{20}
Run 3	Mar. 2012 – Jun. 2012	41-43	205, 250 kA	1.58×10^{20}
Run 4	Oct. 2012 – May 2013	44-49	250 kA	3.56×10^{20}
Run 5	May 2014 – Jun. 2014	55-56	250, -250 kA	0.75×10^{20}
Run 6	Nov. 2014 – Jun. 2015	58-63	250, -250 kA	3.74×10^{20}
neutrino mode	Jan. 2010 – Jun. 2015	29-49, 55, 60	205, 250 kA	7.09×10^{20}
antineutrino mode	May 2014 – Jun. 2015	56, 58-59, 61-63	-250 kA	4.04×10^{20}
Total	Jan. 2010 – Jun. 2015	29-63	205, 250, -250 kA	11.13×10^{20}

[6]The T2K Run number increments after summer every year.

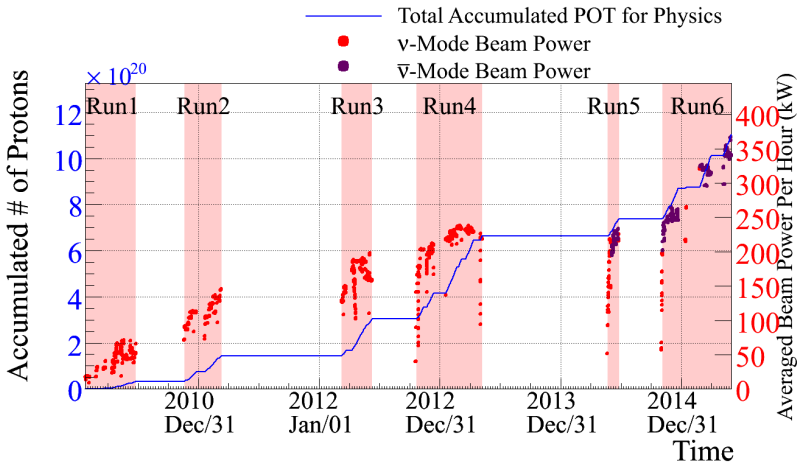

Figure 2.19: History of total accumulated protons and protons per pulse for the good quality beam data.

Chapter 3

Beam studies with the muon monitor

In this Chapter, we will discuss miscellaneous beam studies using the muon monitor (MUMON). As stated in Section 2.4.5, MUMON monitors the beam intensity and the beam direction on a bunch-by-bunch basis by measuring the muon beam. In Section 3.1, additional description of the instruments of the muon monitor is shown. In 2014 June, T2K took the first antineutrino beam data. The muon beam profiles in the antineutrino mode as well as the neutrino mode are described in Section 3.2. Beam commissioning studies with MUMON is essential for stable beam operation because the proton beam orbit is tuned based on the muon beam profile. In Section 3.3, we describe relative alignment between the target and the baffle, correlation of the muon profile center and the proton beam position, and dependence of the muon yield on currents of the magnetic horns [101]. The muon beam intensity at MUMON is very high and the absorbed dose at the muon monitor is estimated at roughly 100 kGy for 100-day operation with a proton beam power of 750 kW. Though we designed the muon monitor considering this high radiation level, signal decrease of the MUMON sensors should be carefully monitored. In Section 3.4, long-term stability of the muon beam profile and replacement of the silicon sensors due to the irradiation damage are described and in Section 3.5, the long-term stability of diamond detectors, which are expected to have the high radiation hardness and were installed for the purpose of the performance estimation, is described.

3.1 Instruments of the muon monitor

Details of the instruments of the monitor are described in [88] and a summary is described here. MUMON comprises two independent detectors for redundancy: an array of ionization chambers (IC) and another array of silicon PIN photodiodes (Si) as shown in figs. 2.12 and 3.1. In both arrays, there are 7×7 (= 49) sensors at 25 cm intervals and covers an area of 150×150 cm^2.

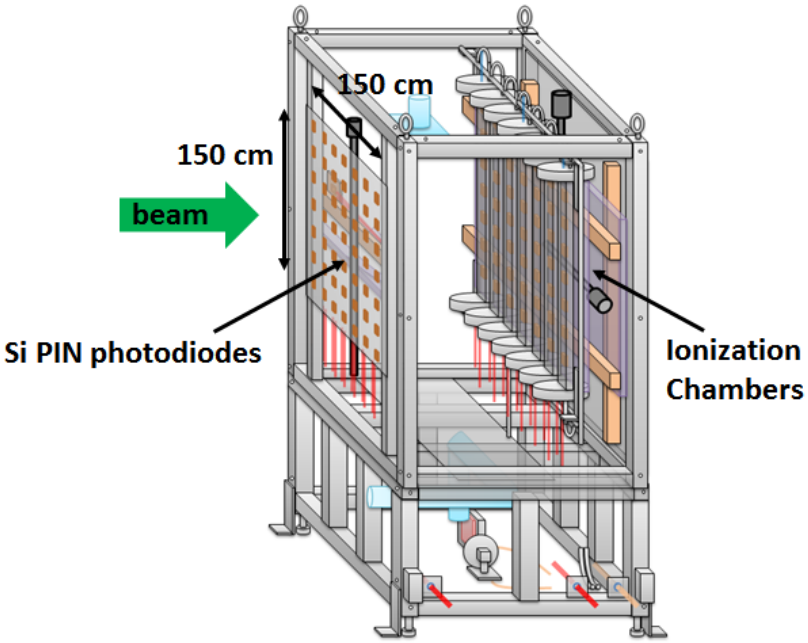

Figure 3.1: Schematic view of the muon monitor. Figure is taken from [88].

3.1.1 Silicon PIN photodiode

The silicon (Si) PIN photodiode (HAMAMATSU ® S3590-08) has an active area of 10×10 mm^2 and a depletion layer thickness of 300 μm. To fully deplete the layer, a bias voltage of 80 V is applied. The Si sensors are not tolerant of the severe irradiation and hence they have to be replaced routinely, which is described in Section 3.4.2. The packages of the Si sensors were designed so that installation or replacement works of the Si sensors could be quickly conducted. Each sensor is put on a PEEK^{TM} base, which has the high radiation resistance, and is covered by an aluminum package. There exists an extra Si sensor for the calibration of the signal size of the Si sensors. This extra sensor is mounted on the moving stage behind the silicon array. We routinely calibrate all the Si sensors by comparing the charge of each sensor to that of the extra sensor placed behind that sensor.

3.1.2 Ionization chamber

Each of the seven ionization chambers (IC) contains seven sets of two parallel 100×100 mm^2 ceramic plates separated by 3 mm. A bias voltage of 200 V is applied to the signal (75×75 mm^2) and the HV (93×93 mm^2) electrodes mounted on the ceramic plates and electron-ion pairs generated only in the 75×75×3 mm^3 contribute to the signal. From the beginning of T2K, we use 98% Ar with 2% N_2 gas. The N_2 gas plays roles as a quencher, which makes the signal response faster, and stabilizing the signal size against the amount of impurities via the Jesse effect [102]. The signal size of the Ar+N_2 gas is roughly 2.9% compared to that of the Si sensors. From the past beam tests [88], good linearity of the Ar+N_2 gas was expected up to roughly 1.8×10^{14} protons per spill for the neutrino mode, which corresponds the proton beam power of 350 kW with a spill interval of 2.48 s. For the higher intensity beam, the 99% He with 1% N_2 gas was planned to be used, where good linearity was expected up to roughly 3×10^{15} protons per spill. During May 2015, we actually used this He+N_2 gas for the physics data for the first time. The signal size of the He+N_2 gas is roughly 13.5% compared to the Ar+N_2 gas. To avoid degradation of the gas by irradiation and reduce O_2 contamination from outside, which causes the signal decrease, the gas is always replaced with a flow rate of around 70 cc/min. Gas pressure is controlled by a solenoid control

valve and kept at 130 kPa. In order to stabilize the temperature around the muon monitor, the support enclosure made of aluminum panels filled with glass wool covers the muon monitor for heat insulation. Inside the support enclosure, there is a heater and the temperature is kept at around 34 °C by controlling the heater. All the IC detectors is calibrated by moving the entire chamber array and measuring the muon profile at different array positions.

Figure 3.2: Photograph of the silicon PIN photodiodes (right) and the ionization chambers (left) in the support enclosure. The beam enters from the right side. Figure is taken from [88].

3.1.3 Reconstruction of the muon beam profile

Signal from each sensor is read out by FADC. Figure 3.3 shows an example of the signal waveform of a Si sensor. The collected charge for each spill is calculated by integrating the waveform. Figure 3.4 shows an example of one-dimensionally projected distribution of the collected charge from each sensor for the horizontal (left) and vertical (right) directions. The muon beam profiles for the Si and the IC sensors are independently reconstructed from the charge distribution of each type of the sensors. The profile of the muon beam is obtained by fitting the charge distribution by a two-dimensional Gaussian function $f(X, Y)$:

$$f(X, Y) = A \exp\left(-\frac{(X-x)^2}{\sigma_x^2} - \frac{(Y-y)^2}{\sigma_y^2}\right), \tag{3.1.1}$$

where X and Y represents the horizontal and vertical position of the fit function and A, x, y, σ_x and σ_y are fit parameters. A represents the amplitude, x and y represent the horizontal and vertical profile center position and σ_x and σ_y represent the horizontal and vertical profile width, respectively. The muon beam direction angles θ_x and θ_y are calculated from the muon beam centers x and y:

$$\theta_x = \frac{x}{L}, \quad \theta_y = \frac{y}{L}, \tag{3.1.2}$$

where L represents the distance from the target to the muon monitor (118 m). The shift of the beam center by 11.8 cm corresponds to the deviation of the neutrino beam direction by 1 mrad, which leads

to 2-3% variation of the off-axis neutrino flux. The uncertainty on the measurement of the muon beam direction was estimated to be 0.2 mrad for both the horizontal and vertical direction [89].

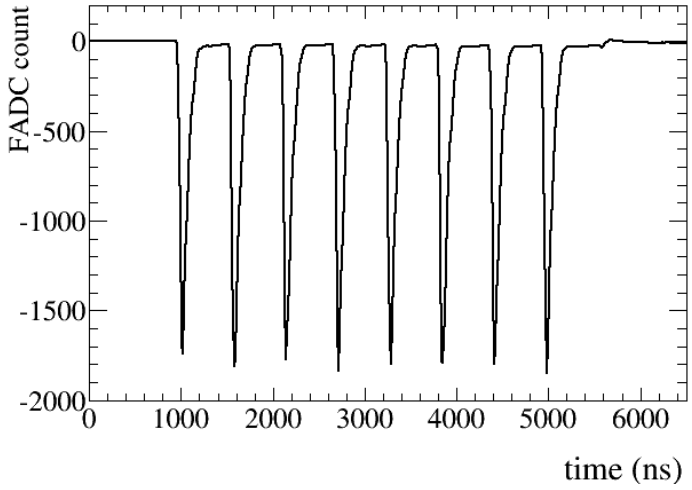

Figure 3.3: An example of the signal waveform of a Si sensor. The time structure of the proton beam is clearly seen.

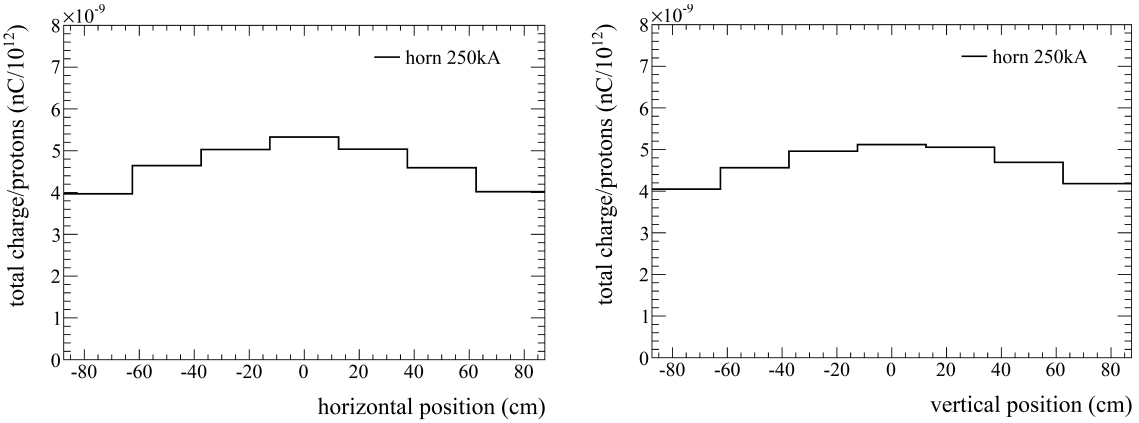

Figure 3.4: Example of muon beam profile for the horizontal (left) and vertical (right) direction measured by the MUMON Si detector in the neutrino mode.

3.2 Muon beam profile in the antineutrino mode

Figure 3.5 shows the muon beam profile by the Si detector projected to the horizontal direction and the vertical direction for the neutrino mode (+250 kA horn operation), antineutrino mode (-250 kA horn operation) and the non-physics mode where magnetic horns are turned off. The muon yield, i.e., the sum of the collected charge from each sensor, in the antineutrino mode is smaller than that in the neutrino mode because the production rate of the parent particle of μ^- (π^- and K^-) is lower than that of μ^+ (π^+ and K^+). The JNUBEAM simulation, which is used for the neutrino flux prediction and is described in Section 4.1, is also used to make a prediction of the muon beam profile. JNUBEAM provides information

such as position where muons pass through the Si and IC planes. Figure 3.6 shows the muon beam profile by the simulation at the Si detector plane projected to the horizontal direction in the neutrino mode and antineutrino mode. In the JNUBEAM simulation, the muon profile is obtained by tagging all the μ^+ and μ^- passing through the MUMON detector planes. The fraction of the wrong sign component in the antineutrino mode (μ^+) is larger than that in the neutrino mode (μ^-). This is because the difference of the production rate between μ^+ and μ^-. Table 3.1 summarizes the muon profile width in the neutrino mode and the antineutrino mode for the data taken in the T2K RUN5 and the MC simulation. The profile width is consistent within 5% between the data and the MC simulation in both the neutrino mode and the antineutrino mode. The profile width in the antineutrino mode is narrower than that in the neutrino mode because the parent particles of the wrong-sign component whose daughter muon arrive at MUMON are mainly emitted from the forward region of the target.

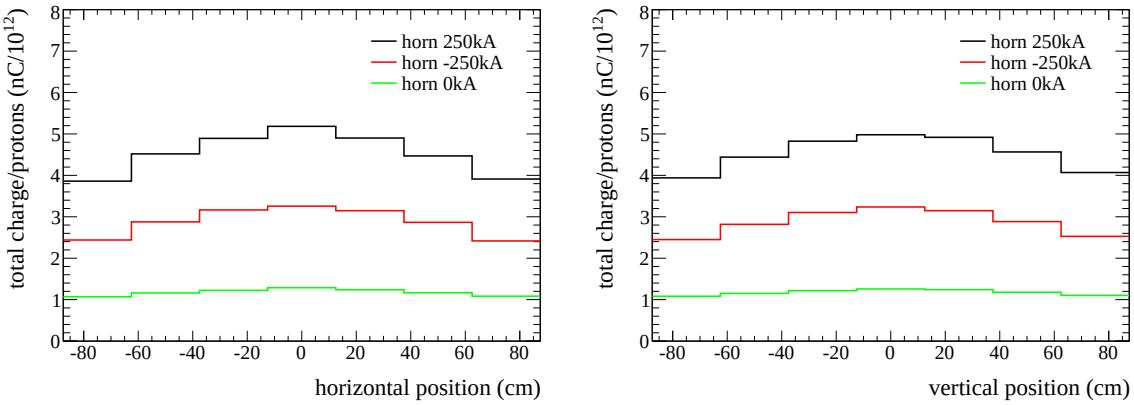

Figure 3.5: Example of the muon beam profile measured by the Si detector projected to the horizontal direction (left) and the vertical direction (right). each bin corresponds to the total charge of the sum of vertical 7 detectors. The labels 250kA, -250kA, 0kA represent the neutrino mode, the antineutrino mode and the non-physics mode where magnetic horns are turned off, respectively.

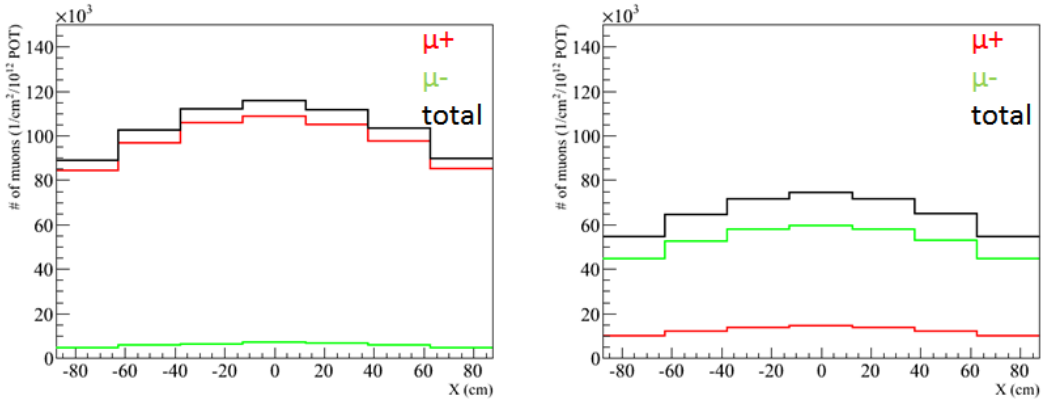

Figure 3.6: Muon beam profile by the simulation at the Si detector plane projected to the horizontal direction in the neutrino mode (left) and antineutrino mode (right). each bin corresponds to the total charge of the sum of vertical 7 detectors.

Table 3.2 shows the ratio of the $\bar{\nu}$-mode muon yield to the ν-mode muon yield between the data and

Table 3.1: Comparison of the muon profile width in the neutrino mode and the antineutrino mode between the data and the MC simulation. The uncertainty of the fitting of the muon beam profile is less than 1 cm. The profile width of IC is wider than that of Si because IC is located downstream Si.

width (cm)	MC horizontal	data horizontal	MC vertical	data vertical
Si in the neutrino mode	105.5	101.7	114.0	113.6
IC in the neutrino mode	111.7	106.4	127.0	123.8
Si in the antineutrino mode	96.2	97.7	104.1	103.8
IC in the antineutrino mode	104.0	103.1	115.0	113.5

the MC simulation. The muon yield ratio between the data and the MC simulation is consistent within 2%. It is difficult to precisely measure the absolute muon flux by using Si or IC detectors because δ-rays which are generated in nearby material objects by the muon beam contaminates into the muon flux. The comparison of the absolute yield between commissioning data using emulsion tracker detector [103] and the MC simulation in the neutrino mode was studied and they are in agreement within the uncertainty of 15% of the predicted muon flux [89]. The good agreement between data and MC demonstrates the validity of the MC prediction, which is important for understanding the MUMON response to the beamline condition.

Table 3.2: Comparison of the ratio of the $\overline{\nu}$-mode muon yield to the ν-mode muon yield between the data and the MC simulation.

muon yield ratio ($Q_{\overline{\nu}}/Q_{\nu}$)	MC	data
Si	0.628	0.637
IC	0.630	0.628

3.3 Beam commissioning studies in the T2K RUN5

In this section we discuss beam commissioning studies conducted during the T2K RUN5. During the maintenance period between the T2K RUN4 and RUN5, the target and the magnetic horns were replaced so that the higher intensity proton beam could be accepted and the baffle was also temporarily moved. For this reason, we investigated the alignment of the secondary beamline by monitoring the muon profiles with various proton beam positions at the target. If there would exist large misalignment, the proton beam could not be accepted because the proton beam may be impinged on the deviated position from the center of the target.

The $\bar{\nu}$-mode data were taken for the first time in the T2K RUN5. We studied the correlation of the profile muon center and the proton beam position and the variation of muon yield as a function of the horn currents. The study in the neutrino mode is reported in [89] and those in the antineutrino mode as well as the neutrino mode are described here. All the results are based on the measurements by the silicon array.

3.3.1 Investigation of the target alignment

Configuration of the beamline instruments

Figure 2.5 shows the top-view schematic configuration of the neutrino beamline around the target. Figure 3.7 is the view from baffle upstream along the beam axis. The diameter of the baffle hole and the target is 30 mm and 26 mm respectively and when the target is aligned ideally to the nominal position, the size of the gap between the target and the baffle is 2 mm. In the commissioning run, horizontal and vertical position of the proton beam at the target was varied roughly between -15 mm to 15 mm with increments of roughly 1 mm by changing the settings of the magnets in the primary beamline so that the proton beam center covers the gap region. The width of the proton beam was set to 2.2-2.5 mm, which is narrower than that (4-4.4 mm) used in the physics data so that to increase the sensitivity of MUMON to the proton beam position. The proton beam was kept parallel to the beam center axis. In order to avoid hardware problems due to the beam irradiation to the off-center position, the proton beam intensity in this study was set to low (4 kW). All the magnetic horns were turned off during this study.

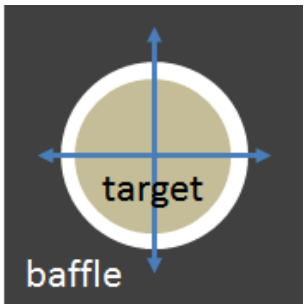

Figure 3.7: Cross-sectional view of the baffle and the target. Arrows are the range of the proton beam position varied during this study.

Results of the alignment study

Figure 3.8 shows the profile width of the muon beam at the silicon array as a function of the proton beam position before and after the replacement of the target and the magnetic horns. When some part of the proton beam enters the gap region, the fraction of the muons generated in the beam dump increases

and the profile width gets narrow. Hence, if narrower profile width is observed, the gap region between the target and the baffle exists. For the horizontal direction, the profile width is narrow at the expected beam position and the target is correctly aligned. By contrast, for the vertical direction, the profile width with the proton beam position at $y < -12$ mm region is significantly wider after the replacement. This represents the gap region in the $-y$ region is narrow or may not exist i.e., the relative alignment of the target to the baffle is shifted to the $-y$ (lower) side.

In order to estimate the size of this misalignment, we compared these muon beam profile data to that of simulations with changing the size of the misalignment. Figure 3.9 shows the predicted profile width of the muon beam as a function of the proton beam position with variating the size of the misalignment. The tendency that when some part of the proton beam enters the gap region the profile width narrow gets narrow, is confirmed in the simulation. By the comparison of this plot to the fig. 3.8, the size of the misalignment is estimated to be larger than 1.5 mm and smaller than 2 mm. Figure 3.10 shows the comparison of the profile center of the muon beam for the vertical direction between the data and the simulation. From this comparison, the size of the misalignment is confirmed again to be larger than 1.5 mm and smaller than 2 mm. Since the estimated misalignment is not very large, we concluded that the experiment can be conducted without re-alignment work. This misalignment has been taken into account in the beam tuning during the T2K RUN5 and RUN6[1].

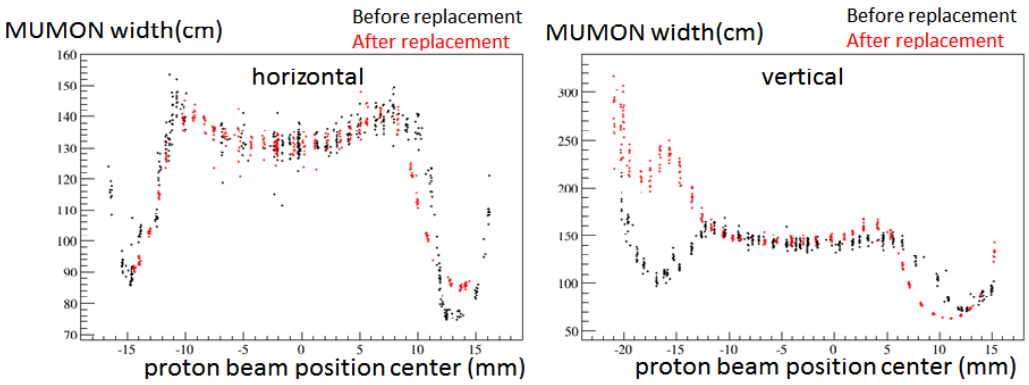

Figure 3.8: Profile width of the muon beam as a function of the proton beam position before and after the replacement of the target and the magnetic horns.

[1] After the T2K RUN6, the target and the baffle was moved again due to the maintenance work and re-aligned.

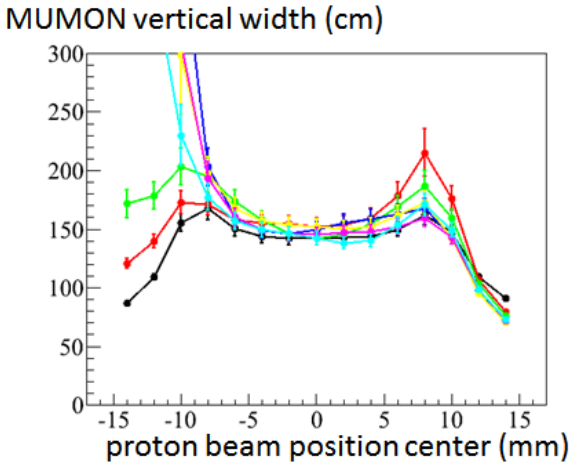

Figure 3.9: Predicted profile width of the muon beam as a function of the proton beam position with variating the size of the misalignment. The black, red, green, blue, yellow, pink and light blue lines represent the profile width distribution with the size of shift to lower position is 0 mm (nominal), 1 mm, 1.5 mm, 2 mm, 2.5 mm, 3 mm and 4 mm, respectively. The error bars represent uncertainties from the fit of the muon beam profile.

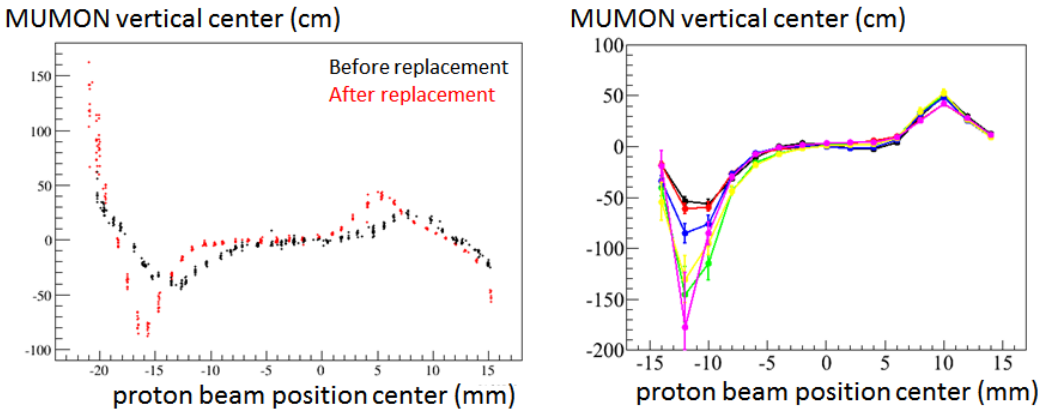

Figure 3.10: Profile center of the muon beam for the vertical direction as a function of the proton beam position for the data (left) and the simulation (right). In the right plot, The black, red, green, blue, yellow and pink lines represent the profile center distribution with the size of shift to lower position is 1.5 mm, 1.6 mm, 1.7 mm, 1.8 mm, 1.9 mm and 2 mm, respectively. The error bars represent uncertainties from the fit of the muon beam profile.

3.3.2 Correlation of the muon profile center and the proton beam position

It is important from the view point of the safety to confirm whether the muon monitor has the sensitivity to the proton beam position during taking physics data. Hence, we studied the variations of the muon beam center when the proton beam center varies separately for the neutrino mode and the antineutrino mode operations. The proton beam position at the target was varied roughly between -5 mm to 5 mm with increments of roughly 1 mm, with the nominal beam width for physics data and with low proton beam intensity.

Figure 3.11 shows the correlation between the muon profile center and the proton beam position. The observed correlation for the antineutrino mode is similar to that for the neutrino mode. This means we can find the unusual deviation of the proton beam in both the neutrino mode and the antineutrino mode. We estimated the slopes of the muon profile center to the proton beam position from MC predictions. Table 3.3 shows the comparison of the slopes of the muon profile center with respect to the proton beam position between data and MC. The slopes of the data are in agreement with those of the MC prediction. Since the resolution of the muon profile measurement is better than 3 mm, we have the sensitivity to the proton beam position with a resolution better than 0.15 mm.

This correlation of the muon profile center and the proton beam position is negative. This reason is considered as follows: When the off-center proton beam, for example vertically positive (+y) direction, is impinged on the target, the larger part of the secondary particles are generated around the +y region of the target and exit from and go to the +y direction. Those particles are then strongly focused by the magnetic horn and are directed in the opposite (-y) direction [2].

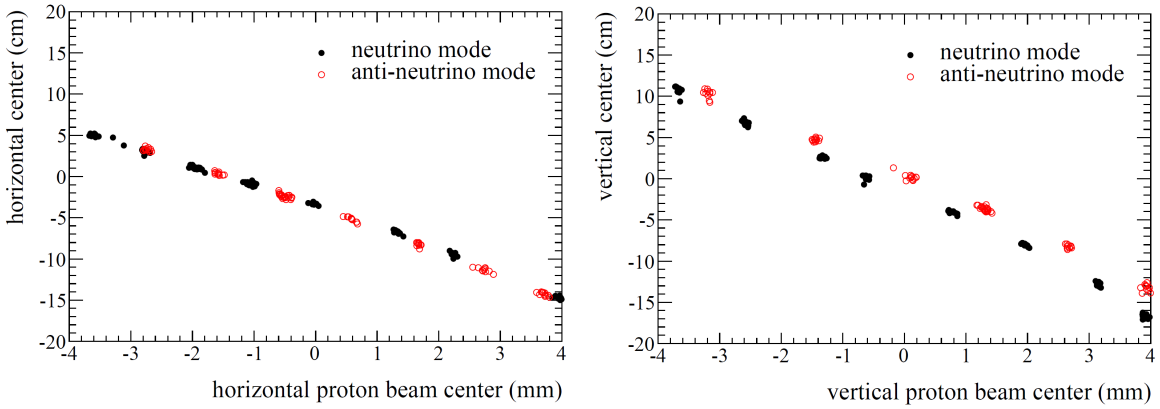

Figure 3.11: Correlation between the muon profile center and the proton beam position in the horizontal (left) and vertical (right) directions.

Table 3.3: The slopes of the muon profile center to the proton beam position.

slope (cm/mm)	MC horizontal	Data horizontal	MC vertical	Data vertical
neutrino mode	-2.8	-2.6	-3.6	-3.4
antineutrino mode	-2.5	-2.7	-3.1	-3.1

[2] If the focusing power of the magnetic horns are weaker than the nominal case (250 kA), the correlation become positive. This tendency is confirmed by the past beam commissioning study [89].

3.3.3 Dependence of the muon yield on the magnetic horn currents

We checked the variation of the muon yield when horn current is varied. All three magnetic horn currents are simultaneously varied ±1% and ±2% from the nominal value (±250 kA). Figure 3.12 shows the dependence of the muon yield on the horn current in the neutrino mode and the antineutrino mode. The slopes of the muon yield with respect to the horn current from this data are determined and the result is shown in table 3.4. The slope in the antineutrino mode is slightly smaller than that in the neutrino mode. This is because the fraction of the wrong sign component in the antineutrino mode is larger than that in the neutrino mode. The wrong-sign component is less sensitive to the horn current compared to the right-sign component because the parent particles of the wrong-sign component whose daughter muon arrive at the muon monitor are mainly emitted from the forward region of the target (inside the inner conductor of the horn-1) where the magnetic field is small as shown in fig. 2.9. We estimated the slopes from MC predictions by generating muon flux with different horn currents. Table 3.4 shows the variation rates of the muon yield to the horn current. The slopes of the data are in agreement with the MC prediction within 4%. These variation rates are used for the correction of the muon yield.

Table 3.4: Variation rates of the muon yield to the horn current.

variation rate (%/kA)	Data	MC
neutrino mode	0.80	0.83
antineutrino mode	0.71	0.72

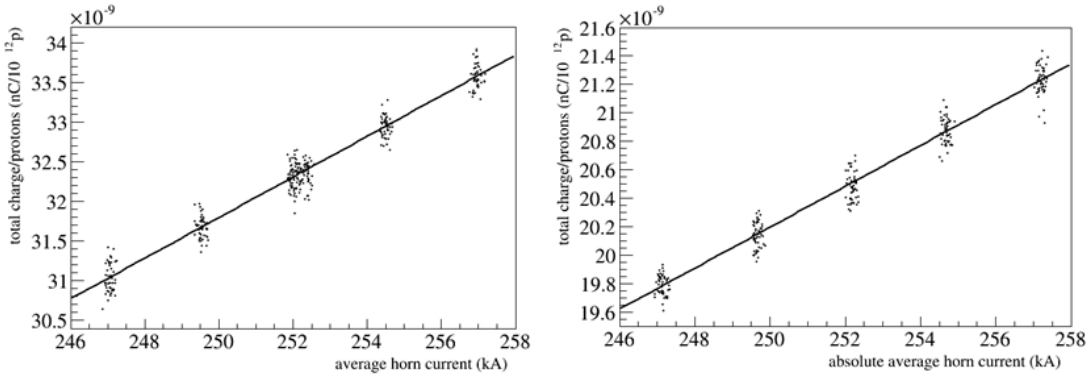

Figure 3.12: Variation of the muon yield as a function of currents of the magnetic horns in the neutrino mode (left) and antineutrino mode (right).

3.4 Long-term stability of the muon beam profile

3.4.1 Long-term stability of the beam center

Figure 3.13 shows the history of the muon beam center measured by MUMON and the neutrino beam center measured by INGRID. Both the muon beam center and the neutrino beam center are stable within 0.4 mrad during the whole period. For the vertical direction in the RUN5 and RUN6, the muon beam center is slightly lower than the neutrino beam center. One possible reason for this discrepancy is the misalignment of the beamline instruments. The effect of the misalignment to the beam center could be

different between MUMON and INGRID because MUMON measures very high energy (>5 GeV) muons while INGRID measures neutrinos whose mean energy is around 1 GeV.

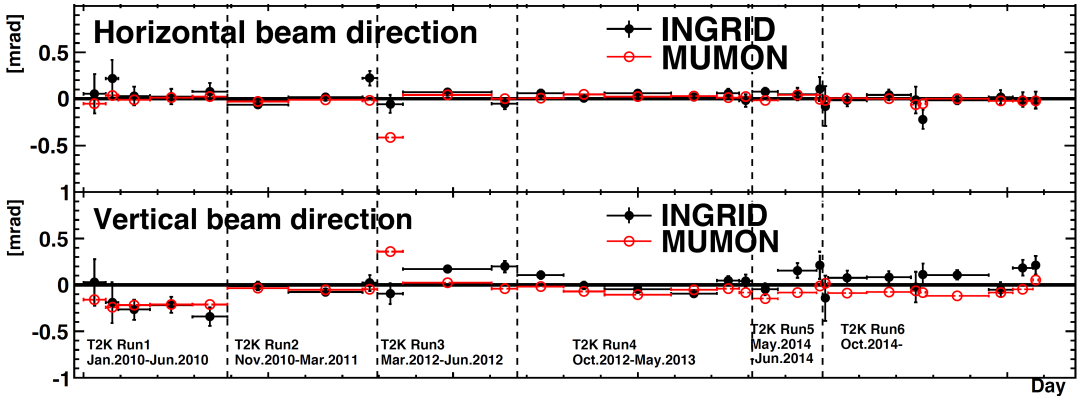

Figure 3.13: History of the muon beam center measured by the muon monitor (MUMON) and the neutrino beam center measured by the on-axis near detector (INGRID). Top: horizontal direction, Bottom: vertical direction.

3.4.2 Replacement of silicon detectors

From past beam tests, the signal size of the Si detector is expected to decrease roughly 1% after the irradiation of 8×10^{20} POT [88]. Before the integrated POT reaches 8×10^{20}, we replaced only two Si sensors in December 2012 and then two other Si sensors in April 2013 (Replacement position is shown in fig. 3.14) in order to confirm the stability of the replaced sensors. Since the Si sensors are calibrated by comparing with the extra Si sensor, the monitoring of the muon beam profile is considered to be hardly affected by this replacement. However, we still selected symmetric two positions for this tentative replacement to minimize the effect on the monitoring. The other sensors except for the extra sensor for calibration were replaced in November 2013. After the replacement, we observed that the signal size of each replaced sensor decreases quickly and after the integrated exposure of roughly 5×10^{8} pC, which corresponds to 1 day operation of the T2K beam, this signal decrease stops and after then the signal size of the replaced sensor becomes stable as shown in fig. 3.15. The size of this signal decrease is around 1% and the effect on the beam direction measurement is small. This phenomenon was not confirmed at the beginning of T2K because the effect is small and the beam condition changed many times at that time. The reason of this signal decrease is not well understood but partial lattice defect of the silicon crystal which quickly saturates is one possible reason.

3.4.3 Correction of the muon yield by the horn current

When we consider the stability of the muon yield, we have to take into account the variation of the horn current. Figure 3.16 shows the history of the electrical horn current averaged over the three magnetic horns. The variation of the horn currents is mainly due to the variation of the temperature of the environment.

The correction is given as:

$$Q' = Q(1 - f(|I| - 250)), \tag{3.4.1}$$

where Q, Q', I and f represent the raw muon yield, the corrected muon yield, the horn current averaged over the magnetic horns and the correction factor, which is estimated from the study of the variation of

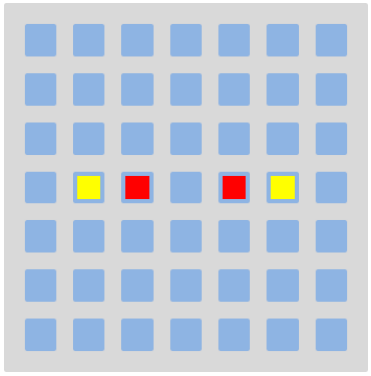

Figure 3.14: Replacement position of the Si sensors. The yellow (red) squares are Si sensors replaced in December 2012 (April 2013) and the other sensors were replaced in November 2013.

the muon yield when horn current is varied (table 3.4, data), respectively. The horn currents are measured for each spill and then this correction is applied for each spill.

3.4.4 Long-term stability of the muon yield

Figure 3.17 shows the history of the muon yield without (left) and with (right) the horn current correction. The muon yield during the identical T2KRUN, where configurations of the beamline instruments were not largely changed, becomes stable after the horn current correction. The muon yield measured by the IC during the T2K RUN2 is lower than the other period probably due to gas contamination. The muon yields for both the Si and IC were decreased roughly 1-2% between the T2K RUN4 and RUN5. The same phenomenon was seen in the muon yield when magnetic horns are turned off as shown in fig. 3.18. This is probably caused by the replacement of the target and the magnetic horns, however we have not yet known the direct reason. So far, no clear evidence of the signal decrease of the Si sensors is observed.

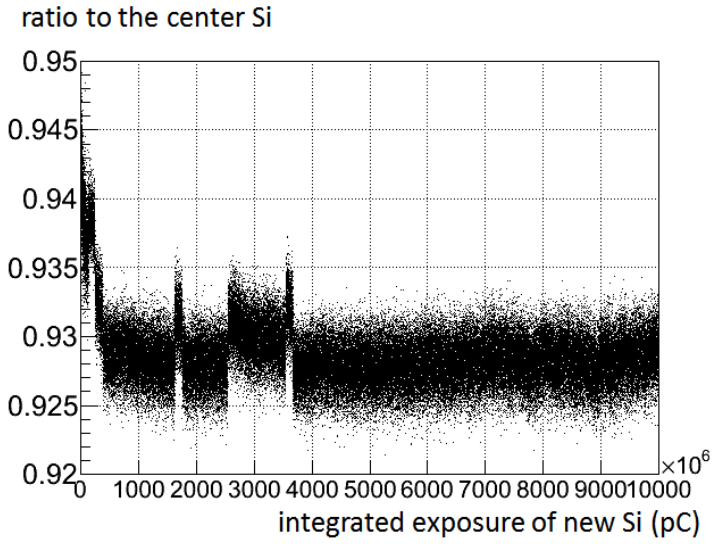

Figure 3.15: The ratio of signal size of a replaced Si sensor to that of the center Si sensor (not replaced yet) as a function of the integrated exposure. The sudden changes after the signal decrease are due to the changes of the beamline condition. This is caused by changes of various settings of the beamline components.

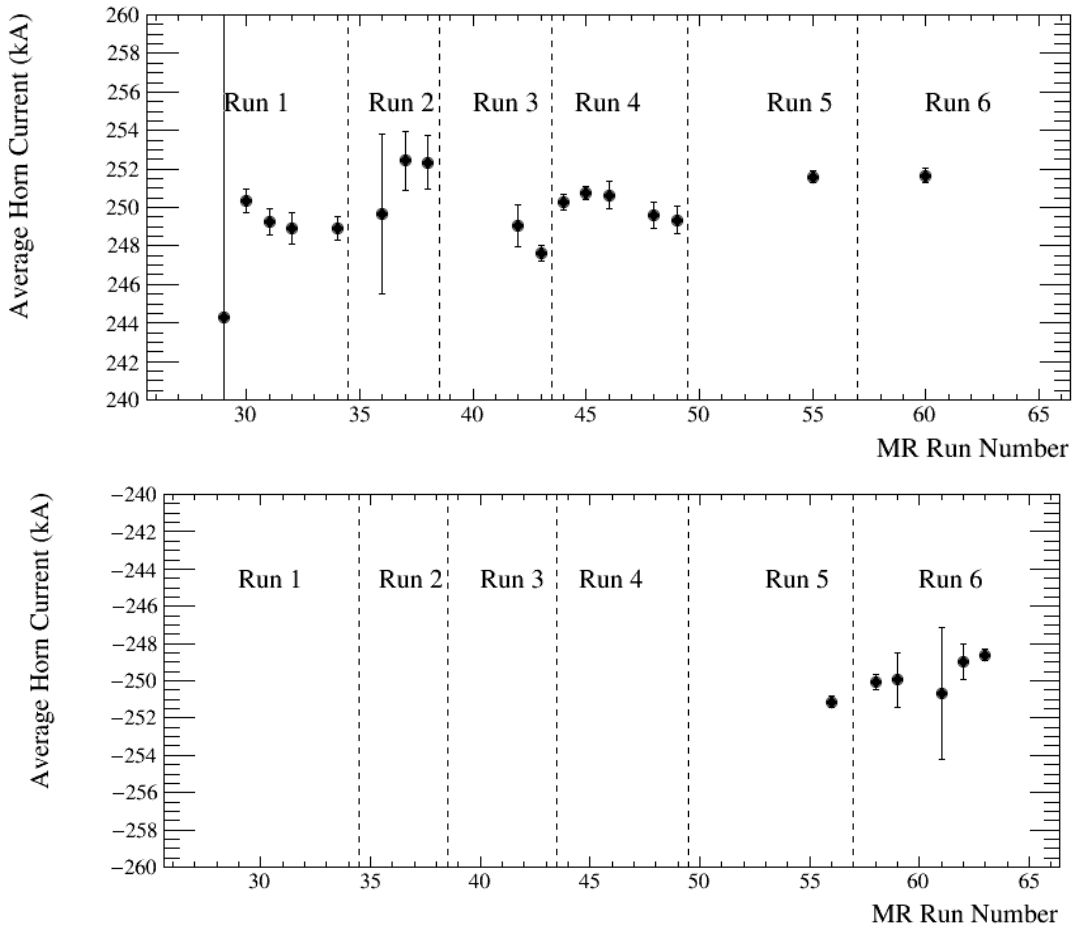

Figure 3.16: History of the average horn current of the three magnetic horns in the neutrino mode (top) and the antineutrino mode (bottom). The horizontal axis represents the Main Ring run number (table 2.2).

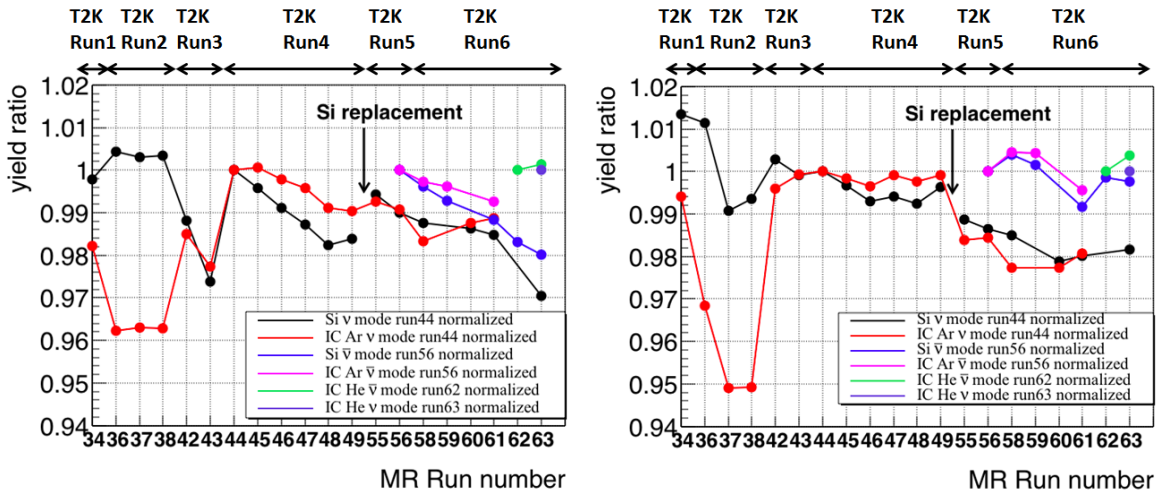

Figure 3.17: History of the muon yield without (left) and with (right) the horn current correction. The yield of the Si and IC-Ar in the neutrino mode is normalized by that in the MR Run 44. The yield of the Si and IC-Ar in the antineutrino mode is normalized by that in the MR Run 56. The yield of the IC-He in the neutrino (antineutrino) mode is normalized by that in the MR Run 62 (63).

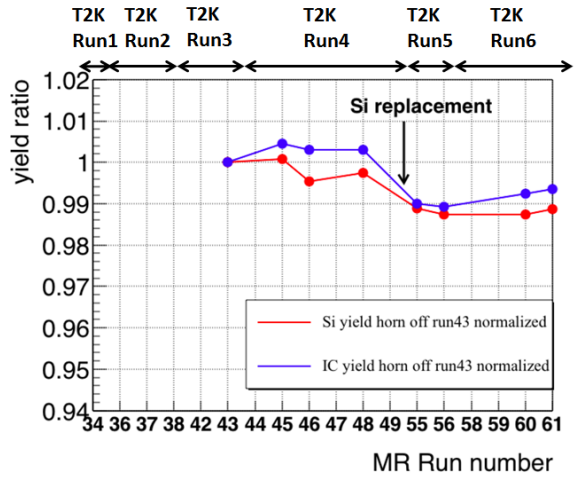

Figure 3.18: History of the muon yield when magnetic horns are turned off (non-physics data). The yield for all period is normalized by that in the MR Run 43.

3.5 Long-term stability of the test diamond sensors

Since Si sensors do not have the high radiation resistance, we have to regularly replace them as described in Section 3.4.2. The diamond sensor is a candidate of an alternative of the Si sensor and is considered to have the high radiation resistance. The crystal of the diamond sensor is artificially produced by the chemical vapor deposition process.

3.5.1 Properties of the diamond sensors

Table 3.5 shows the properties of silicon and diamond. The working principle of the diamond sensor is similar to that of semiconductor sensors in terms of the collection of the electron-hall pairs by applying a bias voltage. Diamond has high electric resistivity and the leakage current of the diamond sensor is very small. The displacement energy, i.e., the minimum kinetic energy necessary for an atom in the crystal to be permanently displaced from its lattice site to a defect position, for diamond is larger than that for Si. This indicates the diamond sensor has higher radiation hardness than the Si sensor. The radiation hardness of diamond sensors has been measured by the CERN-RD42 collaboration [105]. They investigated the signal decrease of the diamond sensor by the irradiation of a 24 GeV proton beam at CERN. They found after the irradiation of 1×10^{15} (2×10^{16}) protons/cm^2, the signal size was roughly 90% (25%) compared to before irradiation. This proton irradiation can be converted to the muon irradiation by using the NIEL scaling [106]. The irradiation of 1×10^{15} 24 GeV protons/cm^2 corresponds to roughly 1×10^{23} POT, which is much larger than the planned integrated POT (7.8×10^{21}) of T2K. This result suggests the diamond sensor has radiation resistance sufficient for the muon monitor. However, there is no direct measurement about the signal decrease of the diamond sensor by the irradiation of the muon beam and the quality of the diamond crystal which the RD42 collaboration used is not clear. Hence, we have installed test diamond sensors in order to investigate whether diamond sensors can be used for the muon monitor.

Table 3.5: Properties of silicon and diamond.

	Si	C (diamond)
atomic number	14	6
density (g/cm^3)	2.33	3.52
band gap at 300 K (eV)	1.12	5.47
e-h pair creation energy (eV)	3.6	13
displacement energy (eV)	15-20	37-47 [104]
electric resistivity ($\Omega \cdot$ cm)	10^5	$> 10^{11}$

3.5.2 diamond sensors installed

Six diamond sensors has been installed just downstream the support enclosure of the muon monitor. The position is close to the center IC sensor. Four diamond sensors were purchased from Element Six [3] and were installed before the T2K RUN4. Two of them are called the "detector grade" and the others are called the "electronic grade". The quality of diamond crystal, which depends on the amount of impurities contaminated into the crystal, for the detector grade is better than that for the electronic grade. Another two "detector grade" diamond sensors were purchased from Cividec [4] and were installed during the T2K RUN4 (April 2013). The size of the crystal is roughly 4 mm $\times$ 4 mm $\times$ 0.5 mm (thickness). Both sides

[3] http://www.e6.com
[4] https://cividec.at

of the diamond crystal surface are coated by thin gold layers, which work as the electrodes. We applied a bias voltage of 200 V to each diamond sensor.

3.5.3 Long-term stability

Figure 3.19 shows the ratio of the signal from the diamond sensors to that from the center IC censor as a function of time. We observed signal decrease for all the diamond sensors and the signal decrease size is significantly different (2-10%) for each detector. The reason for the difference of the signal decrease size is considered to be the difference of the quality of the diamond crystal. The current conclusion is that we cannot use at least electronic grade sensors for the muon monitor.

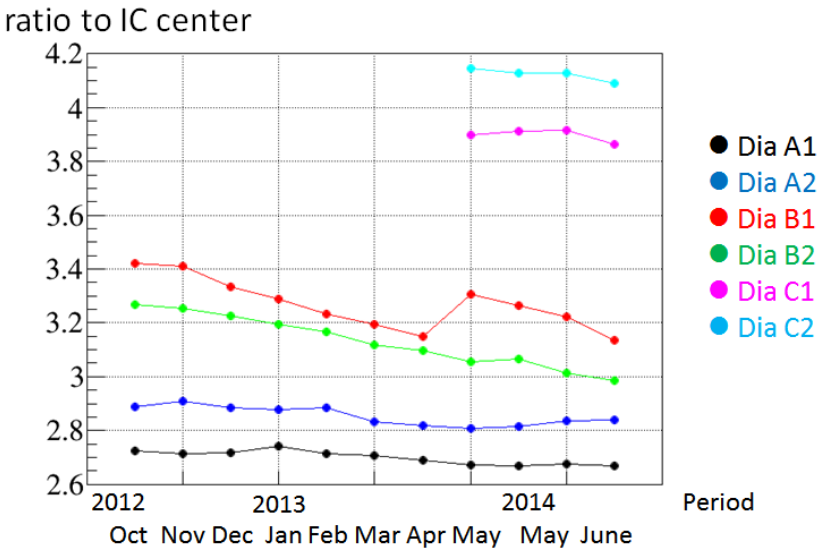

Figure 3.19: Ratio of the signal from the diamond sensors to that from the IC sensor located in the center as a function of time. The diamond sensors labeled as A1 and A2 are the detector grade of E6, those labeled as B1 and B2 are the electronic grade of E6, and those labeled as C1 and C2 are the detector grade of Cividec.

Chapter 4

Neutrino flux prediction

The flux prediction is an essential input to the neutrino event prediction both in the oscillation analysis and in cross section measurements. Here, property of the neutrino flux in the antineutrino mode as well as in the neutrino mode are examined. We evaluated the uncertainty of the flux for each of neutrino energies, neutrino flavors, detectors (the near detector and the far detector) and neutrino modes and the correlation among them in order to refine the flux prediction at the far detector using the near detector data. The uncertainty of the hadron production at the interaction of the primary-beam proton and the target is the dominant source of the flux uncertainty and are reduced by including the recent data from the CERN-NA61/SHINE experiment.

4.1 Overview of the neutrino flux prediction

Figure 4.1 shows the procedure of the neutrino flux prediction. The neutrino flux prediction consists of a two-step simulation and tuning based on the hadron interaction data from external experiments.

FLUKA 2011 [110] [111] is used for simulating the hadronic interactions in the target rod, where the primary proton beam first interacts and produces the majority of the hadrons. This is because FLUKA is found to have the best agreement with the existing external hadron production data. Kinematic information of particles emitted from the target is saved and transferred to the simulation of the succeeding simulation, JNUBEAM.

JNUBEAM simulates [107] the transportation of the particles emitted from the target through the graphite tube and the titanium case surrounding the target, magnetic horns with their magnetic fields, the decay volume, the beam dump, and the muon monitor. JNUBEAM is a custom-made simulation based on GEANT3 [108] and hadronic interactions in JNUBEAM are modeled by GCALOR [109].

Neutrinos are produced by decays of hadrons and muons. When particles decay into neutrinos, the neutrinos are forced to point in the direction of the far detector or a randomly chosen point in the near detector planes in order to save the computing time. In JNUBEAM, the kinematic variables of neutrinos and the decay probability of parent particles based on the decay process and branching fraction are saved. The flux with the energy spectrum is obtained from simulated events by weighting according to the saved probabilities. In addition, the kinematic information of the initial proton, the tracks of particles and full interaction chain which produces the neutrino are saved for the tuning of the hadronic interactions.

Hadronic interactions simulated in FLUKA and GCALOR are then tuned by reweighting each events from the simulation based on external hadronic interaction measurements. The most important external experiment is the NA61/SHINE experiment at CERN, which is described in Section 4.2.

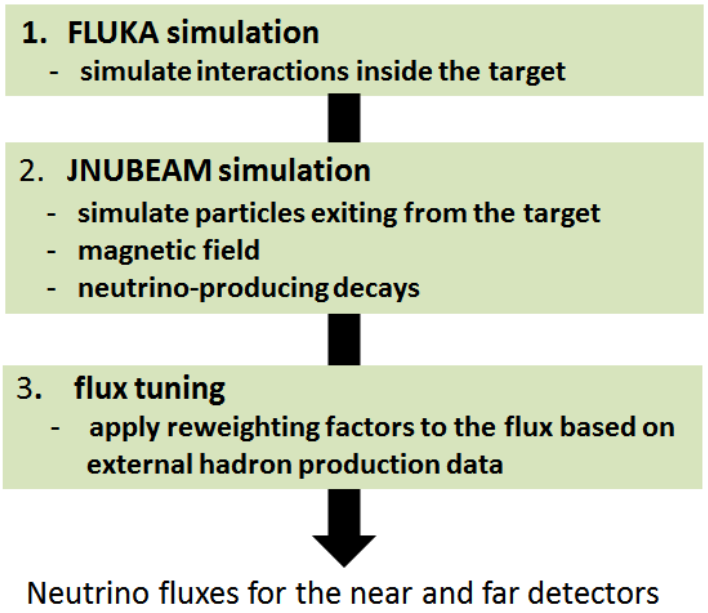

Figure 4.1: Flow of the neutrino flux prediction.

4.1.1 Beamline condition

In order to take into account the actual conditions of the neutrino beamline and precisely predict the neutrino flux, following measurements are used as the input to the flux simulation:

- proton beam parameters upstream the surface of the baffle reconstructed by the data from SSEMs, ESMs and the OTR.
- electric current of the magnetic horns.

The proton beam parameters which are used as the input to the flux simulation are center position, angle to the beam axis, width, emittance, and the Twiss parameter for both horizontal and vertical directions[1]. These parameters are reconstructed by using the data from the ESMs, the SSEMs and the OTR. The horn current is monitored by Rogowski coils wound around striplines of each horn. Measurement uncertainties of the proton beam parameters and the horn current are taken into account to the flux uncertainty.

4.1.2 Neutrino flux

Figure 4.2 shows the predicted neutrino fluxes at the off-axis near detector and the far detector in the neutrino mode and the antineutrino mode. The procedure of the flux tuning will be described in Section 4.3. Around the peak energy, ν_μ flux in the neutrino mode is roughly 20% larger than $\bar{\nu}_\mu$ flux in the antineutrino mode, due to the larger production rate of π^+ compared to π^- as shown in figs. 4.9 and 4.10. The ratio of the wrong-sign component ($\bar{\nu}_\mu$ flux in the neutrino mode and ν_μ flux in the antineutrino mode) to the right-sign component around the peak energy is roughly 3%. At higher energy, the ratio is much

[1]The emittance and the Twiss parameter are the optical parameters related to the proton beam divergence.

Table 4.1: Neutrino-producing decay modes considered in JNUBEAM and their branching ratio. Charge conjugates are omitted.

Decay modes	Branching ratio (%)
$\pi^+ \to \mu^+ \nu_\mu$	99.988
$\pi^+ \to e^+ \nu_e$	1.23×10^{-4}
$K^+ \to \mu^+ \nu_\mu$	63.55
$K^+ \to \pi^0 \mu^+ \nu_\mu$	3.353
$K^+ \to e^+ \nu_e$	5.07
$K^0_L \to \pi^- \mu^+ \nu_\mu$	27.04
$K^0_L \to \pi^- e^+ \nu_e$	40.55
$\mu^+ \to e^+ \bar{\nu}_\mu \nu_e$	100

higher in the antinuetrino mode than that in the neutrino mode because in higher energy region $K^\pm$ is the dominant parent of neutrino as shown in figs. 4.3 and 4.4, and production rate of K^+ is larger than that of K^-.

4.1.3 Parent particles of neutrinos

The neutrinos in the T2K beam are produced in the decays of hadrons or subsequent muons which themselves are produced in hadron decays. In JNUBEAM, $\pi^\pm$, $K^\pm$, K^0_L, $\mu^\pm$ decays listed in Table 4.1 are considered as neutrino sources[2]. Figures 4.3 and 4.4 show the neutrino flux broken down by parent particles. For ν_μ in the neutrino mode ($\bar{\nu}_\mu$ in the antineutrino mode), π^+ (π^-) gives the dominant contribution to the neutrino flux in the low (<3 GeV) energy region and K^+ (K^-) has the dominant contribution to the neutrino flux in the high energy region.

[2] K^0_S mostly decays to 2 pions and neutrino-producing decay modes of K^0_S are not considered.

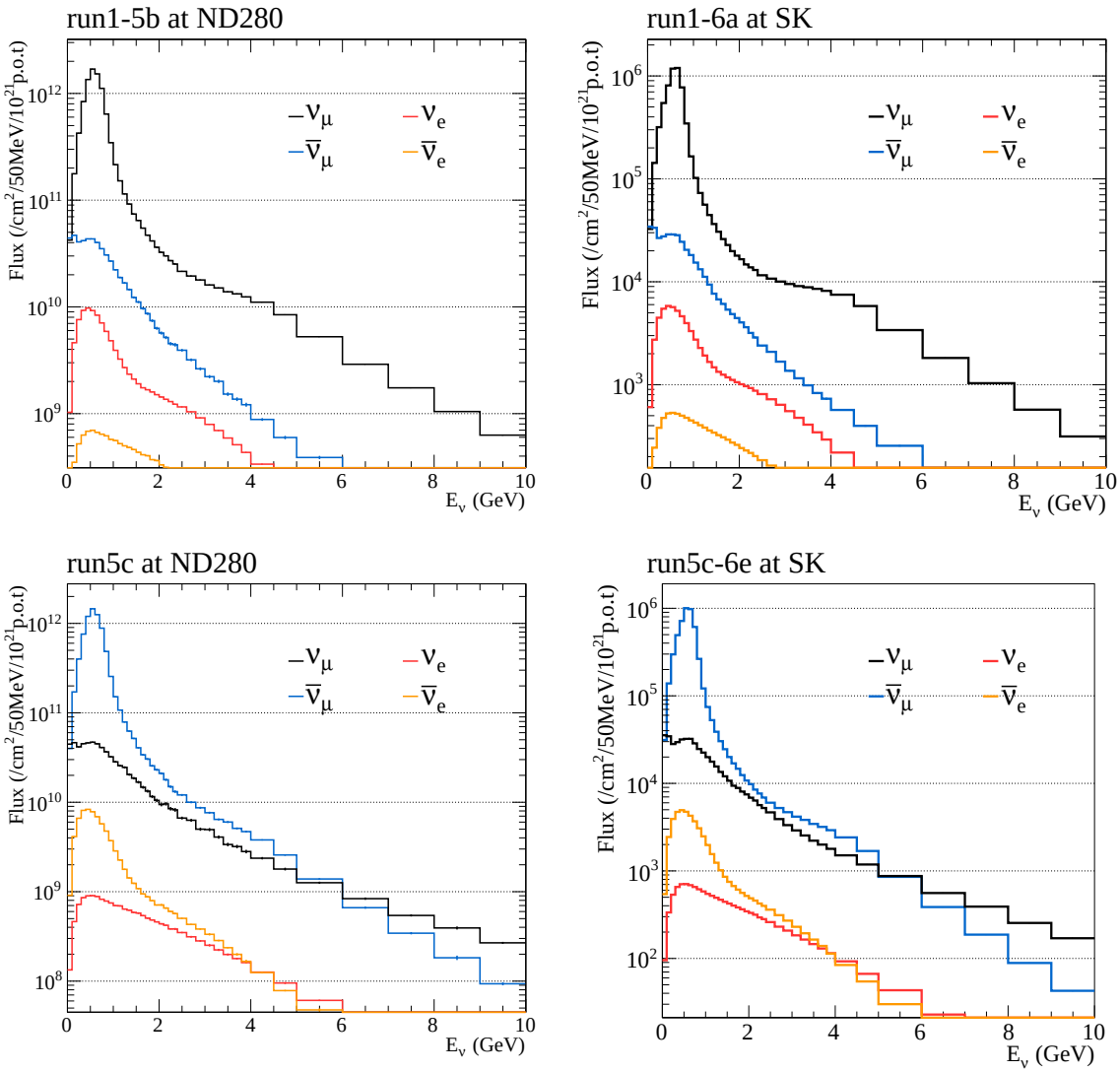

Figure 4.2: Predicted neutrino flux spectra at the off-axis near detector (left) and the far detector (right) in the neutrino mode (top) and the antineutrino mode (bottom). For this $\overline{\nu}_\mu$ disappearance oscillation analysis, the neutrino mode and antineutrino mode flux at the near detector and the antineutrino mode flux at the far detector are used as the input to the neutrino event prediction.

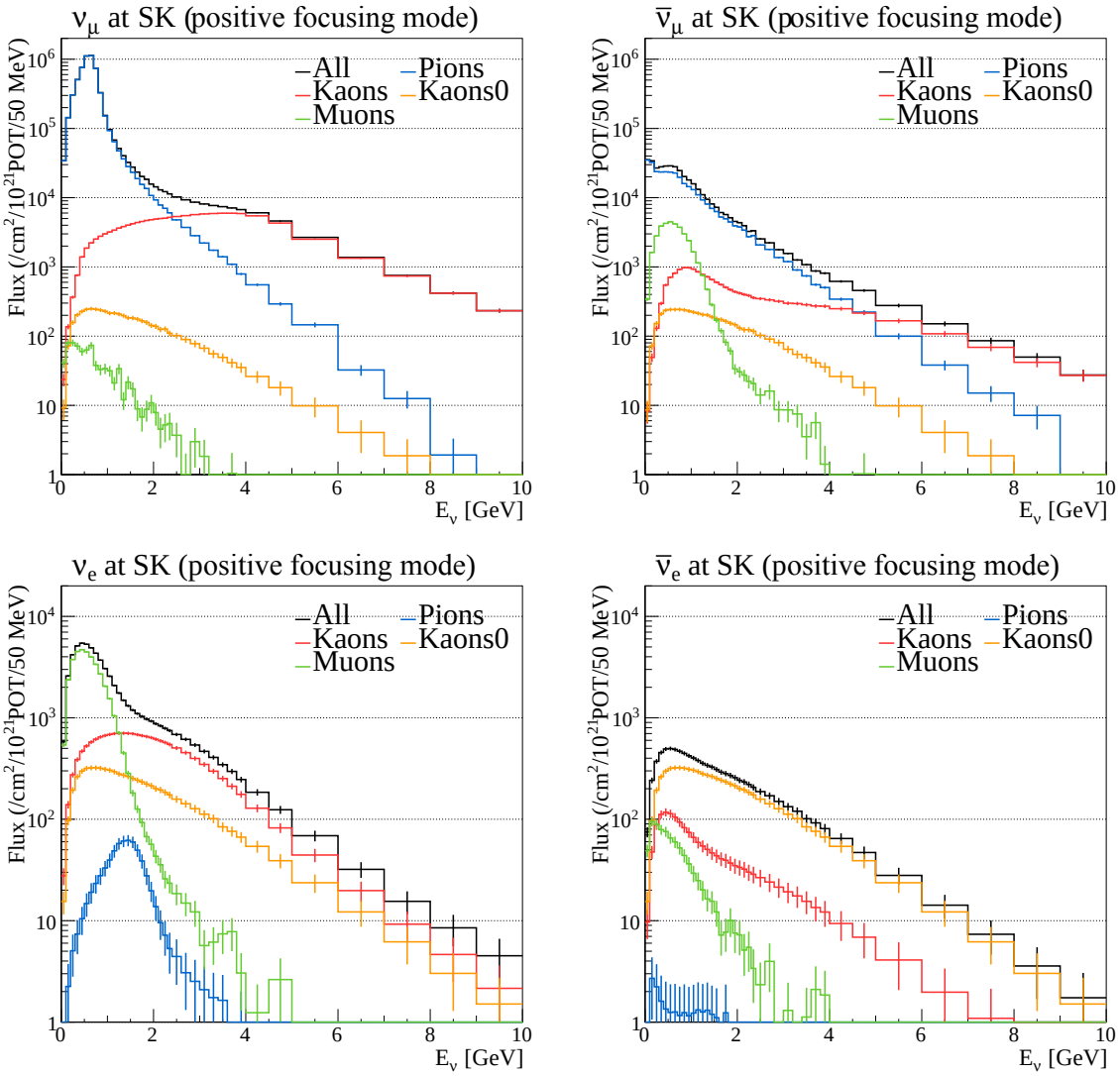

Figure 4.3: Neutrino fluxes broken down by parent particles. Shown here are the fluxes at the far detector in the neutrino mode. In these figures the flux tuning are not applied. Top left: ν_μ, top right: $\bar{\nu}_\mu$, bottom right: ν_e, bottom left: $\bar{\nu}_e$.

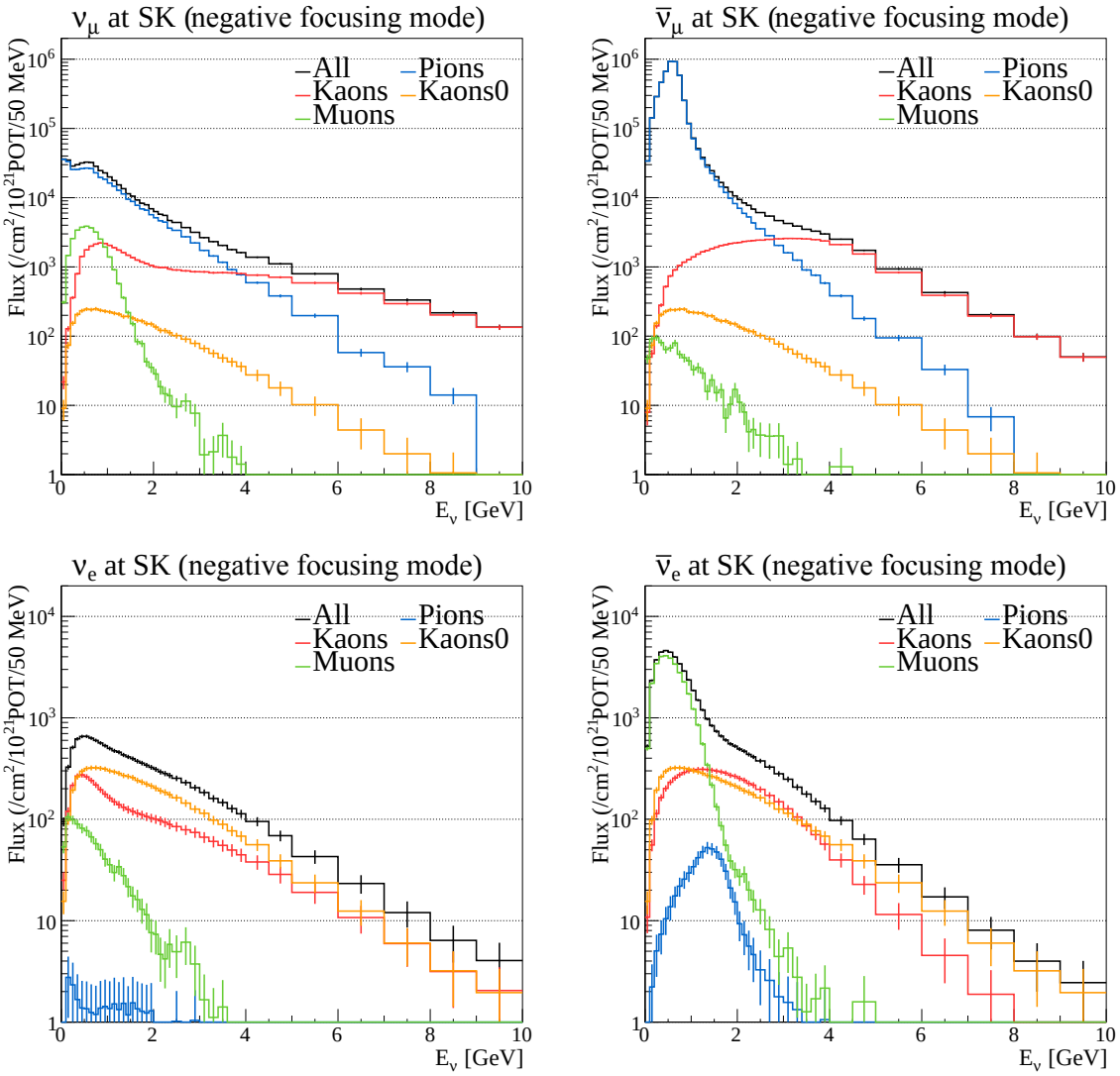

Figure 4.4: Neutrino fluxes broken down by parent particles. Shown here are the fluxes at the far detector in the antineutrino mode. In these figures the flux tuning are not applied. Top left: ν_μ, top right: $\bar{\nu}_\mu$, bottom right: ν_e, bottom left: $\bar{\nu}_e$.

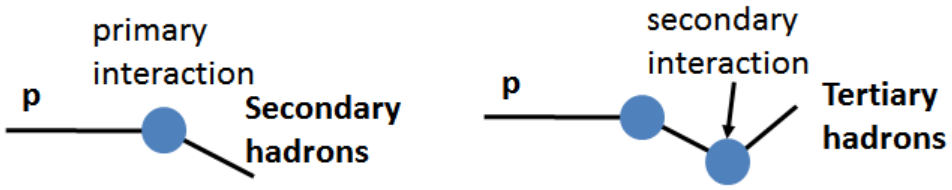

Figure 4.5: Labels of hadronic interactions and produced hadrons.

4.1.4 Interaction category

The length of the target is 90 cm and corresponds to 1.9 interaction length. Thus, greater part of the beam protons interact insides the target more than once. Figure 4.5 shows the labels of hadronic interactions and produced hadrons. The primary particle represents the beam protons and their interactions are the primary interactions. Particles produced in the primary interactions are secondary particles, and their interactions are secondary interactions. Particles which originate in the secondary or subsequent interactions are called tertiary particles and their interactions are referred to as tertiary interactions.

Some interactions occur outside the target. These interactions are called out-of-target interactions. The possible target materials for the out-of-target interactions are C (beam dump), Al (magnetic horn), Fe (decay-volume wall), Ti (case of the target) and He (gas in the Target Station). Hadronic interactions in Al and Fe are majority of the out-of-target interactions. Tables 4.2 and 4.3 show the average fraction of hadronic interactions for each flavor in the neutrino mode and the antineutrino mode, respectively. Most of the primary interactions are inside the target while some fraction of secondary and tertiary particles occurs outside the target. The fraction of the out-of-target interactions in the wrong-sign component is larger than that in the right-sign component because only right-sign secondary hadrons are collected by the magnetic horns. Thus, the effect of the out-of-target interactions to the neutrino event prediction in the antineutrino mode is larger than that in the neutrino mode because the neutrino-nucleus cross section of the wrong-sign component in the antineutrino mode (neutrino) is larger than that in the neutrino mode. As described in Section 4.3.2, we tune the interaction rate of proton inside Al and Fe.

Table 4.2: The average fraction of hadronic interactions broken down by material types in the neutrino mode at the far detector. The numbers are normalized by the number of total primary interactions for each flavor. The label C-in (C-out) represents carbon-hadron interaction in (out of) the target.

	material	C-in	C-out	Al	Fe	Ti
ν_μ	primary	0.993	0.005	0.000	0.000	0.000
	secondary	0.339	0.031	0.056	0.013	0.004
$\bar{\nu}_\mu$	primary	0.955	0.025	0.001	0.001	0.000
	secondary	0.292	0.062	0.132	0.189	0.003
ν_e	primary	0.990	0.007	0.000	0.000	0.000
	secondary	0.319	0.029	0.050	0.017	0.003
$\bar{\nu}_e$	primary	0.972	0.018	0.001	0.001	0.000
	secondary	0.259	0.036	0.075	0.077	0.002

Table 4.3: The average fraction of hadronic interactions broken down by material types in the antineutrino mode at the far detector. The numbers are normalized by the number of total primary interactions for each flavor in the antineutrino mode at the far detector. The label C-in (C-out) represents carbon-hadron interaction in (out of) the target.

	material	C-in	C-out	Al	Fe	Ti
ν_μ	primary	0.953	0.025	0.001	0.002	0.000
	secondary	0.258	0.050	0.118	0.166	0.003
$\overline{\nu}_\mu$	primary	0.993	0.004	0.000	0.000	0.000
	secondary	0.368	0.033	0.061	0.017	0.004
ν_e	primary	0.965	0.023	0.001	0.001	0.000
	secondary	0.245	0.038	0.075	0.084	0.002
$\overline{\nu}_e$	primary	0.991	0.006	0.000	0.000	0.000
	secondary	0.359	0.031	0.057	0.019	0.004

Table 4.4: Summary of the NA61 data used for the T2K flux prediction.

year when data were taken	number of events triggered ($\times 10^6$)	particle types used for the T2K flux prediction
2007	0.7	$\pi^{\pm}$ [113], K^+ [114], K^0_S, Λ [115]
2009	5.4	$\pi^{\pm}$, $K^{\pm}$, p, K^0_S, Λ [116]

4.2 The NA61/SHINE experiment at CERN

The CERN-NA61/SHINE experiment (SPS Heavy Ion and Neutrino physics Experiment) [112] is a fixed target experiment using the CERN SPS accelerator. NA61 has been studying various kinds of hadron-nucleus and nucleus-nucleus interactions and has conducted specific measurements for the T2K experiment.

The SPS accelerator provides a 400 GeV/c proton beam which impinges upon the primary beryllium target. The momentum of secondary particles from the target which are transported to the beamline of the NA61 experiment can be selected by spectrometers.

4.2.1 NA61 data for the T2K flux prediction

A 31 GeV/c proton beam, which is identical to that for T2K, is provided to the target of the NA61/SHINE experiment. The targets used for the T2K flux prediction are made of 1.8 g/cm^3 graphite, which are also the same material and density as that for T2K. Two kinds of target are used for the T2K flux prediction: a 2 cm thick target (thin target) and a 90 cm thick target (T2K replica target). The analysis of the T2K replica target is ongoing and this will be used for the reduction of the flux uncertainties in future. The thin-target data which were taken in 2007 have been used for the T2K flux prediction [107] until 2014. After improvements of the trigger logic, DAQ, and detectors in 2008 in order to reduce both statistical and systematic uncertainties, NA61 took thin-target data in 2009 again [116]. In this analysis, the 2009 thin-target data as well as the 2007 thin-target data are used for the T2K flux prediction.

Table 4.4 shows a summary of the NA61 data used for the T2K flux prediction. The number of triggered events in 2009 is roughly 8 times larger than that in 2007. The particle types used for the T2K flux prediction are $\pi^{\pm}$ [113], K^+ [114], K^0_S and Λ [115]. The number of negatively charged particle produced in the proton-carbon interaction is smaller than that of positively charged particle and yields of K^- in the 2007 thin-target data were not available due to limited statistics. The 2009 thin-target data have larger amount of $\pi^{\pm}$, $K^{\pm}$, p, K^0_S, Λ data. These π^- and K^- data are important for the T2K flux prediction in the antineutrino mode. Figures 4.6 and 4.7 are the momentum-angle phase spaces of π^+, π^-, K^+, K^-, K^0_S and protons contributing to the predicted neutrino flux at the far detector in the neutrino mode and the antineutrino mode and the regions covered by analyses in 2007 and 2009. The coverage of 2009 is wider than that in 2007 due to the upgrade of the detectors. The NA61 data are used to tune both the total cross section and the differential cross section so that hadron productions simulated by the MC prediction reproduce those of the data.

4.2.2 Production cross section in the proton-carbon interaction at 31 GeV/c

The production processes are defined as those in which new hadrons are produced. The production cross section is identical to the difference between the inelastic cross section and the quasi-elastic cross section. A quasi-elastic interaction here is a process where the incoming proton scatters off an nucleon inside the

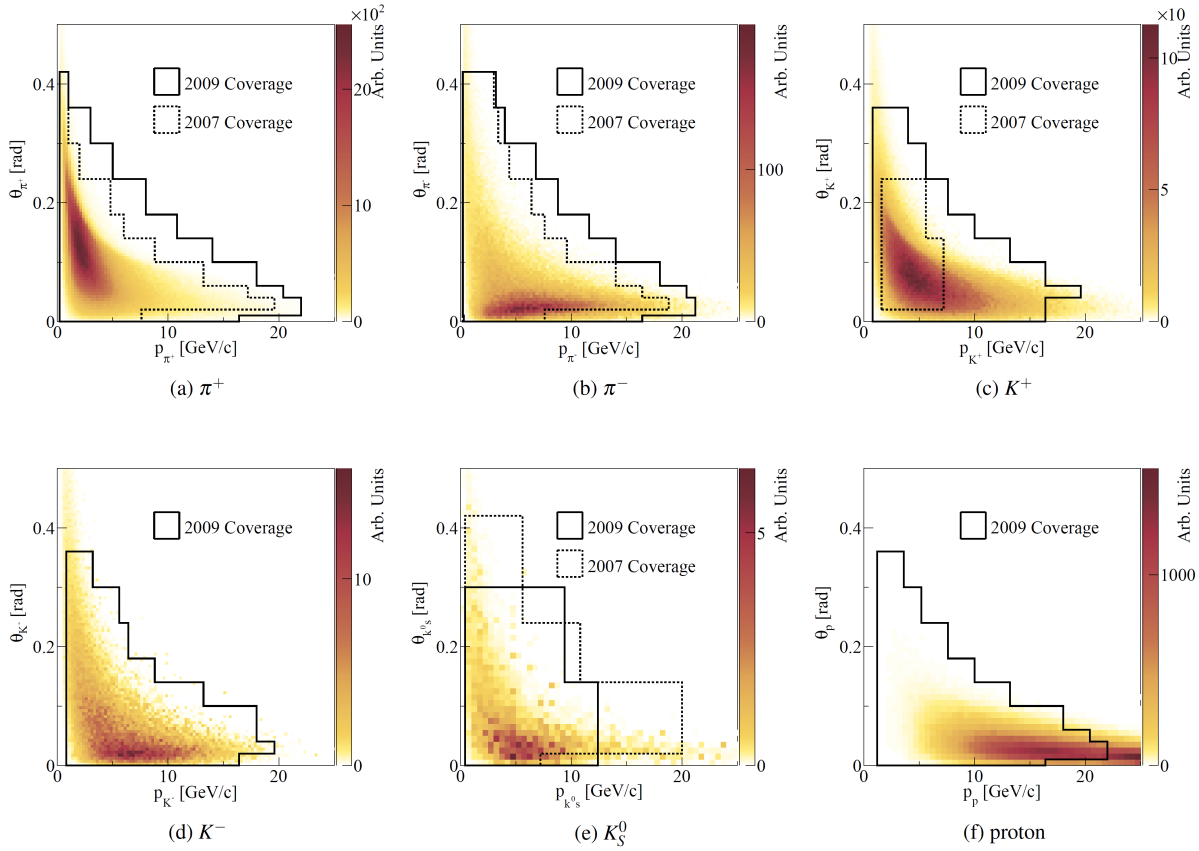

Figure 4.6: The momentum-angle phase space of π^+, π^-, K^+, K^-, K^0_S and protons contributing to the neutrino flux at the far detector in the neutrino mode and the regions covered by 2007 and 2009 thin-target data. Figure is taken from [116].

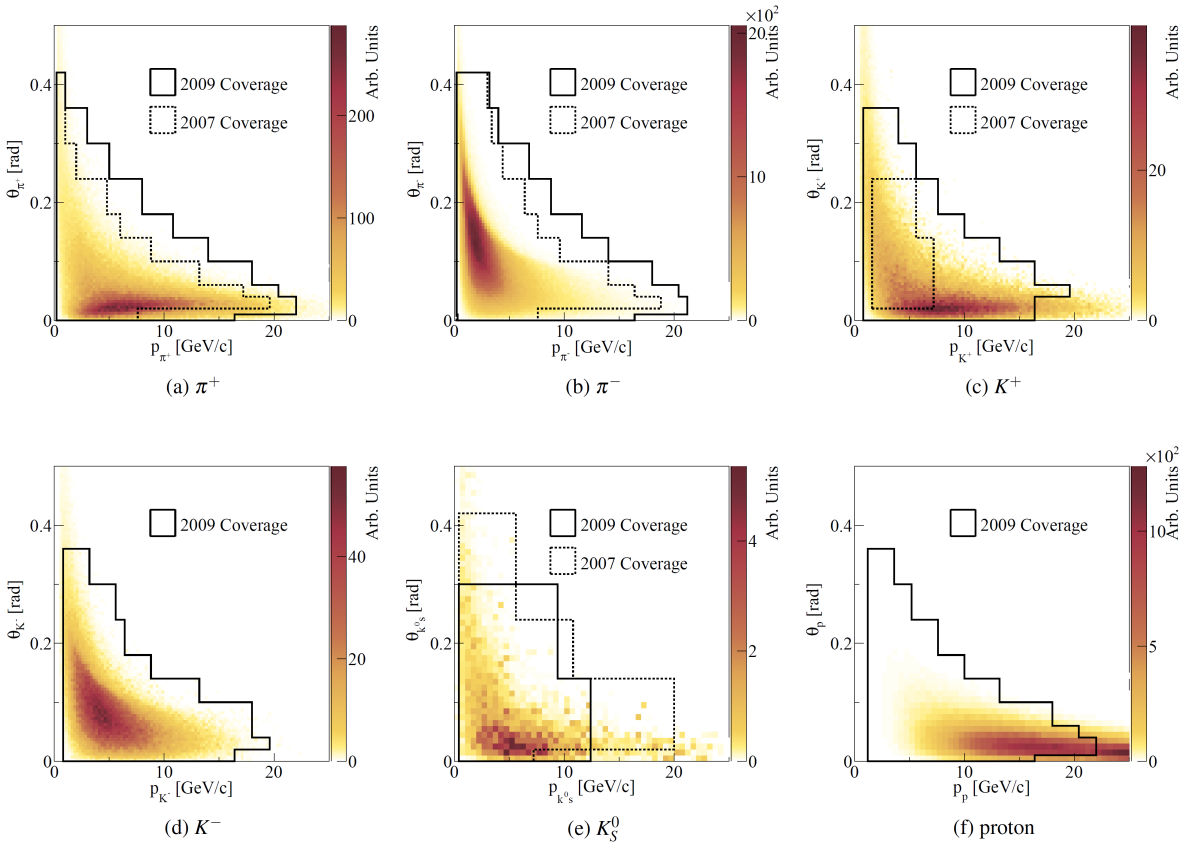

Figure 4.7: The momentum-angle phase space of π^+, π^-, K^+, K^-, K^0_S and protons contributing to the neutrino flux at the far detector in the antineutrino mode and the regions covered by 2007 and 2009 thin-target data. Figure is taken from [116].

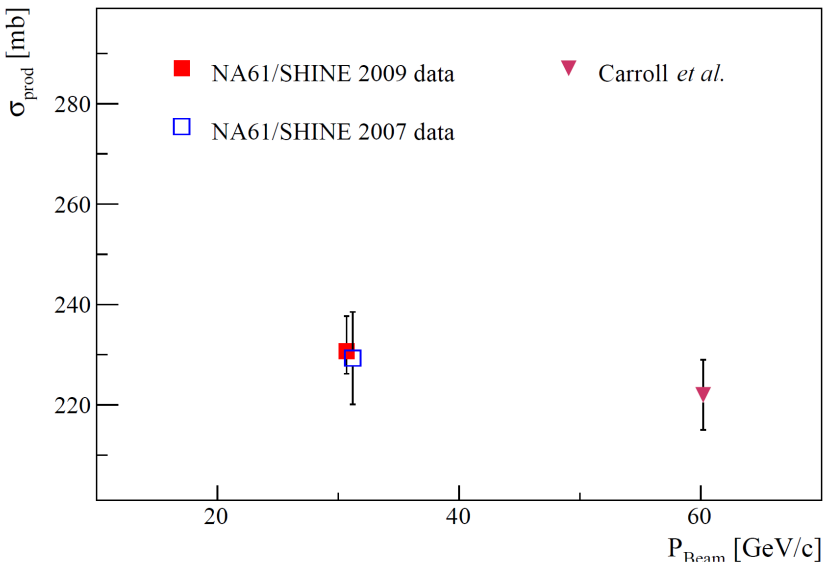

Figure 4.8: Measured production cross section at different momenta with previously published results. The production cross section result by Carroll *et al.* [117] is also shown. Figure is taken from [116].

carbon nucleus. The production cross section obtained by the NA61 measurement [116] is:

$$\begin{aligned} \sigma_{\text{prod}} &= 230.7 \pm 2.7(\text{stat.}) \pm 1.2(\text{detector})^{+6.3}_{-3.4}(\text{model})\ \text{mb} \\ &= 230.7^{+7.0}_{-4.5}\ \text{mb}, \end{aligned} \tag{4.2.1}$$

where model represents the systematic uncertainty on the physics model of MC simulation programs. This uncertainty is significantly smaller than that for the 2007 thin-target data as shown in fig. 4.8.

4.2.3 Multiplicities of charged hadrons

NA61 measured double differential multiplicities, i.e., differential production rates normalized by proton production cross section:

$$\frac{d^2n}{dpd\theta} = \frac{1}{\sigma_{\text{prod}}}\frac{d^2\sigma_h}{dpd\theta}, \tag{4.2.2}$$

where σ_h represents the hadron production cross section for h, p represents momentum of hadron h and θ represents polar angle of hadron h. Differential production rates and their uncertainties are described in [116]. Figures 4.9 and 4.10 show the multiplicity distributions of π^+ and π^- as a function of momentum in bins of θ. Predictions of the multiplicities from FLUKA 2011 are in good agreement with data. Both statistical and systematic uncertainties of 2009 thin-target multiplicity data are decreased compared to those of the 2007 thin-target data.

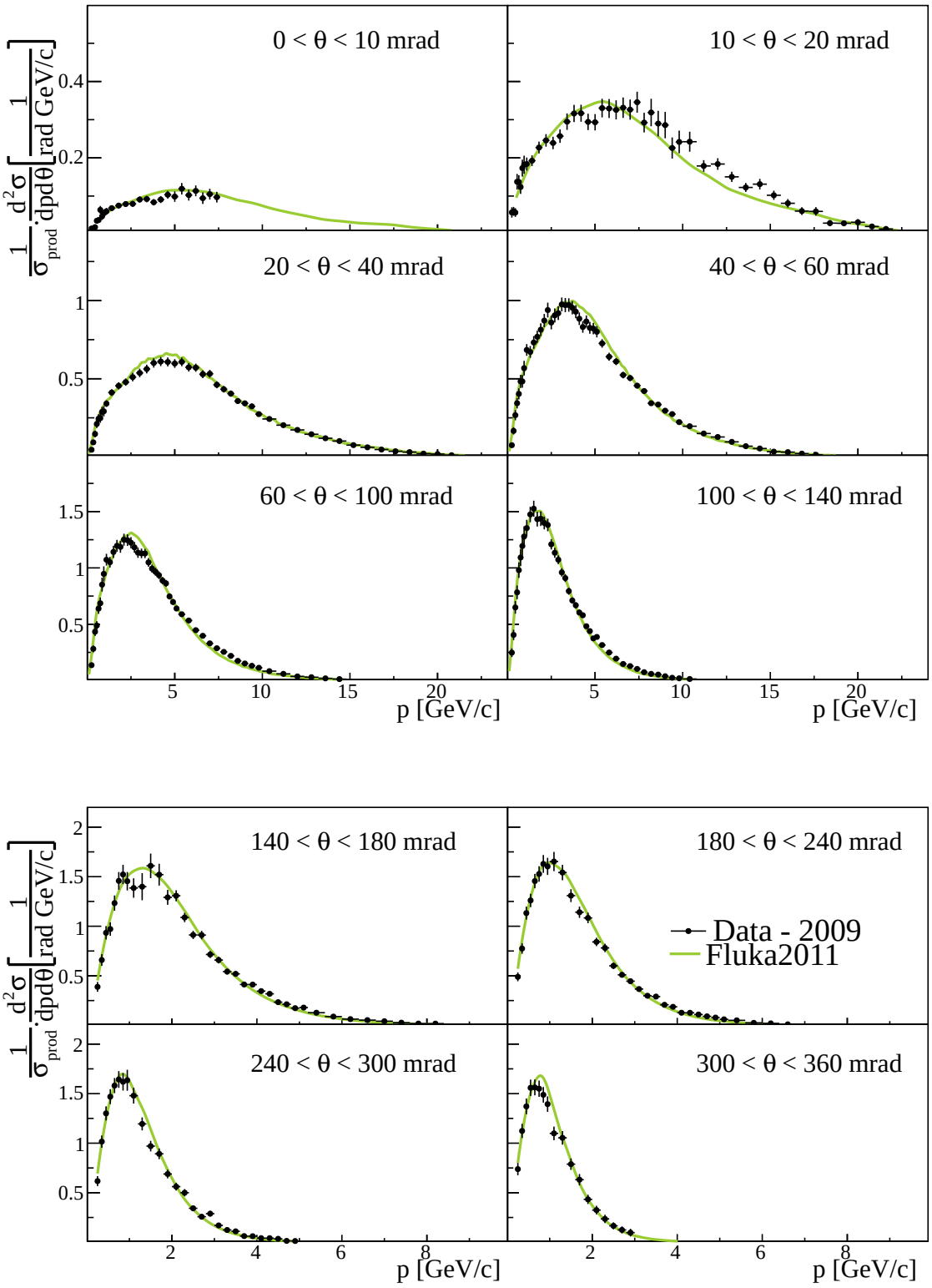

Figure 4.9: Multiplicity distribution of π^+ as a function of momentum in bins of θ. Data points are the weighted average of the 2007 and 2009 thin-target data. Prediction from FLUKA 2011 is also shown.

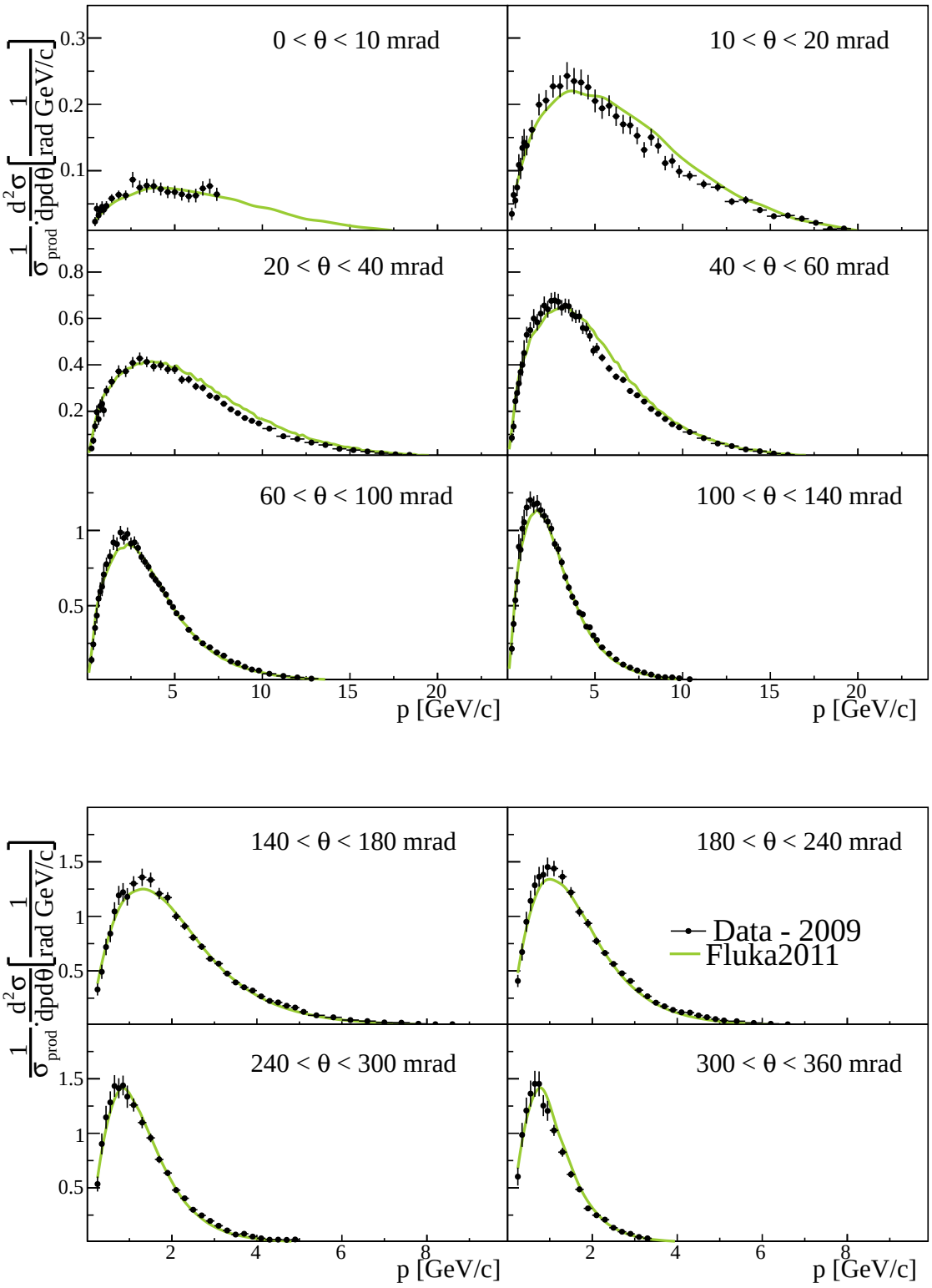

Figure 4.10: Multiplicity distribution of π^- as a function of momentum in bins of θ. Data points are the weighted average of the 2007 and 2009 thin-target data. Prediction from FLUKA 2011 is also shown.

4.3 Hadronic interaction tuning

4.3.1 Introduction

The hadronic interaction tuning is conducted by reweighting each events simulated by the FLUKA (in-target interactions) and GCALOR (out-of-target interactions) models to the data from the NA61/SHINE experiment[3] or other external experiments. We consider the interaction rate tuning and the multiplicity tuning as the reweighting procedure. For the interaction rate tuning, we tune the production cross section obtained by the MC simulations to that obtained by external data. For the multiplicity tuning, the double differential multiplicities obtained by the MC simulations are tuned to that obtained by external data.

4.3.2 Interaction rate tuning

Before we tune the interaction rate, first we compare the production cross sections between the data and the MC simulations. We estimate the production cross sections for MC simulations by using thin targets with incident particle momenta from 0.6 GeV/c to 31.0 GeV/c and derive the production cross sections at intermediate momenta by the interpolation between these points. Data used for the comparison are listed in table 4.5. Some experiments measured inelastic cross sections and for those data the quasi-elastic cross section should be subtracted to obtain the production cross section. The quasi-elastic cross section σ_{qe} is estimated from hadron-nucleon elastic scattering data and the modified empirical atomic mass dependence derived by Bellettini *et al.* [126]:

$$\sigma_{qe} = 0.8(\sigma_{el}^{h-p} + \sigma_{el}^{h-n})A^{\frac{1}{3}}, \tag{4.3.1}$$

where A represents the atomic number and σ_{el}^{h-p} and σ_{el}^{h-n} represent the elastic hadron-proton cross section and the elastic hadron-neutron cross section, respectively. The interaction rate tuning on iron is newly introduced in this analysis. Since most of these data are not on the iron targets, inelastic cross sections on iron are estimated from those on other nuclei targets and a parameterized fit is carried out with the form:

$$\sigma(A) = \sigma_0 A^{\alpha}, \tag{4.3.2}$$

where A represents the atomic mass and σ_0 and α are free parameters determined from dataset with the identical incident momentum. Figures 4.11 and 4.12 show comparisons of the inelastic cross sections or the production cross sections between various external experiments and the simulations of FLUKA and GCALOR as a function of the incident momentum. FLUKA is basically in good agreement with the data, while GCALOR has disagreement in the low incident momentum region. Hence, for FLUKA, the tuning is applied only for the higher momentum ($p > 20$ GeV/c) protons where the result of the NA61 production cross section measurement is available. For GCALOR, the production cross sections of C, Al and Fe are tuned to those obtained by FLUKA.

Fig. 4.13 illustrates the interaction of a particle with momentum p_1 after traveling a distance x_1 in matter to produce a particle with momentum p_2 which travels a distance x_2 and exits the matter. We calculate the corresponding interaction rate by integrating the probability for a particle to survive while traversing a matter before interacting or leaving the matter. The probability for the interaction in an infinitesimal step Δx after traversing a distance x_1 is given as:

$$P_1 = (\rho\sigma_{\mathrm{prod}}(p_1)\Delta x)\exp(-\rho\sigma_{\mathrm{prod}}(p_1)x_1), \tag{4.3.3}$$

[3] In some part of the hadronic interaction tuning, not the latest result of the NA61 is used. That effect is very small in the neutrino flux prediction.

Table 4.5: Datasets from external experiments which are used for the comparison of the production cross sections to the MC simulations.

datasets	incident particle	target nuclei	incident momentum (GeV/c)
NA61/SHINE	p	C	31
Abrams *et al.* [123]	$K^{\pm}$	C, Cu	1-3.3
Allaby *et al.* [124]	π^{-}, K^{-}	C, Al, ...	20-65
Allardyce *et al.* [125]	$\pi^{\pm}$	C, Al, ...	0.71-2
Bellettini *et al.* [126]	p	C, Al, ...	19.3, 21.5
Bobchenko *et al.* [127]	π^{-}, p	C, Al, ...	1.75-9
Carroll *et al.* [117]	$\pi^{\pm}$, $K^{\pm}$, p	C, Al, ...	60-280
Cronin *et al.* [128]	π^{-}	C, Al	0.73-1.33
Chen *et al.* [129]	p	C, Al, ...	1.53
Denisov *et al.* [130]	$\pi^{\pm}$, $K^{\pm}$, p	C, Al, ...	6-60
Longo *et al.* [131]	π^{+}, p	C, Al	3
Vlasov *et al.* [132]	π^{-}	C, Al	2-6.7

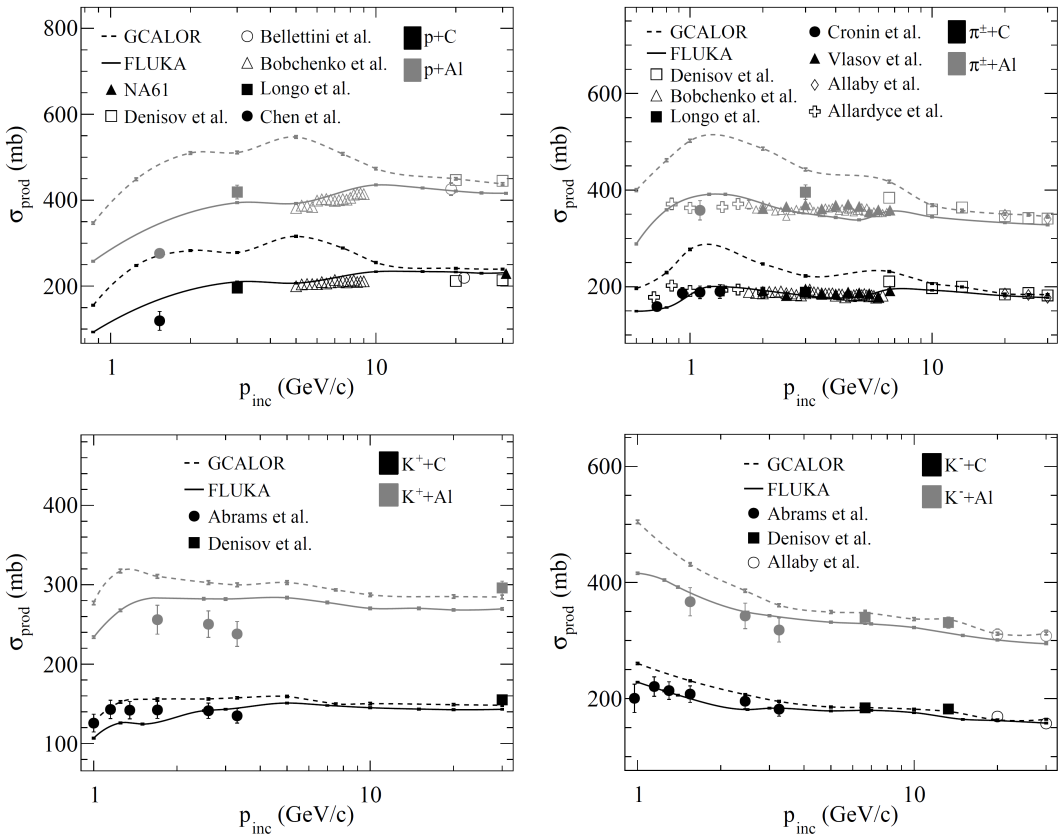

Figure 4.11: Comparisons of the production cross sections on C and Al between the data and the MC simulations for incident p (top left), $\pi^{\pm}$ (top right), K^{+} (bottom left) and K^{-} (bottom right) as a function of the incident momentum.

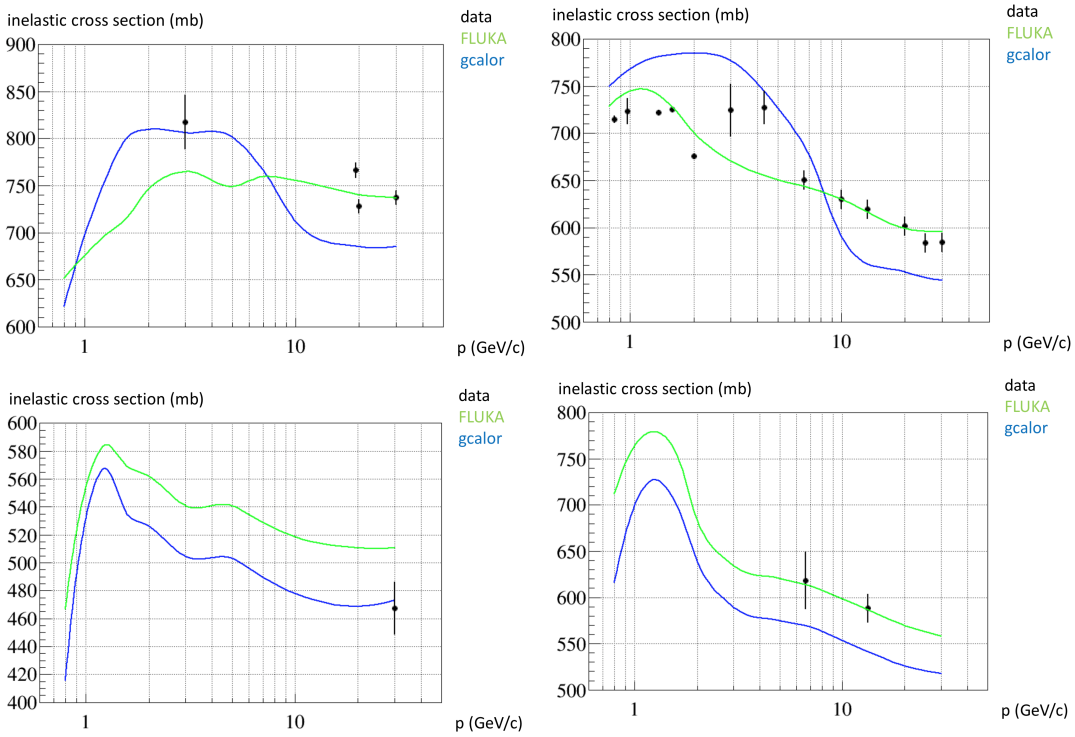

Figure 4.12: Comparison of the inelastic cross sections on Fe between the data and the MC simulations for incident p (top left), $\pi^{\pm}$ (top right), K^{+} (bottom left) and K^{-} (bottom right) as a function of the incident momentum.

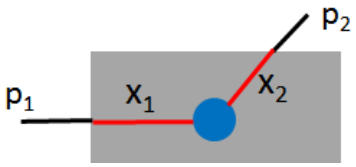

Figure 4.13: Illustration of a particle which interacts inside a matter.

where σ_{prod} represents the production cross section and ρ represents the density of nuclear targets in the matter. The probability for a particle to survive traversing a matter a distance x_2 without interacting is given as:

$$P_2 = \exp(-\rho\sigma_{\text{prod}}(p_2)x_2), \tag{4.3.4}$$

and the probability for the entire process is written as P_1P_2. We obtain the reweighting factor by taking the ratio of the probability with the production cross section from the data to that with the production cross section from the simulated hadron model:

$$W = \frac{\sigma_{\text{data}}(p_1)}{\sigma_{\text{MC}}(p_1)} \exp(-\rho((\sigma_{\text{data}}(p_1) - \sigma_{\text{MC}}(p_1))x_1 + (\sigma_{\text{data}}(p_2) - \sigma_{\text{MC}}(p_2))x_2). \tag{4.3.5}$$

4.3.3 Multiplicity tuning method

The reweighting factor for each event is calculated by taking the ratio of the multiplicity by data to that computed by the simulation:

$$W(p,\theta) = \left[\frac{d^2n(p,\theta)}{dpd\theta}\right]_{\text{data}} \Big/ \left[\frac{d^2n(p,\theta)}{dpd\theta}\right]_{\text{MC}}. \tag{4.3.6}$$

For the primary interactions, the multiplicity tuning is conducted directly with the NA61 pion, kaon and proton multiplicity data. The weights extend beyond the phase space covered by NA61/SHINE. A parametrization of the invariant cross section, called BMPT parametrization [118], is used to extrapolate the momentum-angle phase space covered by the NA61 data. The Basic BMPT parametrization is written as:

$$\left[E\frac{d^3\sigma}{dp^3}\right]_{BMPT} = A(1-x_R)^{\alpha}(1+Bx_R)x_R^{-\beta}(1+\frac{a}{x_R^{\gamma}}p_T+\frac{a^2}{2x_R^{\delta}}p_T^2)e^{-ap_T/x_R^{\gamma}}, \tag{4.3.7}$$

where p_T and x_R respectively represent the transverse momentum of the produced hadron, and the energy of the produced particle in the center of mass frame divided by the its maximum energy. A, α, B, β, a, γ and δ are fit parameters and are determined from external data. In the actual BMPT fit, slightly modified versions of eq. 4.3.7, which depend on the hadron type, are used so that the fit works well.

The NA61 data are also used for the multiplicity tuning for secondary and tertiary interactions where a secondary and tertiary proton or neutron interacts with a nucleus. This tuning requires some additional steps:

- For incident neutrons, the isospin symmetry is assumed: The multiplicities for the interaction of $p + A \to h^{\pm} + X$ are equal to that of $n + A \to h^{\mp} + X$.

- Since the secondary proton or neutron has lower momentum compared to that of the primary proton, a momentum scaling is applied so that the NA61 data can be applied to those interactions. The momentum scaling is carried out assuming the Feynman scaling [119], where the invariant cross section is described as a function of p_T and the Feynman variable x_F, which is defined as:

$$x_F = \frac{p_L}{p_L(\text{max})}, \tag{4.3.8}$$

  where p_L represents the longitudinal momentum of the produced particle in the center of mass frame and $p_L(\text{max})$ represents the allowed maximum of p_L. For each interaction, the momentum and polar angle of the produced particle, p and θ are converted to the variables x_F and p_T. The x_F and p_T are then converted to p_{NA61} and θ_{NA61}, where p_{NA61} and θ_{NA61} represents the momentum and polar angle at the momentum of NA61 (31 GeV/c). The weights of the multiplicities of data to MC are applied as a function of p_{NA61} and θ_{NA61}.

- For the out-of-target interactions, the NA61 data are scaled to multiple nuclear targets using parameterized fits.

$$\frac{d^2\sigma}{dpd\theta}(A_1) = \left[\frac{A_1}{A_0}\right]^{\alpha(x_F,p_T)} \frac{d^2\sigma}{dpd\theta}(A_0), \tag{4.3.9}$$

  where A_0 and A_1 represent the atomic masses of the nuclear targets and $\alpha(x_F, p_T)$ is a polynomial of x_F and p_T. Coefficients of $\alpha(x_F, p_T)$ are derived from a fit to the external data which are listed in table 4.6.

Table 4.6: External hadron production data used to derive the target nucleus scaling.

experiment	target nuclei	incident proton momentum (GeV/c)	produced particles
Allaby *et al.* [120]	Be, Al, Cu	19.2	$\pi^{\pm}$, $K^{\pm}$, p
BNL-E802 [121]	Be, Al, Cu	14.6	$\pi^{\pm}$, $K^{\pm}$, p
HARP [122]	Be, C, Al, Cu	12.0	$\pi^{\pm}$

4.3.4 Meson multiplicity tuning

For the primary interactions, the NA61 2009 pion, kaon and proton multiplicity data are used to tune particle production multiplicities. Fig. 4.14 shows the weights of the meson multiplicity tuning as the ratios of the multiplicity data to that computed by FLUKA. In this section, the tuning of the meson multiplicities is described. The tuned interaction modes in this analysis are:

- Proton interactions on C, Al, Fe and Ti which produce pions, kaons or protons.
- Neutron interactions on C, Al, Fe and Ti which produce pions.

The K^0_S multiplicity data are used to tune the production of the neutral kaons. Since the neutral kaons are produced in the K^0 and $\overline{K^0}$ states but decay weakly as K^0_S and K^0_L, the production rate of K^0+$\overline{K^0}$ is proportional to the measured K^0_S rate. Hence we can tune the production of all the neutral kaons.The NA61 data are also used to tune the production of mesons in secondary (tertiary) interactions by using scalings described in Section 4.3.1.

4.3.5 Baryon multiplicity tuning

The production of the secondary baryons in the proton-carbon interactions, which was not tuned in the flux for the previous ν-mode oscillation analysis, is tuned in this analysis. Protons, neutrons, Λ^0s and Σs are included in this reweighting. The weighting method of the baryon multiplicity tuning is similar to that of the meson multiplicity tuning, but the baryon number conservation is additionally considered, which is used to constrain the integrated baryon multiplicity. In this tuning, the NA61 2009 thin-target data and data from Allaby *et al.* [120], which covers forward region compared to that for NA61, is used for the BMPT fit. Fig. 4.15 shows the weights of the baryon multiplicity tuning as the ratios of data to FLUKA.

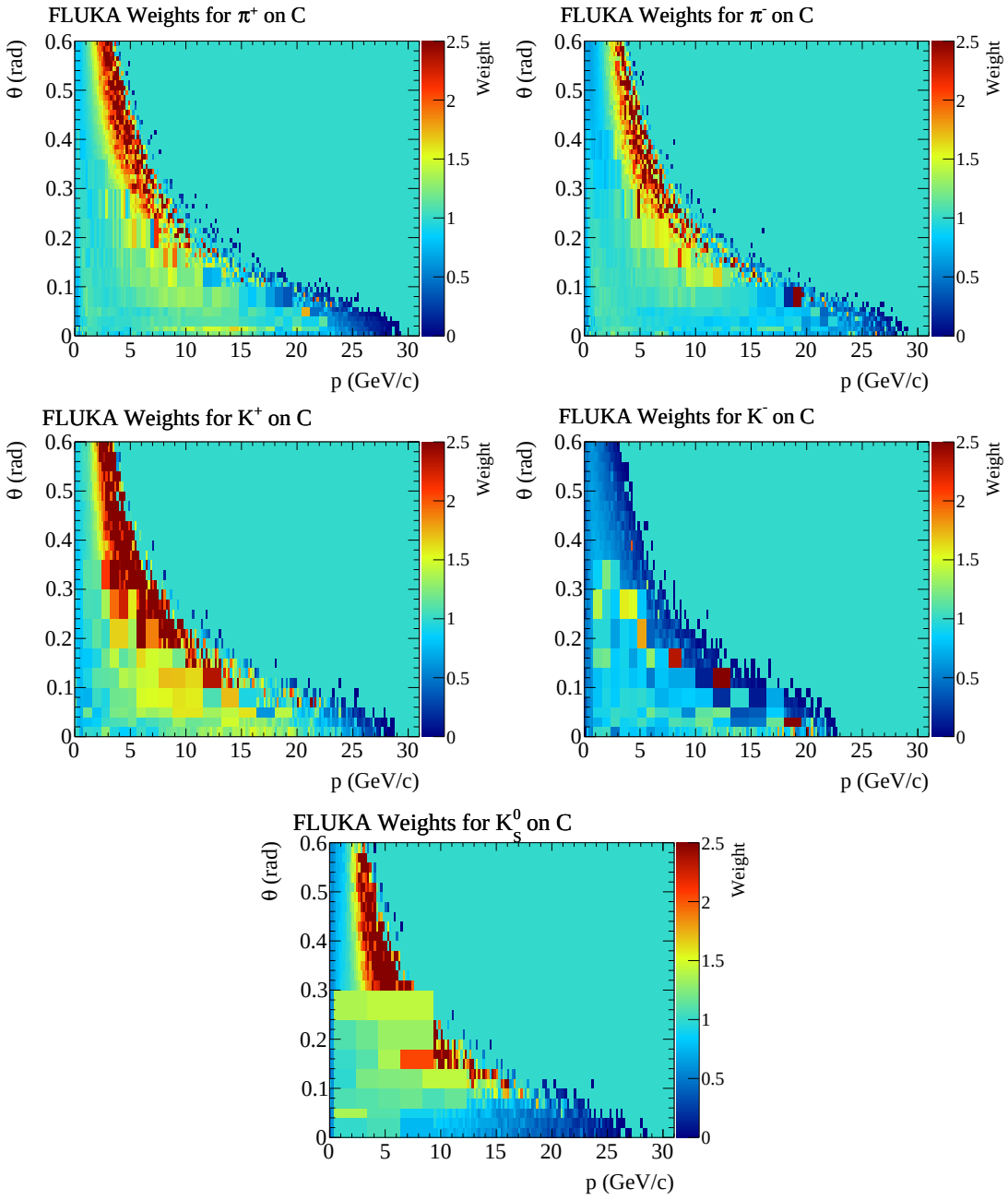

Figure 4.14: Reweighting factors of the meson multiplicity tuning.

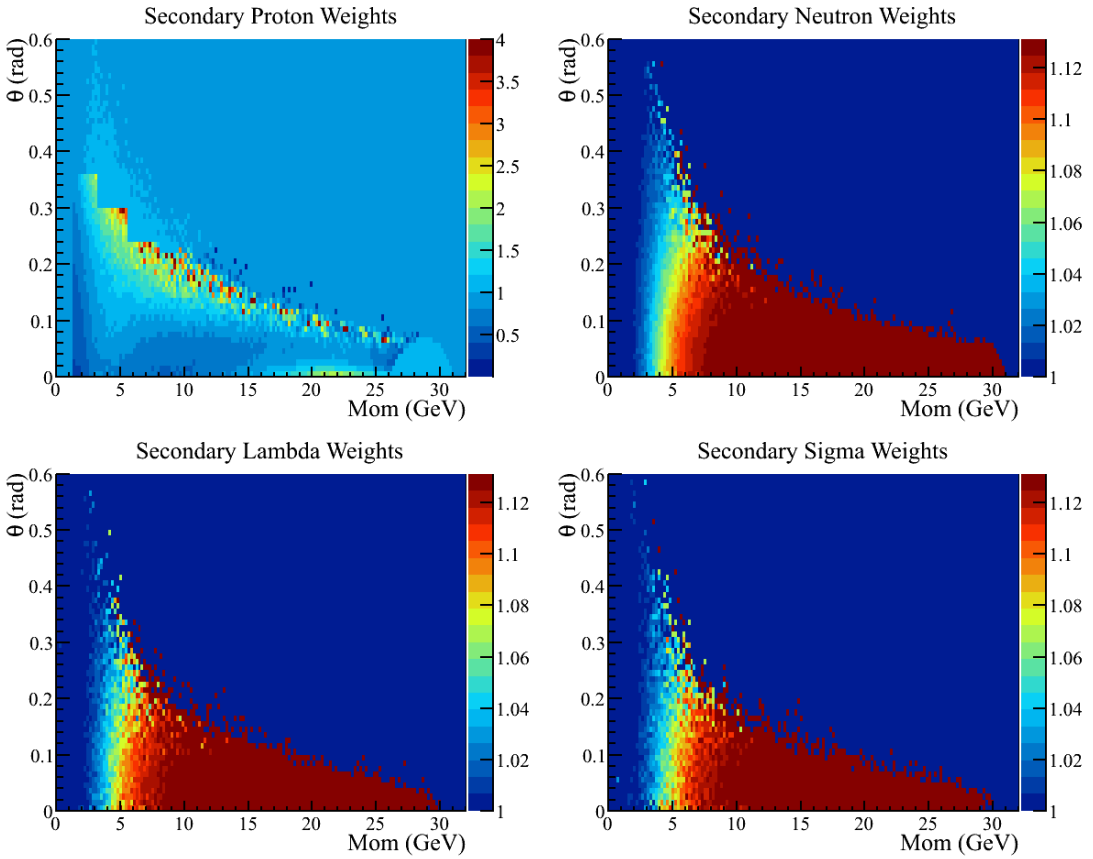

Figure 4.15: Weights of the baryon multiplicity tuning as the ratios of data to FLUKA for proton (top left), neutron (top right), Λ^0 (bottom left) and Σ (bottom right).

4.3.6 Result of hadronic interaction tuning to the neutrino flux

Figures 4.16 and 4.17 show the obtained reweighting factors as a function of neutrino energy in the neutrino mode and the antineutrino mode, respectively. Contributions from each tuning are separately shown. For ν_μ in the neutrino mode and $\bar{\nu}_\mu$ in the antineutrino mode, total flux variation by the tuning is roughly 5% around the peak energy and that for higher energy region is roughly 30% in the neutrino mode and -10% in the antineutrino mode due to the kaon multiplicity tuning. Effect of the interaction rate tuning and the secondary baryon multiplicity tuning are not so large as that of the meson multiplicity tuning.

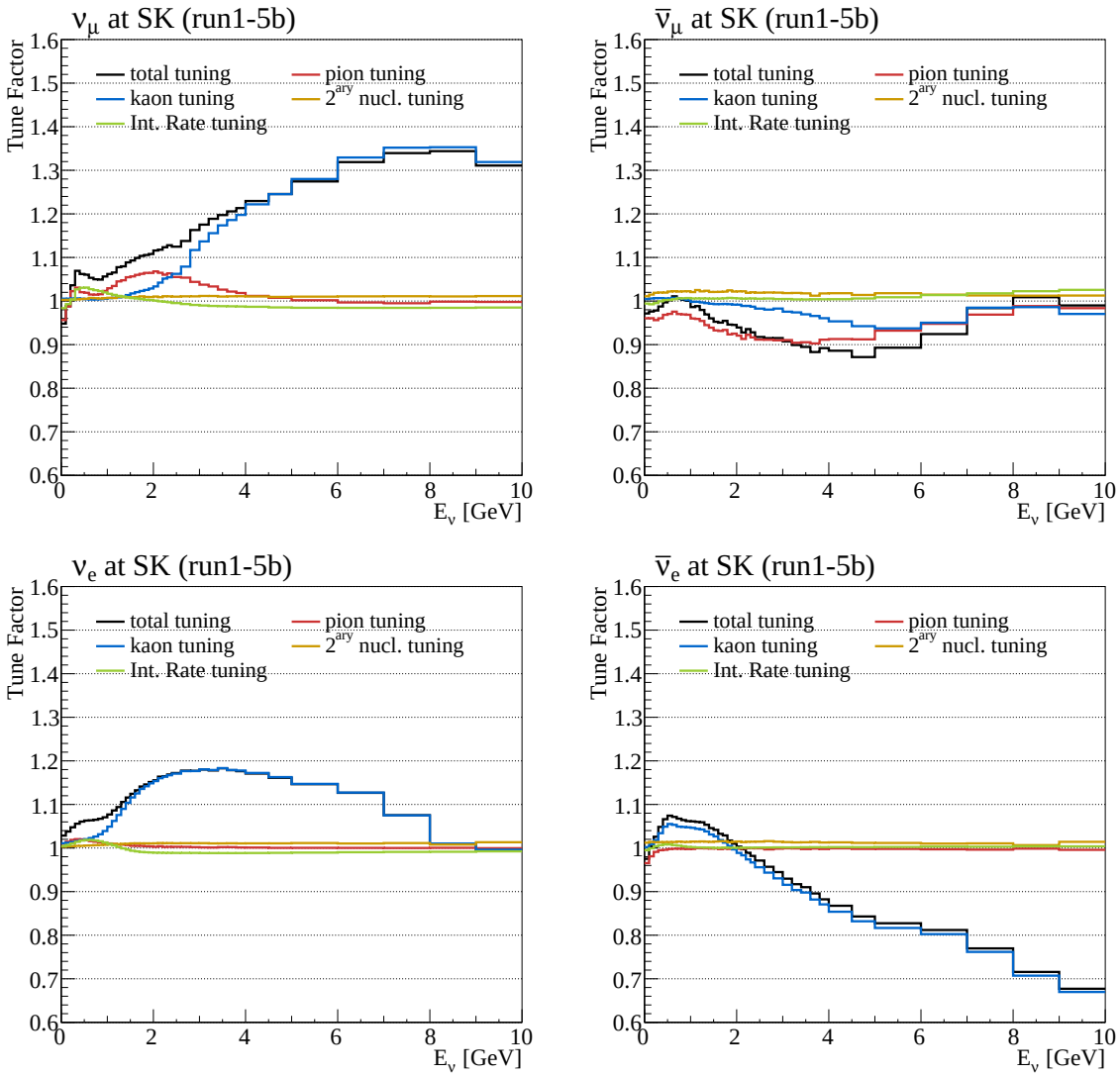

Figure 4.16: Reweighting factors as a function of neutrino energy in the neutrino mode. Contributions from each tuning are separately shown. Top left: ν_μ, top right: $\bar{\nu}_\mu$, bottom right: ν_e, bottom left: $\bar{\nu}_e$. The labels pion tuning, kaon tuning, 2^{ary} nucl. tuning and Int. Rate tuning represent respectively pion multiplicity tuning, kaon multiplicity tuning, baryon multiplicity tuning and interaction length tuning.

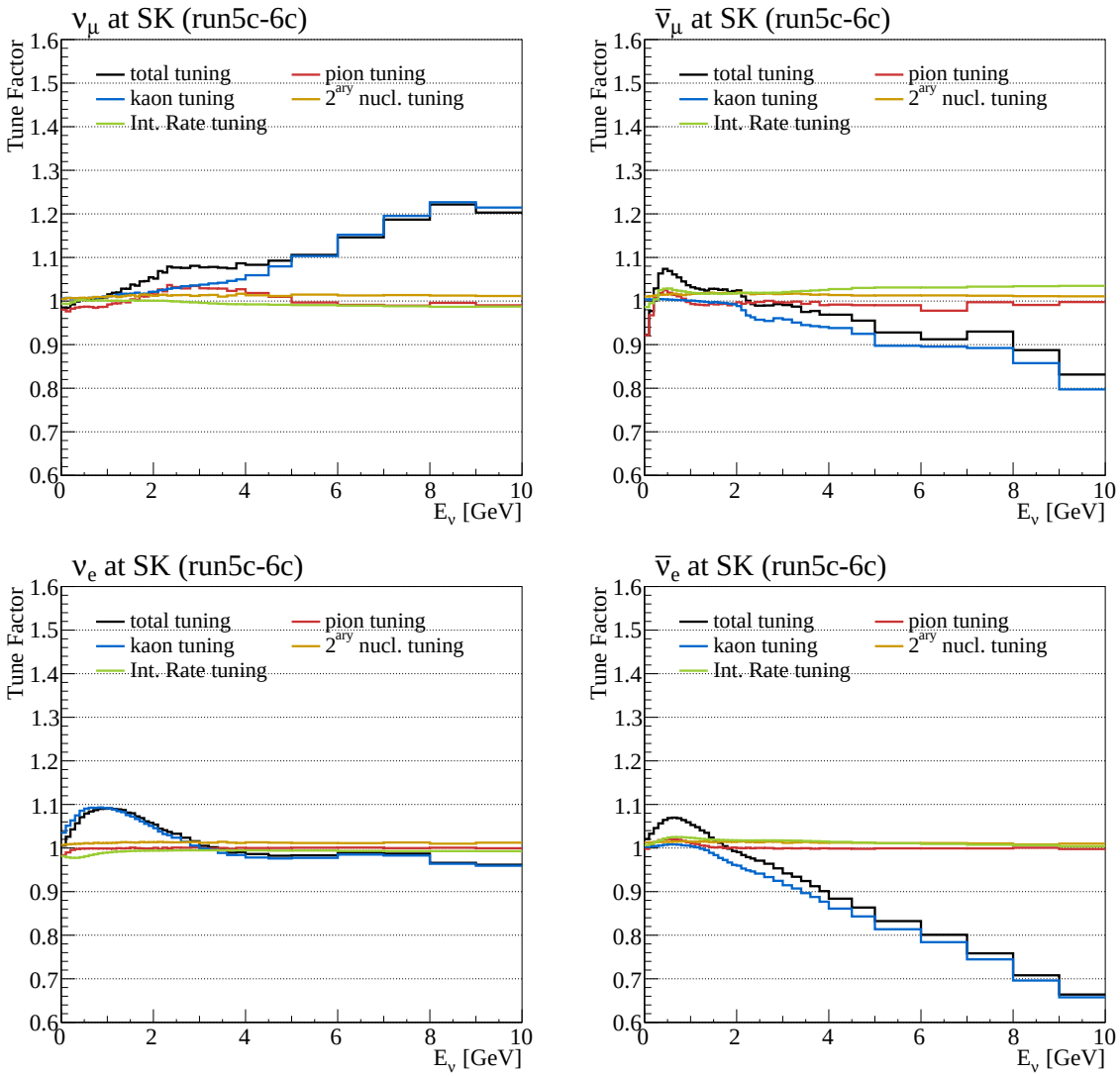

Figure 4.17: Reweighting factors as a function of neutrino energy in the antineutrino mode. Contributions from each tuning are separately shown. Top left: ν_μ, top right: $\bar{\nu}_\mu$, bottom right: ν_e, bottom left: $\bar{\nu}_e$. The labels pion tuning, kaon tuning, 2^{ary} nucl. tuning and Int. Rate tuning represent respectively pion multiplicity tuning, kaon multiplicity tuning, baryon multiplicity tuning and interaction length tuning.

4.4 Uncertainty of the neutrino flux prediction

4.4.1 Introduction

The flux uncertainty comprises the hadron interaction uncertainties, the proton beam parameters, the neutrino beam direction measurement, the magnetic field of the horns, the material objects of the magnetic horns, the beam intensity, and the alignment of the target and the magnetic horns. The flux uncertainties are evaluated for bins of the neutrino energy, the neutrino flavor, the beam mode and the detector (the off-axis near detector and the far detector). In addition to calculating the uncertainty for these bins, we also calculate the correlations between their bins. The uncertainty from each source is evaluated by taking the difference of the nominal flux and the flux estimated by alternative methods or different configurations.

4.4.2 hadronic interaction uncertainties

As stated in Section 4.3, the hadronic interaction tuning is composed of the interaction rate tuning, the meson multiplicity tuning, and the baryon multiplicity tuning. For the hadronic interaction uncertainties, uncertainties from these tunings and in addition the uncertainty of the pion multiplicities in the pion-nucleus interactions are considered.

The uncertainty of the interaction rate tuning comes from the uncertainty of the production cross-section data. As stated, the production cross section is defined as the difference between the inelastic cross section and the quasi-elastic cross section. We use the size of the quasi-elastic cross section as the source of the production cross section. This is because in some of the production cross section measurements used in the tuning, there is an ambiguity in measurements whether the quasi-elastic cross section has been subtracted or not. This treatment results in a conservatively quite large uncertainty of the interaction rate tuning. The quasi-elastic cross section σ_{qe} which will be used as the input of the interaction rate uncertainty is given in eq. 4.3.1. For example, the uncertainty of the production cross section in the proton-carbon interactions measured by NA61 is $^{+7}_{-4.5}$ mb while the size of quasi-elastic interaction around 30 GeV/c is roughly 30 mb. The uncertainty of the interaction rate using this NA61 measurement is described in Section 4.4.5.

The uncertainties for the meson multiplicity tuning comprise the NA61 multiplicity measurements, hadron production in the phase space which is not covered by the NA61 data, the energy scaling method and the nuclear target scaling method. The uncertainty from the NA61 multiplicity measurements is described in the NA61 paper [116]. The uncertainty from production in the phase space which is not covered by the NA61 data is estimated by taking the difference of the hadron production in these regions between the FLUKA model and the BMPT extrapolation. The uncertainty from the energy scaling method is estimated by taking the difference of the scaling using the NA61 data, which is used for the tuning, and that for different external data. The uncertainty from the nuclear target scaling method is estimated from the fit error of the nuclear target scaling (eq. 4.3.9). In addition, by using the data from Eitchen *et al.* [133], actual data on Al and Cu target are compared to data on the same nuclei by the nuclear target scaling of data on Be target and the difference between them are added into the uncertainty from the nuclear target scaling.

The uncertainties for the secondary baryon multiplicity tuning comprise the energy scaling method and the nuclear target scaling method, and the uncertainty from the treatment of the baryon number conservation and the non-primary interactions. The uncertainties from the energy scaling method and the nuclear target scaling method are estimated in similar way as those for the meson multiplicity tuning. The uncertainty from the treatment of the baryon number conservation is estimated by taking the difference of the method which is used for the secondary baryon multiplicity tuning and alternative methods. In the alternative methods, additional multiplicity data, i.e., the NA49 neutron data [134] and the NA61 Λ data, which are not ready in this analysis, are used. The uncertainty from the non-primary interactions

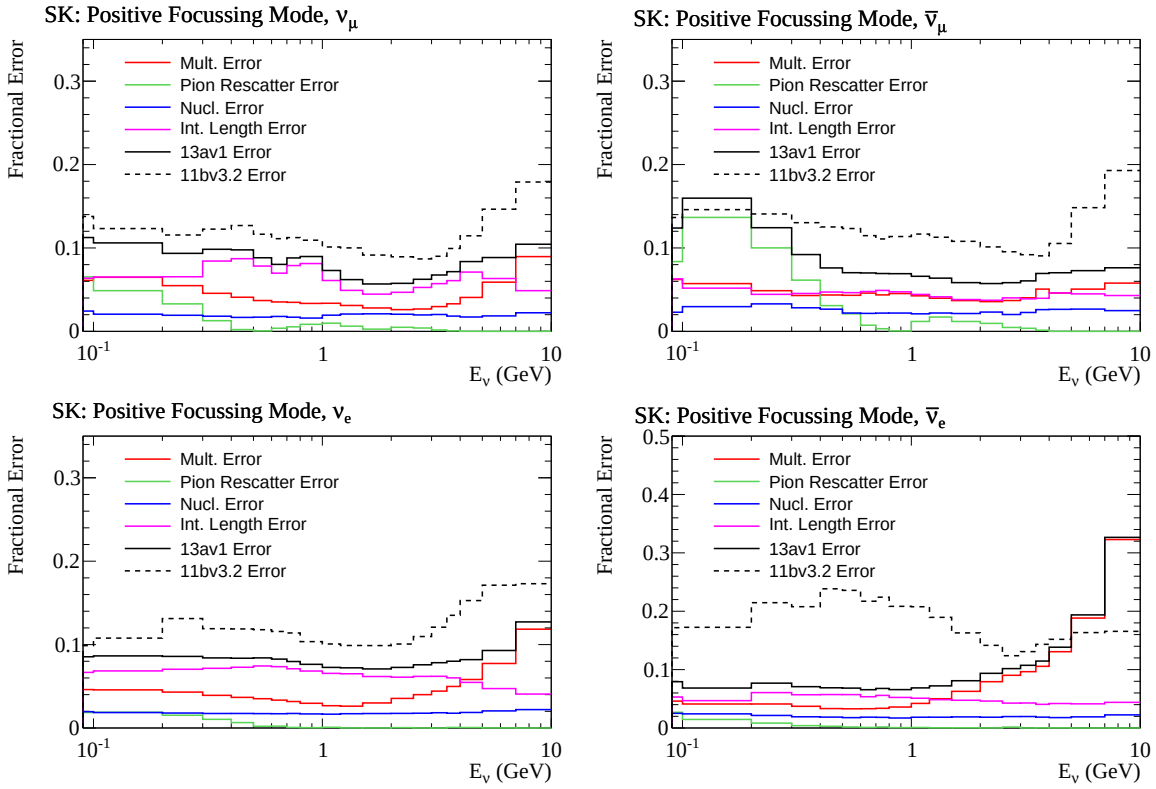

Figure 4.18: The uncertainty of the flux prediction due to the uncertainty of the hadronic interaction. Shown here are the uncertainties at the far detector in the neutrino mode as a function of neutrino energy. Top left: ν_μ, top right: $\bar{\nu}_\mu$, bottom left: ν_e, and bottom right: $\bar{\nu}_e$. The labels 13av1 and 11bv3.2 represent respectively the total hadronic interaction uncertainty for this oscillation analysis and for the previous ν-mode analysis. The labels Mult., Pion Rescatter, Nucl. and Int. Length represent the uncertainty for the meson multiplicities, the uncertainty for the pion multiplicities in pion-nucleus interactions, the uncertainty for the baryon multiplicities, and the uncertainty for the interaction rate tuning.

is estimated by taking the difference of the nominal method, where only primary interactions are tuned, and an alternative method. In the alternative method, not only primary interactions but also secondary and tertiary interactions including interactions out of the target are tuned.

The pion multiplicities in the pion-nucleus interactions is not tuned, but this uncertainty is considered by taking the difference of the nominal flux and the flux with tuning the pion multiplicities. For this tuning, $\pi^\pm + A \to \pi^\pm + X$ and $\pi^\pm + A \to \pi^\mp + X$ data from the HARP experiment [122] are used.

Figure 4.18 shows the size of the uncertainty of the flux prediction due to the uncertainty of the hadronic interactions. Those at the far detector in the neutrino mode are shown. Thanks to the inclusion of the NA61 2009 thin-target data, the size of the hadronic interaction uncertainties is decreased from those for the past ν-mode analyses. Figure 4.19 shows those at the far detector in the antineutrino mode. For the right-sign component, the uncertainties for the interaction rate tuning have the largest contribution around the peak energy. The improvement of the uncertainties for the interaction rate tuning will be discussed in Section 4.4.5.

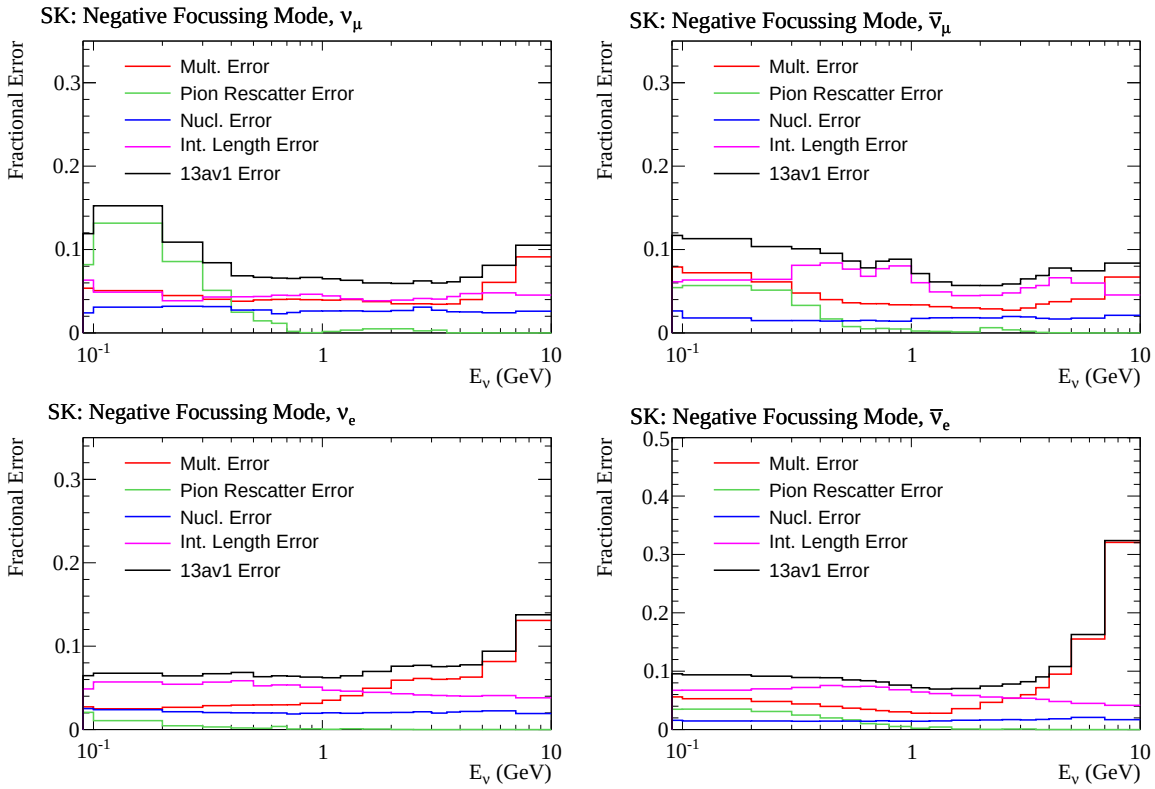

Figure 4.19: The uncertainty of the flux prediction due to the uncertainty of the hadronic interaction. Shown here are the uncertainties at the far detector in the antineutrino mode as a function of neutrino energy. Top left: ν_μ, top right: $\bar{\nu}_\mu$, bottom left: ν_e, and bottom right: $\bar{\nu}_e$. The labels 13av1, Mult., Pion Rescatter, Nucl. and Int. Length represent respectively the total hadronic interaction uncertainty for this oscillation analysis, the uncertainty for the meson multiplicities, the uncertainty for the pion multiplicities in pion-nucleus interactions, the uncertainty for the baryon multiplicities, and the uncertainty for the interaction rate tuning.

4.4.3 Uncertainties other than the hadronic interaction

In this section, source of the uncertainties other than the hadronic interaction are summarized. Details of these uncertainties are described in [107]. We newly considered the uncertainties from the material of the magnetic horns. The sizes of flux uncertainties from these sources are shown in the next section.

Proton beam

The uncertainty of the proton beam measurements comprises systematic uncertainties of beam profile from each beamline monitor and the position misalignment of the most upstream magnetic horn. The position, angle of the beam, and the correlation between them are considered parameters and are summarized in table 4.7. A large number of fluxes were generated by varying these parameters according to the given uncertainty size and the correlation for each period. The uncertainties are estimated by taking the averaged difference of the nominal flux and varied fluxes.

Run	ΔX [mm]	ΔY [mm]	$\Delta\theta_X$ [mrad]	$\Delta\theta_Y$ [mrad]	corr(Y, Y')
Run 1	0.38	0.58	0.06	0.29	0.392
Run 2	0.27	0.62	0.06	0.32	0.398
Run 3b (horn 205kA)	0.28	0.58	0.06	0.29	0.427
Run 3c (horn 250kA)	0.36	0.58	0.07	0.28	0.417
Run 4	0.34	0.58	0.07	0.28	0.401
Run 5	0.34	0.57	0.07	0.28	0.409
Run 6	0.34	0.58	0.07	0.28	0.433

Table 4.7: Measured uncertainties of the position, angle of the proton beam, and the correlations between them for the vertical direction corr(Y, Y').

Off-axis angle

The INGRID beam direction measurement is used for the evaluation of the uncertainty on the off-axis angle of the neutrino flux. Table 4.8 shows the beam direction and uncertainties measured by the INGRID detector. The flux uncertainty from the off-axis angle uncertainty is estimated by taking the difference of the nominal flux and the flux where the positions of the off-axis near detector and the far detector are varied by the amount corresponding to the uncertainties of off-axis angle.

Horn magnetic field

The measured magnetic field strength is consistent with the expected one within 2%. Thus, the 5kA (2%) variation of the horn current is applied as the uncertainty of the absolute magnetic field. The measured magnetic field agrees with the expected magnetic field within 2% for all regions and magnetic field deviations from expected values are additionally taken into account the flux uncertainty.

Alignment of the target and the magnetic horns

The angular alignment precision of the target and the horn-1 is 1 mrad and 0.2 mrad, respectively. The alignment precision of the horn-2 and the horn-3 is 1mm. These alignment errors are considered as sources of the flux uncertainty. Positional mismanagement of the horn1 is included in the proton beam uncertainty. Effect of their angular misalignment is negligibly small.

Table 4.8: Result of the beam direction measured by the INGRID detector. (center value ± statistical uncertainty ± systematic uncertainty).

Run period	Horizontal center (mrad)	Vertical center (mrad)
Neutrino mode		
Run 1	0.057 ± 0.049 ± 0.094	-0.250 ± 0.052 ± 0.105
Run 2	0.011 ± 0.026 ± 0.095	-0.041 ± 0.028 ± 0.104
Run 3b (horn 205kA)	-0.056 ± 0.097 ± 0.112	-0.092 ± 0.110 ± 0.134
Run 3c (horn 250kA)	0.049 ± 0.023 ± 0.094	0.177 ± 0.025 ± 0.105
Run 4	0.043 ± 0.015 ± 0.094	0.014 ± 0.016 ± 0.104
Run 5a+b	0.068 ± 0.036 ± 0.096	0.029 ± 0.058 ± 0.104
Antineutrino mode		
Run 5c	0.050 ± 0.068 ± 0.336	0.153 ± 0.075 ± 0.396

material of the magnetic horns

Though important parts of beamline components around the beam center are modeled in the JNUBEAM simulation, some parts of them are missing. The effects of missing materials are taken into account as the uncertainties on the flux prediction. For the magnetic horns, whose illustration is shown in fig. 2.9, only the conductors have been considered in the JNUBEAM simulation and we additionally consider two sources of material as the flux uncertainty. The first source is the cooling water inside the magnetic horns. During the operation, conductors are heated due to the beam exposure and the Joule loss. Therefore, the inner conductors of the horns are always cooled by sprayed water. Though we know how much water is consumed for spray per unit time [84], we do not know exactly how the water is spread to the inner conductor and how much water adheres to the inner conductor. In this analysis, it is assumed that 1 mm thickness of liquid water is attached around the outside of the inner conductor of the horn-1, where the effect is expected to be the largest. The second source is the striplines, which carry the electric current to the magnetic horns. We consider the upstream front of the horn-2 and the horn-3, where the number of particles which pass through those regions are relatively large (but much smaller than those through the water), with simplified shape.

Proton beam intensity

Proton beam intensity is measured by CTs which have a precision of 2%. In addition, there exists 1.7% systematic uncertainty coming from the analysis method for evaluating proton beam intensity from raw data. In total, an uncertainty of 2.6% is assigned as the normalization of the neutrino flux.

4.4.4 Flux prediction uncertainty for this oscillation analysis

Figures 4.20 and 4.21 show the total uncertainties for the flux prediction used in this oscillation analysis at the off-axis near detector and the far detector in the neutrino mode as a function of neutrino energy. The ν_μ flux uncertainty at the peak energy is decreased roughly from 12% to 9%. The largest uncertainty comes from hadronic interaction uncertainty though this is decreased compared to the previous analysis. The total flux uncertainty for the off-axis near detector is almost same as that for the far detector. Figures 4.22 and 4.23 show the total uncertainties in the case of the antineutrino mode. The $\overline{\nu}_\mu$ flux uncertainty at the peak energy is roughly 10%. The $\overline{\nu}_\mu$ flux uncertainty from the off-axis angle is larger than that of ν_μ flux in the neutrino mode due to larger systematic uncertainty of the neutrino beam direction

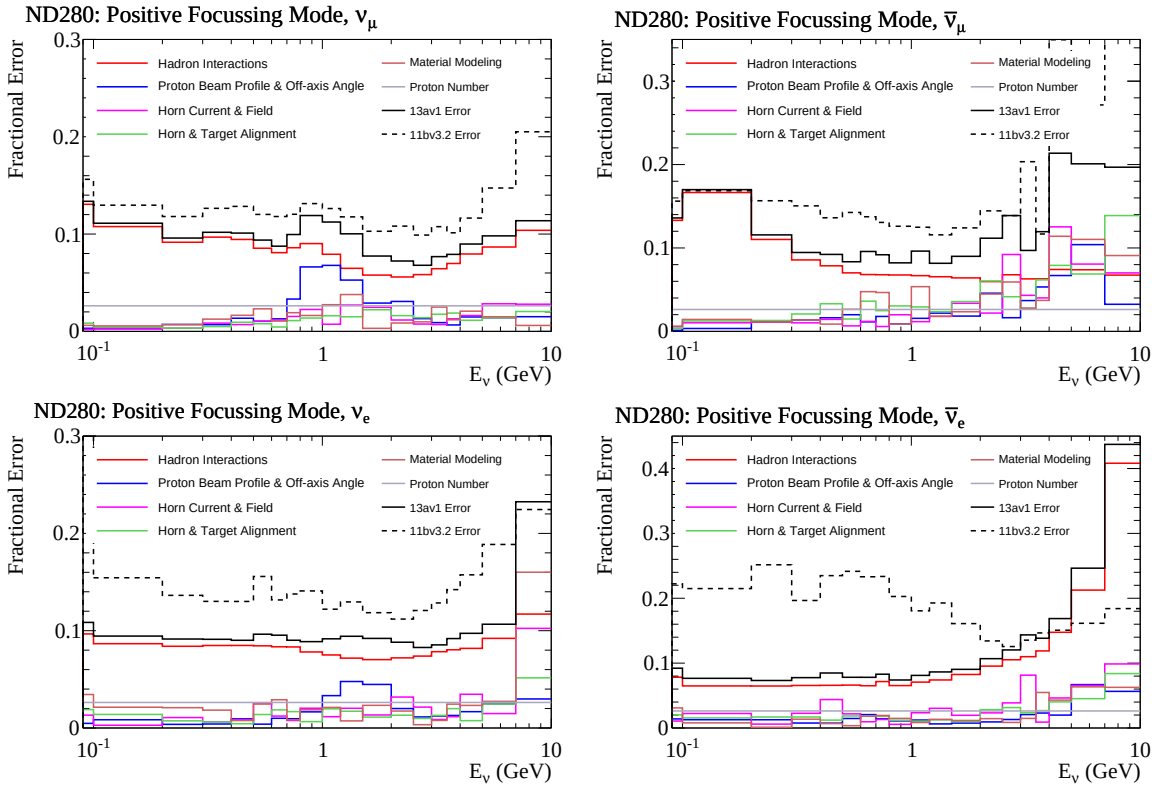

Figure 4.20: Total uncertainties for the flux prediction at the off-axis near detector in the neutrino mode as a function of neutrino energy. Top left: ν_μ, top right: $\bar{\nu}_\mu$, bottom left: ν_e, and bottom right: $\bar{\nu}_e$. The labels 13av1, 11bv3.2, Material modeling and Proton number represent respectively the total uncertainty for this oscillation analysis, the total uncertainty used in the previous ν-mode analyses, the uncertainty from the material of the magnetic horns, and the uncertainty from proton beam intensity.

measurement by INGRID[4].

Figure 4.24 shows the correlation matrix for the bins of the flux prediction which includes all correlations from each uncertainty source. Since the variation of the number of the hadron production similarly affects the neutrino flux for all flavor and that both for the off-axis near detector and the far detector, each neutrino flux strongly correlates. This strong correlations between off-axis near detector and the far detector for all the flavor, with measurements from the off-axis near detector, enable the reduction of the flux uncertainty for the oscillation analysis.

[4]The dominant systematic uncertainty of the INGRID measurement comes from discrepancy in the track reconstruction between the data and the MC prediction.

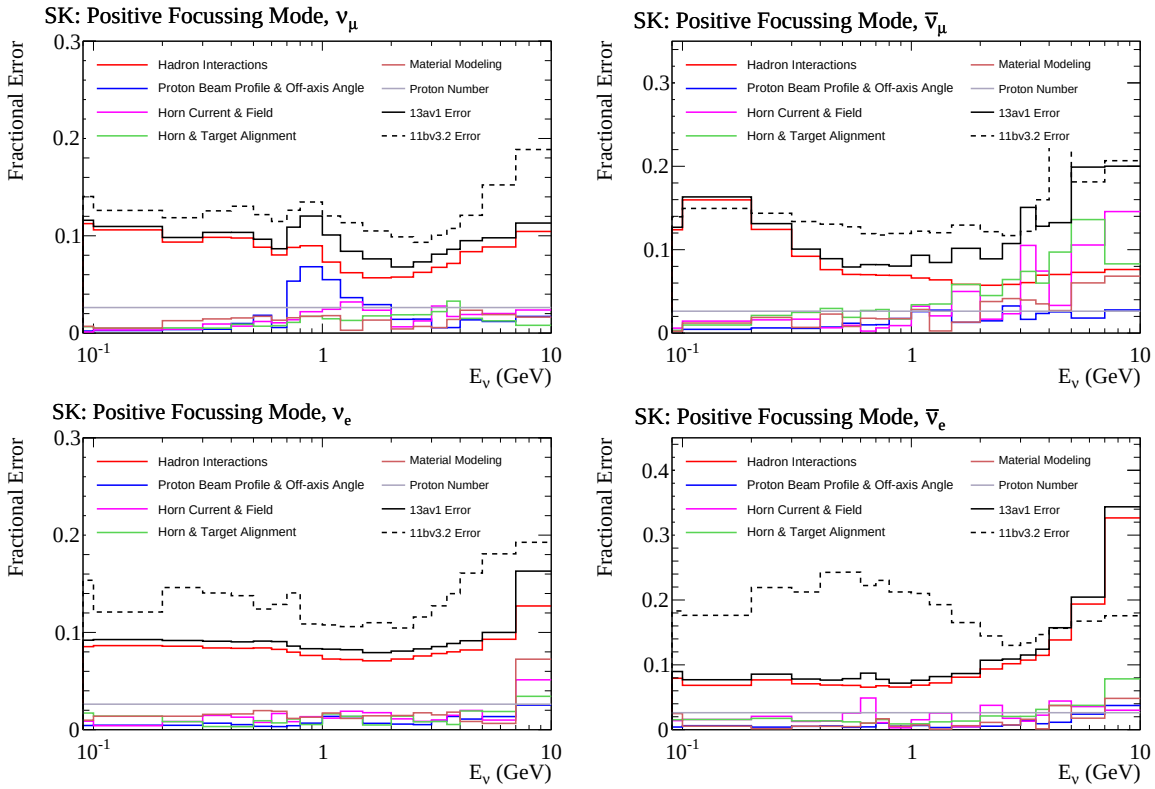

Figure 4.21: Total uncertainties for the flux prediction at the far detector in the neutrino mode as a function of neutrino energy. Top left: ν_μ, top right: $\bar{\nu}_\mu$, bottom left: ν_e, and bottom right: $\bar{\nu}_e$. The labels 13av1, 11bv3.2, Material modeling and Proton number represent respectively the total uncertainty for this oscillation analysis, the total uncertainty used in the previous ν-mode analyses, the uncertainty from the material of the magnetic horns, and the uncertainty from proton beam intensity.

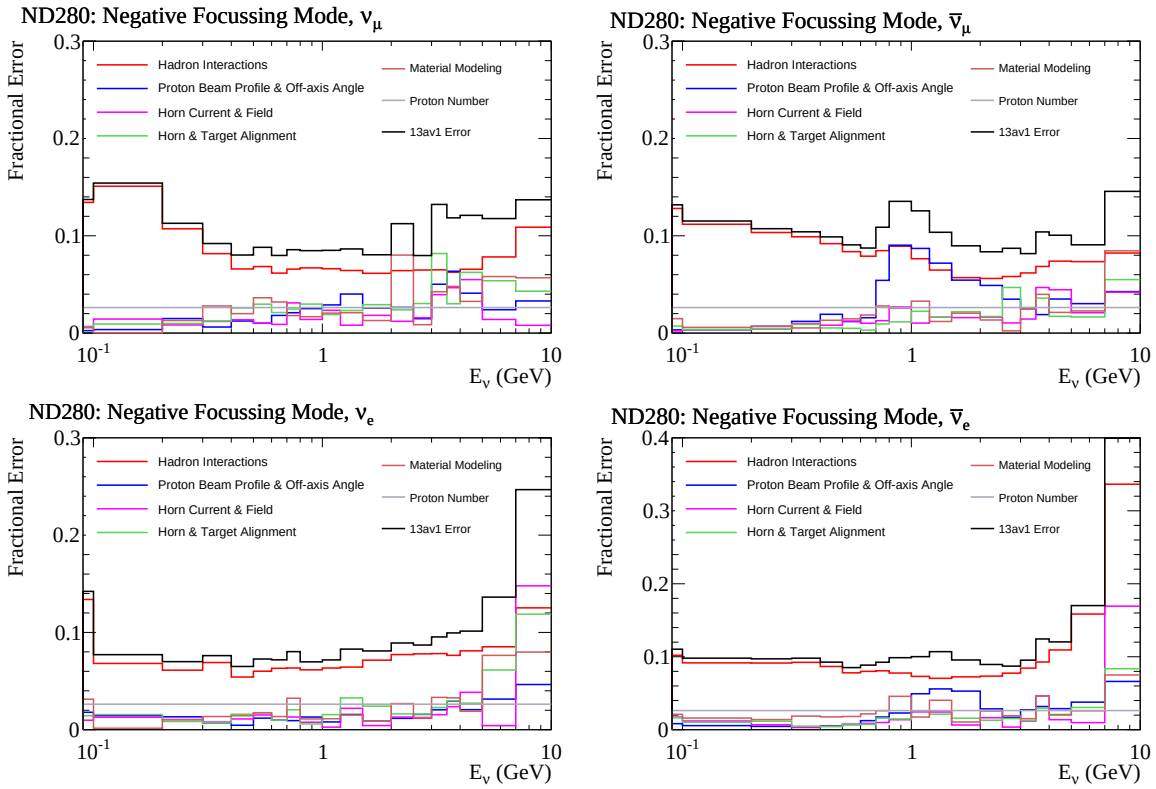

Figure 4.22: Total uncertainties for the flux prediction at the off-axis near detector in the antineutrino mode as a function of neutrino energy. Top left: ν_μ, top right: $\bar{\nu}_\mu$, bottom left: ν_e, and bottom right: $\bar{\nu}_e$. The labels 13av1, Material modeling and Proton number represent respectively the total uncertainty for this oscillation analysis, the uncertainty from the material of the magnetic horns, and the uncertainty from proton beam intensity.

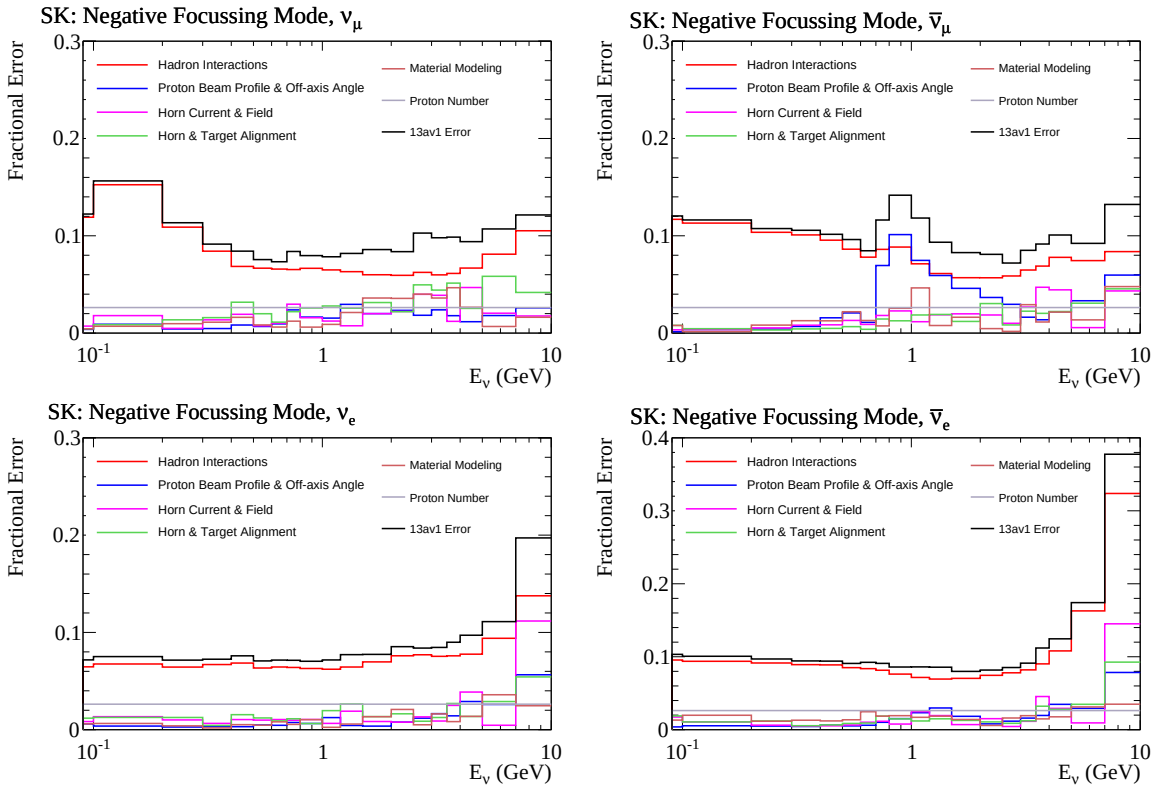

Figure 4.23: Total uncertainties for the flux prediction at the far detector in the neutrino mode as a function of neutrino energy. Top left: ν_μ, top right: $\bar{\nu}_\mu$, bottom left: ν_e, and bottom right: $\bar{\nu}_e$. The labels 13av1, Material modeling and Proton number represent respectively the total uncertainty for this oscillation analysis, the uncertainty from the material of the magnetic horns, and the uncertainty from proton beam intensity.

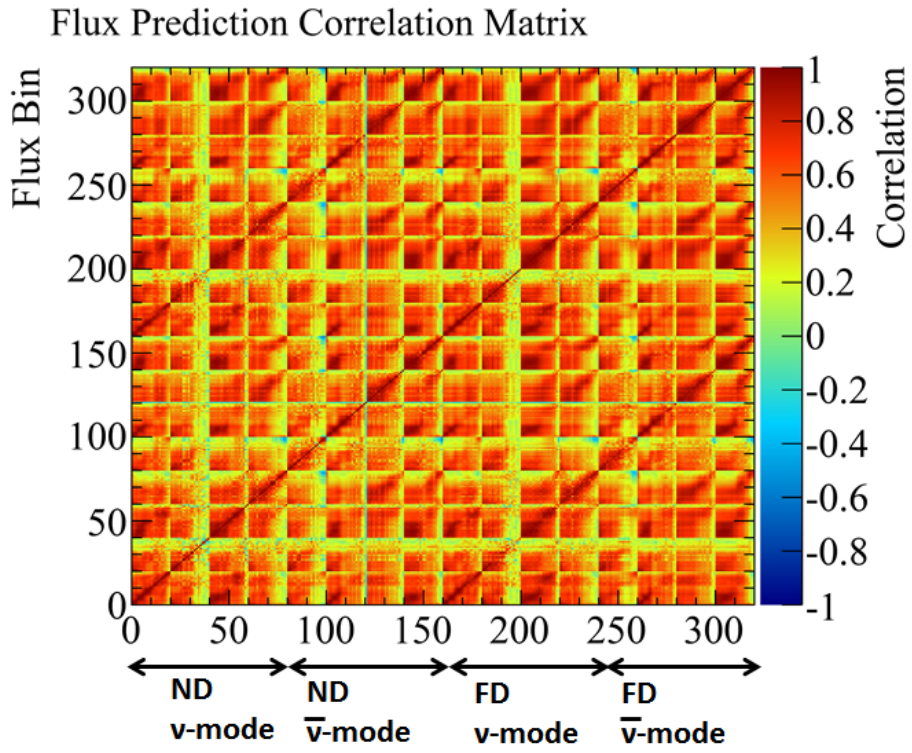

Figure 4.24: Correlation matrix for the bins of the flux prediction. Bin edges the neutrino energy are: 0.0, 0.1, 0.2, 0.3, 0.4, 0.5, 0.6, 0.7, 0.8, 1.0, 1.2, 1.5, 2.0, 2.5, 3.0, 3.5, 4.0, 5.0, 7.0, 10.0 and 30.0 GeV. The ordering of the bins are:
0-19: off-axis near-detector ν_μ bins in the neutrino mode
20-39: off-axis near-detector $\bar{\nu}_\mu$ bins in the neutrino mode
40-59: off-axis near-detector ν_e bins in the neutrino mode
60-79: off-axis near-detector $\bar{\nu}_e$ bins in the neutrino mode
80-99: off-axis near-detector ν_μ bins in the antineutrino mode
100-119: off-axis near-detector $\bar{\nu}_\mu$ bins in the antineutrino mode
120-139: off-axis near-detector ν_e bins in the antineutrino mode
140-159: off-axis near-detector $\bar{\nu}_e$ bins in the antineutrino mode
160-179: far-detector ν_μ bins in the neutrino mode
180-199: far-detector $\bar{\nu}_\mu$ bins in the neutrino mode
200-219: far-detector ν_e bins in the neutrino mode
220-239: far-detector $\bar{\nu}_e$ bins in the neutrino mode
240-259: far-detector ν_μ bins in the antineutrino mode
260-279: far-detector $\bar{\nu}_\mu$ bins in the antineutrino mode
280-299: far-detector ν_e bins in the antineutrino mode
300-319: far-detector $\bar{\nu}_e$ bins in the antineutrino mode

4.4.5 Expected improvement on the flux prediction

Improving the flux prediction is necessary for precise measurements of the neutrino oscillation and the neutrino-nucleus cross section. As stated in Section 4.4.2, the dominant source of the current flux uncertainty is the hadronic interaction uncertainty. For the right-sign muon neutrino flux, the uncertainties from the proton beam and the off-axis angle around 1 GeV are also large. Thus, reducing these uncertainty is especially important.

Both the proton beam and the off-axis angle are related to the neutrino beam direction. In the current analysis, we treat them separately but the proton beam uncertainty can be constrained by the beam direction measurement by INGRID. The dominant source of the off-axis angle uncertainty comes from the systematic uncertainty of the beam direction measurement. This systematic uncertainty will be improved by updates of the analysis of the INGRID.

Among the hadronic interaction uncertainties, the contribution of uncertainties for the interaction rate tuning is the largest source. This uncertainty is conservatively large because we treat the size of the quasi-elastic cross section as the uncertainty of the size of the production cross section. Since the measurement of production cross section in the NA61 thin-target analysis [116] is carefully estimated and is considered to be reliable, we can decrease the uncertainty of the production cross section by adopting the uncertainty of this result (eq.4.2.1).

The result of the NA61 production cross section measurement can be used not only for the primary protons but also for all the higher momentum ($p > 20$ GeV/c) protons because in that momentum region production cross section is flat. Figures 4.25 and 4.26 show comparisons of the uncertainty on the interaction rate tuning between the current analysis used in this oscillation analysis and the improved analysis. The interaction rate uncertainty is significantly decreased and for the right-sign component, the uncertainty around the peak energy is decreased roughly from 7% to 3%. By the improvement of the interaction rate uncertainty, the total right-sign flux uncertainty around the peak energy is decreased roughly from 9-11% to 6-8%.

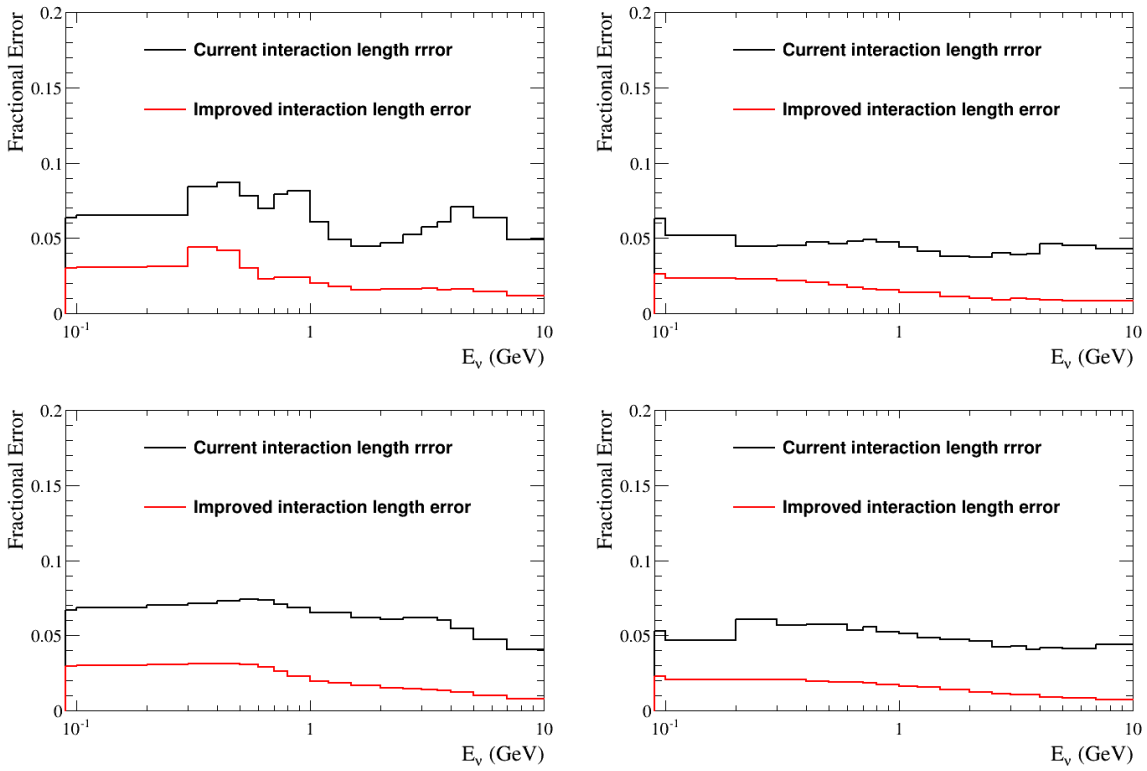

Figure 4.25: Comparison of the uncertainty from the interaction rate tuning in the neutrino mode as a function of neutrino energy. Top left: ν_μ, top right: $\overline{\nu}_\mu$, bottom right: ν_e, bottom left: $\overline{\nu}_e$.

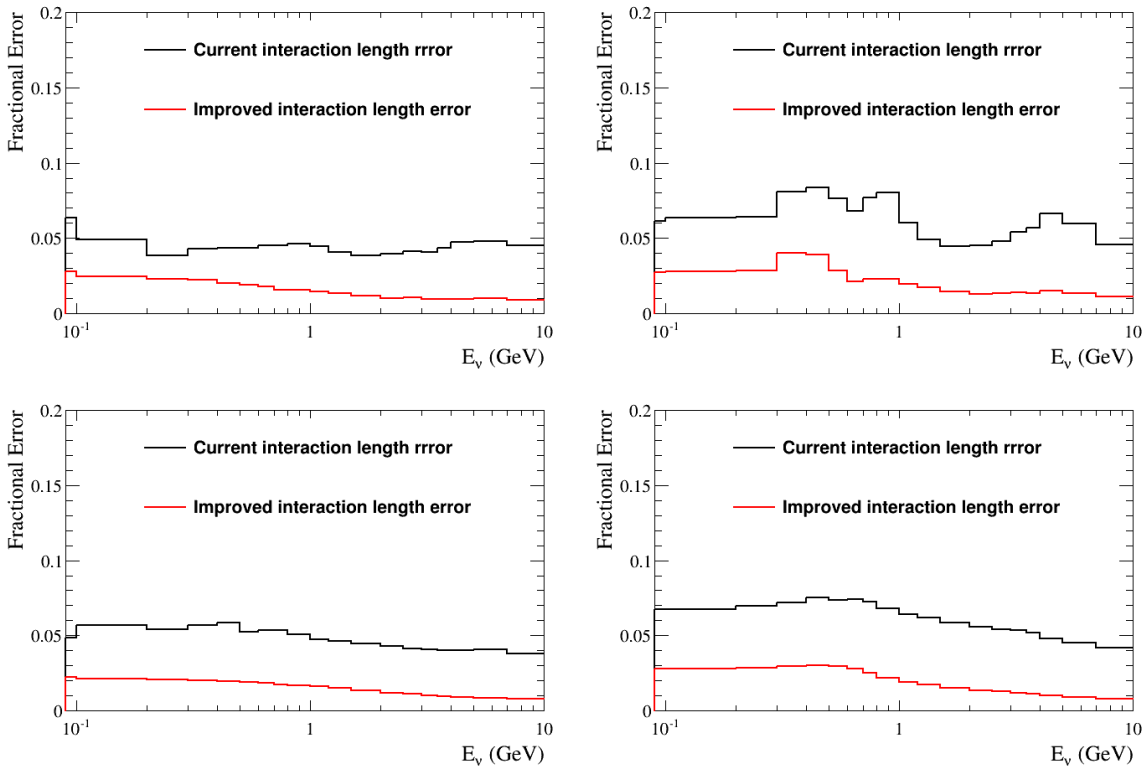

Figure 4.26: Comparison of the uncertainty from the interaction rate tuning in the antineutrino mode as a function of neutrino energy. Top left: ν_μ, top right: $\overline{\nu}_\mu$, bottom right: ν_e, bottom left: $\overline{\nu}_e$.

Chapter 5

Neutrino-nucleus interactions

The range of the neutrino energy is from sub GeV to a few GeV in the T2K experiment. In this energy region, all of the neutrino-nucleus, neutrino-nucleon and neutrino-quark scattering mechanisms contribute [135]. The cross section of the neutrino-electron scattering is much smaller than those processes and we do not discuss this process here. Phenomenogical models have been developed for decades in order to understand these complicated processes. In T2K, a MC neutrino event generator NEUT [136] [137] [138] (version 5.3.2) is used to simulate neutrino interactions and their product particles based on theoretical models. NEUT contains several parameters and they are first derived from data from external experiments. Then, in the oscillation analysis, these parameters and flux parameters are simultaneously constrained by measurements at the T2K near detector.

5.1 Neutrino-nucleus interactions

NEUT simulates following neutrino interactions in both charged current (CC) and neutral current (NC):

- (quasi-)elastic scattering ($\nu_l + N \rightarrow l\,(\nu_l) + N'$),
- meson/γ production via baryon resonances ($\nu_l + N \rightarrow l\,(\nu_l) + N' + m$),
- deep inelastic scattering ($\nu + N \rightarrow l\,(\nu_l) + N'$ + hadrons),
- coherent single pion production ($\nu_l + A \rightarrow l\,(\nu_l) + \pi + A$),

where N and N' represent nucleons (proton or neutron) which can be either free or inside nucleus, l represents a lepton, m represents $(1\pi, K, \eta, \gamma, 2\pi)$ and A represents a nucleus.

Charged current quasi-elastic (CCQE) interaction

The charged current quasi-elastic (CCQE) interaction is used as the signal event of oscillation analyses in T2K. The Llewellyn-Smith model [139] is used as the basis to describe CCQE and neutral current elastic interactions in NEUT. In this model, the differential CCQE cross section for neutrinos and antineutrinos for free nucleon can be written as:

$$\frac{d\sigma_\nu}{dQ^2} = \frac{G_F^2 M^2 \cos^2\theta_c}{8\pi E_\nu^2}\left[A(Q^2) + B(Q^2)\frac{s-u}{M^2} + C(Q^2)\frac{(s-u)^2}{M^4}\right], \tag{5.1.1}$$

$$\frac{d\sigma_{\overline{\nu}}}{dQ^2} = \frac{G_F^2 M^2 \cos^2\theta_c}{8\pi E_\nu^2}\left[A(Q^2) - B(Q^2)\frac{s-u}{M^2} + C(Q^2)\frac{(s-u)^2}{M^4}\right], \tag{5.1.2}$$

$$s - u = 4ME_\nu - Q^2 - m^2,$$

where Q^2, G_F, θ_c and M represent the squared four-momentum transfer, the Fermi coupling constant, the Cabbibo angle, and the mass of the outgoing nucleon respectively, E_ν represents the incident neutrino energy and m represents the mass of the outgoing lepton. The factors $A(Q^2)$, $B(Q^2)$ and $C(Q^2)$ are functions of form factors:

$$\begin{aligned} A(Q^2) &= \frac{m^2+Q^2}{M^2}\Big[(1+\eta)F_A^2-(1-\eta)F_1^2+\eta(1-\eta)F_2^2+4\eta F_1F_2 \\ &\quad -\frac{m^2}{4M^2}\left((F_1+F_2)^2+(F_A+2F_P)^2-4(\eta+1)F_P^2\right)\Big], \qquad (5.1.3) \\ B(Q^2) &= 4\eta F_A(F_1+F_2), \qquad (5.1.4) \\ C(Q^2) &= \frac{1}{4}(F_A^2+F_1^2+\eta F_2^2), \qquad (5.1.5) \\ \eta &= \frac{Q^2}{4M^2}, \end{aligned}$$

where F_A, F_P represent the axial-vector and the pseudo-scalar form factors respectively, and

$$\begin{aligned} F_1 &= F_1^p - F_1^n, \\ F_2 &= F_2^p - F_2^n, \end{aligned}$$

where $F_1^{p,n}$ and $F_2^{p,n}$ represent the electric and magnetic vector form factors of protons or neutrons. Each of these form factors is a function of Q^2. The contribution from F_P can be neglected because F_P in eq. 5.1.3 is multiplied by $m^2/4M^2(\ll 1)$. The vector form factors can be calculated by using data from electron-nucleus scattering experiments. It has been assumed that F_A has a dipole form:

$$F_A = \frac{g_A}{(1+Q^2/M_A^2)^2}, \qquad (5.1.6)$$

where $g_A \simeq -1.267$ was determined from β-decay experiments [140] and M_A^{QE} is called the axial vector mass. The M_A^{QE} has been measured by neutrino-nucleus experiments. If M_A^{QE} gets larger, total CCQE cross section also becomes larger and the ratio of forward scattering to back scattering gets smaller.

We are using carbon and oxygen as the inreraction targets of neutrinos. For these nuclei, nuclear effects should also be considered. Nuclear effects are caused by the fact that each nucleon is bound in its nucleus and has the Fermi momentum. Furthermore, interactions where the nucleon changes to a new state already occupied by other nucleons are not allowed (Pauli blocking). In the previous neutrino oscillation analysis [69] the spectral function model [141] was used as the probability distribution of momentum of nucleons. However, the relativistic Fermi gas (RFG) model by Smith and Moniz [142] [143] with the relativistic random phase approximation (RPA) by Nieves *et al.* [144] is instead used for this oscillation analysis. This is because RFG+RPA model is found to reproduce data from external experiments better than the spectral function model [146] in 2015. These models affect the energy distribution of the CCQE events.

Figure 5.1 shows measurements of ν_μ (black) and $\overline{\nu}_\mu$ (red) CCQE cross sections per nucleon as a function of neutrino energy. It is seen from this plot nominal prediction cannot reproduce cross-section data at around 1 GeV.

Charged current multi-nucleon interaction

In order to resolve the excess of the data over models in the CCQE measurements, the charged current multi-nucleon interaction has been studied. In this interaction, more than one nucleons are emitted from nucleus as shown in fig. 5.2. Since the incident neutrino interacts with nucleons which couple

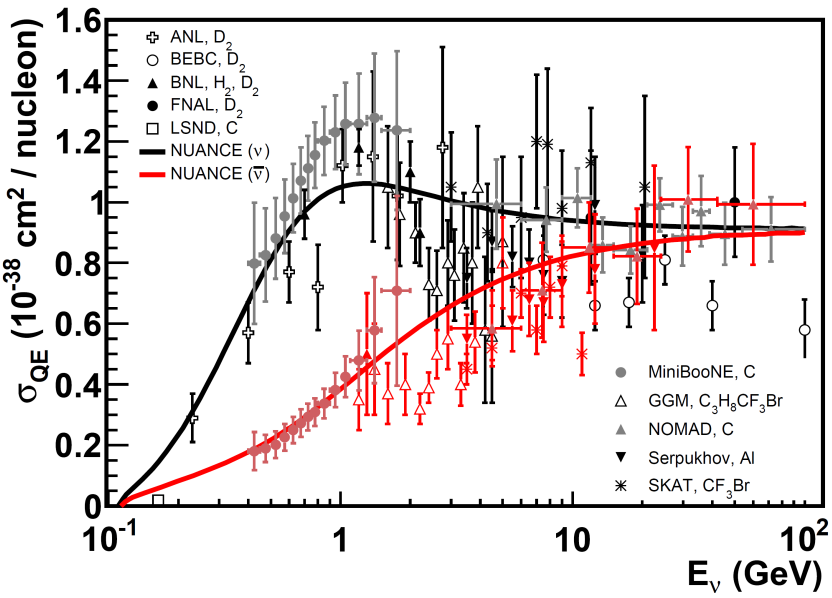

Figure 5.1: Measurements of ν_μ (black) and $\overline{\nu}_\mu$ (red) CCQE cross sections per nucleon as a function of neutrino energy. Lines are predictions from NUANCE event generator [145] assuming M_A^{QE}=1.0 GeV. Figure is taken from [19].

via meson exchange, this interaction is called the meson exchange current model (MEC)[1]. The final state of the MEC interaction observed in the far detector is the same as that of the CCQE interaction because Cherencov lights from the nucleons are not seen. The reconstructed neutrino energy in the MEC interactions at the far detector by using kinematic information on lepton (eq. 2.6.2), where CCQE interaction is assumed, is usually smaller than its true energy because the target mass is heavier than that of a nucleon.

From NEUT version 5.3, MEC is newly included in the code and this new version is used in this oscillation analysis. NEUT adopts a model by Nieves *et al.* [147] [148] for the MEC interaction. This model calculate a many-body reaction of inclusive neutrino-nucleus cross section, whose method has been used in predictions of electron-nucleus cross sections [149]. This model is valid up to roughly 1.5 GeV of neutrino energy, because not all diagrams on MEC are calculated in this model, while neutrino energy region in T2K extends beyond 1.5 GeV. Therefore, a careful treatment to use this model is necessary. It was pointed out by R. Gran *et al.* [150] that the validation of this model is limited by three-momentum transfer $|q_3|$ rather than neutrino energy:

$$|q_3| = |\boldsymbol{p}_l - \boldsymbol{p}_\nu| \leq 1.2 \text{ (GeV)},$$

where $\boldsymbol{p}_l$ and $\boldsymbol{p}_\nu$ represent three-momentum of lepton and neutrino, respectively. Hence, the model by Nieves with this by this $|q_3|$ cut is implemented in NEUT. NEUT uses look-up tables of double differential cross sections ($d^2\sigma/dTd\cos\theta$, where T and θ represent the kinetic energy and the emission angle of lepton) on carbon and oxygen as a function of neutrino energy respectively. These tables are produced by using the codes provided by the author of [148] which compute double differential cross sections of the MEC interactions.

[1] also called $2p-2h$ or $np-nh$ model

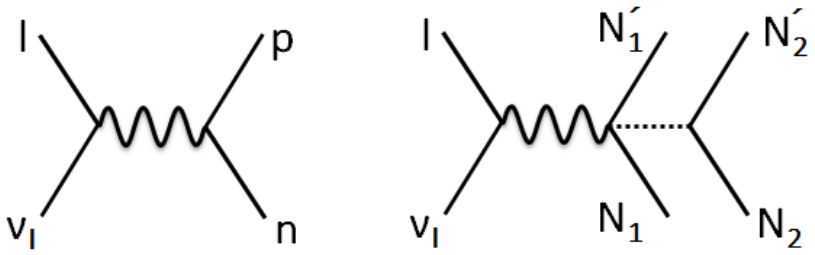

Figure 5.2: Feynman diagrams of CCQE interaction (left) and charged current multi-nucleon interaction (right). N_1 and N_2 represent a nucleon.

Charged current meson/γ production via baryon resonances

A neutrino having energy around 1 GeV sometimes excite a nucleon when interaction happens. The excited-state baryon quickly decay and produce mesons or γs. A model based on Rein and Sehgal [151] with a revision of form factors by K.M. Graczyk and J.T. Sobczyk [152] is used to simulate π, K, η and γ production via baryon resonances. This theory assumes an intermediate baryon resonance, N^* like $\Delta(1232)$:

$$\begin{aligned} \nu + N &\rightarrow l(\nu') + N^*, \\ N^* &\rightarrow N + m. \end{aligned}$$

The amplitude of the resonant production is given by:

$$\mathcal{M} \propto \langle N^* | J_{\mathrm{RES}} | N \rangle, \tag{5.1.7}$$

where J_{RES} the hadronic current operator which contains a vector current and an axial-vector current terms. These terms are parametrized by form factors. The vector form factors are taken from [153]. For the axial-vector form factors, the parametrization by Adler [154] was adopted and the axial-vector form factor C_5^A is the variable parameter in NEUT.

To avoid double counting through deep inelastic scattering, we consider 18 baryon resonances only where their invariant masses (W) are less than 2 GeV and we do not consider multi-pion production here. In the past ν-mode analysis [69], pionless Δ decay, i.e., a resonant baryon interact with other nucleons and disappear without emissions of pions was considered. Since the nucleon which absorbs a pion emits from the nuclei, the pionless Δ decay process in this analysis is included in that of the MEC interactions.

Deep inelastic scattering

For higher energy region, deep inelastic scattering (DIS), where neutrinos interact with quarks is the dominant process. Multi-pion production and DIS are considered for the region of W >1.3 (1.4) GeV in the neutrino (antineutrino) mode. For parton distribution function, the GRV98 (Glück-Reya-Vogt 1998) [155] model is used and corrections by Bodek and Yang [156] [157] is applied so as to improve agreement with experiments in low-Q^2 region. In the region of $W \leq 2$ GeV, multi-pion production is considered and we use a custom-made program [159] In the region of $W > 2$ GeV, the PYTHIA/JetSet program [158] is used.

Coherent pion production

Neutrinos can also interact with an entire nucleus coherently. In this coherent scattering, a pion can be produced. The kinematics of the CC coherent pion production are different from those of the CC pion production interaction via baryon resonances in terms of small Q^2 and small scattering angle. A model by Rein and Sehgal [160], [161] based on the PCAC theorem [162] is used to simulate the coherent pion production. The cross section of the CC coherent scattering is much smaller than those of the CC pion production interaction via baryon resonances.

5.1.1 Final-state and secondary interactions

When hadrons are produced in the neutrino-nucleus scattering, those hadrons can re-interact within the nucleus before they escape. Those intra-nucleus interactions are usually called the final state interactions (FSI). The effect of FSI is to migrate events among different observable topologies in the detector and changes the particle kinematics. In NEUT the FSI model adopted is the microscopic cascade model [163], where a hadron which is produced in the nucleus is transported step by step until it interacts with the other nucleon or escapes from the nucleus. For mesons and nucleons, mean free paths in the nucleus are first calculated by using theoretical models and external data, and those results are used as the inputs in NEUT. For pions in the lower momentum region (<500 MeV/c), in which greater part of FSI occurs, a model by L. Salcedo *et al.* [164] is used for the calculation of interaction probabilities for quasi-elastic interaction, charge exchange interaction, and pion absorption to the nucleus. For pions in the higher momentum region (>500 MeV/c), interaction probabilities for quasi-elastic interaction, charge exchange interaction and inelastic interaction are calculated by using data from pion-nucleus scattering experiments. For the other mesons and nucleons, the mean free paths are estimated by hadron-nucleus scattering experiments. Hadrons after escaping from the nucleus may also interact with other nuclei. This is called the secondary interactions (SI). In T2K, FSI and SI of pions are one of the main systematic uncertainty sources in the the near detector and the far detector analyses.

5.1.2 Neutrino-nucleus cross section as a function of neutrino energy

Figure5.3 shows the ν_μ-oxygen and $\bar{\nu}_\mu$-oxygen charged-current (CC) inclusive and exclusive cross sections per nucleon divided by neutrino energy as a function of neutrino energy. Antineutrino-nucleus cross sections are smaller than neutrino-nucleus cross sections. The ratio of cross section $\sigma(\nu)/\sigma(\bar{\nu})$ is higher than 1 qualitatively because the helicity suppression works only for antineutrinos. $\sigma(\nu)/\sigma(\bar{\nu})$ depends on neutrino energy and is roughly 4 around the peak energy where CCQE scattering is the dominant interaction in NEUT which is used in this analysis.

5.2 Cross section parameters and their uncertainties

Cross-section parameters for each interaction type and their uncertainties are obtained from measurements by external experiments.

For the CCQE interaction, following parameters are considered: axial-vector mass (M_A^{QE}), Fermi momentum (p_F) for nuclei in the near detector (^{12}C) and the far detector (^{16}O), and binding energy (E_b) for C and O. For the MEC interaction, the overall normalization parameters of MEC for C and O are considered. These parameters except for E_b are obtained [146] by the simultaneous fit of the CH_2 and CH target data from MiniBooNE [165] [166] and MINERvA [167] [168]. After this fit, a conservative 100% uncertainty is added in quadrature to the MEC oxygen parameter because the MEC interaction is not well understood. The uncertainty for E_b is determined from electron-nucleus scattering data [169].

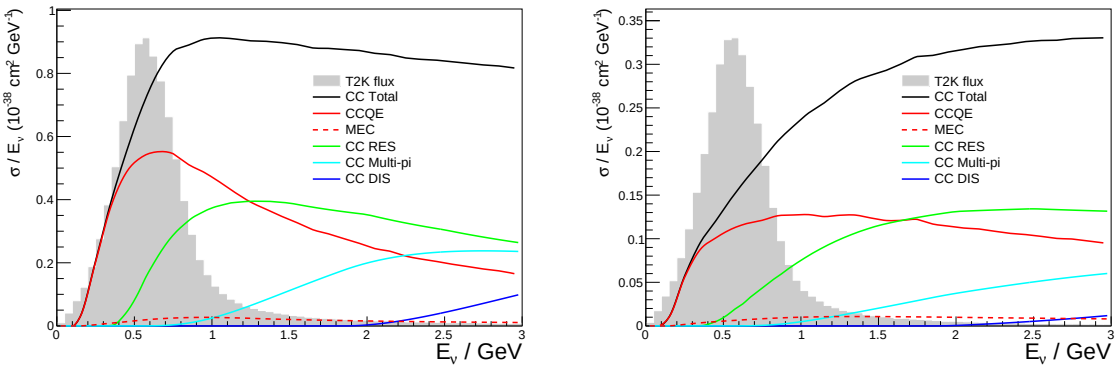

Figure 5.3: Total neutrino-oxygen (left) and antineutrino-oxygen (right) CC cross sections per nucleon divided by neutrino energy as a function of neutrino energy. The T2K unoscillated ν_μ flux in the neutrino mode and $\bar{\nu}_\mu$ flux in the antineutrino mode are also shown.

For the CC and NC single resonant pion interactions, parameters from axial-vector form factor, M_A^{RES} and $C_5^A(0)$, and nonresonant-background scaling factor ($\mathrm{BG}^{\mathrm{RES}}$ or Isospin=1/2 background) are considered. It is assumed that the axial-vector form factor $C_5^A(Q^2)$ has a dipole form:

$$C_5^A(Q^2) = \frac{C_5^A(0)}{(1 + Q^2/M_A^{\mathrm{RES}\ 2})^2}. \tag{5.2.1}$$

Their values and uncertainties are estimated by a recent analysis of the ANL and BNL experiments [170].

A 100% normalization uncertainty for the CC coherent pion production for C and O is conservatively assigned because external data is consistent with no coherent production [171] [172]. This uncertainty size will be updated by including recent results from MINERvA [173]. A 30% normalization uncertainty for the NC coherent pion production is assigned due to the difference of its cross section between NEUT and the SciBooNE experiment [174].

An energy-dependent uncertainty $(0.4/E_\nu)$ for the CC DIS and $(K, \gamma, \eta, 2\pi)$ interactions (CC Other) is assigned from the result from near detector of the MINOS experiment [175]. A 30% normalization uncertainty for the NC DIS and $(K, \gamma, \eta, 2\pi)$ interactions (NC Other) is assigned from parameter variation studies. $\sigma_{\nu_e}/\sigma_{\nu_\mu}$ is the normalization parameter which changes the ratio of cross sections between σ_{ν_e} and σ_{ν_μ} and 3% uncertainty is assigned [176].

Uncertainties of FSI and SI in the far detector will be discussed in Chapter 6. A summary of the neutrino interaction parameters are shown in table 5.1. Effects of the neutrino-nucleus cross-section parameters to the oscillation analysis will be described in Section 7.3.

5.2.1 Treatment of the energy-dependent parameters

Some of the cross-section parameters, M_A^{QE}, p_F, E_b, $C_5^A(0)$, M_A^{RES}, $\mathrm{BG}^{\mathrm{RES}}$, and CCother cause energy dependent variations of the cross sections. These parameters change the kinematics of emitted leptons. It is practically difficult to calculate the effect of these parameters in their analyses framework because computation time gets too long. Hence, the effect of these parameters for some specific values is computed in advance and the effect of these parameters for an arbitrary value is obtained by interpolation. The effect of these parameters is then treated as the reweighting factors which are applied to the nominal

Table 5.1: Summary of the neutrino interaction parameters derived by external data.

Parameter	Nominal value	uncertainty	lower bound	upper bound
M_A^{QE} (GeV)	1.15	0.07	-	-
p_F ^{12}C (MeV)	223	13	200	275
p_F ^{16}O (MeV)	225	13	200	275
E_b ^{12}C (MeV)	25	9	12	42
E_b ^{16}O (MeV)	27	9	12	42
MEC ^{12}C	27%	29%	0	-
MEC ^{16}O	27%	104%	0	-
$C_5^A(0)$	1.01	0.12	-	-
M_A^{RES} (GeV)	0.95	0.15	-	-
$\mathrm{BG}^{\mathrm{RES}}$	1.30	0.20	-	-
CCcoherent ^{12}C	1.0	1.0	0	-
CCcoherent ^{16}O	1.0	1.0	0	-
CCother	0.0	0.40	-	-
NCcoherent	1.0	0.30	0	-
NCother	1.0	0.30	0	-
$\sigma_{\nu_e}/\sigma_{\nu_\mu}$	1.0	0.03	-	-

prediction by MC simulations. Figure 5.4 shows an example (M_A^{QE} parameter) of the reweighing factor to the (CCQE) cross section as a function of difference from the nominal value.

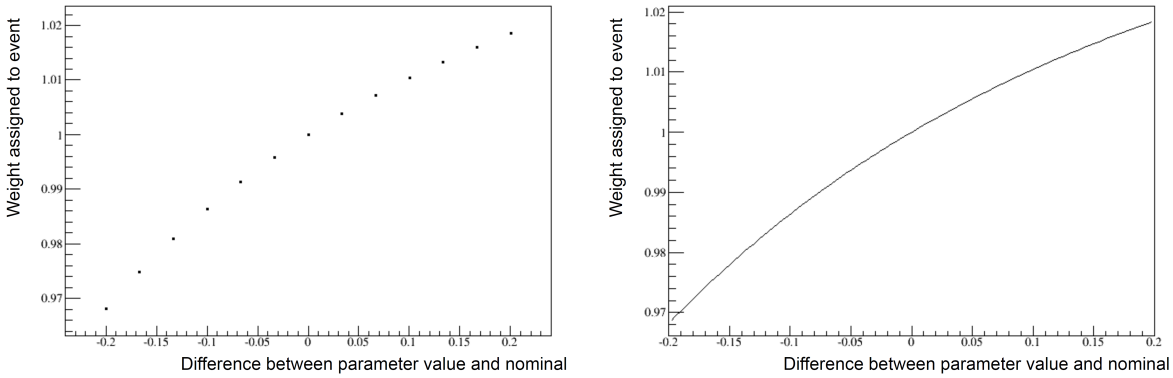

Figure 5.4: Example of the reweighing factor for total CCQE events as a function of the M_A^{QE} parameter, given as the difference from the nominal value. The reweighing factor is computed every 0.5 σ (left) and that for an arbitrary value is obtained by interpolation with a cubic function (right).

Chapter 6

Measurements at the near and far detectors

We describe the measurements at the off-axis near detector and the far detector which are used for this oscillation analysis.

6.1 Analysis overview

In this section, we describe the overview of the oscillation analysis. The overall flow of this oscillation analysis is depicted in fig. 6.1. The neutrino fluxes at the near detector and the far detector are predicted by JNUBEAM and tuned with the beamline measurements and the external hadron production data as discussed in Chapter 4. Neutrino-nucleus interactions in the detectors are simulated by NEUT using the flux prediction and neutrino-nucleus cross-section models, which are tuned based on external cross-section measurements as discussed in Chapter 5. The propagation of the generated particles are implemented by detector simulation codes. For the detector simulation of the near detector, GEANT4 [177] is used to simulate the energy deposits from the final state particles that pass through the detector, and the response of the active detectors is simulated through custom-written code [178]. For the detector simulation of the far detector, SKDETSIM [62], a GEANT3 [108]-derived simulation, is used to simulate generation and propagation of Cherencov lights in water. the GCALOR package [109] is used to simulate hadronic interactions around 1 GeV/c and for pions with momentum below 500 MeV/c, custom routines are employed. SKDETSIM also simulates the response of PMTs and the electronics.

The measurements at the near detector in both the neutrino mode and the antineutrino mode are then used to constrain the uncertainties of the neutrino flux and the neutrino-nucleus interactions at the far detector. They are used to predict the event rate and the energy spectrum of muon antineutrinos at the far detector. Finally, we obtain the oscillation parameters by comparing the prediction and the data.

6.1.1 Dataset

In this analysis, the off-axis near detector (ND) data corresponding to 5.82×10^{20} POT in the neutrino mode and 4.30×10^{19} POT in the antineutrino mode are used in order to constrain the flux and the cross-section uncertainties. The $\overline{\nu}$-mode ND data used in this analysis are taken in the T2K RUN5. We use data at the far detector (SK) corresponding to 4.01×10^{20} POT in the antineutrino mode, which correspond to the full T2K RUN5 and RUN6 data. Figure 6.2 shows the history of the data taking at SK. The dead fraction of the data acquisition at SK is roughly 1% during the whole period.

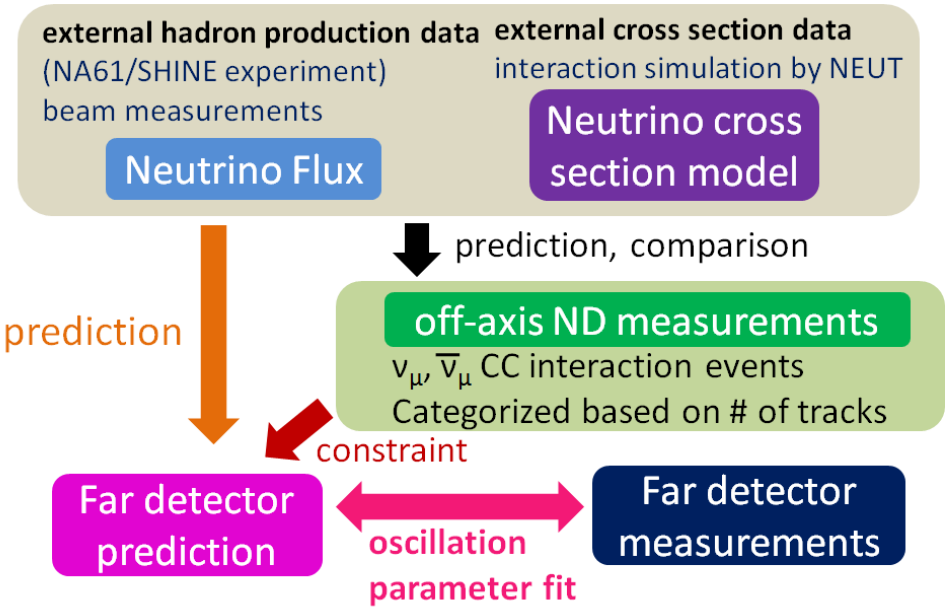

Figure 6.1: Overview of this oscillation analysis.

6.2 Measurements at the off-axis near detector

The ν_μ and $\overline{\nu}_\mu$ charged-current (CC) interaction events which arise inside the hydrocarbon target of the upstream FGD (FGD1) are used. The flux and neutrino-nucleus cross-section parameters are constrained by fitting the predictions of the momentum-angle distributions of those events to those measured by varying these parameters. The selected events are categorized by interaction types to be sensitive to different interaction types.

6.2.1 Event selection

The ν_μ and $\overline{\nu}_\mu$ CC events are selected by identifying one muon track in an event. The selection criteria for the CC inclusive events are followings: Tracks in the event are only accepted if they are within 60 ns from the center of the timing of one of the bunches. The vertex of the highest momentum track exists in the fiducial volume of the FGD1 [1]. The fiducial volume begins 21 mm (2 layers) inward from the upstream boundary in the beam direction and 58 mm inward from the boundaries both in the horizontal and vertical directions. To reduce the background events, any tracks which pass through the upstream TPC (TPC1) are rejected. The highest momentum track must have more than 18 reconstructed clusters in the TPC2 (just downstream the FGD1) for reducing short-track events and an energy deposit of it in the TPC2 must be consistent with a muon. For the antineutrino mode data, in order to reduce the pion background, the following criterion is additionally included to the criteria which are used for the neutrino mode data: For the $\overline{\nu}_\mu$ (ν_μ) CC events, the highest-momentum, positively (negatively) charged track must be the highest momentum track in the event.

We then classify the selected inclusive CC events according to the number of the final state particles. For the ν-mode data, the CC inclusive events are classified into three categories: CC0π, CC1π^+ and CCother, defined by the number of final state pions. CC0π events have no pions and are dominated

[1] Events occurred in the FGD2 are not used in this oscillation analysis but will be used in near future.

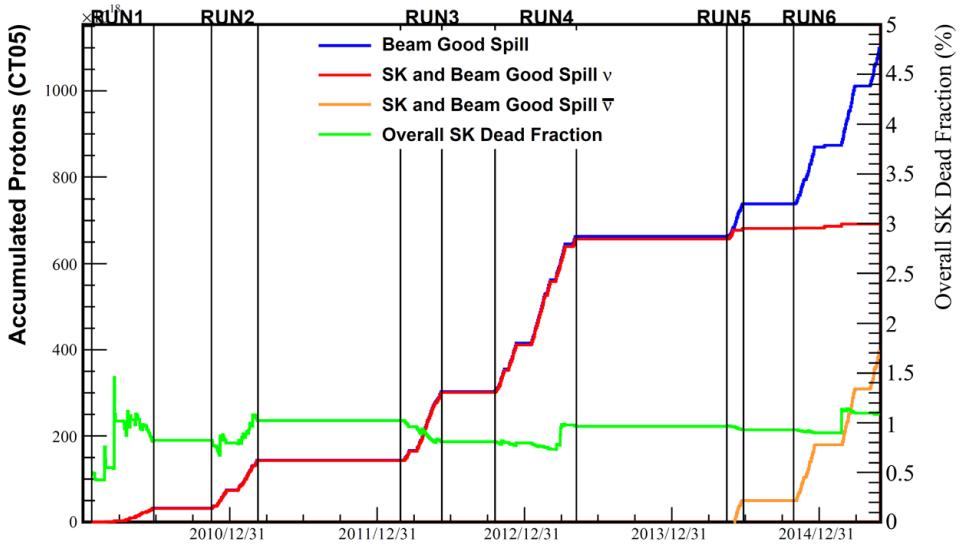

Figure 6.2: Accumulated number of POT as a function of date for the beam good spills (blue), the SK+beam good spills in the neutrino mode (red) and SK and beam good spills in the antineutrino mode (orange). Dead POT fraction is also shown (green = (blue-red-orange)/blue).

by the CCQE interactions. CC1π^+ events have 1 μ^- and 1 π^+, and are dominated by resonant pion production interactions. CCother events are the rest of the CC events and are dominated by deep inelastic interactions. Due to this classification, the CC0π-related parameters (M_A^{QE}, p_F, E_b and MEC), the CC1π-related parameters ($C_5^A(0)$, M_A^{RES}, BG$^{\mathrm{RES}}$, CC and NC coherent) and the CCother-related parameters can be constrained effectively.

For the antineutrino mode data, since the number of events is much smaller than that of the neutrino mode data, the CC1π^+ and CCother events are not divided. For the $\overline{\nu}$-mode data, the ν_μ and $\overline{\nu}_\mu$ events are classified into different categories because the fraction of the wrong-sign events are much larger than that for the neutrino mode. A precise understanding of the ν_μ background is important for this oscillation analysis because the far detector cannot distinguish the charge of each event and ν_μ events are the dominant background. Thus, the CC inclusive events are classified into four categories: $\overline{\nu}_\mu$ CC 1-track and $\overline{\nu}_\mu$ CC N-tracks, ν_μ CC 1-track and ν_μ CC N-tracks (N>1). The CC 1-track sample is the same category as the CC0π category in the neutrino mode while the CC N-tracks sample is a mixture of CC1π^+ and CCother samples in the neutrino mode. Figure 6.3 shows an example of the $\overline{\nu}_\mu$ CC 1-track and N-tracks events.

6.2.2 Results of the near detector measurement

Figures 6.4, 6.5 and 6.6 show the muon momentum and $\cos\theta$ distributions and table 6.1 shows the number of the observed events for each subsample in the neutrino mode and the antineutrino mode. The number of the observed events for the ν-mode CC0π subsample is larger than that of prediction. By contrast, the number of the observed events for the ν-mode CC1π subsample is smaller than that of the prediction The number of the observed events in the antineutrino mode is larger than that of the prediction.

Tables 6.2 and 6.3 summarize the efficiencies and purities of the ν-mode subsamples and the $\overline{\nu}$-mode subsamples, respectively. Here the efficiency and the purity for the subsample A is defined as (selected true CC interactions classified to A)/(all the true CC interactions classified to A) and (selected

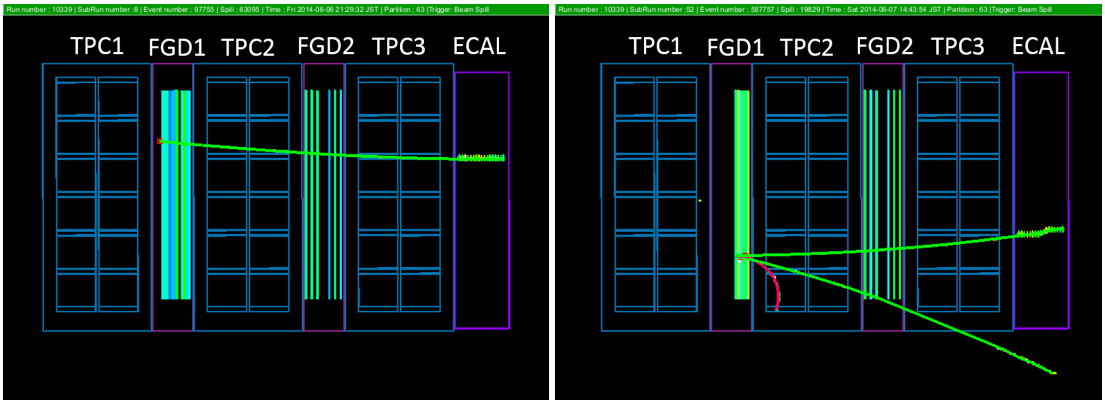

Figure 6.3: Example events observed in the off-axis near detector. left: $\bar{\nu}_\mu$ CC 1-track event. right: $\bar{\nu}_\mu$ CC N-track event.

Table 6.1: Number of the observed events and the pre-fit MC prediction for the different samples.

subsample	Data	pre-fit MC
neutrino mode		
CC0π	17362	15625
CC1π^+	3988	4748
CCother	4219	3772
antineutrino mode		
$\bar{\nu}_\mu$ CC 1-Track	435	387
$\bar{\nu}_\mu$ CC N-Tracks	136	128
ν_μ CC 1-Track	131	141
ν_μ CC N-Tracks	145	147

true CC interactions classified to A)/(all the selected interactions classified to A), respectively. The false association of an event to the wrong category is caused by various reasons such as the misidentification of a particle in the TPC or the FGD and the reconstruction failure. The efficiency for the ν-mode CC0π ($\bar{\nu}$-mode CC 1-track) subsample is larger than that for the ν-mode CC1π and CCother ($\bar{\nu}$-mode CC N-tracks) subsamples. This is because for some events pions cannot be identified due to interactions with the surrounding material.

Table 6.2: Summary of the efficiencies and the purities of the ν-mode subsamples.

	CC0π	CC1π^+	CCother
efficiency	47.6%	27.5%	27.6%
purity	66.5%	54.5%	72.3%

Table 6.3: Summary of the efficiencies and the purities of the $\overline{\nu}$-mode subsamples.

	$\overline{\nu}_\mu$ CC 1-track	$\overline{\nu}_\mu$ CC N-tracks	ν_μ CC 1-track	ν_μ CC N-tracks
efficiency	66%	29%	46%	37%
purity	74%	46%	51%	66%

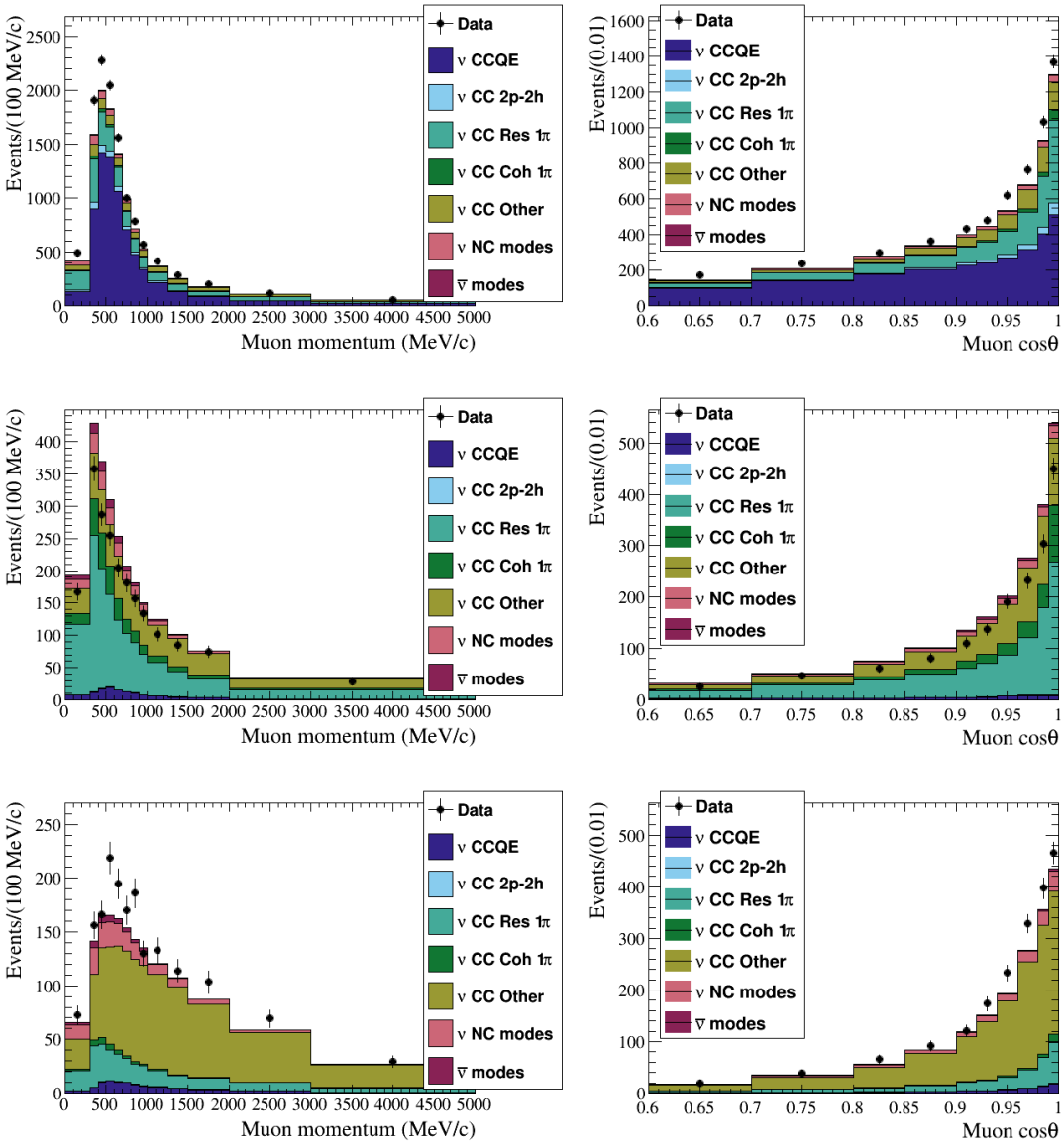

Figure 6.4: Muon momentum (left) and cos θ (right) distributions of the CC events in the neutrino mode. top: CC0π subsample, middle: CC1π^+ subsample, bottom: CCother subsample. Overlaid are the pre-fit MC predictions broken down into different interaction types.

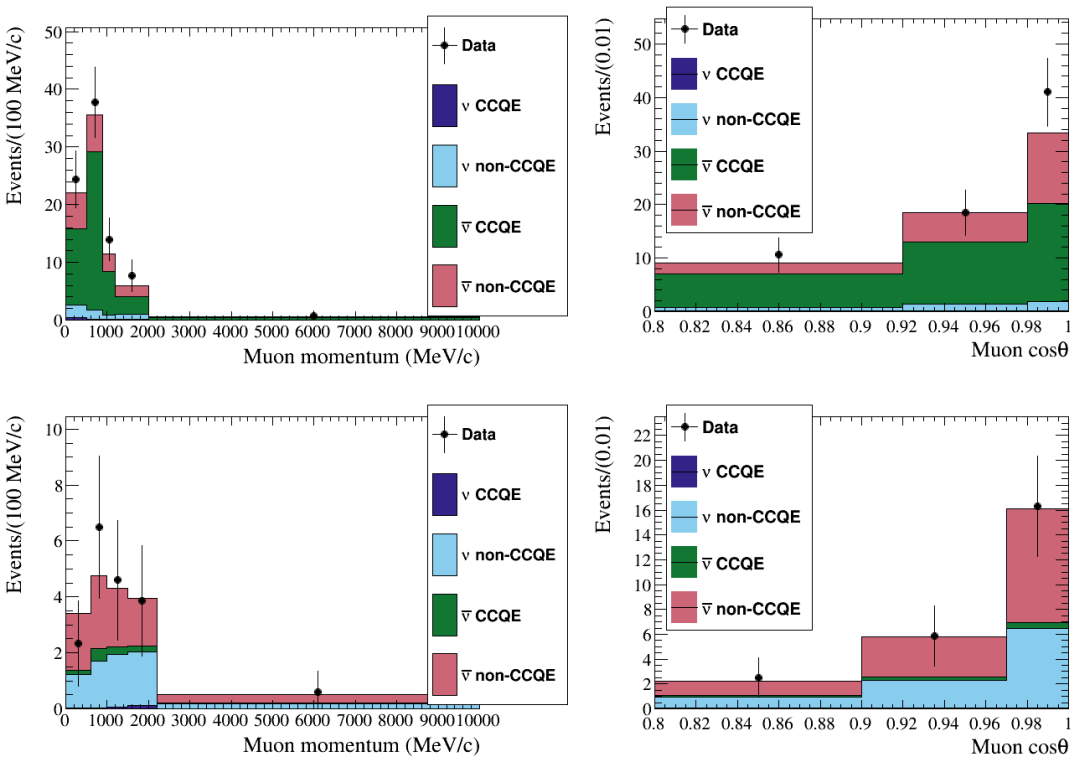

Figure 6.5: Muon momentum (left) and cos θ (right) distributions of the $\overline{\nu}_\mu$ CC events in the antineutrino mode. top: $\overline{\nu}_\mu$ CC 1-track subsample, bottom: $\overline{\nu}_\mu$ CC N-tracks subsample. Overlaid are the pre-fit MC predictions broken down into different interaction types.

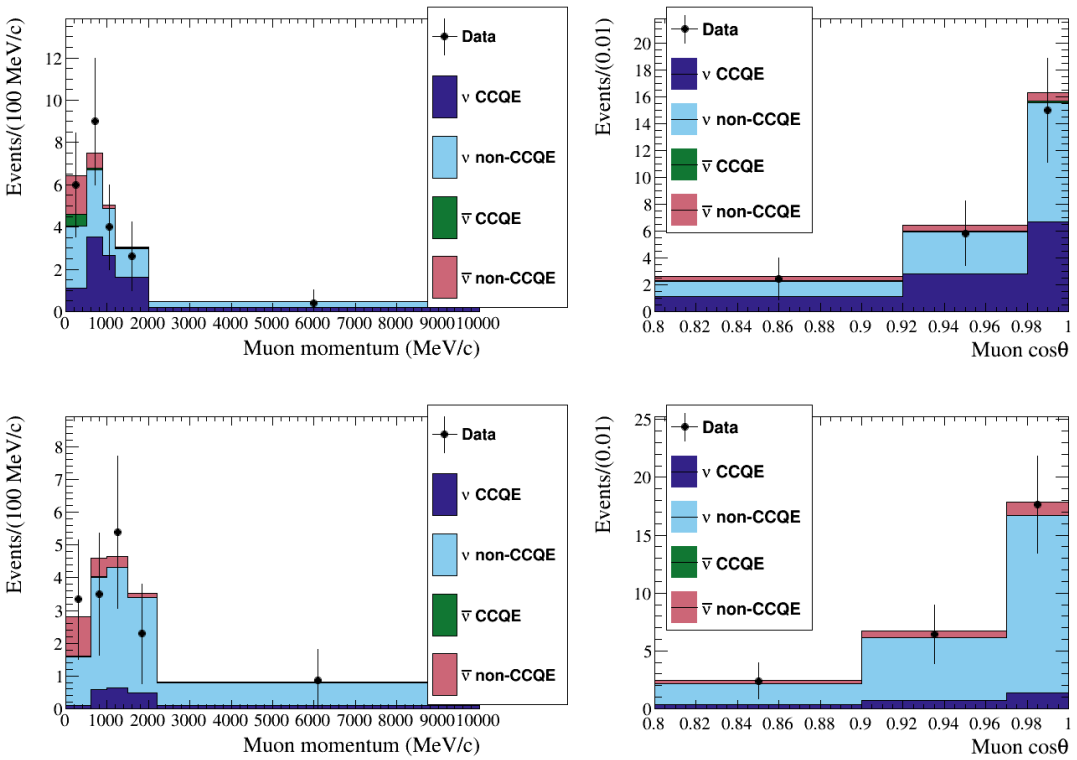

Figure 6.6: Muon momentum (left) and cos θ (right) distributions of the ν_μ CC events in the antineutrino mode. top: ν_μ CC 1-track subsample, bottom: ν_μ CC N-tracks subsample. Overlaid are the pre-fit MC predictions broken down into different interaction types.

6.3 Constraints from the near detector on the uncertainties for the oscillation analysis

6.3.1 Analysis overview

The seven subsamples are binned in the kinematic variables of the muon momentum (p) and the muon emission angle ($\cos\theta$) as shown below:

Bin edges in the neutrino mode

p (MeV/c): 0, 300, 400, 500, 600, 700, 800, 900, 1000, 1250, 1500, 2000, (3000)[2], 5000, 30000
$\cos\theta$: -1.0, 0.6, 0.7, 0.8, 0.85, 0.9, 0.92, 0.94, 0.96, 0.98, 0.99, 1

Bin edges of the 1-track subsamples in the antineutrino mode

p (MeV/c): 0, 500, 900, 1200, 2000, 10000
$\cos\theta$: -1.0, 0.8, 0.92, 0.98, 1

Bin edges of the N-tracks subsamples in the antineutrino mode

p (MeV/c): 0, 600, 1000, 1500, 2200, 10000
$\cos\theta$: -1.0, 0.8, 0.9, 0.97, 1

The binnings are optimized to ensure sufficient amount of data in each bin. The binning in the antineutrino mode is coarser than that in the neutrino mode due to the limited amount of data.

The fit is carried out by maximizing the p-$\cos\theta$ binned likelihood ratio $\mathcal{L}_{\mathrm{ND}}$:

$$\mathcal{L}_{\mathrm{ND}} = \prod_{i=1}^{\mathrm{Bins}} P_{\mathrm{Poisson}}(N_i^{\mathrm{pred}}(\boldsymbol{f}), N_i^{\mathrm{obs}}) \times \mathcal{L}_{\mathrm{syst}}(\boldsymbol{f}) \tag{6.3.1}$$

where N_i^{obs} and N_i^{pred} are the number of the observed and predicted events in the p-$\cos\theta$ bin i respectively, and $\boldsymbol{f}$ represents the systematic parameters. The systematic parameters comprise the ND flux parameters, the cross-section parameters and the ND systematic parameters. The center values and the uncertainties of the flux parameters at the far detector and some of the cross-section parameters are varied after the fit due to the correlations to the ND-related parameters. The neutrino energy bins (GeV) used in the flux parameters are:

- ν-mode ν_μ and $\overline{\nu}$-mode $\overline{\nu}_\mu$: 0.0, 0.4, 0.5, 0.6, 0.7, 1.0, 1.5, 2.5, 3.5, 5.0, 7.0, 30.0
- ν-mode $\overline{\nu}_\mu$ and $\overline{\nu}$-mode ν_μ: 0.0, 0.7, 1.0, 1.5, 2.5, 30.0
- ν-mode ν_e and $\overline{\nu}$-mode $\overline{\nu}_e$: 0.0, 0.5, 0.7, 0.8, 1.5, 2.5, 4.0, 30.0
- ν-mode $\overline{\nu}_e$ and $\overline{\nu}$-mode ν_e: 0.0, 2.5, 30.0

The same flux binning is used in the near detector and the far detector analyses. For the other systematic sources, detector systematic uncertainties and the uncertainties from the pion secondary interactions (SI) are considered. The detector systematic uncertainties comprise magnetic field, momentum resolution, momentum scale, particle identification, time of flight, charge identification efficiencies, track efficiencies, TPC-FGD track matching efficiency, Michel electron detection efficiency, background events coming from out of fiducial volumes (OOFV), event pile up and FGD absolute mass are considered and the

[2] 3000 MeV/c momentum bin does not exist for the CC1π^+ subsample.

total uncertainty is typically 1-2% level [53]. Pion secondary interactions are modeled in Geant4 [177], which is used for the MC simulations in the near detector. This uncertainty is calculated by taking into account the discrepancy between the model implemented in Geant4 and the external pion scattering data. This uncertainty is the dominant systematic source for all the subsamples. Tables 6.4 and 6.5 summarize the detector and SI systematic uncertainties of the ν-mode subsamples and the $\overline{\nu}$-mode subsamples, respectively.

Table 6.4: Summary of the systematic uncertainties of the near detector analysis of the ν-mode subsamples.

systematic error source	CC inclusive	CC0π	CC1π^+	CCother
field distortions	0.04%	0.02%	0.06%	0.07%
momentum resolution	0.08%	0.05%	0.09%	0.29%
momentum scale	0.09%	0.06%	0.07%	0.23%
TPC PID	0.34%	0.32%	0.79%	0.62%
FGD PID	0.00%	0.01%	0.03%	0.01%
time of flight	0.04%	0.03%	0.07%	0.02%
charge ID efficiency	0.13%	0.18%	0.27%	0.47%
TPC track efficiency	0.42%	0.26%	0.44%	1.79%
FGD track efficiency	0.04%	0.11%	0.10%	0.53%
TPC-FGD matching efficiency	0.23%	0.15%	0.27%	0.60%
Michel electron	0.00%	0.06%	0.25%	0.01%
OOFV background	0.40%	0.39%	0.54%	0.29%
pile up	0.11%	0.11%	0.11%	0.11%
FGD mass	0.59%	0.59%	0.58%	0.60%
sand muon background	0.07%	0.07%	0.08%	0.03%
secondary pion interactions	2.12%	1.43%	3.17%	6.12%
total	2.29%	1.66%	3.33%	6.47%

Table 6.5: Summary of the systematic uncertainties of the near detector analysis of the $\overline{\nu}$-mode subsamples.

systematic uncertainty source	CC inclusive	CC 1-track	CC N-tracks
	ν_μ		
field distortions	0.03%	0.00%	0.16%
momentum resolution	0.08%	0.05%	0.25%
momentum scale	0.06%	0.04%	0.12%
TPC PID	0.32%	0.31%	0.54%
time of flight	0.01%	0.02%	0.01%
charge ID efficiency	0.08%	0.12%	0.12%
TPC track efficiency	0.57%	0.44%	1.20%
TPC-FGD matching efficiency	0.17%	0.11%	0.39%
OOFV background	0.38%	0.34%	0.61%
pile up	0.24%	0.24%	0.24%
FGD mass	0.59%	0.60%	0.58%
sand muon background	0.17%	0.15%	0.25%
secondary pion interactions	5.68%	4.90%	9.20%
total	6.27%	5.37%	10.38%
	$\overline{\nu}_\mu$		
field distortions	0.04%	0.04%	0.13%
momentum resolution	0.19%	0.10%	0.33%
momentum scale	0.11%	0.10%	0.16%
TPC PID	0.41%	0.42%	0.47%
time of flight	0.02%	0.02%	0.03%
charge ID efficiency	0.12%	0.07%	0.19%
TPC track efficiency	0.68%	0.30%	1.22%
TPC-FGD matching efficiency	0.22%	0.08%	0.37%
OOFV background	0.81%	1.20%	0.50%
pile up	0.31%	0.31%	0.31%
FGD mass	0.57%	0.55%	0.59%
sand muon background	0.30%	0.48%	0.17%
secondary pion interactions	2.98%	1.92%	4.22%
total	3.42%	2.49%	4.76%

6.3.2 Constraints of the neutrino flux and neutrino-nucleus interaction parameters

Figures 6.7, 6.8 and 6.9 show the muon momentum and $\cos\theta$ distributions with predictions before and after the ND fit. The distributions by the MC prediction show better agreement with the data when the post-fit parameters are used. The uncertainties of the predicted distributions get significantly small after the ND fit. Figure 6.10 and table 6.6 (top) show the $\overline{\nu}$-mode SK flux post-fit center values relative to the prefit ones and their uncertainties. Figure 6.11 and table 6.6 (bottom) show the cross-section parameters and their uncertainties before and after the fit. The center values of all the flux parameters are increased because the number of observed CC inclusive events is larger than that of prediction. The center value of the MEC (2p-2h) ^{12}C and ^{16}O normalization parameter is significantly increased because the number of observed events in the CC0π subsample is larger than that of prediction and the pre-fit uncertainty of the MEC parameter is large. The uncertainty of the MEC ^{16}O normalization parameter does not so varied after the ND fit because the conservatively assigned 100% uncertainty to that parameter is uncorrelated to the MEC ^{12}C normalization parameter. Figure 6.12 shows the pre-fit and post-fit correlation matrices. After the ND fit, the flux parameters and some of the cross-section parameters have anticorrelation because the number of the observed events is the product of the neutrino flux and the neutrino-nucleus cross section. This anticorrelation will further decrease uncertainties of the SK prediction compared to the case of no correlation.

To check the validity of this fit, a goodness-of-fit test is performed. The $\Delta\chi^2 = -2\ln\mathcal{L}$ at the best-fit point (The likelihood is defined in eq. 6.3.1) is calculated for the data and a large number of toy experiments. The p-value is then calculated as the fraction for which $\Delta\chi^2$ for the toy experiment is larger than that for data. Figure 6.13 shows the χ^2 distribution of the goodness-of-fit test. The obtained p-value is 0.05025 which we consider barely acceptable.

Table 6.6: Summary of the flux and cross-section parameters before and after the ND fit. The flux parameters in the antineutrino mode and the cross-section parameters which are used for oscillation analysis are described.

Parameter number	Parameter category	Pre-fit value	Post-fit value
0	ν_μ 0.0-0.7 GeV	1.0±0.09	1.14±0.07
1	ν_μ 0.7-1.0 GeV	1.0±0.08	1.09±0.05
2	ν_μ 1.0-1.5 GeV	1.0±0.08	1.08±0.05
3	ν_μ 1.5-2.5 GeV	1.0±0.08	1.07±0.06
4	ν_μ 2.5-30.0 GeV	1.0±0.08	1.05±0.05
5	$\overline{\nu}_\mu$ 0.0-0.4 GeV	1.0±0.10	1.20±0.07
6	$\overline{\nu}_\mu$ 0.4-0.5 GeV	1.0±0.10	1.21±0.06
7	$\overline{\nu}_\mu$ 0.5-0.6 GeV	1.0±0.10	1.18±0.05
8	$\overline{\nu}_\mu$ 0.6-0.7 GeV	1.0±0.08	1.13±0.04
9	$\overline{\nu}_\mu$ 0.7-1.0 GeV	1.0±0.13	1.12±0.08
10	$\overline{\nu}_\mu$ 1.0-1.5 GeV	1.0±0.11	1.12±0.07
11	$\overline{\nu}_\mu$ 1.5-2.5 GeV	1.0±0.08	1.12±0.05
12	$\overline{\nu}_\mu$ 2.5-3.5 GeV	1.0±0.07	1.12±0.05
13	$\overline{\nu}_\mu$ 3.5-5.0 GeV	1.0±0.09	1.12±0.06
14	$\overline{\nu}_\mu$ 5.0-7.0 GeV	1.0±0.09	1.11±0.06
15	$\overline{\nu}_\mu$ 7.0-30.0 GeV	1.0±0.13	1.11±0.11
16	ν_e 0.0-2.5 GeV	1.0±0.07	1.11±0.05
17	ν_e 2.5-30.0 GeV	1.0±0.08	1.09±0.07
18	$\overline{\nu}_e$ 0.0-0.5 GeV	1.0±0.09	1.19±0.05
19	$\overline{\nu}_e$ 0.5-0.7 GeV	1.0±0.09	1.18±0.05
20	$\overline{\nu}_e$ 0.7-0.8 GeV	1.0±0.09	1.17±0.05
21	$\overline{\nu}_e$ 0.8-1.5 GeV	1.0±0.08	1.14±0.04
22	$\overline{\nu}_e$ 1.5-2.5 GeV	1.0±0.08	1.12±0.05
23	$\overline{\nu}_e$ 2.5-4.0 GeV	1.0±0.09	1.12±0.07
24	$\overline{\nu}_e$ 4.0-30.0 GeV	1.0±0.16	1.18±0.14
25	M_A^{QE} (GeV)	1.15±0.07	1.14±0.03
26	p_F ^{16}O (MeV)	225±13	224±12
27	E_b ^{16}O (MeV)	27±9	27±9
28	MEC ^{16}O (%)	27±104	103±101
29	$C_5^A(0)$	1.01±0.12	0.86±0.07
30	M_A^{RES} (GeV)	0.95±0.15	0.72±0.05
31	BG^{RES}	1.30±0.20	1.49±0.19
32	CCother	0.0±0.40	0.02±0.19
33	CCcoherent ^{16}O	1.0±1.0	1.08±0.97
34	NCcoherent	1.0±0.30	0.98±0.30
35	NCother	1.0±0.30	1.41±0.19
36	$\sigma_{\nu_e}/\sigma_{\nu_\mu}$	1.0±0.03	1.0±0.03

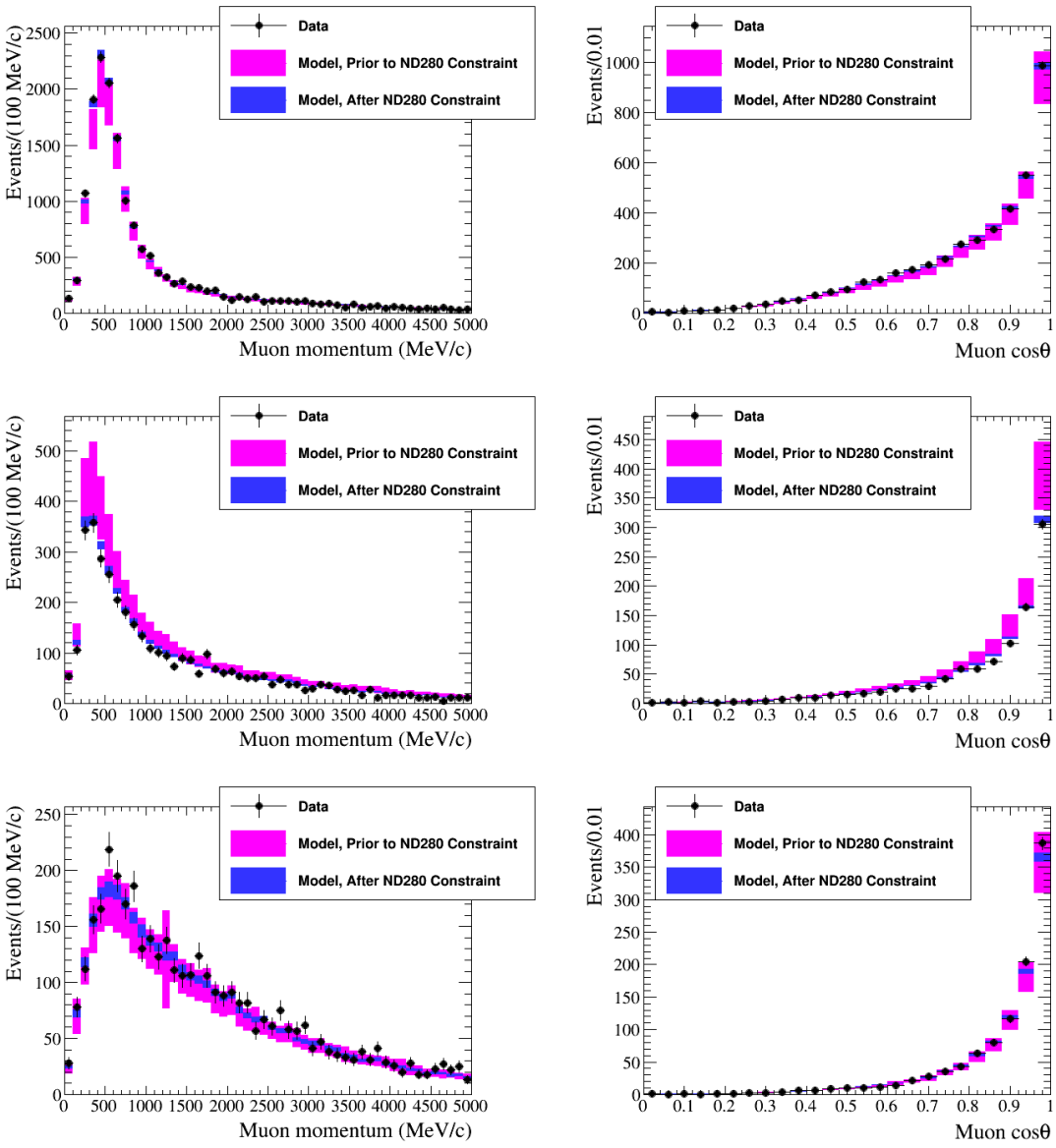

Figure 6.7: Muon momentum (left) and cos θ (right) distributions of the CC events in the neutrino mode. top: CC0π subsample, middle: CC1π^+ subsample, bottom: CCother subsample. The error bands represent the prediction uncertainties before and after the ND fit.

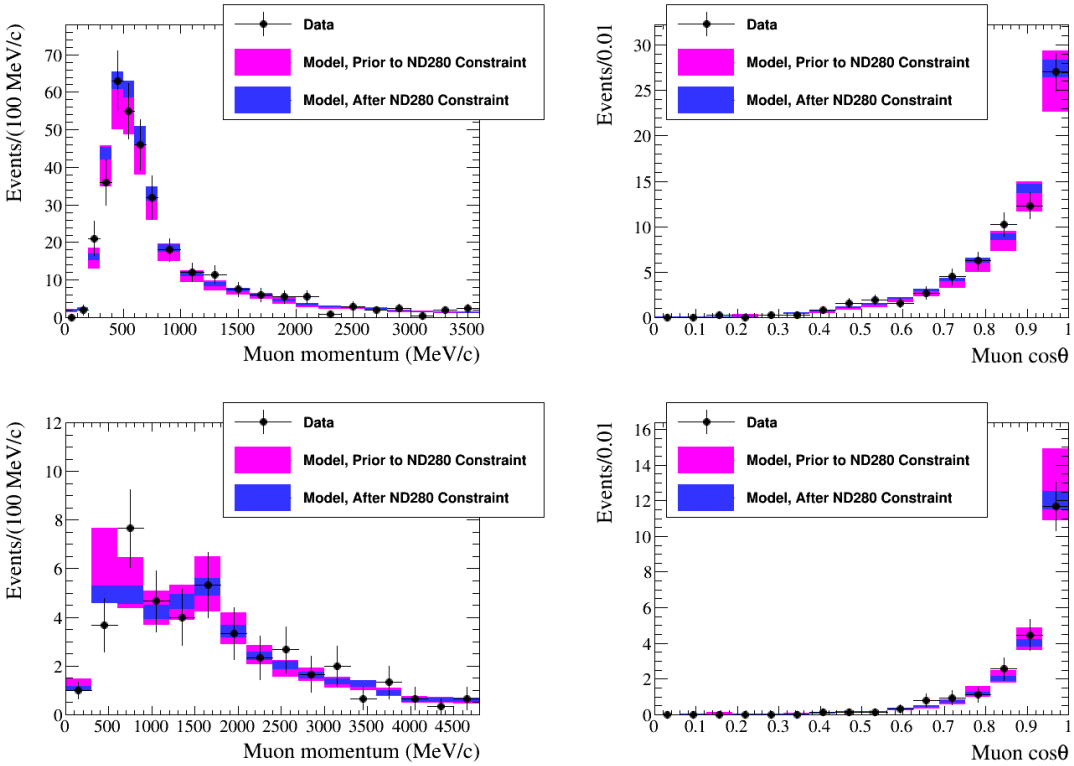

Figure 6.8: Muon momentum (left) and $\cos\theta$ (right) distributions of the $\overline{\nu}_\mu$ CC events in the antineutrino mode. top: $\overline{\nu}_\mu$ CC 1-track subsample, bottom: $\overline{\nu}_\mu$ CC N-tracks subsample. The error bands represent the prediction uncertainties before and after the ND fit.

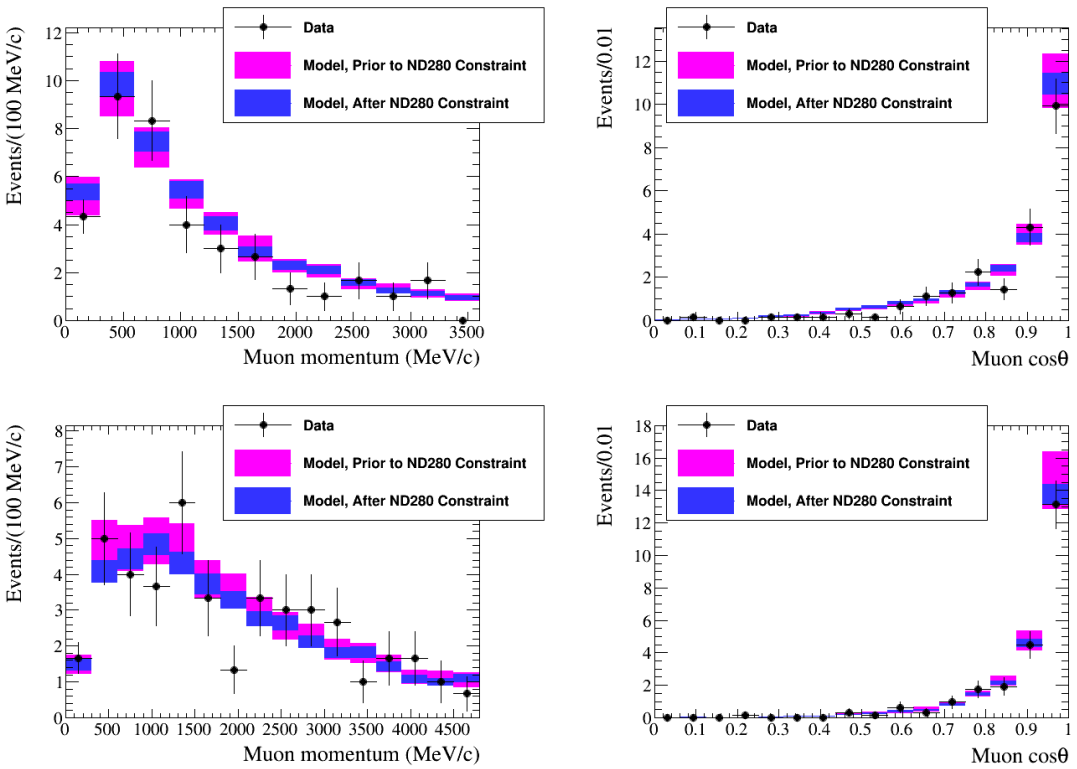

Figure 6.9: Muon momentum (left) and cos θ (right) distributions of the ν_μ CC events in the antineutrino mode. top: ν_μ CC 1-track subsample, bottom: ν_μ CC N-tracks subsample. The error bands represent the prediction uncertainties before and after the ND fit.

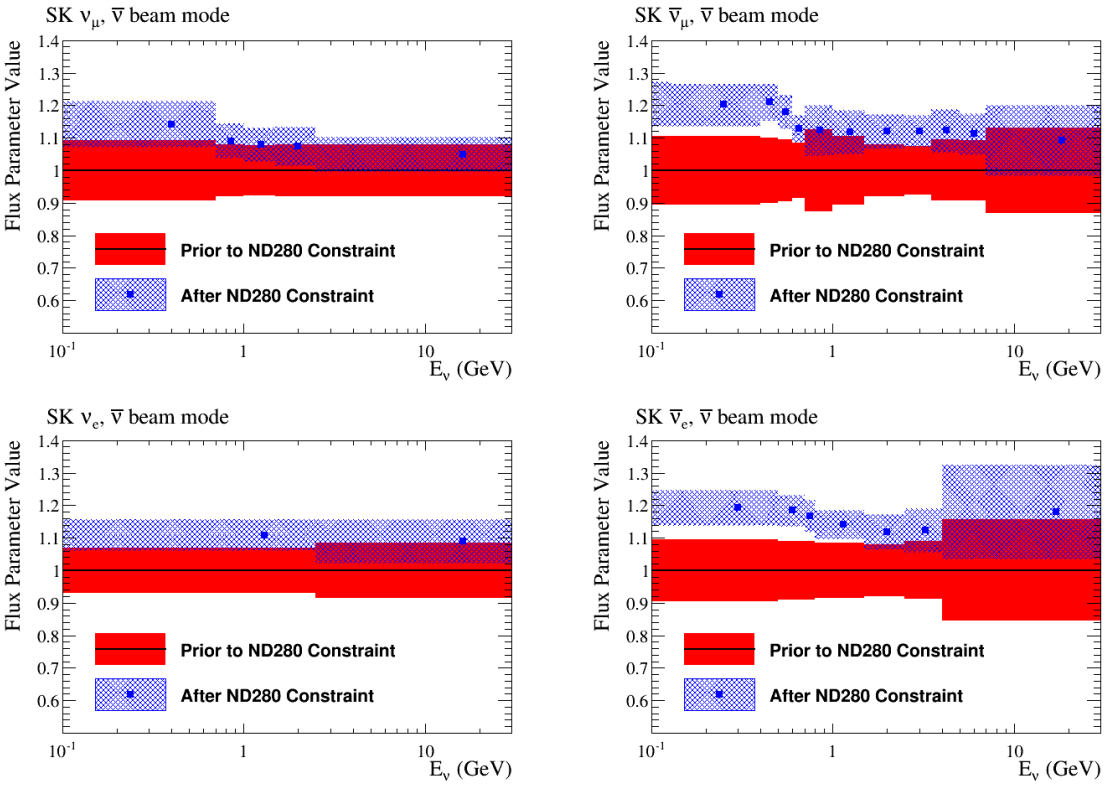

Figure 6.10: Pre-fit and post-fit center values and uncertainties of the flux parameters.

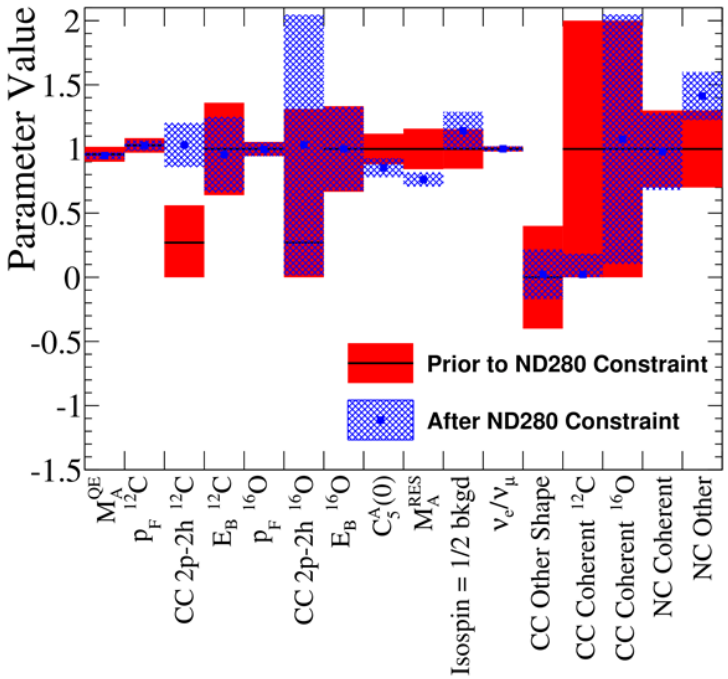

Figure 6.11: Pre-fit and post-fit center values and uncertainties of the cross-section parameters.

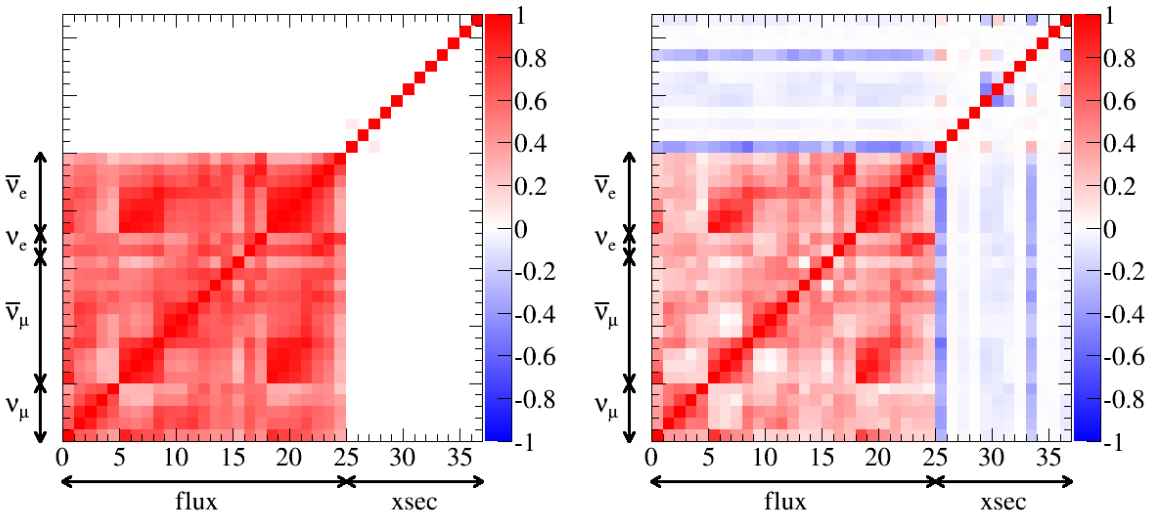

Figure 6.12: Pre-fit (left) and post-fit (right) correlation matrices of the flux and cross-section parameters. The ordering of the parameters is described in table 6.6.

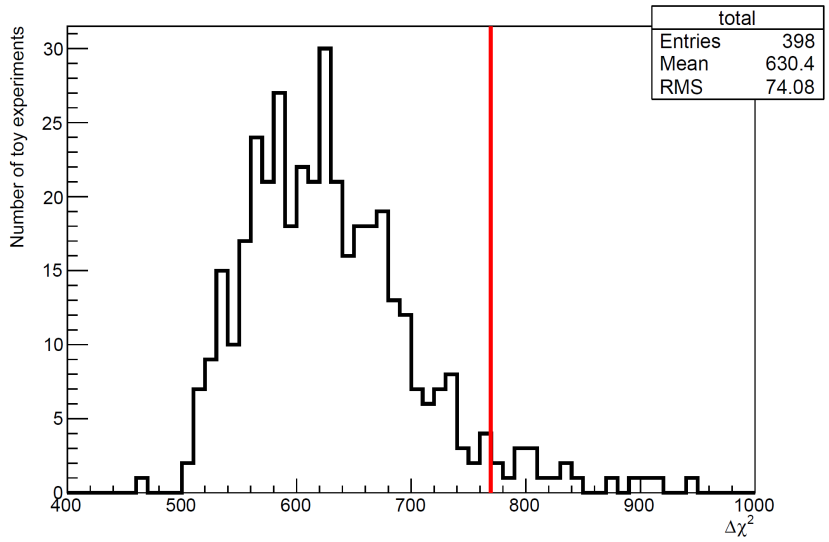

Figure 6.13: χ^2 distribution of the goodness-of-fit tests for the toy experiments. The red line represents the χ^2 for the data fit.

6.4 Measurements at the Super-Kamiokande detector

6.4.1 Event selection

The event selection at the far detector, Super-Kamiokande (SK), is optimized to a CCQE-enriched $\overline{\nu}_\mu$ sample for the oscillation analysis. First, the "fully-contained fiducial-volume" (FCFV) events are selected. Then, main selections are applied to the FCFV events so that the ν_μ and $\overline{\nu}_\mu$ CCQE events are extracted.

FCFV selection

The events coming from outside the detector are rejected by requiring that almost all the energy deposits inside the inner detector (ID). If the number of neighboring hit PMTs in the outer detector (OD) exceeds 15, that event is rejected. Low energy (LE) events, which mainly come from the decays of radioactive substances, are removed by requiring the total charge in the ID PMTs to be greater than 200 photoelectrons.

To identify whether a neutrino event comes from J-PARC, the timing information by the GPS time synchronization system is used. In the timing selection, ΔT_0 is defined as the difference of the observed time and the expected arrival time of the leading edge of each spill. On-timing events where ΔT_0 is from -2 μs to 10 μs are selected. Due to this timing selection, the expected number of the selected atmospheric neutrinos events is much smaller than that from the T2K-beam events. Figure 6.14 shows the timing distributions of the LE, OD and FC during the T2K RUN 1-6. A clear peak is observed around ΔT_0=0 μs.

Events which passed these selections are called fully-contained (FC) events. In the FC events, if reconstructed vertex is inside the fiducial volume (FV), which is 2 m away from the ID wall, and the visible energy (E_{vis}) is larger than 30 MeV, they are called FCFV events. E_{vis} is calculated from total amount of Cherenkov light.

In the past analyses [69], flasher events, where light emitted by internal discharges of PMTs is observed, were rejected based on their PMT hit timing distribution. These flasher events were investigated before this oscillation analysis. The flasher event selection has been used for the atmospheric neutrino analyses and the same cut was applied to the T2K beam sample. During the T2K RUN 1-4, 18 events in the T2K beam sample were rejected by the flasher cut. However, the expected number of the flasher events estimated by using the atmospheric neutrino sample is very small (less than 10^{-4} events) due to the timing selection. It was found that the flasher events appeared to be beam-induced based on the eye-scanning of the data and the timing information of flasher events. Consequently, this selection is not applied in this analysis because the contamination of flasher events into the beam sample is expected to be very small.

ν_μ+$\overline{\nu}_\mu$ CCQE event selection

As discussed in Section 2.6, each $\overline{\nu}_\mu$ CCQE event has only a single muon-like ring. Thus, events which have a single muon-like ring are selected. Then, events with the muon momentum greater than 200 MeV/c are selected to ensure the PID performance. Finally, events whose number of the decay electrons ≤ 1 are selected in order to reject events where charged pions are not reconstructed. The selection criteria are the same as those of past ν_μ disappearance analyses.

Figure 6.15 shows distributions of event selection variables in the data and the MC prediction at each selection stage. The neutrino oscillation parameters and the earth matter density used in the MC prediction are shown in table 6.7. In this prediction, the maximum disappearance of the ν_μ and $\overline{\nu}_\mu$ events is assumed. The number of the events which passed all the selections in the data is 34. Table 6.8 shows

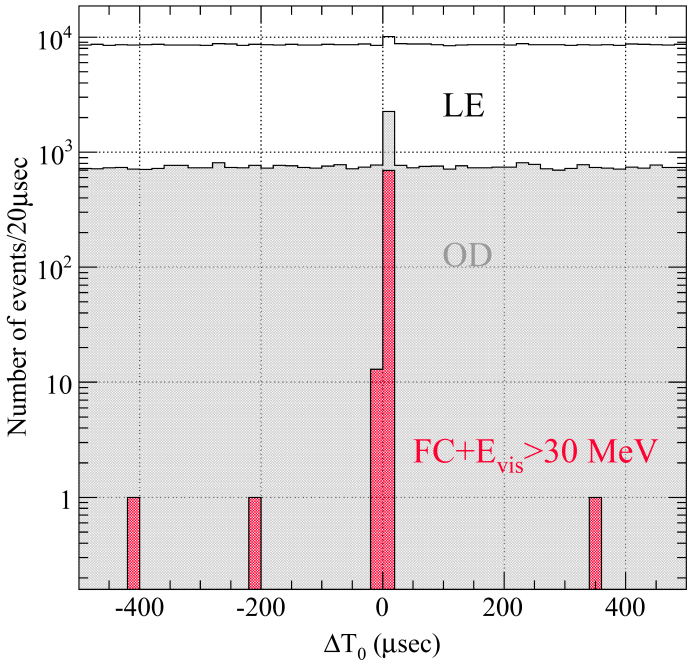

Figure 6.14: ΔT_0 distributions of the LE, OD and FC with E_{vis} >30 MeV events during T2K RUN 1-6.

the number of events for the observed data and the MC prediction at each selection stage. The selection efficiency of the $\overline{\nu}_\mu$ CCQE and ν_μ CCQE events from the FCFV selection is 95% and 87%, while that of the ν_e+$\overline{\nu}_e$ CC events and the NC events are 0.7% and 7.8%, respectively. NC events which pass these selections mainly come from those where single charged pion or single proton is ejected. The distributions of the event selection variables of the ν_μ CCQE events are similar to those of the $\overline{\nu}_\mu$ CCQE events except for following points:

- Momenta of ν_μ CCQE events are higher than those of $\overline{\nu}_\mu$ CCQE events because the fraction of the wrong-sign component of the flux is higher in high energy region.
- The ratio of $N_{\mathrm{decay}-e} = 1$ to $N_{\mathrm{decay}-e} = 0$ for the $\overline{\nu}_\mu$ CCQE sample is larger than that of the ν_μ CCQE sample due to the μ^- capture to the oxygen nuclei.

Figure 6.16 shows two dimensional vertex distribution of the $\overline{\nu}_\mu$ candidate events. The distribution of the $\overline{\nu}_\mu$ candidate events is homogeneous.

Table 6.7: The neutrino oscillation parameters and the earth matter density used in the MC prediction.

parameter	Value
Δm^2_{21}	7.6×10^{-5} eV^2
Δm^2_{32}	2.4×10^{-3} eV^2
$\sin^2\theta_{23}$	0.5 (maximal mixing)
$\sin^2 2\theta_{12}$	0.8495
$\sin^2 2\theta_{13}$	0.1
δ_{CP}	0
earth matter density	2.6 g/cm^3
mass hierarchy	normal
baseline length	295 km

Table 6.8: Numbers of events for the observed data and the MC prediction at each selection stage. Selection efficiency of each sample is listed in the bottom.

	data	prediction					
		MC total	$\overline{\nu}_\mu$ CCQE	ν_μ CCQE	$\overline{\nu}_\mu$+ν_μ CC nonQE	$\overline{\nu}_e$+ν_e CC	NC
FV interaction	-	186.66	17.79	11.35	56.51	9.45	91.55
FCFV	90	99.70	14.36	8.58	41.67	9.21	25.88
single ring	50	52.24	13.97	7.66	16.79	6.81	7.01
μ-like	40	39.39	13.78	7.59	15.84	0.06	2.12
$P_\mu > 200$ MeV	40	39.33	13.76	7.58	15.83	0.06	2.10
$N_{\text{decay}-e} < 2$	34	36.14	13.71	7.46	12.90	0.06	2.01
efficiency from FV interaction[%]			77.1	65.7	22.8	0.6	2.2
efficiency from FCFV[%]			95.5	87.0	31.0	0.7	7.8

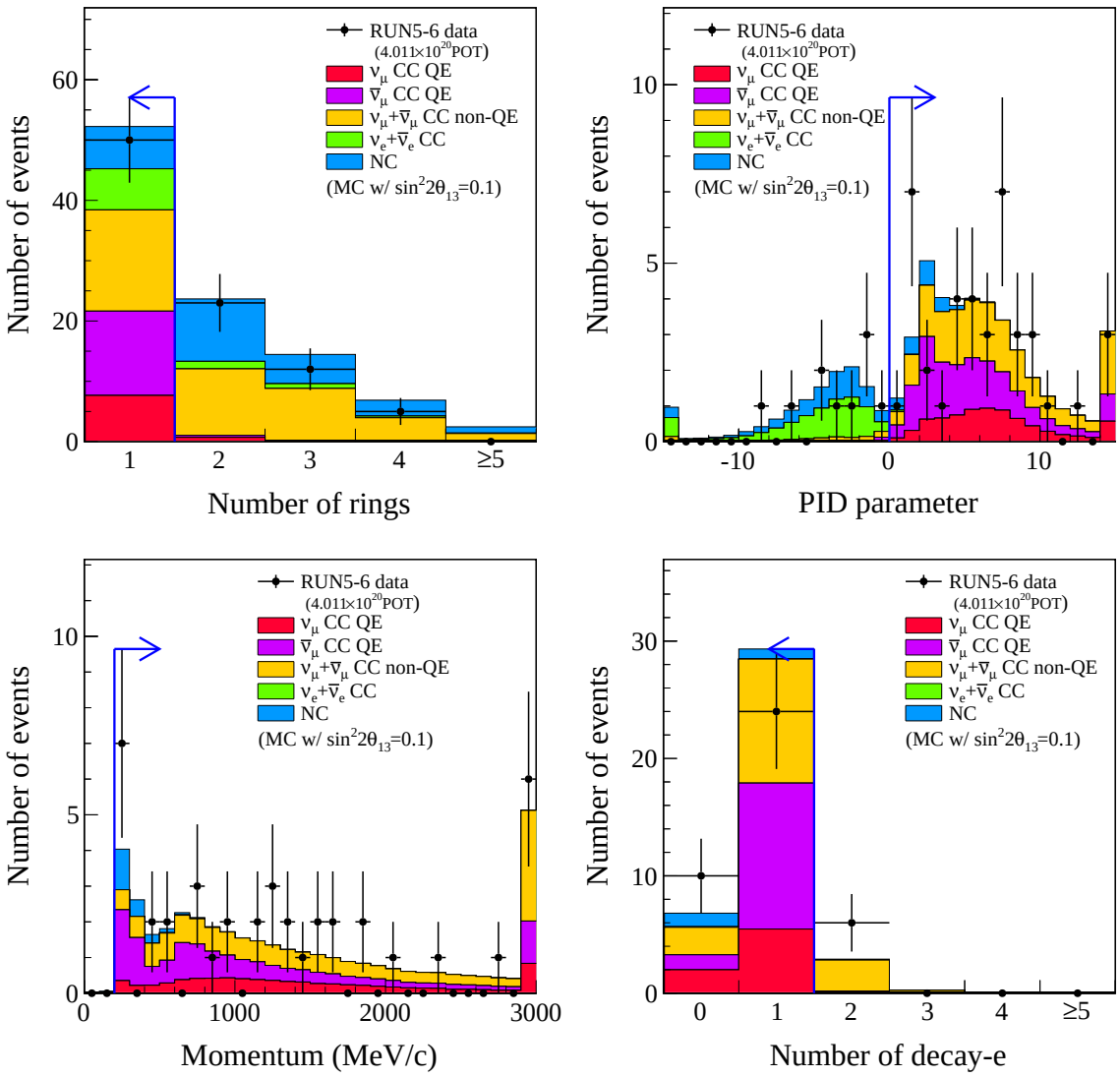

Figure 6.15: Distributions of the event selection variables at each selection stage. Top left: the number of rings, Top right: PID parameter, Bottom left: reconstructed muon momentum and Bottom right: the number of the decay electrons.

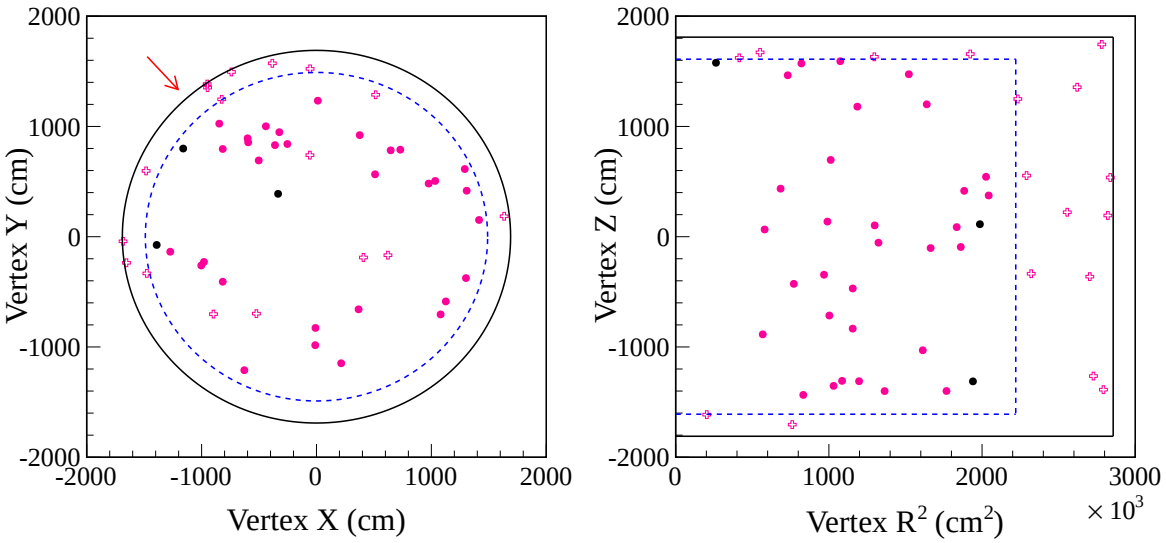

Figure 6.16: Two dimensional vertex distribution of the $\overline{\nu}_\mu$ candidate events. Left figure shows the vertex distribution projected onto the $X-Y$ plane and the red arrow represents the neutrino beam direction. Right figure shows the vertex distribution projected onto the R^2-Z plane (R is the distance from the central vertical axis of the SK tank). Dashed blue lines represents the fiducial volume boundary. Black markers are events observed during the T2K Run 5 and pink markers are events during the T2K RUN 6. Hollow crosses represent events passing all the selection cuts other than the fiducial cut.

6.4.2 Systematic uncertainties

The systematic uncertainty sources for SK comprise the detector efficiency, the final state interaction and the secondary interaction of pion (FSI-SI), and the energy scale uncertainty. We use these sources as the uncertainty of the oscillation analysis. Both the detector efficiency uncertainties and the FSI-SI uncertainty are evaluated for each of six samples below:

- $\nu_\mu, \bar{\nu}_\mu$ CCQE sample which is divided into three reconstructed neutrino energy regions: 0.0-0.4 GeV, 0.4-1.1 GeV and 1.1-30.0 GeV.
- $\nu_\mu, \bar{\nu}_\mu$ CCnonQE sample
- $\nu_e, \bar{\nu}_e$ CC sample
- NC sample

Systematic sources for the SK detector uncertainty and the control samples used for the estimation of each systematic source is listed in table 6.9. Fiducial volume cut uncertainty is estimated from the difference of vertex distributions between the MC simulations and the data for the cosmic-ray muon events and 1% uncertainties to the all samples are assigned.

Ring counting uncertainty is estimated by using 1632 days of the atmospheric neutrino data observed in SK. The atmospheric neutrino data are divided into subsamples by observable parameters such as the number of ring, the PID parameter and the visible energies. The number of ring is determined by the ring counting likelihood. The ring counting likelihood distributions for the atmospheric neutrino MC prediction are fitted to the data for each subsample by variating the ring counting efficiency. Atmospheric neutrino flux and cross section parameters are considered as the systematic uncertainties of the fit of ring counting. Uncertainties from the result of the fit and the difference of best-fit parameter and nominal parameter are added in quadrature. Estimated uncertainties are roughly 1% for the ν_μ CCQE samples, 4% for the ν_μ CCnonQE sample, and 22% for the NC sample.

PID uncertainty for the ν_μ+$\bar{\nu}_\mu$ CC samples are estimated by the difference of PID probability between data and MC for cosmic-ray muons and 0.3% is assigned. To estimate the PID uncertainty for the NC sample, an enriched sample of the NC background events is produced from the atmospheric neutrinos. Then, that NC enriched sample is compared to the MC simulation with varying the PID efficiencies. Consequently, 55% uncertainty is assigned to the NC sample and this uncertainty is the largest source of the whole SK uncertainty in this oscillation analysis which is described in the next Chapter. For the PID and ring counting uncertainty for the $\nu_e, \bar{\nu}_e$ CC sample, a conservative 100% uncertainty in total is assigned.

The decay electron cut uncertainty is estimated by comparing the tagging efficiencies of the decay electrons between the MC simulations and the data for cosmic-ray muons and 1% uncertainties to all the samples are assigned.

The uncertainties on the SK measurement from the FSI and SI are estimated in a same procedure, i.e., by varying the pion-nucleus interaction cross sections in NEUT. The pion-nucleus cross sections are parametrized by six scale factors as shown in table 6.10. First, nominal values and uncertainties of each scale parameter are estimated by comparison to external pion-nucleus scattering data [180]. Then, uncertainties to the SK samples are estimated by varying the parameters by the size of uncertainties (table 6.10). The obtained uncertainties on the SK measurement from the FSI and SI are shown in table 6.11. For the CCQE events, where pions are not produced, the uncertainty is negligibly small. For the CCnonQE events, the FSI-SI uncertainty is the dominant source in the SK uncertainties. In future, the FSI-SI uncertainties are expected to be reduced by incorporating recent pion scattering data [181] into their evaluation.

Table 6.9: Systematic sources of the SK detector uncertainty and the control samples used for the estimation of each systematic source.

systematic uncertainty source	control sample
fiducial volume cut	cosmic-ray muons
ring counting	atmospheric neutrinos
PID (CC)	cosmic-ray muons
PID (NC)	atmospheric neutrinos (NC)
decay electron cut	cosmic-ray muons

Table 6.10: Scale parameters for pion-nucleus cross sections. Nominal values and uncertainty ranges of these parameters are also shown.

parameter (momentum region)	nominal value	minimum value	maximum value
pion absorption interaction (< 500 MeV/c)	1.0	0.6	1.6
quasi-elastic interaction (< 500 MeV/c)	1.8	1.1	2.3
charge exchange interaction (< 500 MeV/c)	1.0	0.5	1.5
quasi-elastic interaction (> 500 MeV/c)	1.1	0.6	1.6
charge exchange interaction (> 500 MeV/c)	1.0	0.4	1.6
inelastc interaction (> 500 MeV/c)	1.8	1.3	2.3

Table 6.11: Systematic uncertainties in the measurement at SK.

parameter number	parameter category	detector uncertainty	FSI-SI uncertainty
0	$\nu_\mu, \bar{\nu}_\mu$ CCQE 0.0-0.4 GeV	1.8%	<0.1%
1	$\nu_\mu, \bar{\nu}_\mu$ CCQE 0.4-1.1 GeV	1.6%	<0.1%
2	$\nu_\mu, \bar{\nu}_\mu$ CCQE 1.1-30.0 GeV	1.6%	0.1%
3	$\nu_\mu, \bar{\nu}_\mu$ CCnonQE	4.3%	8.2%
4	$\nu_e, \bar{\nu}_e$ CC	100.2%	2.2%
5	NC	59.2%	7.3%

Figure 6.17 shows the correlation matrices of the systematic uncertainties from the SK detector (left) and the FSI-SI (right) parameters. The uncertainty covariance from the detector efficiency and the FSI-SI parameters are combined in quadrature in the oscillation analysis.

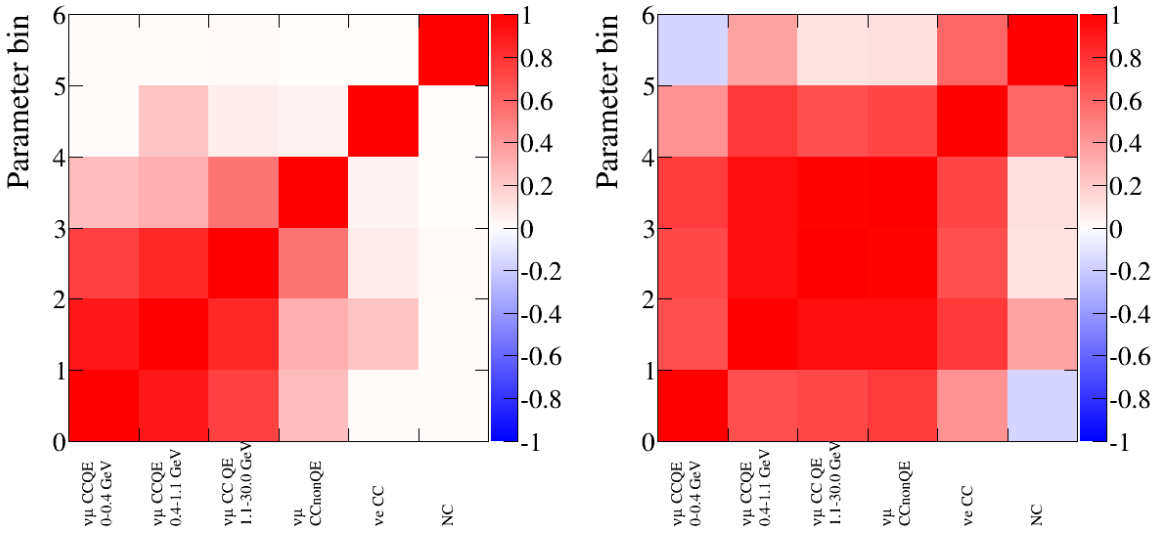

Figure 6.17: Correlation matrices of the systematic uncertainties from the detector efficiency (left) and the FSI-SI (right) parameters.

The energy scale is calibrated by considering decay electrons, π^0 invariant mass from the atmospheric neutrino interactions, and the cosmic-ray muons which stop inside the ID so that wide energy range can be covered. The energy scale uncertainty is estimated by taking into account the difference of the data and the MC prediction. The largest difference is seen in the cosmic-ray muon samples, and that value, 2.4%, is assigned for the energy scale uncertainty. In the oscillation analysis, the reconstructed energy distribution is binned to a histogram. We approximate that events are uniformly distributed in each bin when calculating the event migration to the neighboring bin by the energy scale change as illustrated in fig. 6.18. The reconstructed neutrino energy histogram is recalculated when energy scale is varied in the oscillation fit.

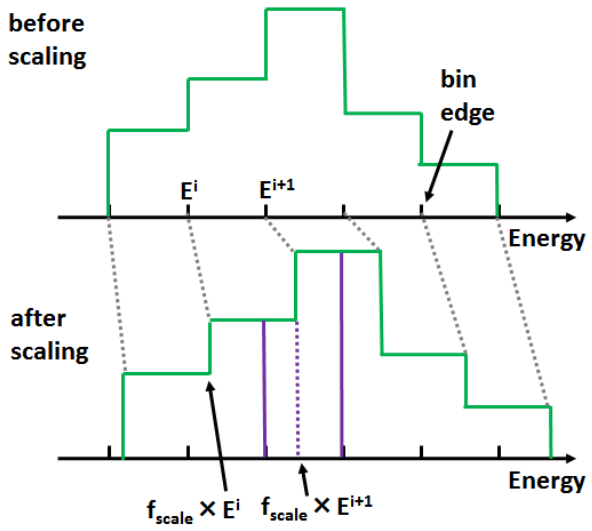

Figure 6.18: Illustration of the implementation of the SK energy-scale uncertainty.

Chapter 7

Measurement of the muon antineutrino disappearance

We performed a first $\overline{\nu}_\mu$ disappearance analysis in the T2K experiment with the dataset corresponding to 4.011×10^{20} POT for the antineutrino mode [71]. We fit the $\sin^2\overline{\theta}_{23}$ and $\Delta\overline{m}^2_{32}$ using the reconstructed neutrino energy spectrum of 1-ring muon-like events observed at the far detector. Confidence regions of the $\sin^2\overline{\theta}_{23}$ and $|\Delta\overline{m}^2_{32}|$ are shown by using the constant $\Delta\chi^2$ method.

7.1 Analysis overview

In this section, we introduce basic information in this oscillation analysis, i.e., oscillation parameters, neutrino flavors, and categories of the neutrino-nucleus interaction types. Then, we describe how we predict the expected number of events and the reconstructed neutrino energy spectrum as a function of relevant oscillation parameters.

7.1.1 Oscillation parameters and oscillation probabilities

As we described in Section 1.5.3, the ν_μ ($\overline{\nu}_\mu$) disappearance analysis is sensitive to θ_{23} and $|\Delta m^2_{32}|$. In this analysis we treat (θ_{23}, Δm^2_{32}) for neutrinos and ($\overline{\theta}_{23}$, $\Delta\overline{m}^2_{32}$) for antineutrinos as independent parameters, where the barred parameters refer to the antineutrino oscillations. For the other oscillation parameters, identical values are used for neutrinos and antineutrinos. The CPT symmetry ensures the disappearance probability for neutrinos and antineutrinos in vacuum is identical. In T2K, the size of matter effect to the survival probability is as small as $O(0.1)\%$ and this cannot be measured. Therefore, if the difference of the survival probabilities with neutrino and antineutrino was observed, it could be said that we discovered a new physics. Table 7.1 summarizes the neutrino oscillation parameters and the earth matter density used in the calculation of the oscillation probabilities. Values of the θ_{13}, θ_{12} and Δm^2_{21} are taken from the Particle Data Group 2014 [19]. Values of the θ_{23} and Δm^2_{32} are taken from ν_μ+ν_e joint fit results from the T2K in the neutrino mode [69] for the comparison between neutrinos and antineutrinos. For the main result, we adopt the normal mass hierarchy because this is slightly favored in the ν_μ+ν_e joint fit result from T2K in the neutrino mode [69]. The dependence of the result on the mass hierarchy is marginal.

Table 7.1: Neutrino oscillation parameters and the earth matter density used in the calculation of the oscillation probabilities.

parameter	value
Δm^2_{21}	7.53×10^{-5} eV^2
Δm^2_{32}	2.51×10^{-3} eV^2
$\sin^2\theta_{23}$	0.527
$\sin^2 2\theta_{12}$	0.846
$\sin^2 2\theta_{13}$	0.0967
δ_{CP} (rad)	-1.55
Earth matter density	2.6 g/cm^3
Mass hierarchy	normal
Baseline length	295 km

We compute the oscillation probabilities in the three-flavor neutrino oscillation scheme. A slightly modified version[1] of the Prob3++ software [182] is used for the computation of the oscillation probabilities [183]. If we assume the PMNS framework, the disappearance probabilities $P(\nu_\mu \to \nu_\mu)$ and $P(\overline{\nu}_\mu \to \overline{\nu}_\mu)$ are almost the same. The difference comes from the matter effect, but the size of the difference of the disappearance probabilities is roughly 0.1% level and this effect is too small to be observed. The matter effect is taken into account in the computation of the oscillation probabilities with a constant Earth density of 2.6 g/cm^3 [184].

7.1.2 Neutrino flavors considered in this analysis

There exists in total 18 types of neutrino oscillations, i.e., $|\nu_\alpha\rangle \to |\nu_\beta\rangle$ and $|\overline{\nu}_\alpha\rangle \to |\overline{\nu}_\beta\rangle$ ($\alpha,\beta = e,\ \mu,\ \tau$). Among them, contributions from six types of neutrino oscillations are considered in this analysis in order to make the oscillation fit faster: $\nu_\mu \to \nu_\mu$, $\overline{\nu}_\mu \to \overline{\nu}_\mu$, $\nu_e \to \nu_e$, $\overline{\nu}_e \to \overline{\nu}_e$, $\nu_\mu \to \nu_e$, and $\overline{\nu}_\mu \to \overline{\nu}_e$. The contribution of the ν_τ and $\overline{\nu}_\tau$ flux and the $\nu_e \to \nu_\mu$, $\overline{\nu}_e \to \overline{\nu}_\mu$ probabilities are negligibly small. For ν_τ ($\overline{\nu}_\tau$) coming from the oscillations, only the neutral current interactions are considered because the charged current interactions of ν_τ and $\overline{\nu}_\tau$ rarely happen given the energies of neutrinos in the T2K beam.

The NC cross section of the neutrino interactions does not depend on the neutrino flavor. Hence, we do not consider the neutrino oscillation effect to the NC events.

7.1.3 Categories of the neutrino-nucleus interaction types

We break up the selected samples into seven different categories by the types of neutrino-nucleus interactions in order to take into account the effect of systematic sources from the neutrino-nucleus interaction: charged-current quasi-elastic interaction (CCQE), charged-current multi-nucleon interaction (MEC), charged-current interaction associated with single-pion resonant production (CC1π), charged-current coherent pion production (CC coherent), other charged-current processes (CC other), neutral current interaction with single pion production (NC1π), and other neutral current interactions (NC other).

7.1.4 Prediction of the reconstructed neutrino energy spectrum of 1-ring μ-like events

The nominal reconstructed neutrino energy spectrum of the 1-ring muon-like events $N(E_{\rm rec})$ is calculated as:

[1] A speed-up of the calculation is implemented.

$$N(E_{\mathrm{rec}}) = \sum_{\mathrm{I},\alpha} \int dE_\nu dE_{\mathrm{rec}}\ \Phi(E_\nu, \alpha) \cdot P_{\mathrm{osc}}(\mathrm{C}, \mathrm{I}, E_\nu) \cdot \sigma_{\mathrm{H_2O}}(E_\nu, \mathrm{I}, \alpha) \cdot N_t \cdot \varepsilon(E_\nu, \mathrm{I}, \alpha) \cdot R(E_\nu, E_{\mathrm{rec}}, \mathrm{I}, \alpha),$$

where

- I and α are the neutrino interaction type and the neutrino flavor, respectively.
- E_ν and E_{rec} are the true and reconstructed energies of neutrino, respectively.
- $\Phi(E_\nu, \alpha)$ represents the predicted neutrino flux at the far detector.
- $P_{\mathrm{osc}}(\mathrm{I}, \alpha, E_\nu)$ represents the oscillation probability.
- $\sigma_{\mathrm{H_2O}}(E_\nu, \mathrm{I}, \alpha)$ represents the neutrino-nucleus interaction cross section on the target (water).
- N_t is the number of target nuclei.
- $\varepsilon(E_\nu, \mathrm{I}, \alpha)$ represents the detection and selection efficiency at the far detector.
- $R(E_\nu, E_{\mathrm{rec}}, \mathrm{I}, \alpha)$ represents the response function at the far detector, i.e., the probability of observing an event with E_ν as that with E_{rec}. Here the energy resolution of the SK detector is considered.

The systematic sources of the neutrino flux, the neutrino-nucleus interaction and the SK detector-FSI-SI parameters substantially change $\Phi(E_\nu, \alpha)$, $\sigma_{\mathrm{H_2O}}(E_\nu, \mathrm{I}, \alpha)$ and $\varepsilon(E_\nu, \mathrm{I}, \alpha)$, respectively. In the actual analysis, we store the number of selected events for each flavor, interaction type, binned true neutrino energy and binned reconstructed neutrino energy for simulated events. They are reweighted according to the systematic parameters and summed over flavor, interaction types, true neutrino energies to produce the reconstructed energy spectrum.

Reconstructed and true neutrino energy binnings used in this analysis are shown in table 7.2 and 7.3. These binnings are defined so that the shape of energy spectrum around the oscillation maximum is kept fine and the computation time is reduced by making high energy bins coarse.

Table 7.2: Binning used for the reconstructed neutrino energy spectrum.

range	width per one bin	number of bins
0-3 GeV	50 MeV	60
3-4 GeV	250 MeV	4
4-6 GeV	500 MeV	4
6-10 GeV	1 GeV	4
10-30 GeV	20 GeV	1

Table 7.3: Binning used for the true neutrino energy spectrum.

range	width per one bin	number of bins
0-10 GeV	50 MeV	200
10-30 GeV	20 GeV	1

7.1.5 The expected number of events and the reconstructed neutrino energy spectrum for the nominal set of the oscillation parameters

Tables 7.4 and 7.5 show the expected number of events in the unoscillated and oscillated case, respectively. Here in the nominal oscillation parameters, which are shown in table 7.1, identical values for neutrinos and antineutrinos are used. The total expected numbers of events in the unoscillated and oscillated cases are 103.6 and 34.6, respectively. As stated in Chapter 6, the number of observed muon-like events at the far detector is 34. This number is close to the expected number of events in the case of maximal disappearance. Figure 7.1 shows the reconstructed neutrino energy distributions in the unoscillated and oscillated case.

Table 7.4: Expected number of events in each flavor and interaction mode in the case of no neutrino oscillation.

	$\nu_\mu \to \nu_\mu$	$\overline{\nu}_\mu \to \overline{\nu}_\mu$	$\nu_e \to \nu_e$	$\overline{\nu}_e \to \overline{\nu}_e$	$\nu_\mu \to \nu_e$	$\overline{\nu}_\mu \to \overline{\nu}_e$
CCQE	15.412	57.968	0.004	0.005	0.000	0.000
MEC	3.022	9.037	0.001	0.001	0.000	0.000
CC1π	3.666	6.750	0.003	0.002	0.000	0.000
CC coherent	0.245	3.082	0.000	0.001	0.000	0.000
CC other	1.393	1.005	0.001	0.000	0.000	0.000
NC1π	0.391	0.428	0.016	0.012	-	-
NC other	0.707	0.420	0.035	0.017	-	-
subtotal	24.836	78.691	0.060	0.039	0.000	0.000
total			103.625			

Table 7.5: The expected number of events in each flavor and interaction mode with the nominal set of the oscillation parameters. Oscillation parameters listed in table 7.1 are used.

	$\nu_\mu \to \nu_\mu$	$\overline{\nu}_\mu \to \overline{\nu}_\mu$	$\nu_e \to \nu_e$	$\overline{\nu}_e \to \overline{\nu}_e$	$\nu_\mu \to \nu_e$	$\overline{\nu}_\mu \to \overline{\nu}_e$
CCQE	6.870	13.258	0.004	0.005	0.007	0.017
MEC	1.578	2.347	0.001	0.001	0.001	0.003
CC1π	2.414	3.046	0.003	0.002	0.003	0.003
CC coherent	0.167	0.696	0.000	0.000	0.000	0.002
CC other	1.222	0.880	0.001	0.000	0.000	0.000
NC1π	0.391	0.428	0.016	0.012	-	-
NC other	0.707	0.420	0.035	0.017	-	-
subtotal	13.349	21.076	0.059	0.038	0.011	0.025
total			34.559			

7.2 Definitions of the likelihood and fitting method

7.2.1 Definition of the likelihood

The analysis is based on an extended maximum likelihood method [185]. The likelihood $\mathcal{L}$ is defined as:

$$\mathcal{L}(N_{\mathrm{obs}}, \boldsymbol{x}, \boldsymbol{o}, \boldsymbol{f}) = \mathcal{L}_{\mathrm{norm}}(N_{\mathrm{obs}}, \boldsymbol{o}, \boldsymbol{f}) \times \mathcal{L}_{\mathrm{shape}}(N_{\mathrm{obs}}, \boldsymbol{x}, \boldsymbol{o}, \boldsymbol{f}) \times \mathcal{L}_{\mathrm{syst}}(\boldsymbol{f}), \tag{7.2.1}$$

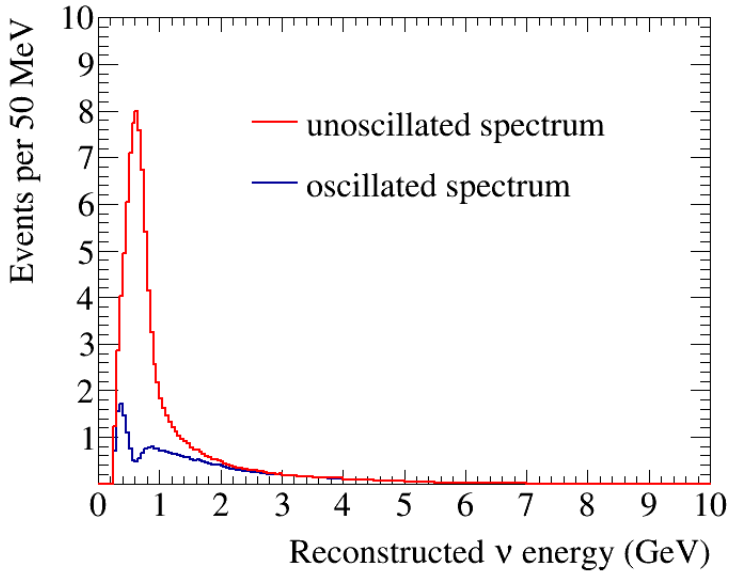

Figure 7.1: Reconstructed neutrino energy distributions in the unoscillated and oscillated case. For the oscillated case, oscillation parameters listed in table 7.1 are used.

where

- N_{obs} is the number of the 1-Ring μ-like events observed in at the far detector.
- $\boldsymbol{x}$ represents the reconstructed neutrino energy of the observed 1-Ring μ-like events. $\boldsymbol{x}$ varies by the energy scale parameter.
- $\boldsymbol{o}$ represents the oscillation parameters we are trying to measure ($\bar{\theta}_{23}$, $|\Delta\overline{m}^2_{32}|$).
- $\boldsymbol{f}$ corresponds to the nuisance parameters describing systematic uncertainties.

$\mathcal{L}_{\mathrm{norm}}$ represents the normalization term of the likelihood. This is given as the probability to observe N_{obs} events for the Poisson distribution with the mean expected number of events $N_{\mathrm{pred}}(\boldsymbol{o}, \boldsymbol{f})$:

$$\mathcal{L}_{\mathrm{norm}}(N_{\mathrm{obs}}, \boldsymbol{o}, \boldsymbol{f}) = P_{\mathrm{Poisson}}(N_{\mathrm{pred}}, N_{\mathrm{obs}}) = \frac{N_{\mathrm{pred}}^{N_{\mathrm{obs}}} \mathrm{e}^{N_{\mathrm{pred}}}}{N_{\mathrm{obs}}!}. \tag{7.2.2}$$

$\mathcal{L}_{\mathrm{shape}}$ represents the shape term of the likelihood, and uses the information coming from the shape of the distribution of the reconstructed neutrino energy:

$$\mathcal{L}_{\mathrm{shape}}(N_{\mathrm{obs}}, \boldsymbol{x}, \boldsymbol{o}, \boldsymbol{f}) = \prod_{i=1}^{N_{\mathrm{obs}}} \rho(\boldsymbol{x}_i, \boldsymbol{o}, \boldsymbol{f}). \tag{7.2.3}$$

where $\rho(\boldsymbol{x}, \boldsymbol{o}, \boldsymbol{f})$ represents the probability density function for the reconstructed neutrino energy of each event.

$\mathcal{L}_{\mathrm{syst}}$ is the systematic term of the likelihood. If the difference of one systematic parameter i from its center value is called a_i, the likelihood is calculated as:

$$\mathcal{L}_{\mathrm{syst}} = \exp(-0.5 \sum_{i,j} a_i M_{ij} a_j), \tag{7.2.4}$$

where M_{ij} represents the element (i, j) of the inverted covariance matrix of the systematic parameters.

7.2.2 Fitting method

Global best-fit point

We define the best-fit point as the set of values of the parameters for which the likelihood $\mathcal{L}$ gets the maximum value. This corresponds to a maximum likelihood estimate for the oscillation parameters $\boldsymbol{o}$ and the systematic parameters $\boldsymbol{f}$:

$$(\boldsymbol{o}, \boldsymbol{f})_{\text{Bestfit}} = \underset{\boldsymbol{o},\boldsymbol{f}}{arg\,max}\, \mathcal{L}(N_{\text{obs}}, \boldsymbol{x}, \boldsymbol{o}, \boldsymbol{f}), \tag{7.2.5}$$

where a*rg max* represents the argument of the maximum. We actually minimize $-\ln\mathcal{L}$ by using the Minuit2 package [186]. It is likely that $-\ln\mathcal{L}$ has multiple local minima in the $\sin^2\overline{\theta}_{23}$-$|\Delta\overline{m}^2_{32}|$ plane. Therefore, the fitting is repeated several times with various initial values of the parameters in the $\sin^2\overline{\theta}_{23}$-$|\Delta\overline{m}^2_{32}|$ plane. The global best-fit point is the point which gives the lowest value of $-\ln\mathcal{L}$ among the fits.

Marginal likelihood

The likelihood $\mathcal{L}$ depends not only on the oscillation parameters we are trying to measure ($\boldsymbol{o}$) but also on the systematic parameters $\boldsymbol{x}$ (the energy-scale parameter) and $\boldsymbol{f}$. To obtain the confidence regions in the $\sin^2\overline{\theta}_{23}$-$|\Delta\overline{m}^2_{32}|$ plane, we need to construct a likelihood function which depends only on $\boldsymbol{o}$ while taking into account the effect of the systematic uncertainties. In this analysis we use a Bayesian marginalization method, where we compute the marginal likelihood $\mathcal{L}_{\text{marg}}$ by integrating the likelihood over the systematic parameters $\boldsymbol{x}$ and $\boldsymbol{f}$. In practice, we throw $\boldsymbol{x}$ and $\boldsymbol{f}$ according to their prior distribution $\mathcal{L}_{syst}(\boldsymbol{f})$ $N(= 10^4)$ times and calculate the averaged likelihood using the obtained random-number parameters $\boldsymbol{x}_i$ and $\boldsymbol{f}_i$:

$$\mathcal{L}_{\text{marg}}(N_{\text{obs}}, \boldsymbol{o}) = \frac{1}{N}\sum_{i=1}^{N} \mathcal{L}(N_{\text{obs}}, \boldsymbol{x}_i, \boldsymbol{o}, \boldsymbol{f}_i) \tag{7.2.6}$$

Confidence level intervals

Confidence regions of the oscillation parameters are obtained by the constant $\Delta\chi^2$ method [19]. $\Delta\chi^2$ is defined as:

$$\Delta\chi^2(\boldsymbol{o}) = -2\ln\left(\frac{\mathcal{L}_{\text{marg}}(\boldsymbol{o})}{\max(\mathcal{L}_{\text{marg}}(\boldsymbol{o}))}\right), \tag{7.2.7}$$

where $\max(\mathcal{L}_{\text{marg}}(\boldsymbol{o}))$ represents the maximum of the marginal likelihood over the range of values of the oscillation parameters considered. We then define the interval as the region of the parameter space where $\Delta\chi^2$ is smaller than a certain fixed value. We use the standard values presented in table 7.6. When we obtain 1-dimensional $\Delta\chi^2$ distributions of the $\sin^2\overline{\theta}_{23}$ ($|\Delta\overline{m}^2_{32}|$), the other oscillation parameter, $|\Delta\overline{m}^2_{32}|$ ($\sin^2\overline{\theta}_{23}$), is marginalized by using the results from the ν_μ+ν_e joint fit analysis in the neutrino mode [69].

Table 7.6: Standard $\Delta\chi^2$ values for confidence intervals.

coverage probability	1 parameter	2 parameters
68.3% (1σ)	1	2.3
90.0%	2.71	4.61

7.3 Effect of the systematic uncertainties

Systematic uncertainties in this analysis are composed of the neutrino flux uncertainties, the neutrino-nucleus cross-section uncertainties, and the far detector uncertainties. These uncertainties are described in Chapter 6. The uncertainty sizes of each parameter and the full correlation matrix are shown in fig. 7.2.

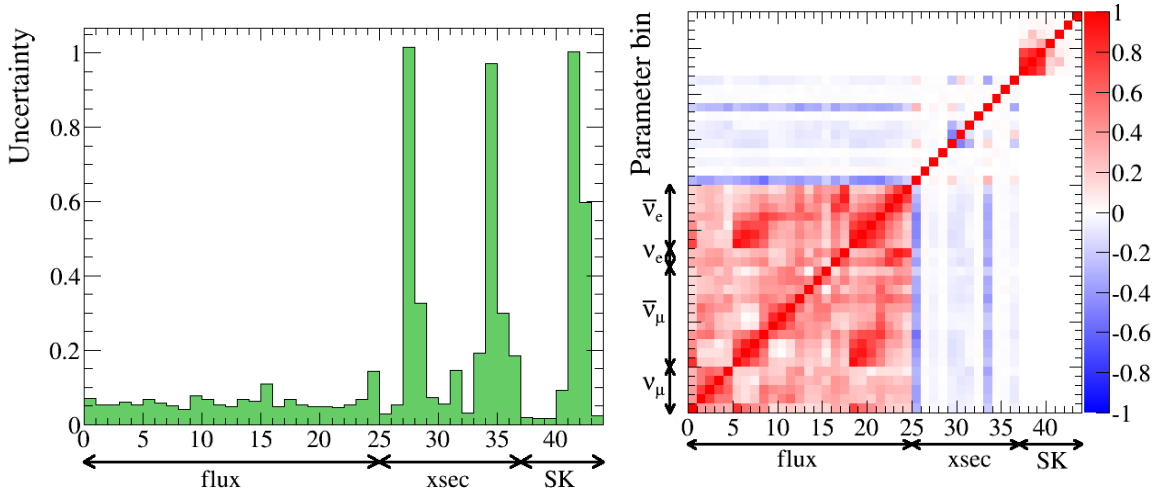

Figure 7.2: Uncertainty size (left plot) and correlations (right plot) between the 44 systematic parameters of the analysis. First 25 parameters are the neutrino flux parameters, next 12 parameters are the neutrino-nucleus cross-section parameters, next 6 parameters are the SK detector and FSI-SI parameters, and the final parameter is the energy-scale parameter at the far detector.

7.3.1 Variation of the expected number of events from each systematic source

In order to see the contribution from each systematic source, variations of the expected number of events for the nominal oscillation parameters are computed. Tables 7.7, 7.8, 7.9 show -3σ, -1σ, 1σ, 3σ variations of the expected number of events with each parameter. Here only 1 parameter is varied at a time and the other parameters are fixed. For the p_F, E_B, MEC, CC coherent and SK NC parameters, -3σ and/or +3σ variations in the table 7.8 are not shown due to physical boundaries of their parameters. The far-detector energy-scaling parameter does not vary the expected number of events. The largest uncertainty comes from the MEC normalization parameter, and the second largest one comes from the SK NC normalization parameter.

Table 7.7: Variation of the expected number of events with the flux parameters.

flavor	E_ν (GeV)	-3σ	-1σ	+1σ	+3σ
ν_μ	0-0.7	34.448 (-0.320%)	34.522 (-0.107%)	34.595 (0.107%)	34.669 (0.320%)
	0.7-1.0	34.421 (-0.397%)	34.513 (-0.132%)	34.604 (0.132%)	34.696 (0.397%)
	1.0-1.5	34.130 (-1.239%)	34.416 (-0.413%)	34.701 (0.413%)	34.987 (1.239%)
	1.5-2.5	33.824 (-2.127%)	34.314 (-0.709%)	34.804 (0.709%)	35.294 (2.127%)
	2.5-30.0	33.888 (-1.940%)	34.335 (-0.647%)	34.782 (0.647%)	35.229 (1.940%)
$\bar{\nu}_\mu$	0-0.4	34.123 (-1.261%)	34.413 (-0.420%)	34.704 (0.420%)	34.994 (1.261%)
	0.4-0.5	34.307 (-0.726%)	34.475 (-0.242%)	34.642 (0.242%)	34.810 (0.726%)
	0.5-0.6	34.507 (-0.149%)	34.541 (-0.050%)	34.576 (0.050%)	34.610 (0.149%)
	0.6-0.7	34.523 (-0.102%)	34.547 (-0.034%)	34.570 (0.034%)	34.594 (0.102%)
	0.7-1.0	33.875 (-1.977%)	34.331 (-0.659%)	34.786 (0.659%)	35.242 (1.977%)
	1.0-1.5	33.878 (-1.968%)	34.332 (-0.656%)	34.785 (0.656%)	35.239 (1.968%)
	1.5-2.5	33.956 (-1.745%)	34.358 (-0.582%)	34.760 (0.582%)	35.161 (1.745%)
	2.5-3.5	34.256 (-0.875%)	34.458 (-0.292%)	34.659 (0.292%)	34.861 (0.875%)
	3.5-5.0	34.221 (-0.976%)	34.446 (-0.325%)	34.671 (0.325%)	34.896 (0.976%)
	5.0-7.0	34.473 (-0.248%)	34.530 (-0.083%)	34.587 (0.083%)	34.644 (0.248%)
	7.0-30.0	34.540 (-0.052%)	34.552 (-0.017%)	34.565 (0.017%)	34.577 (0.052%)
ν_e	0-2.5	34.555 (-0.011%)	34.557 (-0.004%)	34.560 (0.004%)	34.562 (0.011%)
	2.5-30	34.553 (-0.016%)	34.557 (-0.005%)	34.560 (0.005%)	34.564 (0.016%)
$\bar{\nu}_e$	0-0.5	34.558 (-0.001%)	34.558 (-0.000%)	34.559 (0.000%)	34.559 (0.001%)
	0.5-0.7	34.558 (-0.001%)	34.558 (-0.000%)	34.559 (0.000%)	34.559 (0.001%)
	0.7-0.8	34.558 (-0.001%)	34.558 (-0.000%)	34.559 (0.000%)	34.559 (0.001%)
	0.8-1.5	34.558 (-0.002%)	34.558 (-0.001%)	34.559 (0.001%)	34.559 (0.002%)
	1.5-2.5	34.557 (-0.004%)	34.558 (-0.001%)	34.559 (0.001%)	34.560 (0.004%)
	2.5-4.0	34.557 (-0.006%)	34.558 (-0.002%)	34.559 (0.002%)	34.560 (0.006%)
	4.0-30.0	34.556 (-0.006%)	34.558 (-0.002%)	34.559 (0.002%)	34.561 (0.006%)

7.3.2 Total variation of the expected number of events from systematic sources

Variations of the expected number of events with partial and all the parameters considering the correlation between each parameter are shown in table 7.10. They are obtained by throwing the parameters using their covariance matrix 100000 times and calculating the average variations. The neutrino-nucleus interaction parameters which are common between the near detector and the far detector are followings: M_A^{QE}, C_5^A, M_A^{RES}, BG^{RES}, CCother and NCother, where uncertainty sizes are constrained to some extent by the measurement of the near detector. Uncertainties from the flux parameters and the neutrino-nucleus interaction parameters which are common to the near detector are significantly decreased by the measurement of the near detector. The remaining neutrino-nucleus interaction parameters which are specific to the far detector are the largest uncertainties in this analysis and in particular the MEC oxygen parameter alone gives a 9.5% uncertainty. This value is smaller than the 1σ variation of the MEC parameter in table 7.8 due to the physical boundary stated in Chapter 5. The cause of the significant uncertainty of the MEC oxygen parameter is the conservatively assigned 100% uncertainty to the MEC cross section as discussed in Section 5.2.

Table 7.8: Variation of the expected number of events with the neutrino-nucleus cross-section parameters. Effect of the NC coherent parameter is merged to that of the NC other parameter. For some parameters, $\pm 3\ \sigma$ variations are not shown due to the upper and lower limits of the parameters.

parameter	-3σ	-1σ	+1σ	+3σ
M_A^{QE}	33.262 (-3.751%)	34.125 (-1.256%)	34.997 (1.269%)	35.876 (3.811%)
p_F	-	34.869 (0.898%)	34.244 (-0.910%)	33.605 (-2.759%)
MEC	-	30.690 (-11.194%)	38.427 (11.194%)	46.164 (33.582%)
E_B	-	34.555 (-0.011%)	34.564 (0.014%)	-
C_5^A	33.248 (-3.794%)	34.060 (-1.443%)	35.119 (1.621%)	36.424 (5.399%)
M_A^{RES}	33.709 (-2.458%)	34.246 (-0.906%)	34.899 (0.986%)	35.656 (3.177%)
BG^{RES}	33.740 (-2.368%)	34.243 (-0.914%)	34.918 (1.039%)	35.766 (3.493%)
ν_e/ν_μ CC	34.554 (-0.014%)	34.557 (-0.005%)	34.560 (0.005%)	34.563 (0.014%)
CC other	34.177 (-1.105%)	34.431 (-0.368%)	34.686 (0.368%)	34.940 (1.105%)
CC coherent	-	33.777 (-2.261%)	35.340 (2.261%)	36.902 (6.782%)
NC other	34.093 (-1.346%)	34.403 (-0.449%)	34.714 (0.449%)	35.024 (1.346%)

Table 7.9: Variation of the expected number of events with the far-detector parameters. For the NC parameter, -3 σ variation is not shown due to the lower limit of the parameters.

parameter	-3σ	-1σ	+1σ	+3σ
ν_μ, $\overline{\nu}_\mu$ CCQE 0-0.4 GeV	34.417 (-0.409%)	34.511 (-0.136%)	34.606 (0.136%)	34.700 (0.409%)
ν_μ, $\overline{\nu}_\mu$ CCQE 0.4-1.1 GeV	34.182 (-1.091%)	34.433 (-0.364%)	34.684 (0.364%)	34.935 (1.091%)
ν_μ, $\overline{\nu}_\mu$ CCQE 1.1-30 GeV	33.905 (-1.891%)	34.341 (-0.630%)	34.776 (0.630%)	35.212 (1.891%)
ν_μ, $\overline{\nu}_\mu$ CCnonQE	32.213 (-6.787%)	33.777 (-2.262%)	35.340 (2.262%)	36.904 (6.787%)
ν_e, $\overline{\nu}_e$ CC	34.505 (-0.155%)	34.505 (-0.155%)	34.612 (0.155%)	34.720 (0.466%)
NC	-	33.349 (-3.500%)	35.768 (3.500%)	38.187 (10.499%)

Table 7.10: Variations (RMS) of the expected number of events with partial and all the parameters.

uncertainty source		1σ variation	
		without the the ND constraint	with the the ND constraint
flux and cross section	flux only	7.1%	3.5%
	cross section common to ND	5.8%	1.4%
	(flux)×(cross section common to ND)	9.2%	3.4%
	cross section (SK only)	10.0%	
	total	13.0%	10.1%
SK	detector	3.8%	
	FSI and SI	2.1%	
	total	4.4%	
All		14.4%	11.6%

7.4 Results

In this section, we show the results of the oscillation fit. Figure 7.3 shows the two-dimensional confidence regions in the $\sin^2\overline{\theta}_{23}$–$|\Delta\overline{m}^2_{32}|$ plane. The 90% confidence regions of the T2K neutrino data [69], the SK atmospheric antineutrino data [61], the MINOS beam and atmospheric antineutino data [60] are also shown. This antineutrino disappearance result is consistent with $\sin^2\theta_{23}$ and $|\Delta m^2_{32}|$ measured by T2K. Thus, no indication of the CPT violation nor the non-standard interactions is obtained. The contour of the muon antineutrino disappearance result is much wider than the neutrino result due to smaller amount of data and larger background. This $\overline{\nu}_\mu$ disappearance result is also in good agreement with the measurements from MINOS and SK. The 90% confidence region of the T2K $\overline{\nu}_\mu$ disappearance without systematic uncertainties is also shown in fig. 7.3. This contour overlaps with that with systematic uncertainties, i.e., the effect of systematic uncertainties is negligible in this analysis. Figure 7.4 shows the one-dimensional $\Delta\chi^2$ distributions as a function of $\sin^2\overline{\theta}_{23}$ and $|\Delta\overline{m}^2_{32}|$. The best-fit values obtained are $\sin^2\overline{\theta}_{23} = 0.45$ and $|\Delta\overline{m}^2_{32}| = 2.51\times10^{-3}$ eV^2. The 68.3% confidence interval for $\sin^2\overline{\theta}_{23}$ is 0.38–0.64 and that for $|\Delta\overline{m}^2_{32}|$ is $2.26 - 2.80\times10^{-3}$ eV^2. The precision of $|\Delta\overline{m}^2_{32}|$ is slightly worse compared to MINOS (The 68.3% confidence interval for $|\Delta\overline{m}^2_{32}|$ is $2.25 - 2.73\times10^{-3}$ eV^2) and better than recent analysis of the Super-Kamiokande atmospheric data [187] (The 68.3% confidence interval for $|\Delta\overline{m}^2_{32}|$ is $2.13 - 3.00\times10^{-3}$ eV^2). The significance of excluding $\overline{\theta}_{23}= 0$ of this analysis is 7.7 σ. The precision of $\sin^2\overline{\theta}_{23}$ is similar compared to MINOS and recent analysis of the Super-Kamiokande atmospheric data [187] (The 68.3% confidence interval for $\sin^2\overline{\theta}_{23}$ is $0.36 - 0.64$). The mass-squared difference of neutrino and antineutrino is $||\Delta\overline{m}^2_{32}|-|\Delta m^2_{32}|| < 0.31\times10^{-3}$ eV^2. This precision of the mass-squared difference of neutrino and antineutrino is slightly worse compared to MINOS ($|\Delta\overline{m}^2| - |\Delta m^2| = (0.12^{+0.24}_{-0.26})\times10^{-3}$ eV^2).

The left plot of fig. 7.5 shows the reconstructed neutrino energy distribution of the 34 $\overline{\nu}_\mu$ candidate events observed at the far detector with the predictions of the cases of the best fit and no oscillation. The best-fit spectrum reproduces the data well. The bottom left plot of fig. 7.5 shows the observed data and the best-fit prediction as a ratio to the unoscillated prediction. The observed dip at the maximum disappearance energy is obvious. The right plot of fig. 7.5 shows the reconstructed neutrino energy distribution broken down into the interaction types. For lower (higher) energy region the main background comes from the NC (ν_μ) event.

7.5 Goodness-of-fit test

A goodness-of-fit test was performed in order to confirm the validity of the oscillation fit. Using the obtained best-fit values, 4000 toy datasets are generated with systematic variations and statistical fluctuations. In this test, a very coarse binning of the reconstructed neutrino energy ($0-0.4$, $0.4-0.7$, $0.7-1.0$, $1.0-2.0$ and $2.0-30.0$ GeV) is used so that each bin has a few events and the goodness-of-fit test works. Then each toy dataset is fitted in the same way as the oscillation fit of the data and $\chi^2 = -2\ln\mathcal{L}_{\text{bestfit}}$ is computed. This likelihood is the same as that used in the sensitivity study. From this χ^2 set, p-value is calculated as the fraction for which χ^2 for the toy experiment is larger than that for the data. Figure 7.6 shows the χ^2 distribution of the goodness-of-fit tests. The obtained p-value is 0.38 which indicates no disagreement between the data and the MC prediction.

7.6 Future sensitivity of the $\overline{\nu}_\mu$ disappearance analysis

By using the Asimov dataset, i.e., the dataset where all the observed quantities are set equal to their expected values, the sensitivities of the $\overline{\nu}_\mu$ disappearance analysis with larger dataset are computed. Here the sensitivities with 9.5×10^{20} POT, which is the expected total POT with an additional 1-year $\overline{\nu}$-mode

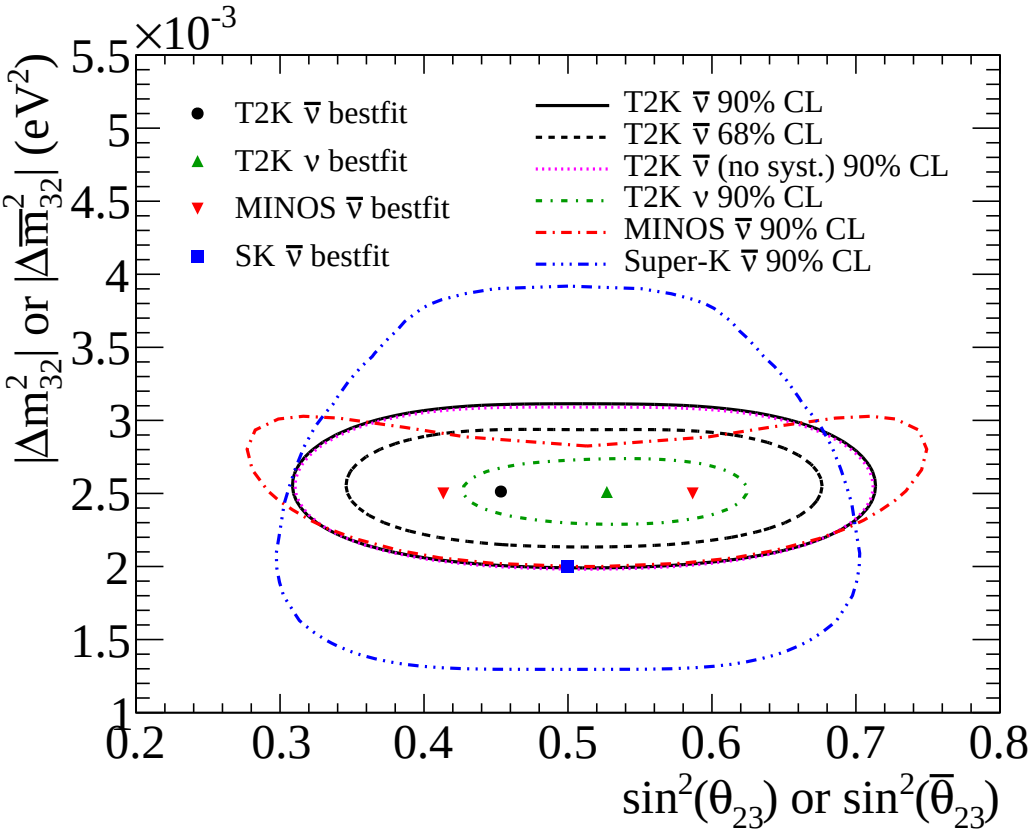

Figure 7.3: The confidence regions of $\sin^2\bar{\theta}_{23}$ and $|\Delta\bar{m}^2_{32}|$. The 90% confidence regions of the T2K neutrino data [69] in the $\sin^2\theta_{23}$ and $|\Delta m^2_{32}|$ plane, the SK atmospheric antineutrino data [61], the MINOS beam and atmospheric antineutrino data [60] and the T2K antineutrino disappearance (this data) without systematic uncertainties are also shown. There are two best-fit points of result from the MINOS experiment because MINOS measured $\sin^2 2\bar{\theta}_{23}$ and we converted that data to $\sin^2\bar{\theta}_{23}$.

data acquisition, and 39×10^{20} POT, which is half of the total planned POT data T2K will take, are shown. The oscillation parameters used are the same as those in table 7.1 and it is assumed that the neutrino and antineutrino oscillation parameters are identical. To be able to use the Asimov dataset, we need to use a different likelihood than the one used in the oscillation fit of the actual data because the number of events for each reconstructed neutrino energy bin take non-integer value, which cannot be treated in the likelihood of eq. 7.2.1. We used a binned Poisson likelihood in this case:

$$\mathcal{L}(N_{\rm obs}, \boldsymbol{x}, \boldsymbol{o}, \boldsymbol{f}) = \prod_{i=1}^{\rm Emax} P_{\rm Poisson}(N_{\rm pred}(i), N_{\rm obs}(i)) \times \mathcal{L}_{\rm syst}(\boldsymbol{f}), \tag{7.6.1}$$

where $N_{\rm pred}(i), N_{\rm obs}(i)$ are the expected and observed number of events in the ith reconstructed neutrino energy bin respectively. This likelihood and the one used in the data fit give identical results for the best-fit parameters.

Figure 7.7 shows the 90% confidence regions of this antineutrino result, the T2K neutrino result [69], Asimov dataset of the antineutrino mode with 9.5×10^{20} POT and 39×10^{20} POT with and without the systematic uncertainty. In the case of 39×10^{20} POT, it is seen that the systematic uncertainty make the

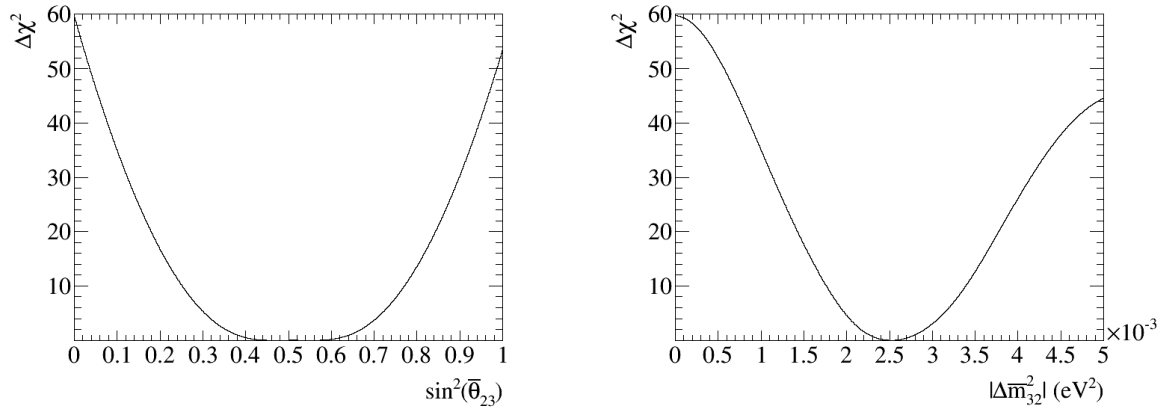

Figure 7.4: $\Delta\chi^2$ distributions as a function of $\sin^2\overline{\theta}_{23}$ (left) and $|\Delta\overline{m}^2_{32}|$ (right).

sensitivity slightly worse, but the statistical uncertainty is still the dominant uncertainty source. The precision of the sensitivity of $\overline{\nu}_\mu$ disappearance with the $\overline{\nu}$-mode dataset with 39×10^{20} POT is similar to that of the T2K neutrino result where 6.6×10^{20} POT was used.

7.7 Brief summary of the oscillation analysis

We performed the first $\overline{\nu}_\mu$ disappearance analysis in the T2K experiment using a $\overline{\nu}$-mode dataset corresponding to 4.01×10^{20} POT at the far detector. We obtained the following best-fit oscillation parameters:

$$\sin^2\overline{\theta}_{23} = 0.45, \quad |\Delta\overline{m}^2_{32}| = 2.51\ (\times10^{-3}\ \mathrm{eV}^2),$$

and 1σ confidence intervals:

$$0.38 < \sin^2\overline{\theta}_{23} < 0.64, \quad 2.26 < |\Delta\overline{m}^2_{32}| < 2.80\ (\times10^{-3}\ \mathrm{eV}^2).$$

We observed the clear $\overline{\nu}_\mu$ disappearance. A goodness-of-fit test was performed, giving a p-value of 0.38 which indicates no disagreement between the data and the MC prediction. This antineutrino disappearance result is consistent with the neutrino result from T2K. Thus, no indication of new physics, i.e., the CPT violation nor the non-standard interactions is obtained. This antineutrino result is also in good agreement with the measurements from MINOS and SK. The precision of this measurement is totally dominated by the statistical uncertainty, and will be significantly improved by accumulating more data. The dominant systematic source comes from the neutrino-nucleus interactions on oxygen, especially the charged current multi-nucleon interaction. The systematic uncertainty of the oscillation analysis can be improved, which is mentioned in the next Chapter.

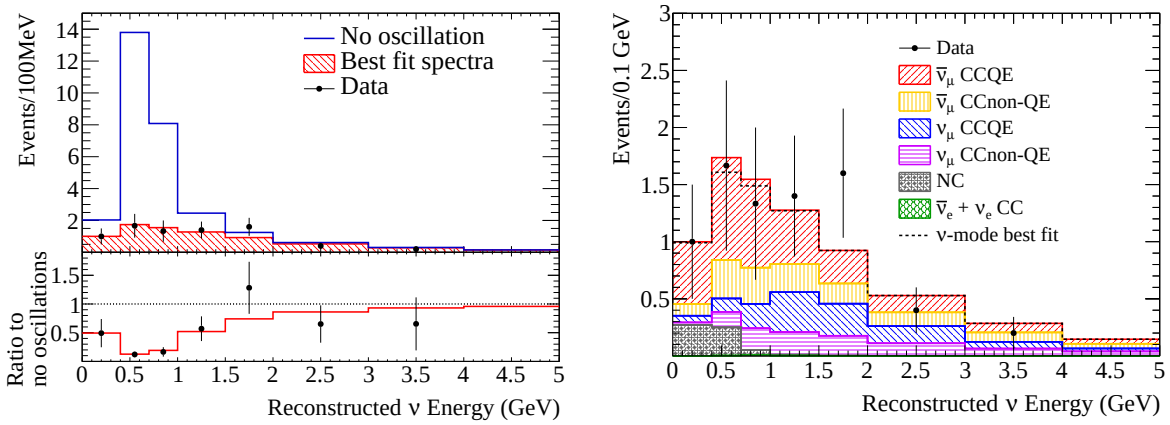

Figure 7.5: Left: reconstructed neutrino energy distribution of the 34 $\bar{\nu}_\mu$ events observed at the far detector with the predictions in the cases of best fit and no oscillation. Here a coarser binning of the reconstructed neutrino energy compared to that used in the data fit is shown for visibility. Bottom left: observed data and best-fit prediction as a ratio to the unoscillated prediction. Right: reconstructed neutrino energy distribution with different vertical axis. The best-fit prediction spectrum is broken down by the interaction types. This best-fit prediction spectrum is compared to the predicted spectrum assuming that the antineutrino oscillation parameters are identical to the default neutrino parameters (table 7.1).

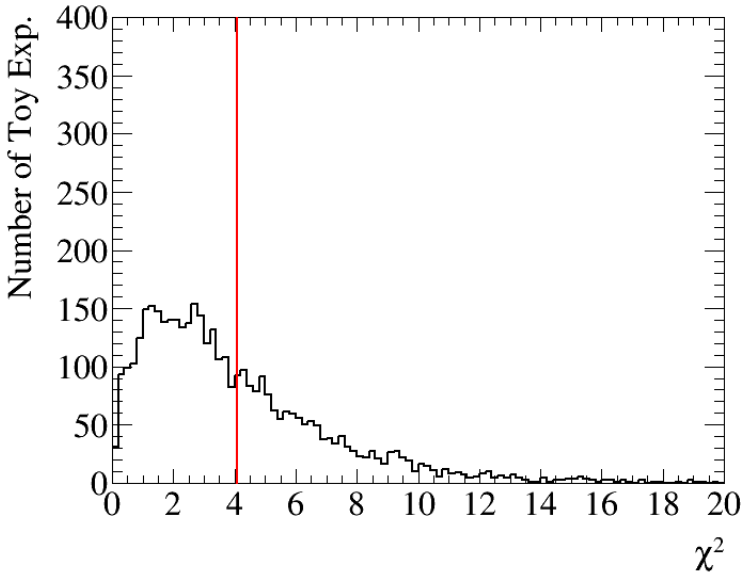

Figure 7.6: χ^2 distribution of the goodness-of-fit tests with 4000 toy datasets. The red line represents the χ^2 for the data.

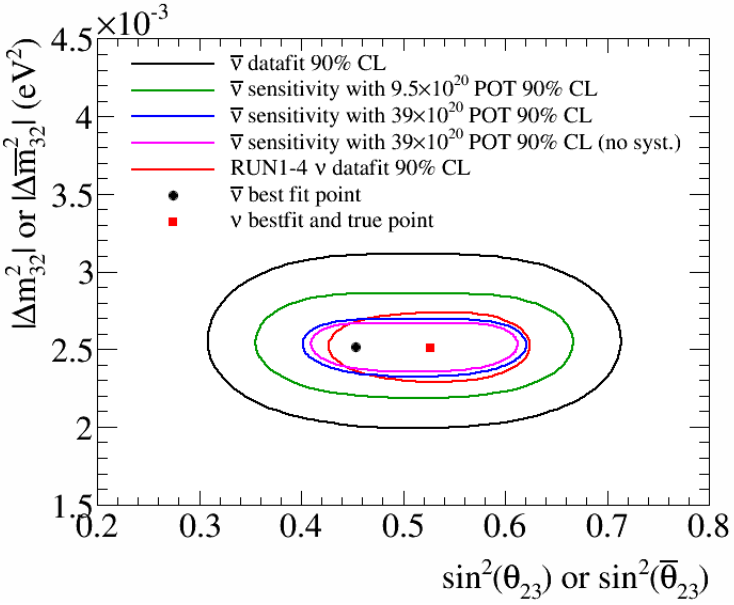

Figure 7.7: 90% confidence regions of this antineutrino result, the T2K neutrino result in the $\sin^2\theta_{23}$-$|\Delta m^2_{32}|$ plane, Asimov dataset with 9.5×10^{20} POT data and 39×10^{20} POT data with and without the systematic uncertainty.

Chapter 8

Conclusions and outlook

T2K is a long-baseline neutrino oscillation experiment which adopts the off-axis method. The quasi-monochromatic neutrino beam with a peak energy of 0.6 GeV, is measured at the near and far detectors. For the neutrino mode, observation of ν_e appearance, precise measurement of ν_μ disappearance and constraint on $\delta_{\rm CP}$ was achieved. In 2014 June, T2K started to take the antineutrino beam data by reversing the horn current and has taken 4.04×10^{20} POT data until the end of 2015. The antineutrino beam data are important not only for the $\overline{\nu}_\mu$ disappearance, but also for $\overline{\nu}_e$ appearance and the $\delta_{\rm CP}$ measurement.

The beam direction has been monitored by MUMON and INGRID and has been well controlled during the whole ν-mode and $\overline{\nu}$-mode periods. The responses of MUMON on the horn current and the proton beam position were studied during the beam commissioning, and the results are consistent with the MC prediction. We confirmed that MUMON has high sensitivity to variations of the proton beam position and horn current in both the neutrino mode and the antineutrino mode.

The neutrino fluxes and their uncertainties at the near and far detectors in the antineutrino mode as well as in the neutrino mode are predicted by the MC simulation tuned with the data from external hadron production experiments. The new CERN-NA61/SHINE 2009 thin-target data are included in the hadron production tuning for this analysis, reducing the total flux uncertainty to roughly 10% around the peak energy for both the neutrino mode and the antineutrino mode.

Phenomenogical models of neutrino-nucleus interactions has been developed and in this oscillation analysis charged current multi-nucleon interactions are newly considered. This interaction is not well understood and we assigned a conservatively large uncertainty to the cross-sectional normalization parameter of this interaction. By using the improved predictions of the neutrino flux and the neutrino-nucleus interactions, we performed the first muon antineutrino ($\overline{\nu}_\mu$) disappearance analysis in the T2K experiment.

For the near detector analysis, data in the off-axis near detector corresponding to 5.82×10^{20} POT in the neutrino mode and 4.30×10^{19} POT in the antineutrino are used. The ν_μ and $\overline{\nu}_\mu$ charged-current interaction events which arise inside the hydrocarbon target of the upstream side of the FGD are analyzed. The neutrino flux parameters and some of the neutrino-nucleus cross-section parameters are significantly constrained by the measurement at the near detector. At the far detector, Super-Kamiokande, 34 fully contained μ-like events were observed during the $\overline{\nu}$-mode beam operation.

In this oscillation analysis, to be able to see potential effects coming from new physics, the dominant antineutrino oscillation parameters for the $\overline{\nu}_\mu$ disappearance, $\overline{\theta}_{23}$ and $\Delta\overline{m}^2_{32}$, are treated independently from θ_{23} and Δm^2_{32}, where the barred parameters refer to the antineutrino oscillations. For the other oscillation parameters, identical values are used for neutrinos and antineutrinos. Total systematic uncertainties of the number of events is 11.6%, and the dominant systematic uncertainty comes from the neutrino-nucleus interactions on oxygen, especially the charged current multi-nucleon interaction. Their uncertainty are not constrained due to the difference of the nucleus target between the near and

the far detector. The analysis is based on the extended maximum likelihood method using the information on the reconstructed neutrino energy for μ-like events at the far detector. By this measurement, we clearly observe the $\overline{\nu}_\mu$ disappearance. The best-fit oscillation parameters are: $\sin^2\overline{\theta}_{23} = 0.45$ and $|\Delta\overline{m}^2_{32}| = 2.51 \times 10^{-3}$ eV^2. The 68.3% confidence interval of $\sin^2\overline{\theta}_{23}$ is $0.38 - 0.64$ and that of $|\Delta\overline{m}^2_{32}|$ is $2.26 - 2.80$ ($\times 10^{-3}$ eV^2). These results are in agreement with the $\sin^2\theta_{23}$ and $|\Delta m^2_{32}|$ measured by T2K (The 68.3% confidence interval of $\sin^2\theta_{23}$ is 0.465-0.581 and that of Δm^2_{32} is $2.39 - 2.62$ ($\times 10^{-3}$ eV^2)). The mass-squared difference of neutrino and antineutrino is $||\Delta\overline{m}^2_{32}| - |\Delta m^2_{32}|| < 0.31 \times 10^{-3}$ eV^2. We do not obtain any indication of new physics such as the CPT violation or the non-standard interactions from this measurement. This precision of the mass-squared difference of neutrino and antineutrino is slightly worse compared to MINOS ($|\Delta\overline{m}^2| - |\Delta m^2| = (0.12^{+0.24}_{-0.26}) \times 10^{-3}$ eV^2).

We already obtain competitive results with those from the beam and atmospheric antineutrino data from MINOS and the atmospheric antineutrino data from Super-Kamiokande. Since the MINOS experiment finished and the Super-Kamiokande antineutrino data used were accumulated from 1996 to 2007, which means the amount of data will not be largely increased compared to that of T2K, in near future T2K will continue to give the most precise measurement of the $\overline{\nu}_\mu$ disappearance. The precision of this measurement is totally dominated by the statistical uncertainty, but the improvements of the neutrino flux prediction and the neutrino-nucleus interaction models will be useful for future oscillation analysis.

In T2K oscillation analysis, statistical uncertainty is dominant in the neutrino mode as well as in the antineutrino mode. Hence, taking data as much as possible is most important for T2K, which will be achieved by increasing the beam power of the J-PARC main ring accelerator. The beam power is planned to be upgraded to 750 kW by increasing the number of protons per spill to 2.0×10^{14} and shortening the spill interval from 2.48 s to 1.3 s by 2019. The planned full statistics of T2K is 7.8×10^{20} POT, which will be achieved around 2021. If we take the full amount of data with the identical running time of the neutrino mode and the antineutrino mode, the amount of $\overline{\nu}$-mode data will become roughly 10 times larger than current data. Sensitivities of the $\overline{\nu}_\mu$ disappearance analysis in the case of that amount of POT are studied. The precision of the sensitivity of $\overline{\nu}_\mu$ disappearance with the $\overline{\nu}$-mode dataset with 39×10^{20} POT is similar to that of the T2K neutrino result where 6.6×10^{20} POT was used.

For future oscillation analyses, as the statistical uncertainty will decrease, reducing systematic uncertainties will be important. The flux uncertainty will be reduced by using the uncertainty of the proton-carbon production cross section measured by the NA61/SHINE experiment. Furthermore, NA61 has taken the data of the replica target, which is the same target as what T2K uses. It is expected that those replica target data will significantly reduce the flux uncertainty. The hadronic interaction uncertainty around the peak energy before the near detector constraint is expected to decrease from 9% to 4%.

There exist various kinds of ongoing neutrino interaction experiments and results from these experiments will help us understand the neutrino-nucleus interaction mechanisms and reduce uncertainties of neutrino interaction cross sections. In this analysis, data from the downstream FGD (FGD2), which contains the water target, were not used. By using the FGD2 data, the systematic uncertainty of the neutrino-nucleus interactions on oxygen, which is the dominant uncertainty in this analysis, will be significantly reduced from 10% to 4-5%. The total uncertainty in oscillation analyses is expected to decrease to a level of 5% in near future.

List of Tables

List of Figures

References

[1] W. Pauli, Letter to L. Meitner and her colleagues (1930)
[2] J. Chadwick, Verh. Phys. Gesell. **16**, 383 (1914)
[3] C.L. Cowan *et al.*, Science **124**, 103 (1956)
[4] G. Danby *et al.*, Phys. Rev. Lett. **9**, 36 (1962)
[5] K. Kodama *et al.* (DONUT Collaboration), Phys. Lett. B **504**, 218 (2001)
[6] S.M. Bilenky, arXiv:1210.3065 (2012)
[7] K. Hirata *et al.* (Kamiokande Collaboration), Phys. Rev. Lett. **58**, 1490 (1987)
[8] R. M. Bionta *et al.* (IMB Collaboration), Phys. Rev. Lett. **58**, 1494 (1987)
[9] E.N. Alekseev, L.N. Alekseeva, I.V. Krivosheina and V.I. Volchenko, Phys. Lett. B **205**, 209 (1988)
[10] M. G. Aartsen *et al.* (IceCube Collaboration), Phys. Rev. Lett. **113**, 101101 (2014)
[11] B. Pontecorvo, J. Exp. Theor. Phys. **33**, 549 (1957)
[12] B. Pontecorvo, J. Exp. Theor. Phys. **34**, 247 (1958)
[13] B. Pontecorvo, J. Exp. Theor. Phys. **26**, 984 1968)
[14] Z. Maki, M. Nakagawa, and S. Sakata, Prog. Theor. Phys. **28**, 870 (1962)
[15] M. Nakagawa, H. Okonogi, S. Sakata and A. Toyoda, Prog. Theor. Phys. **30**, 727 (1963)
[16] S. Tanaka, Y. Katayama, K. Matsumoto and E. Yamada, Prog. Theor. Phys. **28**, 675 (1962)
[17] J. Schechter and J.W.F. Valle, Phys. Rev. D **22**, 2227 (1980)
[18] M. Kobayashi and T. Maskawa, Prog. Theor. Phys. **49**, 652 (1973)
[19] K.A. Olive *et al.* (Particle Data Group), Chin. Phys. C **38**, 090001 (2014)
[20] L. Wolfenstein, Phys. Rev. D, **17**, 2369 (1978)
[21] S.P. Mikheyev and A.Y. Smirnov, Sov. J. Nucl. Phys. **42**, 913 (1985)
[22] G. Lüders, K. Dan. Vidensk. Selsk. Mat.-fys. Medd. **28**, 1 (1954)
[23] W. Pauli, Niels Bohr and the development of physics, Pergamon Press (1955)
[24] R. Jost, Hel. Phys. Acta. **30**, 409 (1957)
[25] V.A. Kostelecky and M. Mewes, Phys. Rev. D **85**, 096005 (2012)
[26] D. Colladay and V.A. Kostelecky, Phys. Rev. D **55**, 6760 (1997)
[27] D. Colladay and V.A. Kostelecky, Phys. Rev. D **58**, 116002 (1998)
[28] J.S. Diaz, V.A. Kostelecky, M. Mewes, Phys. Rev. D **80**, 076007 (2009)
[29] V.A. Kostelecky and N. Russell, Rev. Mod. Phys. **83**, 11 (2011)
[30] G.G. Raffelt, Astrophysical and Cosmological Neutrinos, arXiv:hep-ph/0208024 (2002)
[31] A. G. Cocco, G. Mangano and M. Messina, J. Phys. Conf. Ser. **110**, 082014 (2008)
[32] P. Langacker *et al.*, Nucl. Phys. B **282**, 589 (1987)
[33] T. Ohlssen, Rep. Prog. Phys. **76**, 044201 (2013)
[34] J.N. Bahcall, Phys. Rev. Lett. **12**, 300 (1964)
[35] R. Davis, D.S. Harmer, and K.C. Hoffman, Phys. Rev. Lett. **20**, 1205 (1968)
[36] K.S. Hirata *et al.* (Kamiokande Collaboration), Phys. Rev. Lett. **63**, 16 (1989)
[37] P. Anselmann *et al.* (GALLEX Collaboration), Phys. Lett. B **285**, 376 (1992)
[38] J.N. Abdurashitov *et al.* (SAGE Collaboration), Phys. Lett. B **328**, 234 (1994)
[39] T.K. Gaisser, Nucl. Phys. B (Proc. Suppl.) **35**, 209 (1994)
[40] Y. Fukuda *et al.* (Kamiokande Collaboration), Phys. Lett. B **335**, 237 (1994)
[41] D. Casper *et al.* (IMB Collaboration), Phys. Rev. Lett. **66**, 2561 (1991)
[42] T. Kafka *et al.* (Soudan Collaboration), Nucl. Phys. B (Proc. Suppl.) **35**, 427 (1994)
[43] Y. Fukuda *et al.* (Super-Kamiokande Collaboration), Phys. Rev. Lett. **81**, 1562 (1998)
[44] A. Gando *et al.* (KamLAND-Zen Collaboration), Phys. Rev. Lett. **110**, 062502 (2012)
[45] P.A.R. Ade *et al.* (Planck Collaboration), arXiv:1502.01589
[46] V.N. Aseev *et al.* (Troitsk Collaboration), Phys. Rev. D **84**, 112003 (2011)
[47] Q.R. Ahmad *et al.* (SNO Collaboration), Phys. Rev. Lett. **87**, 071301 (2001)

[48] Q.R. Ahmad *et al.* (SNO Collaboration), Phys. Rev. Lett. **89**, 011301 (2002)
[49] S. Fukuda *et al.* (Super-Kamiokande Collaboration), Phys. Rev. Lett. **86**, 5651 (2001)
[50] A. Gando *et al.* (KamLAND Collaboration), Phys. Rev. D **88**, 033001 (2013)
[51] J. Hosaka *et al.* (Super-Kamiokande Collaboration), Phys. Rev. D **74**, 032002 (2006)
[52] P. Adamson *et al.* (MINOS Collaboration), Phys. Rev. Lett. **110**, 251801 (2013)
[53] K. Abe *et al.* (T2K Collaboration), Phys. Rev. D **91**, 072010 (2015)
[54] F.P. An *et al.* (Daya Bay Collaboration), Phys. Rev. Lett. **115**, 111802 (2015)
[55] Y. Abe *et al.* (Double Chooz Collaboration), JHEP **1410**, 086 (2014)
[56] S.B. Kim *et al.* (Reno Collaboration), Phys. Rev. Lett. **108**, 191802 (2012)
[57] B.Ritcher, arXiv:hep-ph/0008222 (2000).
[58] J. Arafune, M. Koike, and J. Sato, Phys. Rev. D, **56**, 3093 (1997).
[59] A. Renshaw (Super-Kamiokande Collaboration), Phys. Procedia **61**, 345 (2015)
[60] P. Adamson *et al.* (MINOS Collaboration), Phys. Rev. Lett. **108**, 191801 (2012)
[61] K. Abe *et al.* (Super-Kamiokande Collaboration), Phys. Rev. Lett. **107**, 241801 (2011)
[62] K. Abe *et al.* (T2K Collaboration), Nucl. Instrum. Meth. A **659**, 106 (2011)
[63] K. Abe *et al.* (T2K Collaboration), Phys. Rev. Lett. **107** 041801 (2011)
[64] K. Abe *et al.* (T2K Collaboration), Phys. Rev. D **85** 031103 (2012)
[65] K. Abe *et al.* (T2K Collaboration), Phys. Rev. D **88** 032002 (2013)
[66] K. Abe *et al.* (T2K Collaboration), Phys. Rev. Lett. **111** 211803 (2013)
[67] K. Abe *et al.* (T2K Collaboration), Phys. Rev. Lett. **112** 061802 (2014)
[68] K. Abe *et al.* (T2K Collaboration), Phys. Rev. Lett. **112** 181801 (2014)
[69] K. Abe *et al.* (T2K Collaboration), Phys. Rev. D **91**, 072010 (2015)
[70] D. Beavis *et al.*, Physics Design Report, BNL-52459 (1995)
[71] K. Abe *et al.* (T2K Collaboration), arXiv:1512.02495 (2015)
[72] K. Abe *et al.* (T2K Collaboration), Prog. Theor. Exp. Phys. **2015**, 043C01 (2015)
[73] ,H. Murayama, Phys. Lett. B **597**, 73 (2004)
[74] K. Abe *et al.* (Super-Kamiokande Collaboration), Phys. Rev. D **84**, 113008 (2011)
[75] Y. Yamazaki *et al.*, KEK-Report 2002-13, JAERI-Tech 2003-044 (2003)
[76] T. Nakamoto *et al.*, IEEE Trans. on Appl. Superconductivity **14**, 616 (2004)
[77] T. Nakamoto *et al.*, Proc. of 2005 Particle Acc. Conf. (2005)
[78] T. Ogitsu *et al.*, IEEE Trans. on Appl. Superconductivity **15**, 1175 (2005)
[79] K. Yamada, Master thesis, University of Tokyo (2007)
[80] S. Bhadra *et al.*, Nucl. Instrum. Meth. A **703**, 45 (2013)
[81] T. Nakadaira *et al.*, AIP Conf. Proc. **981**, 290 (2008)
[82] T. Sekiguchi , AIP Conf. Proc. **981**, 345 (2008)
[83] A.K. Ichikawa, Nucl. Instrum. Meth. A **690**, 27 (2012)
[84] T. Sekiguchi *et al.*, Nucl. Instrum. Meth. A **789**, 57 (2015)
[85] S.Y. Suzuki *et al.*, DOI:10.1109/RTC.2014.7097441 (2014)
[86] M. Thorpe *et al.*, IEEE Nucl. Sci. Symp. Conf. Rec. **58**, 1800 (2011)
[87] K. Matsuoka *et al.*, Nucl. Instrum. Meth. A **623**, 385 (2010)
[88] K. Matsuoka *et al.*, Nucl. Instrum. Meth. A **624**, 591 (2010)
[89] K. Suzuki *et al.*, Prog. Theor. Exp. Phys. **2015** 053C01 (2015)
[90] K. Abe *et al.* (T2K Collaboration), Nucl. Instrum. Meth. A **694**, 211 (2012)
[91] T. Kikawa *et al.* (T2K Collaboration), Nucl. Phys. B, Proc. Suppl. **229** 451 (2012)
[92] M. B. Luque *et al.* (UA1 Collaboration), Nucl. Instrum. and Meth. **176**, 175 (1980)
[93] J. Altegoer *et al.* (NOMAD Collaboration), Nucl. Instrum. Meth. A **404**, 96 (1998)
[94] S. Assylbekov *et al.*, Nucl. Instrum. Meth. A **686**, 48 (2012)
[95] N. Abgrall *et al.*, Nucl. Instrum. Meth. A **637**, 25 (2011)
[96] P. A. Amaudruz *et al.*, Nucl. Instrum. Meth. A **696**, 1 (2012)

[97] I. Giomataris *et al.*, Nucl. Instrum. Meth. A **560**, 405 (2006)
[98] D. Allan *et al.*, Journal of Instrum. **8**, 10019 (2013)
[99] S. Aoki *et al.*, Nucl. Instrum. Meth. A **698**, 135 (2013)
[100] Y. Fukuda *et al.* (Super-Kamiokande Collaboration), Nucl. Instrum. Meth. A **501**, 418 (2003)
[101] T.Hiraki (T2K Collaboration), Proceedings of Science, **PoS(FPCP2015)**, 068 (2015)
[102] S.J. Harris and C.E. Doust, Radiat. Res. **66**, 11 (1976)
[103] T. Nakamura *et al.*, Nucl. Instrum. Meth. A **556**, 80 (2006)
[104] J. Koike, D.M. Parkin, and T.E. Mitchell, Appl. Phys. Lett. **60-12**, 1450(1992)
[105] W. Adam *et al.* (RD42 Collaboration), Nucl. Instrum. Meth. A **565**, 278 (2006)
[106] A. Vasilescu, ROSE/TN/97-2 (1997)
[107] K. Abe *et al.* (T2K Collaboration), Phys. Rev. D **87**, 012001 (2013)
[108] R. Brun, F. Carminati and S. Giani, CERN-W5013 (1993)
[109] C. Zeitnitz and T.A. Gabriel, Nucl. Instrum. Meth. A **349**, 106 (1994)
[110] A. Ferrari *et al.*, CERN-2005-10, INFN-TC-05-11, SLAC-R-773 (2005)
[111] T.T. Böhlen *et al.*, Nuclear Data Sheets 120, 211-214 (2014)
[112] N. Abgrall *et al.* (NA61/SHINE Collaboration), JINST **9**, P06005 (2014)
[113] N. Abgrall *et al.* (NA61/SHINE Collaboration), *Phys. Rev. C* **84**, 034604 (2011)
[114] N. Abgrall *et al.* (NA61/SHINE Collaboration), *Phys. Rev. C* **85**, 035210 (2012)
[115] N. Abgrall *et al.* (NA61/SHINE Collaboration), *Phys. Rev. C* **89**, 025205 (2014)
[116] N. Abgrall *et al.* (NA61/SHINE Collaboration), arXiv:1510.02703 (2015)
[117] A. S. Carroll *et al.*, Phys. Lett. B **80**, 319 (1979)
[118] M. Bonesini *et al.* Eur. Phys. J. C, **20** (2001)
[119] R. Feynman, Phys. Rev. Lett. **23**, 1415 (1969)
[120] J.V. Allaby *et al.*, Technical Report No. CERN-70-12 (1970)
[121] T. Abbott *et al.*, Phys. Rev. D **45**, 3906 (1992)
[122] M. Apollonio *et al.*, Phys. Rev. C **80**, 035208 (2009)
[123] R.J. Abrams *et al.*, Phys. Rev. D **1**, 1917 (1970)
[124] J.V. Allaby *et al.*, Yad. Fiz. **12**, 538 (1970)
[125] B.W. Allardyce *et al.*, Nucl. Phys. A **209**, 1 (1973)
[126] G. Bellettini *et al.*, Nucl. Phys. **79**, 609 (1966)
[127] B.M. Bobchenko *et al.*, Sov. J. Nucl. Phys. **30**, 805 (1979)
[128] J.W. Cronin *et al.*, Phys. Rev. **107**, 1121 (1957)
[129] F.F. Chen *et al.*, Phys. Rev. **99** ,857 (1955)
[130] S.P. Denisov *et al.*, Nucl. Phys. B **61**, 62 (1973)
[131] M.J. Longo and B. J. Moyer, Phys. Rev. **125**, 701 (1962)
[132] A.V. Vlasov *et al.*, Sov. J. Nucl. Phys. **27**, 222 (1978)
[133] T. Eichten *et al.*, Nucl. Phys. B **44**, 333 (1972)
[134] B. Bartar *et al.*, Eur. Phys. J. C **73**, 2364 (2013)
[135] J.A. Formaggio and G.P. Zeller, Rev. Mod. Phys. **84**, 1307 (2012)
[136] Y. Hayato, Nucl. Phys. Proc. Suppl. B **112**, 171 (2002)
[137] Y. Hayato, Acta Phys. Pol. B **40**, 2477 (2009)
[138] G. Mitsuka, AIP Conf. Proc. **981**, 262 (2008)
[139] C.L. Smith, Phys. Rept. **3**, 261 (1972)
[140] D. Mund *et al.*, Phys. Rev. Lett. **110**, 172502 (2012)
[141] O. Benhar *et al.*, Nucl. Phys. A **579**, 493 (1994)
[142] R.A. Smith and E.J. Moniz, Nucl. Phys. B **43**, 605 (1972)
[143] R.A. Smith and E.J. Moniz, Nucl. Phys. B **101**. 547 (1975)
[144] J. Nieves, J.E. Amaro, and M. Valverde, Phys. Rev. C **70**, 055503 (2004)
[145] D. Casper, Nucl. Phys. (Proc. Supp.) **112**, 161 (2002)

[146] C. Wilkinson *et al.*, arXiv:1601.05592 (2016)
[147] J. Nieves, I.R. Simo, and M.J.V. Vacas, Phys. Rev. C **83**, 045501 (2011)
[148] J. Nieves *et al.*, Phys. Rev. D **85**, 113008 (2012)
[149] A. Gil, J. Nieves, and E. Oset, Nucl. Phys. A **627**, 543 (1997)
[150] R. Gran *et al.*, Phys. Rev. D **88**, 113007 (2013)
[151] D. Rein and L.M. Sehgal, Ann. Phys. **133**, 79 (1981)
[152] K.M. Graczyk and J.T. Sobczyk, Phys. Rev. D **77**, 053001 (2008)
[153] O. Lalakulich and E.A. Paschos, Phys. Rev. D **71**, 074003 (2005)
[154] S.L. Adler, Ann. Phys. **50**, 189 (1968)
[155] M. Glück, E. Reya, and A. Vogt, Eur. Phys. J. C **5**, 461 (1998)
[156] A. Bodek and U.K. Yang, AIP Conf. Proc. **670**, 110 (2003)
[157] A. Bodek, I. Park, and U.K. Yang, Nucl. Phys. B, Proc. Suppl. **139**, 113 (2005)
[158] T. Sjostrand, Comput. Phys. Commun. **82**, 74 (1994)
[159] M. Nakahata *et al.*, J. Phys. Soc. Jpn. **55**, 3786 (1986)
[160] D. Rein and L.M. Sehgal Nucl. Phys. B **223**, 29 (1983)
[161] D. Rein and L.M. Sehgal Nucl. Phys. B **657**, 207 (2007)
[162] S.L. Adler, Phys. Rev. **135**, 963 (1964)
[163] N. Metropolis *et al.*, Phys. Rev. **110**, 185 (1958)
[164] L.L. Salcedo *et al.*, Nucl. Phys. A **484**, 557 (1988)
[165] A. Aguilar-Arevalo *et al.* (MiniBooNe Collaboration), Phys. Rev. Lett. **100**, 032301 (2008)
[166] A. Aguilar-Arevalo *et al.* (MiniBooNe Collaboration), Phys. Rev. D **88**, 032001 (2013)
[167] L. Fields *et al.* (MINERvA Collaboration), Phys. Rev. Lett. **111**, 022501 (2013)
[168] G. Fiorentini *et al.* (MINERvA Collaboration), Phys. Rev. Lett. **111**, 022502 (2013)
[169] E.J. *Moniz et al.*, Phys. Rev. Lett. **26**, 445 (1971)
[170] C. Wilkinson *et al.*, Phys. Rev. D **90**, 112017 (2014)
[171] M. Hasegawa *et al.* (K2K Collaboration), Phys. Rev. Lett. **95**, 252301 (2005)
[172] K. Hiraide *et al.* (SciBooNE Collaboration), Phys. Rev. D **78**, 112004 (2008)
[173] A. Higuera *et al.* (MINERvA Collaboration), Phys. Rev. Lett. **113**, 261802 (2014)
[174] Y. Kurimoto *et al.* (SciBooNE Collaboration), Phys. Rev. D **81**, 111102 (2010)
[175] P. Adamson *et al.* (MINOS Collaboration), Phys. Rev. D **81**, 072002 (2010)
[176] M. Day and K. McFarland, Phys. Rev. D **86**, 053003 (2012)
[177] S. Agostinelli *et al.* (GEANT4 Collaboration), Nucl. Instrum. Meth. B **506**, 250 (2003)
[178] A. Cervera-Villanueva *et al.*, Nucl. Inst. Methrum. A **534**, 180 (2004)
[179] R.B. Patterson *et al.* (Super-Kamiokande Collaboration), Nucl. Instrum. Meth. A **608**, 206 (2009)
[180] P. Perio, AIP Conf.Proc. **1405**, 223 (2011)
[181] K. Ieki *et al.*, Phys. Rev. C **92**, 035205 (2015)
[182] `http://www.phy.duke.edu/~raw22/public/Prob3++/`
[183] V. Barger *et al.*, Phys. Rev. D **22**, 2718 (1980).
[184] K. Hagiwara, N. Okamura, and K. Senda, Journal of High Energy Physics **2011**, 82 (2011)
[185] R. Barlow, Nucl. Instr. and Meth. A **297**, 496 (1990)
[186] `http://seal.web.cern.ch/seal/snapshot/work-packages/mathlibs/minuit/`
[187] M.F. Thomas, Ph.D. thesis, University of Tokyo (2015)